Advances in Atom and Single Molecule Machines
Series Editor: Christian Joachim

Christian Joachim *Editor*

Atomic Scale Interconnection Machines

Proceedings of the 1st AtMol European Workshop Singapore 28th–29th June 2011

Springer

Advances in Atom and Single Molecule Machines

For further volumes:
http://www.springer.com/series/10425

Christian Joachim
Editor

Atomic Scale Interconnection Machines

Proceedings of the 1st AtMol European Workshop Singapore 28th–29th June 2011

Springer

Christian Joachim
CNRS
GNS
Rue J. Marvig 29
31055 Toulouse Cedex
France

ISSN 2193-9691
ISBN 978-3-642-28171-6
DOI 10.1007/978-3-642-28172-3
Springer Heidelberg New York Dordrecht London

e-ISSN 2193-9705
e-ISBN 978-3-642-28172-3

Library of Congress Control Number: 2012933100

Printed on acid-free paper

Springer is part of Springer Science+Business Media (www.springer.com)

Preface

Atom Technology is essential for the construction and study of dangling bond logic circuits, single molecule logic gates and for single molecule mechanical machineries. One of the first instruments urgently required for experimental work at the atomic scale is a machine with an atomic scale precision offering the possibility to exchange information and energy with single and well-identified molecule machineries. These nano-communication-like machines must also offer dedicated navigation abilities for the interconnection probes to be positioned on the device with atomic scale precision. As a result of this need for such instruments in many laboratories around the world, the Integrated European Project AtMol decided to organize its first biannual workshop on the topic of "Atomic Scale Interconnection Machines". Fully supported by the ICT-FET of INFSO at the European level, AtMol was launched on 1 January 2011, for 4 years, with the objective to construct the first ever complete molecular chip. This Atomic Scale Interconnection Machines workshop event took place at IMRE in June 2011, where IMRE-A*STAR is the AtMol partner based in Singapore.

This first volume of the new Springer Series "Advances in Atom and Single Molecule Machines" compiles all the contributions presented during this workshop. The workshop was the first to involve a large number of laboratories from all around the world working on the construction, the development or usage of atomic scale interconnection machines. All the possible categories of these very often large, ultra high vacuum (UHV) instruments were presented by different communities, from academics to high-tech companies who develop the new hardware, or control the software of these machines. Examples include, multiple LT-UHV STM systems, multiple LT-NC-AFM systems, optical navigation, SEM navigation and even the first machines demonstrating single atom and molecular manipulation capability together with the nano-communication setup.

The organizing committee of the first workshop of the AtMol series is happy to thank the ICT-FET division of European Commission and A*STAR of Singapore for the financial support to organize this first workshop. We are expecting to

launch a quite unique series of events to boost Atom Technologies from a practical point of view. The upcoming workshops in the AtMol series will be announced on the www.atmol.eu official web site. The organizing committee also wishes to thank all the participants in Singapore for a very dynamic workshop.

For the organizing committee
C. Joachim

Contents

High Precision Local Electrical Probing: Potential and Limitations for the Analysis of Nanocontacts and Nanointerconnects

B. Guenther, M. Maier, J. Koeble, A. Bettac, F. Matthes, C. M. Schneider and A. Feltz

Abstract The variety of approaches for individual nanoscale devices is tremendous. In contrast however, comprehensive concepts toward electrically integrated and therefore functional devices are rare. The individual metallic contact interface represents one of the main challenges and high precision local electrical probing has the potential to increase efficiency in evaluating different approaches. To meet the involved requirements, we have established and being advancing an approach for nano-scale electrical probing at low temperatures by integrating scanned probe microscopic (SPM) technology with high resolution electron microscopy.

1 Introduction

A major challenge in the development of novel devices in nano- and molecular electronics is their interconnection with larger scale electrical circuits required to control and characterize their functional properties. Local electrical probing by multiple probes with ultimate scanning tunneling microscope (STM) precision can significantly improve efficiency in analyzing individual nano-electronic devices without the need of a full electrical integration.

Among a very few commercial approaches, the Omicron UHV NANOPROBE has been established as a suitable instrument for local electrical probing on

B. Guenther · M. Maier (✉) · J. Koeble · A. Bettac · A. Feltz
Omicron NanoTechnology GmbH, Limburger Strasse 75, 65323 Taunusstein, Germany
e-mail: m.maier@omicron.de

A. Bettac · F. Matthes · C. M. Schneider
Forschungszentrum Jülich, Jülich, Germany
e-mail: a.bettac@omicron.de

C. Joachim (ed.), *Atomic Scale Interconnection Machines*, Advances in Atom and Single Molecule Machines, DOI: 10.1007/978-3-642-28172-3_1,

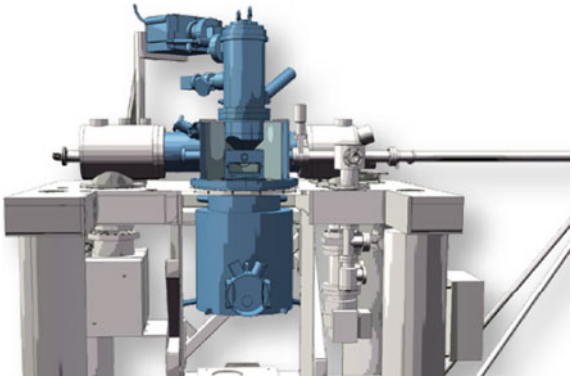

Fig. 1 Schematic showing the LT NANOPROBE concept. LHe/LN2 bath cryostats at the *bottom*, SEM column at the *top*

nano-structures down to structure sizes in the 10–100 nm range [1–9]. The major technical requirements of such sophisticated instrumentation are:

- Rapid and simultaneous scanning electron microscopy (SEM) navigation of four local STM probes on small structures
- Localization of nanostructures by high resolution SEM (UHV Gemini)
- Individual probe fine positioning by atomic scale STM imaging
- STM-based probe approach for "soft-landing" of sharp and fragile probes and controlled electrical contact for transport measurements
- Preparation techniques toward sharp and clean STM tips
- Temperature variation from 50 to 500 K
- Suitable low noise signal re-routing for transport measurements with third party electronics

Although the UHV NANOPROBE has been successfully used for various applications, today's scientific requirements motivated the development of the next generation probing system. As a sophisticated instrument the LT NANOPROBE has been specifically designed for local and non-destructive 4-point probe measurements at low temperatures. It opens up new research opportunities in nano-electronics, spintronics and molecular electronics. Besides STM probe fine navigation and imaging, the excellent STM performance level of the LT NANOPROBE expands applications to tunneling spectroscopy and even the creation or modification of nano-structures by an ultimately precise STM probe.

The R&D project is driven by the following major milestones:

- Operation at temperatures of $T < 5$ K for STM imaging and STM-based probing
- SEM navigation at base temperature of $T < 5$ K
- Thermal equilibrium of sample and probes for (i) extremely low thermal drift and electrode positioning accuracy in time and (ii) defined temperature of the local electrical contact
- Performance and stability level of each individual STM Probe suitable for STM spectroscopy and atom manipulation (Fig. 1).

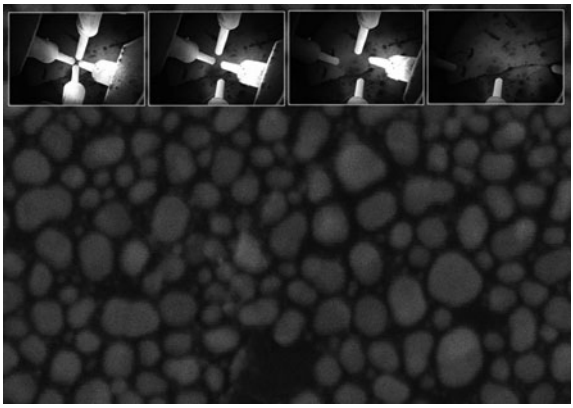

Fig. 2 Sequence of SEM images taken at T < 5 K. *Inserts.* Coarse positioning of the four STM probes under SEM navigation. *Main image.* High resolution SEM imaging on Au islands on carbon with a typical island size of smaller than 100 nm

2 SEM Imaging and Tip Navigation

For the navigation of four independent STM probes, simultaneous SEM imaging is indispensable to bridge dimensions from the mm-down to the nm-scale. The SEM enables a large field of view for probe coarse positioning as well as fine positioning and rapid localization of small structures with its high resolution capabilities. As a suitable tool for that purpose, the UHV Gemini column offers unsurpassed resolution under true UHV conditions (Fig. 2).

In combination with the Low Temperature UHV NANOPROBE, the in-lens Secondary Electron Detector (SED) represents a key advantage. Only one small access port in the thermal shield compartment of the microscope stage (at T < 5 K) is needed, thus minimizing thermal impact, while still offering a suitable signal for high resolution imaging.

3 Microscope Stage Design

Cooling the whole microscope to LHe temperatures requires the stage to be extremely compact with only 100 × 100 mm in size—a real challenge if 4 STM need to be fully functional, independent and highly stable.

An efficient thermal shield compartment allows for temperatures well below 5 K, extremely low thermal drift and thermal equilibrium of sample and probes. In addition, the integration of high resolution SEM navigation requires a small SEM working distance and thus makes a dedicated STM concept indispensable. A sophisticated shared stack scanner allows for a very compact and flat design, while ensuring highly linear, orthogonal and stable STM scanning characteristics.

For ultimate STM performance the microscope stage employs an effective eddy current damped spring suspension. The system provides a locking mechanism to lock the spring suspension for optimal SEM working conditions (Fig. 3).

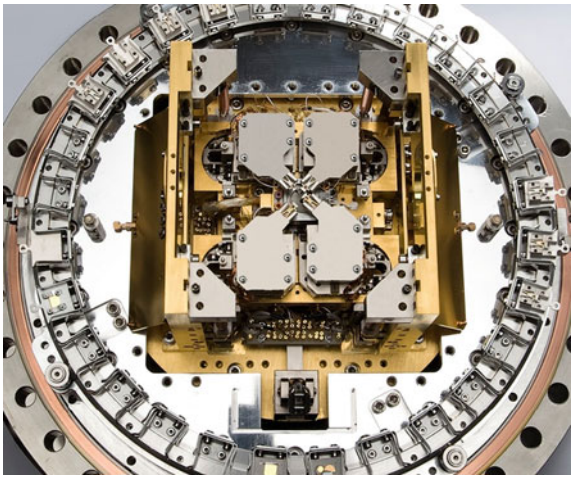

Fig. 3 Image of the LT NANOPROBE stage

4 Independent SPM's

The microscope stage carries four individual SPM modules with independent and guided 3D coarse positioning of XYZ = 5 × 5 × 3 mm. The sample can be independently positioned by XY = 4 × 4 mm. Omicron's patented piezo-electric inertia drives provide highly reliable and efficient navigation with step sizes from a few tens of nm′s up to several hundred nm. Fine positioning and STM imaging with atomic resolution is achieved by shared stack scanners with XY = 1 × 1 μm scan (fine positioning) range at LHe temperatures (Fig. 4).

The sample reception stage is compatible with Omicron's standard flat sample plates with a maximum sample size of 10 × 10 mm. A fast and secure tip and sample exchange is crucial for ease of use and high throughput. Individual probe modules are moved to a tip exchange position and spring loaded tip carriers can easily be exchanged by wobble-stick. Twenty-eight samples or tips are accessible from the stage-integrated storage carousel.

5 Cryostat Design: Cooling Down to T < 5 K

The use of a high resolution SEM column for tip navigation from above implies an unconventional cryostat concept. A specifically designed bath cryostat with LN2 and LHe reservoirs allows for a measurement time of >36 h at T < 5 K and cools the microscope stage from below. A LN2 and LHe double shielding minimizes thermal impact on the stage and employs doors for tip/sample exchange, operated by wobble-sticks. In addition, the sample stage facilitates a controlled thermal coupling for a defined sample temperature and quick sample cool down (Fig. 5).

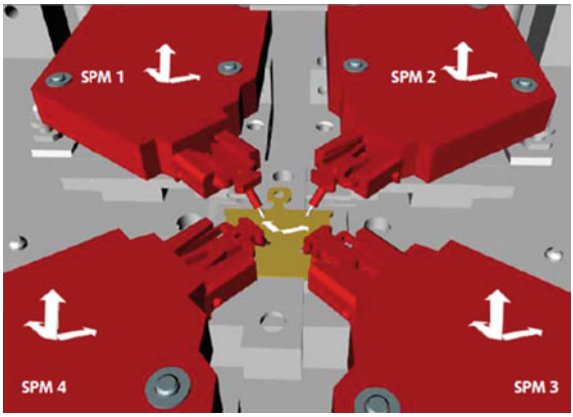

Fig. 4 Schematic showing the four dedicated shared stack scanners

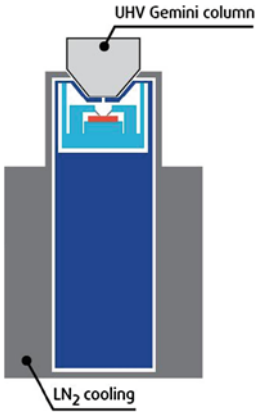

Fig. 5 Schematic showing the cryostat and shielding set-up. *Blue*: LHe reservoir, *gray*: LN2 reservoir

6 Electrical Transport Measurements

During STM approach the distance control is based on tunneling current feedback and therefore requires a dedicated low noise I/V converter. When the tunneling contact is established, the probe-sample distance is well controlled in the nm range. To establish an electrical contact and to control its resistance, the STM feedback is de-activated and the probe is manually approached by piezo scanner z-offset. However, a permanently connected I/V converter in the signal line prevents transport measurements in four point configuration. Thus, a pA STM compatible and TTL trigger controlled switching technology is used to route signals of the four probes to external BNC connectors. Based on LabVIEW, experimental workflows are integrated with third party measurement electronics (Fig. 6).

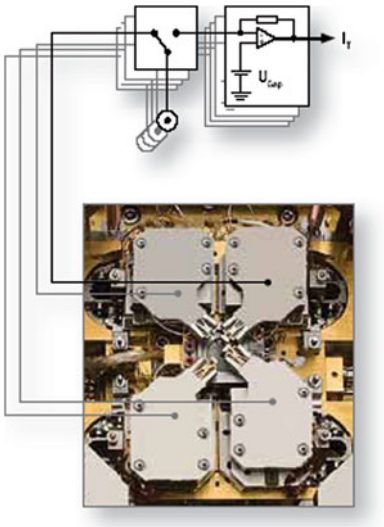

Fig. 6 The schematic is showing the function principle of signal re-routing from the probe tip either to the I/V converter for STM feedback or to a BNC connector

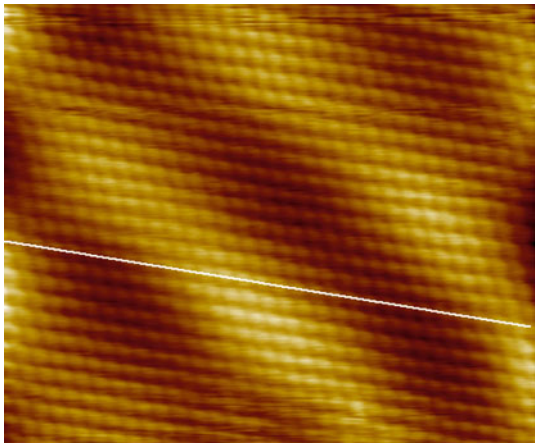

Fig. 7 STM on Au(111) at a temperature below 5 K. $U_{GAP} = 310$ mV, $I_T = 3$ nA, $T_{SAMPLE} = 4.5$ K. The Herringbone structure is clearly visible

7 STM

STM is the key to advancing probing technology into the nanometer scale. It ensures extremely accurate probe positioning and STM-based safe tip approach of fragile probe tips having diameters in the range of a few ten's of nanometers or less. STM imaging is required for final precise positioning of the probe tip when it shadows nm-sized structures in the SEM field of view or if the structures are even smaller than accessible by SEM.

All four probe modules of the LT NANOPROBE achieve state of-the-art STM performance on metals with pm stability and thus open up the route for new experiments beyond local electrical probing (Figs. 7 and 8).

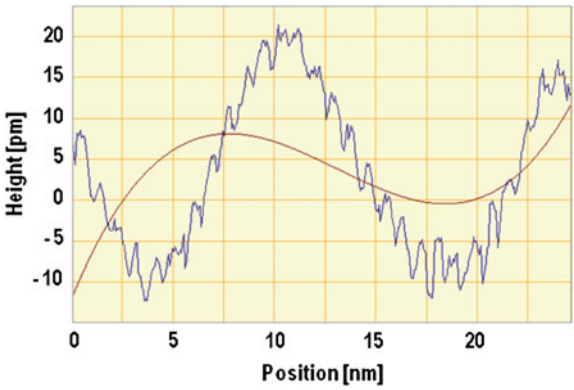

Fig. 8 Line profile of the STM image. The typical corrugation is approx. 6 pm, the z-stability is in the range of 1–2 pm

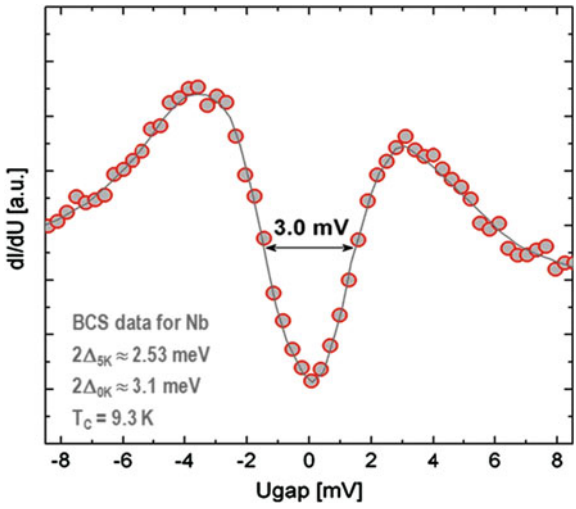

Fig. 9 Scanning Tunneling Spectroscopy (STS) measurement at temperatures below 5 K, using a Nb-tip on a Au(111) sample. UGAP = 80 mV, I_{SET} = 40 nA, f_{MOD} = 540 Hz, U_{MOD} = 140 μV

To further evaluate the STM/STS performance, tunneling spectroscopy measurements have been performed. As a very simple but reliable experiment, superconducting Niobium has been used as tunneling tip on a Au(111) sample. Modulation spectroscopy measurements at a temperature below 5 K reveal the superconducting gap with size of approx. 3 meV. Deviations of the gap shape and size from BCS can be attributed to a non-clean Nb-tip and related parallel tunneling processes (e.g. ohmic shunt). Nevertheless the measurements represent a physical proof of (i) the tunneling tip being superconducting and (ii) at a temperature significantly below T_C (Fig. 9).

8 Summary

The Low Temperature NANOPROBE defines a new class of analytical instrumentation that merges SEM navigated nanoprobing at LHe temperatures with high performance STM imaging, spectroscopy and manipulation. It thus may represent a "next generation SPM" for creating functional devices by SPM technologies and investigate electrical properties in one experiment. The shown measurements in SEM, STM and scanning tunneling spectroscopy (STS) at low temperatures represent a first performance proof for its suitability for advanced STM modes such as STS, Inelastic electron tunneling spectroscopy (IETS), SP-STM (Spin-polarized STM) and atom manipulation.

References

1. Gorzny, M.L., Walton, A.S., Wnek, M., Stockley, P.G., Evans, S.D.: Four-probe electrical characterization of Pt-coated TMV-based nanostructures. Nanotechnology **19**, 165704–165708 (2008)
2. Wei, Z., Wang, D., Kim, S., Kim, S.Y., Hu, Y., Yakes, M.K., Laracuente, A.R., Dai, Z., Marder, S.R., Berger, C., King, W.P., de Heer, W.A., Sheehan, P.E., Riedo, E.: Nanoscale tunable reduction of graphene oxide for graphene electronics. Science **328**, 1373–1376 (2010)
3. Bannani, A., Bobisch, C., Möller, R.: Ballistic electron microscopy of individual molecules. Science **315**, 1824–1828 (2007)
4. Sutter, P.W., Flege, J.I., Sutter, E.A.: Epitaxial graphene on ruthenium. Nat. Mater. **7**, 406–411 (2008)
5. Soubiron, T., Stiufiuc, R., Patout, L., Deresmes, D., Grandidier, B., Stievenard, D., Koeble, J., Maier, M.: Transport limitations and Schottky barrier height in titanium silicide nanowires grown on the Si(111) surface. Appl. Phys. Lett. **90**, 102112–102114 (2007)
6. Walton, A.S., Allen, C.S., Critchley, K., Gorzny, M.L., Mc Kendy, J.E., Brydson, R.M.D., Hickey, B.J., Evans, S.D.: Four-probe electrical transport measurements on individual metallic nanowires. Nanotechnology **18**, 065204–065209 (2007)
7. Borras, A., Groening, O., Koeble, J., Groening, P.: Connecting organic nanowires. Adv. Mater. **21**, 4816–4819 (2009)
8. Huang, Q., Lilley, C.M., Divan, R.: An in situ investigation of electromigration in Cu nanowires. Nanotechnology **29**, 075706–075711 (2009)
9. Simpkins, B.S., Pehrsson, P.E., Laracuente, A.R.: Electronic conduction in GaN nanowires. Appl. Phys. Lett. **88**, 072111–072113 (2006)

Ultra-Compact Multitip Scanning Probe Microscope with an Outer Diameter of 50 mm

Vasily Cherepanov, Evgeny Zubkov, Hubertus Junker, Stefan Korte, Marcus Blab, Peter Coenen and Bert Voigtländer

Abstract We present a multitip scanning tunneling microscope (STM) where four independent STM units are integrated on a diameter of 50 mm. The coarse positioning of the tips is done under the control of an optical microscope or an SEM in vacuum. The heart of this STM is a new type of piezoelectric coarse approach called Koala Drive which can have a diameter greater than 2.5 mm and a length smaller than 10 mm. Alternating movements of springs move a central tube which holds the STM tip or AFM sensor. This new operating principle provides a smooth travel sequence and avoids shaking which is intrinsically present for nanopositioners based on inertial motion with saw tooth driving signals. Inserting the Koala Drive in a piezo tube for *xyz*-scanning integrates a complete STM inside a 4 mm outer diameter piezo tube of <10 mm length. The use of the Koala Drive makes the scanning probe microscopy design ultra-compact and accordingly leads to a high mechanical stability. The drive is UHV, low temperature, and magnetic field compatible. The compactness of the Koala Drive allows building a four-tip STM as small as a single-tip STM with a drift of <0.2 nm/min and lowest resonance frequencies of 2.5 (*xy*) and 5.5 kHz (*z*). We present examples of the performance of the multitip STM designed using the Koala Drive.

1 Introduction

The controlled fabrication of self-organized nanostructures with dimensions in the single digit nanometer range is becoming possible [1]. However, the measurement of charge transport through such nanostructures is still a challenge.

V. Cherepanov · E. Zubkov · H. Junker · S. Korte · M. Blab · P. Coenen · B. Voigtländer (✉)
JARA-Fundamentals of Future Information Technology, Peter Grünberg Institut (PGI-3), Forschungszentrum Jülich, 52425 Jülich, Germany
e-mail: b.voigtlaender@fz-juelich.de

C. Joachim (ed.), *Atomic Scale Interconnection Machines*, Advances in Atom and Single Molecule Machines, DOI: 10.1007/978-3-642-28172-3_2,

One problem is to provide electrical contacts to individual nanostructures. One approach is to establish such contacts by a multitip STM in order to enable charge transport and scanning potentiometry measurements at self-assembled nanostructures. Key requirements for multitip scanning probe instruments are that (a) all tips are independently positionable from the millimeter range down to the nanometer or atomic scale; (b) optical microscopy imaging or better scanning electron microscopy (SEM) imaging is necessary in order to navigate the tips close to each other without tip–tip crashes and in order to find specific structures on the surface in case of lithographically structured samples; (c) the final electric measurements (e.g. four point measurements) should be performed at one specific position on the nanometer/atomic scale and destruction free, i.e. without indenting the tip in an uncontrolled way into the surface or a nanostrucure. In order to meet the last requirement an instrument with currently unsurpassed stability has to be constructed. The construction of single tip instruments has shown over the last decades that the smaller an instrument is, the less drift results and the lower is the vibrational noise. This was the starting point for us to develop an ultra-compact multitip scanning probe instrument with a drift of <0.2 nm/min at room temperature.

A limit for the size of a scanning probe microscope is the size of the scanner tube, since tube scanners are used in virtually every modern scanning probe instrument. On top of the size of the scanner there comes the size of the tip-sample coarse approach. This is usually the largest part of a scanning probe microscopy instrument. We developed an ultra-compact Koala Drive which can be used for the tip-approach. It is so small that it can be even integrated inside the tube scanner, leading to an ultimate minimum size scanning probe instrument only limited by the size of the scanner tube. Apart from its small size the Koala Drive has several other advantages like a smooth travel, different from the saw tooth signal driven inertial nanopositioners [2–5] which utilizes large accelerations and correspondingly induces vibrations and undesirable power dissipations in the system. Moreover, the Koala Drive is low temperature, magnetic field and ultrahigh vacuum compatible.

In the current context the Koala Drive will be the heart of our multitip scanning probe microscope and allows to construct it with the ultra-compact size of 50 mm outer diameter. Apart from the low drift and low vibrational noise, the small size facilitates the use of such an instrument in environments where the space is limited, such as inside a cryostat or inside an electron microscope.

We will first introduce the working principle of the Koala Drive and demonstrate its operation characteristics. Then we demonstrate how the Koala Drive can be used to construct ultra-compact scanning probe instruments, specifically multitip instruments. We will present the specifications and some initial applications of our ultra-compact multitip scanning probe microscope.

2 The Koala Drive

The Koala Drive consists of two tube piezo elements mounted in series (one after another) as shown in Fig. 1a. At the ends and between the two tube piezos three springs are mounted, which can be moved by an extension or compression of the tube piezos along their axes. A central tube is held by these three springs. The working principle of the Koala Drive relies on concerted consecutive motions in which the frictional surfaces between a spring and the tube are alternating between static friction and sliding friction. Whenever only one spring moves, the other two will hold the tube (by static friction) and only at the single moving spring the frictional engagement will be lifted and sliding friction will occur.

One cycle of motion is shown in Fig. 1a. In step 1 of the cycle the upper piezo element contracts and the upper spring goes into sliding friction. The central tube is held stationary by the lower two springs which stay in static friction with the tube. Subsequently, in step 2 the middle spring is moving downwards while the upper and the lower spring stay at their positions. For the upper spring this is realized by a simultaneous contraction of the lower piezo element and a corresponding expansion of the upper one, leaving the upper spring unmoved. Also here a single spring (middle one) is moving, while the other two holds the tube fixed. Finally, in step 3 the lower piezo extends and moves the two upper springs up simultaneously. In this case the lower spring goes into sliding friction and the upper two springs move the tube up (static friction). Simplified, the working principle follows the rule: "Two are stronger than one". If two springs move simultaneously, the central tube moves with them. If only one spring moves, the tube is held stationary by the other two. In Fig. 1b a photo of a Koala Drive is shown. The ultra-compact Koala Drive can have a diameter <2.5 mm and length smaller than 10 mm.

In Fig. 2 the principle of a voltage pattern at the piezo tubes (piezo 1 and piezo 2) and the resulting motion of the tube during one cycle are shown as function of time. One single cycle can induce a motion in the range between several μm and 100 nm which is ideally suited for coarse approach in scanning probe microscopy. A long stroke, only limited by the length of the tube, and speeds up to ~ 1 mm/s are possible.

Most other nanopositioners used for tip-sample approach in scanning probe microscopy use the inertial motion with sawtooth like signals inducing large accelerations causing vibrations in the system. The operation mode of the Koala Drive is quasi static (one cycle can even last several seconds) avoiding large accelerations which lead to a continuous motion without shaking. Avoiding steep slope signals means also less demands for the power supply (no high slew rate needed) and for the cabling (no high currents flow).

Movies of the motion of the Koala Drive measured using an SEM during one cycle of motion are available in the web under www.fz-juelich.de/pgi/pgi-3/koala. These real time movies show the motion of a STM tip attached to the central tube.

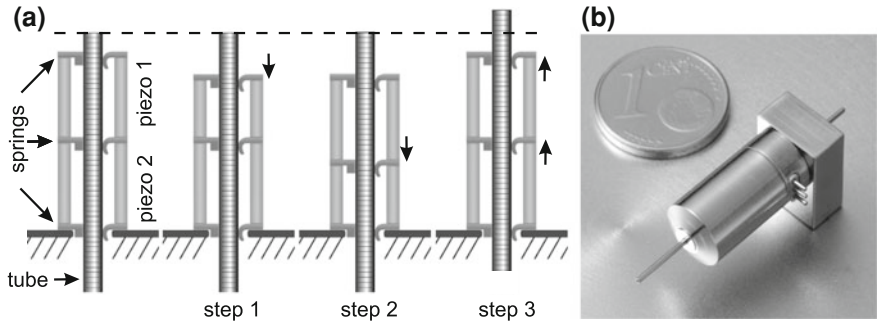

Fig. 1 **a** Principle of the design of the Koala Drive. **a** Working principle of the Koala Drive: concerted interplay between static friction and sliding friction. If only one spring moves, the tube is held stationary by the other two. The motion of the springs during the different steps of a *cycle* is indicated by *arrows*. If two springs move simultaneously, the central tube moves together with them. **b** Photo of the Koala Drive

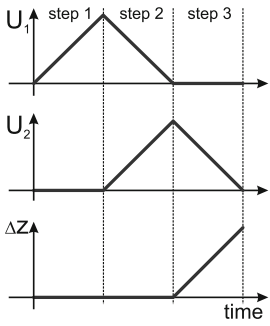

Fig. 2 Voltage pattern applied to both piezo tubes and the resulting motion of the central tube as function of time

The performance of the Koala Drive can also be seen in graphs showing the motion of the tube induced by a single cycle (step) as function of the amplitude of the excitation voltage shown in Fig. 3. Starting from low amplitudes, there is a threshold voltage above which the motion of the Koala Drive starts. For lower voltages the extension of the piezo tubes results in a buildup of stress in the system, but only beyond the threshold voltage a transition to sliding friction occurs. For amplitudes larger than this threshold voltage the single step displacement increases linearly with the signal voltage. Due to the smaller piezo constant at low temperatures, the threshold and the slope of the curves decrease for operation at low temperatures. This shows that the Koala Drive works at cryogenic temperatures (down to liquid helium temperatures) and moreover it is also ultra-high vacuum compatible and works in magnetic fields.

Depending on the particular application the design of the Koala Drive can be modified. If, for instance, the length of the drive should be small, the two tubes can alternatively be coaxially placed into each other instead of one after the other as can be seen in Fig. 4.

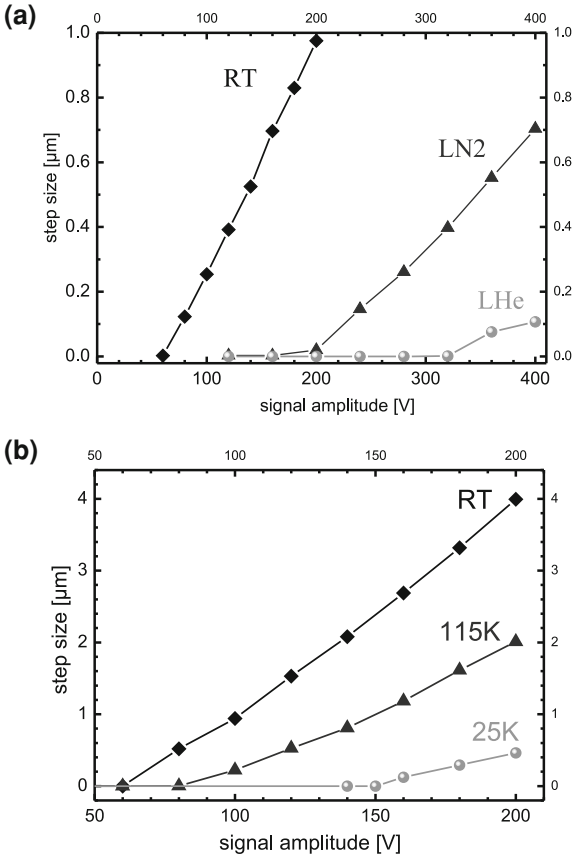

Fig. 3 Koala Drive performance: single step displacement as function of signal amplitude. **a** The data are shown for a 12 mm long Koala Drive at room temperature, liquid nitrogen temperature and at 10 K. **b** Data for a 20 mm long Koala Drive

3 The Koala Drive STM

In the next step the Koala Drive can be used to build an ultra-compact STM. The Koala Drive is used for the tip-sample coarse approach and is integrated into a segmented (scanning) tube piezo element used for the *xyz*-scanning fine motion as shown in Fig. 5a. The STM is completed by attaching a tip (plus tip holder) to the central tube and an outer frame, which holds the sample Fig. 5a. Since the coarse approach mechanism is integrated into the piezoelectric tube scanner, no extra space for the coarse approach is required. Thus this design leads to a minimal size STM. In this way a complete STM scanner can be integrated inside a 4 mm outer diameter piezo tube of <10 mm length. The use of the Koala Drive makes the scanning probe microscopy design ultra-compact and leads accordingly to a high mechanical stability. An STM image of the Si(111)-(7 × 7) surface taken with a Koala Drive STM is shown in Fig. 5b.

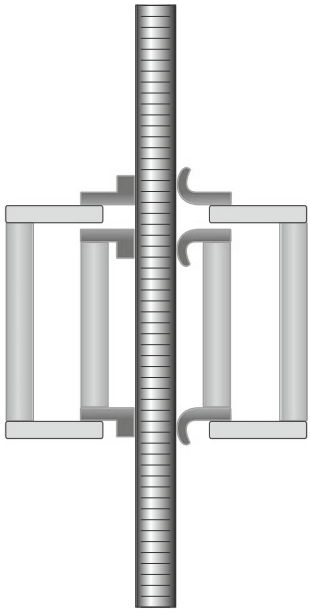

Fig. 4 Another variant of the Koala Drive design where the two piezoelectric tubes are coaxially stacked into each other

4 The Koala Drive Multitip STM

The advantage of the Koala Drive is utilized fully in the design of an ultra-compact four-tip STM using the Koala Drive. The modular design consists of four identical units. Each unit consists of a Koala Drive used for the coarse tip-approach toward the sample. The tip is mounted under 45° relative to the vertical direction in order to allow for the positioning of the tip apex to the same region as the ends of the other tips. The Koala Drive is fixed to a plate which is moved according to the design of the beetle STM [4].

Four of these units can be integrated inside a housing of 50 mm outer diameter. A photo of this ultra-compact four-tip STM is shown in Fig. 6a. The whole instrument is built ultrahigh vacuum compatible. With the sample holder placed on top, the housing is closed completely leading to a good shielding from outer electric disturbances. The sample holder can be moved in *xy* directions over several mm in coarse motion by shear piezo elements on top of the housing. The coarse motion of the four tips and the sample can be observed by an optical microscope from below, or in future by a scanning electron microscope. The view onto the four tips brought within couple of μm together on a lithographically structured test sample is shown in Fig. 6b. The working distance of the optical microscope is 50 mm. Videos showing tip positioning and sample positioning under the control of the optical microscope can be found in the web under www.fz-juelich.de/pgi/pgi-3/koala.

STM images of a Pt(111) single crystal were taken under ambient conditions with all four tips [6]. An example which shows one atomic layer high steps is

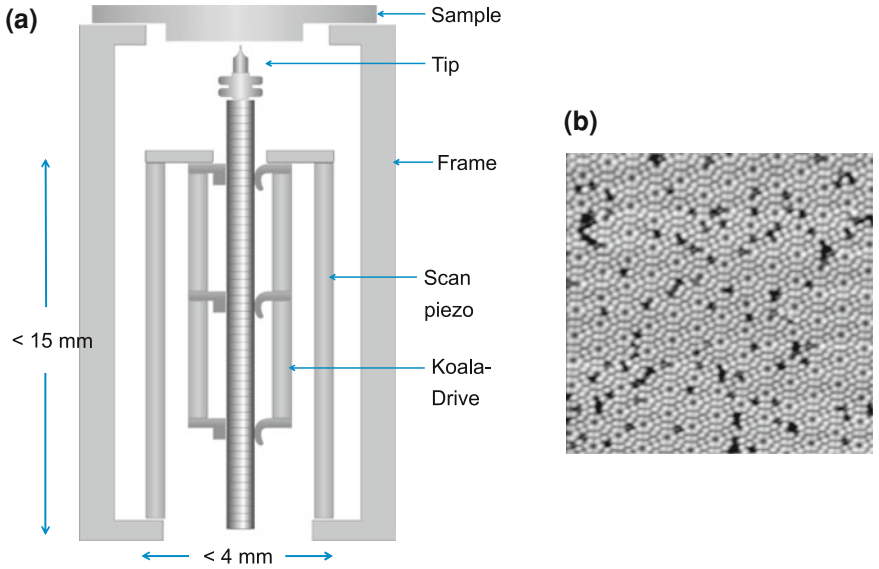

Fig. 5 **a** Design of a single tip STM using the Koala Drive leading to a minimal size STM. **b** Atomically resolved STM image of the (7 × 7) structure on a Si(111) sample (lateral scan size 30 × 30 nm)

shown in Fig. 7. The drift of the system was measured by taking continuously many scans over a time of several hours and identifying same features (defects) in those images. The *xy*-drift was measured in this way to <0.2 nm/min and the *z*-drift to <0.1 nm/min under ambient conditions at room temperature in an ordinary lab which was not specifically temperature stabilized.

The specifications of the ultra-compact four-tip STM are summarized in the following:

- Coarse tip *xy*-positioning: type: inertial slider, range: ±2 mm (each unit).
- Coarse tip *z*-positioning: type: Koala Drive range: ±5 mm (each unit).
- Coarse sample *xy*-positioning: type: inertial slider, range: ±2 mm.
- Scanning: *xy*-range: 10 µm (each unit at RT), *z*-range: 1 µm (each unit at RT).
- Measured lowest resonance frequencies: *xy*: 2.5, *z*: 5.5 kHz.

A multitip STM has the disadvantage that only conducting samples can be studied. However, many interesting samples important in nanoelectronics consist of conducting structures on insulating substrates. In order to perform electrical measurements on insulating substrates (e.g. SiO_2) a multitip scanning force microscope (AFM) is required. In the future we would like to extend our multitip STM to a multitip AFM (atomic force microscope). However, AFM detection method most widely used (the beam deflection detection) is not suitable for this, since four optical systems would have to be adjusted and interference between the four laser beams is likely to occur. For this reason a completely electrical

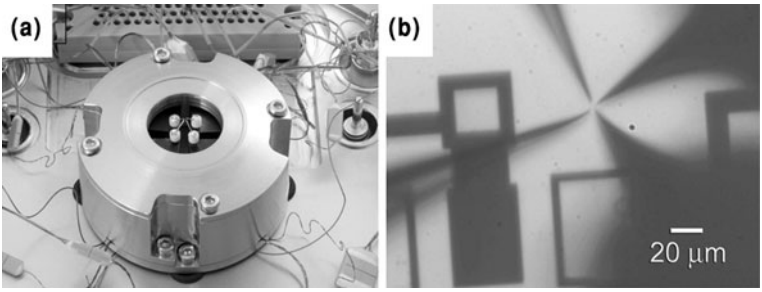

Fig. 6 **a** Photo of an ultra-compact four-tip STM with an outer diameter of 50 mm. **b** Optical microscope image of the four tips of the ultra-compact four-tip STM brought within a couple of µm together. The optical microscope views to the tips and sample from below

excitation and detection is desirable. This can be achieved by quartz crystal sensors like the tuning fork sensor [7] or the needle sensor. We have chosen the needle sensor, because of its small footprint which is advantageous in the context of multitip instruments. We have performed tests which showed that the needle sensor can be used to upgrade an STM in an easy way to an AFM [8, 9].

5 Measurements Performed with a Multitip STM

In the following we report on some measurements performed with one of our multitip STM instruments. These results were obtained with the multitip STM shown in Fig. 8a. These results demonstrate a proof of principle for electrical measurements with a four-tip STM.

Making electrical measurements with a four-tip STM is more than to have four tips and to be able to scan with them. Concerted measurements of currents and voltages with all four tips have to be performed on a real time basis. A typical measurement is performed as follows. Initially all four tips are scanning in STM mode and positioned to the desired positions at which the electrical measurement will be performed. Then the feedback (e.g. for all four tips) is disabled and the tips are approached toward the sample by a desired distance (or remain in the original position). Subsequently, different I/V ramps are applied between different tips (and/or the sample). In the simplest case a current is injected between the two outer tips and a potential difference is measured between the inner tips (classical four probe measurement). However, also various kinds of other measurements can be performed, for instance I/V measurements of every tip to the sample in order to measure the resistance of the contact which has been established by approaching the tip. We usually perform such kind of calibration measurements before and after the actual measurement in order to test the stability of the contacts formed. These different I/V ramps can last altogether 10–20 s and we observe a change in the measured currents of $<10\%$ for the same measurements performed at the

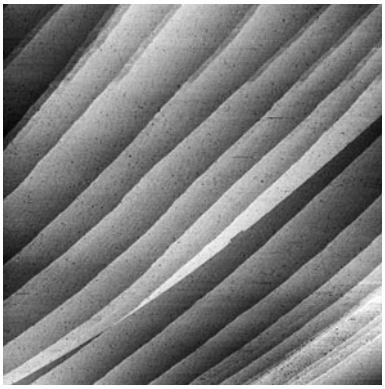

Fig. 7 STM image of atomically high steps on a Pt(111) crystal under ambient conditions (lateral scan size 500 × 500 nm). Corresponding images were acquired with all four tips

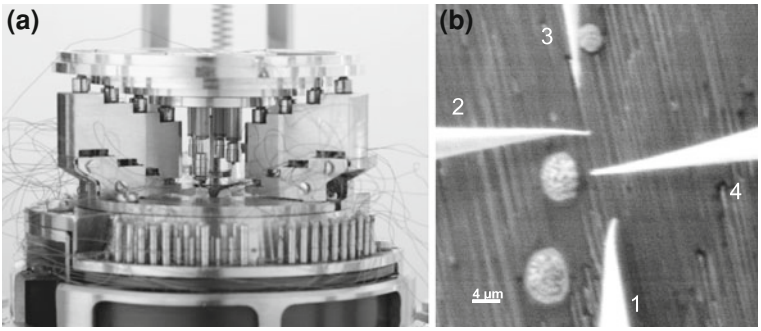

Fig. 8 **a** Photo of our multitip STM with which the results presented in the following were obtained. **b** SEM image of Y-silicide nanowires grown on Si(110). Due to the crystal symmetry of the Si(110) substrate the silicide nanowires are aligned in the vertical direction. The four STM tips are positioned in a line in order to contact one nanowire

beginning or the end of this time frame. The stability of the electric tip-sample contacts established over a measurement period is important in order to obtain reliable results. If all desired voltage ramps are finished the tips are moved back to the original tunneling tip-sample distance and the feedback is resumed.

In order to perform such concerted measurements the control electronics of all for tips have to communicate to each other.

5.1 Four Point Measurements at an Yttrium Silicide Nanowire

As a first example we show a four-tip measurement at an yttrium silicide nanowire. The yttrium silicide nanowires were grown by depositing 0.6 nm yttrium at 1070 K sample temperature. Due to the crystal structure of the Si(110) substrate

the silicide nanowires are aligned along one direction which is vertically in the SEM image shown in Fig. 8b. The silicide nanowires have a height of 5–30 nm, a width between 30 and 50 nm and length of several μm. The four tips of the STM are positioned in a line in order to contact one nanowire as shown in Fig. 8b.

Unlike in a conventional four probe measurement where the two outer probes inject the current and the two inner probes act as voltage probes, here we used only current probes. The principle of the measurement setup is shown in Fig. 9a and consists of four current probes which are biased to a certain potential. Technically they are built by biased STM preamplifiers. The difference between the bias potentials of the outer probes drives a current through the nanowire which is measured by the two (outer) current probes. Before we come to the measurement of the potential by the two inner probes, we consider a possible leakage of the injected current to the substrate.

In principle the current injected by one of the outer probes can run not only through the nanowire as desired, but can also leak to the substrate. In this context it is important to keep in mind that the interface between silicide nanowire to the silicon substrate forms a Schottky barrier. If this Schottky barrier is reverse biased, no current will flow to the substrate. We confirmed this by measuring the current to the substrate by a fifth current preamplifier Fig. 9a. If the Schottky barrier was reverse biased, only a negligible current was detected proving that the current runs almost only through the silicide nanowire.

After establishing a current through the nanowire by the outer probes (probes 1 and 3 in Fig. 8b), the potential of the inner probes was determined by recording successively I/V curves of tip 2 and tip 4. The potential at which no current flows corresponds to the potential at the position of tip 2 and tip 4, respectively. Technically tip 2 and tip 4 are contacted one after the other to the nanowire, and the bias voltage of each tip (2 and 4) was ramped and the current flowing through the corresponding preamplifier was recorded. The voltage for which no current flows corresponds to the potential present on the nanowire at the position of the tip. The two I/V curves recorded for tip 2 and tip 4 while a current of 200 μA was flowing through the nanowire are shown in Fig. 9b. As can be seen from this image, the voltage difference between tip 2 and tip 4 is 167 mV, which results in a resistance of 935 Ω. Taking into account the distance between tips 2 and 4 (2.4 μm), as well as the height (∼15 nm) and the average width (∼50 nm), results in a resistivity of 26 μΩ cm. This value can be compared to a resistivity of about 50 μΩ cm measured on thin yttrium silicide thin films [10, 11].

5.2 Four Point Measurements on Graphene

In the following we present four probe measurements performed on graphene exfoliated on SiO_2. The fact that the graphene is located on top of an insulating SiO_2 layer without any outer contacts to the graphene flake makes it difficult to contact such graphene flakes by a multitip STM. Using an SEM the tip can be

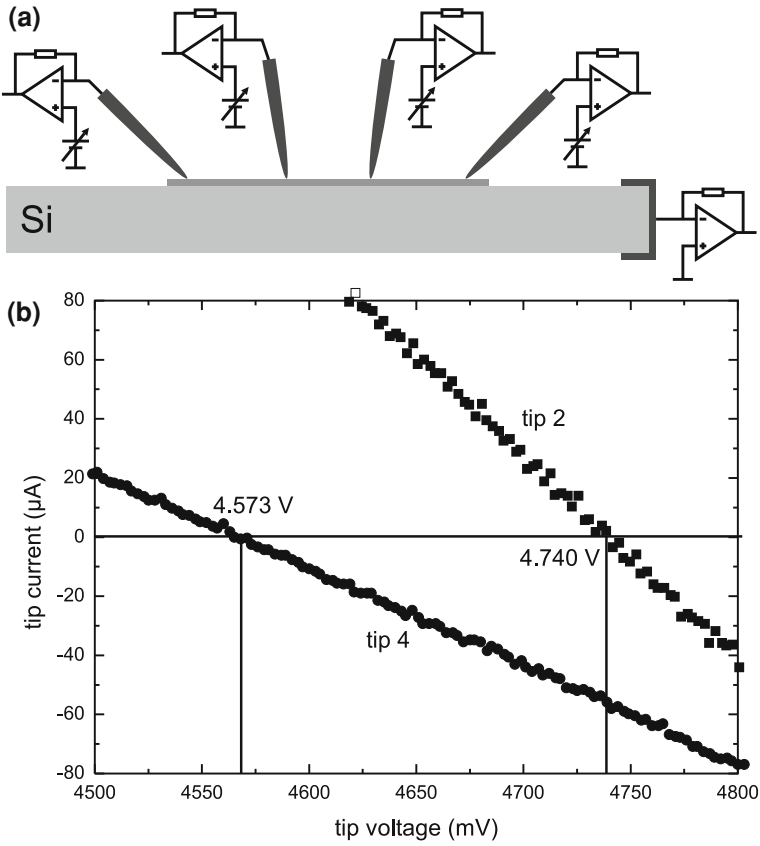

Fig. 9 **a** Principle of a four point measurement using biased preamplifiers as current probes. **b** I/V measurements of tip 2 and tip 4 in Fig. 8b. The voltage at which the current vanishes corresponds to the potential of the tip

positioned above the graphene flake, but the distance between tip and sample is difficult to estimate from the SEM images.

Here we present a method to detect the point of contact between tip and graphene flake using SEM images and a biased tip. Figure 10a shows a SEM image in which a graphene flake is imaged with dark contrast on the silicon dioxide substrate. The tip approaching the surface is still not in contact with the flake. If the tip is negatively biased at −10 V, the SEM contrast of the graphene flake reverses to a bright contrast if the biased tip comes into contact with the graphene flake, as seen in Fig. 10b. The negative potential of the graphene flake relative to the sample leads to an enhanced emission of secondary electrons. Vice versa a positive tip voltage leads to a darker contrast in the SEM image at the

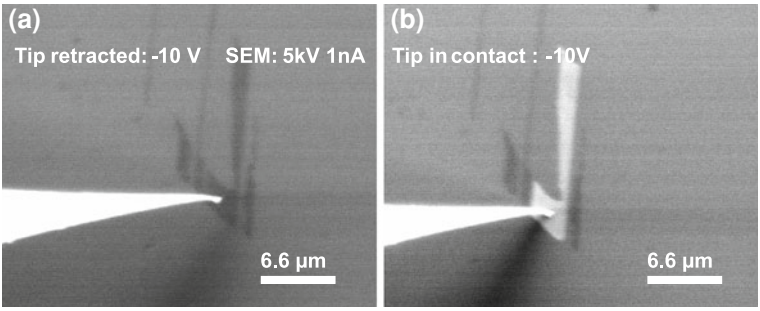

Fig. 10 Contacting of a graphene flake under SEM control using a biased tip. **a** The tip is not in contact with the flake: the flake appears to be darker than substrate. **b** The flake, when contacted with a biased tip, appears to be brighter than the substrate

point of contact. The method described above allows to contact graphene flakes on an insulating oxide substrate nondestructively by an STM tip.

After the first tip has been brought nondestructively into contact to the graphene flake a bias voltage can be applied to the flake and the other tips can be contacted using the ordinary STM mode approaching the tip to a biased flake. This has been done on a several layers thick graphene (graphite) flake shown in the SEM image in Fig. 11a. Tip 3 and especially tip 4 are bent quite much (from previous experiments) but can be still used to drive a current into the graphene sheet. The potential present at the positions of tip 1and tip 4 is measured using these tips as voltage probes, disconnected from the current preamplifiers during the concerted measurement. This conventional four probe measurement with the inner tips used as voltage probes results in a I/V curve which is shown in Fig. 11b. A linear dependence between the measured voltage difference and the injected current is measured. The slope corresponds to a resistance of 9.43 Ω which results in a sheet resistance of 60 Ω/□ taking into account an infinite flake model and the actual distances between the tips. After the measurement of the I/V curve is finished, tip 1 and tip 4 return to the tunneling position.

6 Conclusions

We have shown that the development of a new type of piezoelectric motor serves as the basis for ultra-compact scanning probe microscopes. The Koala Drive is the heart of our ultra-miniature STMs. The Koala Drive can tap its full potential for the miniaturization for the case of multitip scanning probe instruments. We constructed an ultra-compact multitip STM with an outer diameter of 50 mm with a drift of <0.2 nm/min at ambient conditions. This instrument can be combined with an optical microscope or a SEM in order to navigate the positioning of the tips.

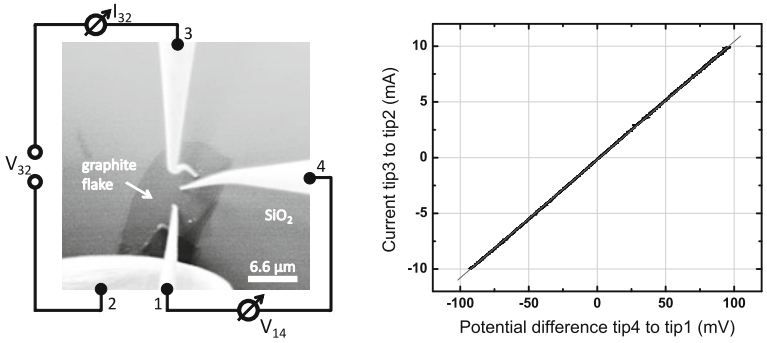

Fig. 11 **a** SEM image of four tips positioned on a multi-layer graphene flake in order to perform a four probe measurement. Tip 2 (at the lower left edge of the image) is very much bent. **b** Measured I/V curve during a four probe measurement resulting in a sheet conductance of 60 Ω/□

We demonstrate the capabilities of the instrument by four point measurements at a yttrium silicide nanowire and on a graphene flake. Here concerted measurement processes starting and ending with the tips in tunneling conditions are essential in order to perform nondestructive electrical measurements at the nanoscale.

Acknowledgments We would like to acknowledge Ch. Stampfer for the preparation of the graphene sample.

References

1. Kawamura, M., Paul, N., Cherepanov, V., Voigtländer, B.: Nanowires and nanorings at the atomic level. Phys. Rev. Lett. **91**, 096102 (2003)
2. Pan S.H.: International Patent Publication WO 93/19494
3. Pohl D.W: Dynamic piezoelectric translation devices. Rev. Sci. Instr. **58**, 54 (1987)
4. Besocke, K.: An easily operable scanning tunneling microscope. Surf. Sci. **181**, 145 (1987)
5. Frohn, J., Wolf, J.F., Besocke, K., Teske, M.: Coarse tip distance adjustment and positioner for a scanning tunneling microscope. Rev. Sci. Instrum. **60**, 1200 (1989)
6. Voigtländer, B., Cherepanov, V., Elsaesser, Ch., Linke, U.: Metal bead crystals for easy heating by direct current. Rev. Sci. Instrum. **79**, 033911 (2008)
7. Giessibl, F.J., Pielmeier, F., Eguchi, T., An, T., Hasegawa, Y.: Comparison of force sensors for atomic force microscopy based on quartz tuning forks and length-extensional resonators. Phys. Rev. B **84**, 125409 (2011)
8. Morawski, I., Voigtländer, B.: Simultaneously measured signals in scanning probe microscopy with a needle sensor: Frequency shift and tunneling current. Rev. Sci. Instr. **81**, 033703 (2010)
9. Morawski, I., Blicharski, J., Voigtländer, B.: Voltage preamplifier for extensional quartz sensors used in scanning force microscopy. Rev. Sci. Instrum. **82**, 063701 (2011)
10. Gurvitch, M., Levi, A.F.J., Tung, R.T., Nakahara, S.: Epitaxial yttrium silicide on (111) silicon by vacuum annealing. Appl. Phys. Lett. **51**, 311 (1987)
11. Siegal, M.P., Kaatz, F.H., Graham, W.R., Santiago, J.J., Van der Spiegel, J.: Formation of epitaxial yttrium silicide on (111) silicon. J. Appl. Phys. **66**, 2999 (1989)

Atomic Scale Interconnection Machine

O. A. Neucheva, R. Thamankar, T. L. Yap, C. Troadec, J. Deng and C. Joachim

Abstract An atomic scale multiprobe interconnection machine is described in the context of building of the molecular devices. It combines various techniques for fabrication and surface analysis. The characterization part consists of low temperature scanning tunneling microscope (LT-STM), four probes variable temperature scanning tunneling microscope (Multiprobe), high resolution scanning electron microscope (SEM). The fabrication part has field ion microscope (FIM), evaporators and nanoimprinter. The characteristics of every part of the instrument and the preliminary experiments on Si(100) surface are discussed.

O. A. Neucheva (✉) · R. Thamankar · T. L. Yap · C. Troadec · J. Deng · C. Joachim
A*STAR (Agency for Science, Technology and Research),
Institute of Materials Research and Engineering, 3 Research Link,
Singapore 117602, Singapore
e-mail: neuchevaoa@imre.a-star.edu.sg

T. L. Yap
Department of Physics,
National University of Singapore,
Singapore 117542, Singapore

T. L. Yap
GLOBALFOUNDRIES Singapore Pte Ltd,
60 Woodlands Industrial Park D Street 2,
Singapore 738406, Singapore

C. Joachim
Centre d'Elaboration de Matériaux et d'Etudes Structurales (CEMES-CNRS),
29, rue Jeanne Marvig, BP 94347
31055 Toulouse Cedex 4, France

C. Joachim (ed.), *Atomic Scale Interconnection Machines*, Advances in Atom and Single Molecule Machines, DOI: 10.1007/978-3-642-28172-3_3,

1 Introduction

The atomic scale interconnection machine is a complex instrument for fabricating, analyzing and operating the molecular devices. Depending on the substrate properties the two sets of equipment can be used, combination of a scanning tunneling microscope (STM) with a SEM for the surfaces with moderate band gap and an atomic force microscope (AFM) together with an optical microscope for the large band gap substrates [1].

In the first part of this work the interconnection machine with the main functional parts of STM and SEM will be described. The equipment is built by Omicron GmbH and is located at Institute of Materials Research and Engineering, Singapore. The machine consists of the variable temperature 4 probes STM, high resolution Gemini SEM and low temperature STM (LT-STM) (Fig. 1). The multiprobe STM is used to perform the final measurements of the built nanodevices whereas the SEM is used for navigating the STM tips. The machine also has an LT-STM which is used for manipulation and more delicate surface investigation. Transfer of the sample at liquid helium temperature is possible between the multiprobe and the LT-STM sides with a help of manipulator which is cooled down by liquid helium flow. Besides that there is a preparation side where all prior work of surface preparation is done (Fig. 2).

In the second part of this work the process of building the molecular logic gate [1–4] on Si(100) surface will be described and preliminary experimental results will be shown.

2 Experimental Setup

2.1 Introduction

The Omicron Multiprobe System has three main parts: preparation, LT-STM and multiprobe. The idea of building this machine rose from the necessity of bringing all the preparation and characterization steps of the device fabrication and characterization in situ. Due to high reactivity of the silicon surface special attention should be paid to the vacuum during the experiment.

Preparation of the experiment is the most time consuming process which contains 3 main steps: vacuum preparation, tip preparation and sample preparation. The ultra-high vacuum is essential for all chambers of the machine and is the first target when the machine is assembled. Ultra-high vacuum is reached after baking of the machine at 150°C. The multiprobe chamber has to be baked for at least 60 h whereas the LT-STM and preparation chambers—for at least 40 h. Once the pressure is in the desirable range the next steps begin: namely, making the device and testing it.

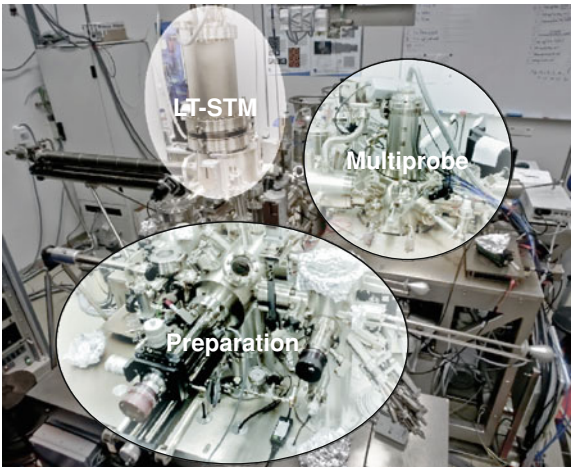

Fig. 1 Omicron Interconnection Machine (picture is taken from the preparation side). The machine has 3 long Z-direction rotatable manipulators (load-lock, multiprobe and LT-STM) and 6 wobble sticks which are used to manipulate the samples. The manipulator on the LT-STM side can be cooled down to liquid helium temperature, whereas the other 2 are at room temperature only. The X, Y, Z rotatable manipulator is attached to the preparation chamber

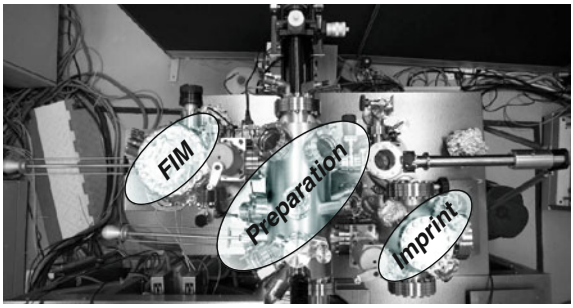

Fig. 2 Preparation side of the interconnection machine: FIM, preparation and imprinting chambers separated by the gate valves. The load-lock is attached to the preparation chamber. The FIM chamber is not yet fully equipped

In order to separate "dirty" preparation process from the "clean" experiment complex preparation chamber was designed to split the machine into fabrication and characterization parts.

2.2 Preparation Side

Preparation side consists of three parts: FIM chamber, preparation chamber and imprint chamber (Fig. 2). It has one turbo pump attached to the FIM chamber and two ion pumps at the preparation and imprinting chambers. All the parts are

separated by gate valves and the pressure of low −10 mbar can be reached after baking and outgassing the filaments with all the valves open. When the valves between the parts are closed the pressure of low −11 mbar can be reached in the preparation and imprinting chambers.

The FIM chamber is designed to have low temperature field ion microscope which allows preparing the atomically sharp tips in situ. The sharpness of the tips is very important because the tip apex shape defines the point of tip-surface interaction. Single atom contact ensures cleanness and reproducibility of the experiments. Prior the FIM sharpening the tungsten tips are chemically etched in KOH solution to the sharpness of few tens of nm (checked with outside SEM and TEM). In order to remove the oxide the tips are heated to high temperatures using the resistive heating. After the chemical etching and oxide removal the tips are ready for the FIM finishing [5].

The lack of this particular machine is different design of the probes. Each part (LT-STM, high resolution probe and normal probe) has completely different tip holders which require modification of the manipulators in order to handle all the designs.

The preparation chamber is used for sample preparation and tip flashing. It is equipped with an X, Y, Z rotatable manipulator, a quadruple mass spectrometer, an atomic hydrogen source, an e-beam evaporator and a sputter gun. External pyrometer is used to monitor the sample temperature during Si(100) preparation. A "fast" load-lock which can be pumped down to low −8 mbar overnight without baking is attached to this part.

For atomically clean silicon sample preparation the direct heating of the substrate is needed. The manipulators at the preparation and the imprinting chambers have the possibility of the direct and resistive heating of the substrates. In the preparation chamber the sample can be also cooled down to liquid nitrogen temperature.

Silicon is a very reactive surface and an oxide layer is formed when kept at the atmospheric conditions. Therefore, prior to loading it into the load-lock, the sample is "refreshed" in the low concentration HF to minimize the time for the surface oxidation. After that the sample is loaded to the load-lock which is pumped for 12 h following by transferring the sample into preparation part and outgassing at 600°C for another 12 h (till the pressure remains below 5e-10 mbar) using the direct current to heat. After that the sample is flashed to 1,100–1,200°C during 10–30 s several times until the pressure remains below 1e-9 mbar following by slow cool down with a rate of 20°C/min.

If the sample requires further processing (molecule deposition or passivation) all the processes are done in the preparation chamber after the sample is cooled down to room temperature. For passivation of the Si substrate atomic hydrogen source FOCUS EFM-H is used. There are different recipes for Si surface passivation [6]. In our experiments the Si(100) surface is exposed to atomic hydrogen source for a few minutes at the base pressure of middle −8 mbar. The power to heat the tungsten capillary is set to 30 W. After passivation in the case of intended imprinting the sample is transferred to the imprinting chamber.

The imprinting part is equipped with rotatable manipulator, nanoimprinter and electron beam evaporator. The electron beam evaporator is used to deposit the gold islands onto various surfaces in situ. The golden rod is mounted into evaporator and heated with the electron beam till the evaporation temperature is reached. (Previously the deposition was done "outside" and gave a lot of contamination to the surface).

There are two carousels with 6 slots each are available in the preparation and imprinting chamber to keep samples or tips under vacuum.

When the sample is fully prepared for the experiments it is transferred back to the manipulator of the preparation chamber and cooled down to the liquid nitrogen temperature in order to reduce the consumption of the liquid helium at the LT-STM side. With a help of the wobble sticks the sample is transferred to the long magnetic manipulator which connects the preparation chamber with the multiprobe and the LT-STM chambers.

For the characterization chambers the vibration isolation of the systems becomes very important. Despite the location of the laboratory at the basement of the building and the solid rock ground underneath there were vibrations detected during the preliminary tests. Therefore, special vibration isolation was built separating the rectangular shape pad for the machine from the rest of the building. Moreover, the machine is floating on the 4 vibration isolation legs which damp the vibrations of the high frequencies.

2.3 LT-STM Side

LT-STM is the most precise technique in the whole interconnection machine. It is operating at 4.2 K and has base pressure of high -11 mbar. The STM stage requires additional vibration decoupling therefore it is suspended by the three soft springs vibrations of which in turn are damped using the eddy current mechanism. This further reduces the noise level to the pm range and providing higher sensitivity.

LT-STM has two cryostats: outer one is filled with liquid nitrogen and has to be refilled every 50 h. Inner cryostat has liquid helium inside and needs to be refilled every 60 h.

The LT-STM has the options to operate at room temperature, liquid nitrogen and liquid helium temperatures. However, the thermal drift in the first two cases leads to the poor quality of images and spectroscopy. The machine can be cooled down from room temperature to liquid helium temperature within 10 h but full thermal stabilization can be achieved only after 24 h.

When thermal stabilization is reached the drift of the system at liquid helium temperature lies within a range of few nm per 10 h (Fig. 3).

The sensitivity of the machine allows measuring the tunneling current starting from few pA and to 333 nA (using 2 regimes of the current preamplifier from 0 to

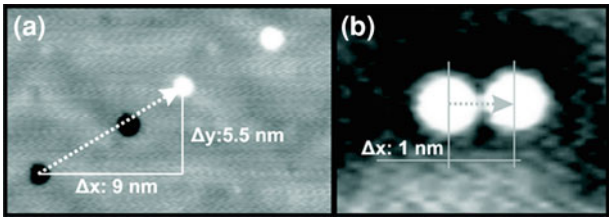

Fig. 3 STM images of the Au(111) surface representing thermal drift of the sample with respect to the tip during 13 h. Dotted lines correspond to the direction of the drift: **a** After the course motion of the piezos of the STM; **b** After the fine motion of the piezos

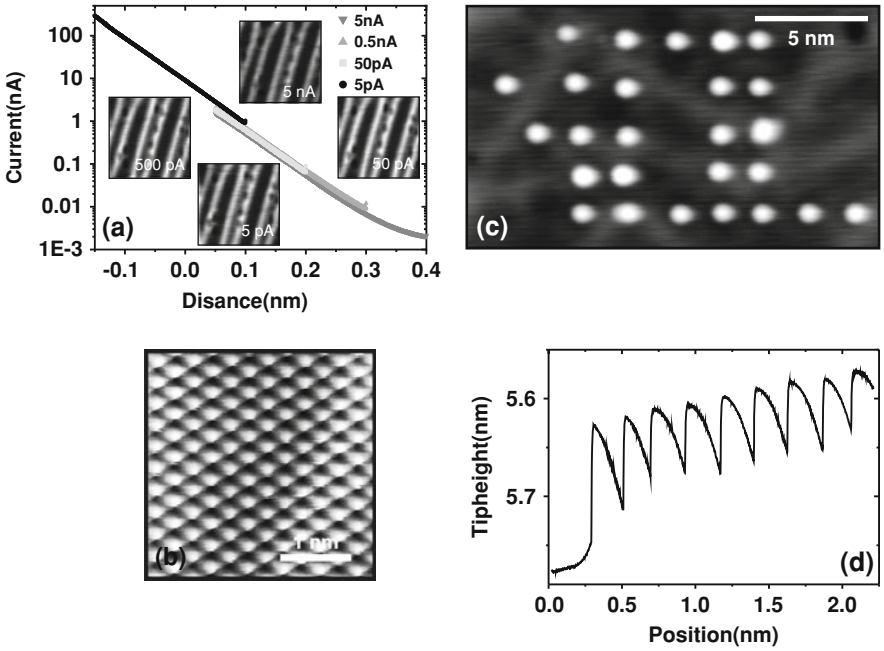

Fig. 4 STM images and spectroscopy of Si(100) and Au(111) surfaces: **a** I(z) spectroscopy of the Si(100) surface at different tip heights and corresponding images (*inset*: 500 mV, 1 nA; 18.7 × 18.7 nm); **b** Atomically resolved image of Au(111) (5 mV, 5 nA); **c** Image of the Au(111) surface after atomic manipulations of the gold adatoms (500 mV, 1 nA); **d** I(r) spectroscopy on Au(111) during atomic manipulation

3.3 nA and from 0 to 333 nA, respectively). The noise level within the whole range does not exceed few pm (Fig. 4a).

Atomically resolved images were obtained on metal (Au(111): Fig. 4b) and semiconductor (Si(111) and Si(100)) surfaces at liquid helium temperatures.

Manipulation of gold adatoms on Au(111) [7] surface was done in a controlled way by pulling the adatoms with the STM tip along different directions on the

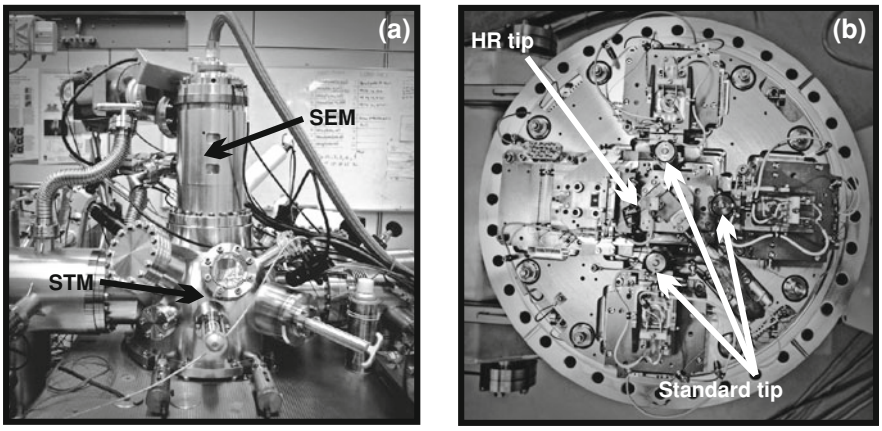

Fig. 5 UHV-Multiprobe chamber: **a** Outside view; **b** Inside view: 4 probes STM

surface. In total 30 adatoms were moved one by one forming the letters (Fig. 4c). Hopping of the atoms along the surface was recorded using the I(r) spectroscopy (Fig. 4d) revealing the hopping distance of 0.22 nm which agrees with interatomic distance of Au(111) (Fig. 4c).

2.4 Multiprobe Side

The multiprobe side of the machine is the final destination of the sample. After it is processed in the preparation chamber and all necessary measurements and manipulations are done with the LT-STM the sample can be transferred to the multiprobe chamber for the conclusive measurements. Two to four probes can be used to perform both surface conductance measurements [8] and mechanical manipulations of the nanoobjects [9].

Some of the molecules or molecular structures are only stable on the surface at liquid helium temperatures. Therefore, the possibility of transfer at low temperatures is essential for conserving the built structures. The transfer mechanism between the LT-STM and the multiprobe chambers was designed to be cooled to liquid helium temperature (Fig. 1). Additional differential pumping of the cold transfer mechanism ensures clean transfer of the sample from the LT-STM to the multiprobe side.

The main advantage of the multiprobe chamber in comparison with the LT-STM one is that it has 4 probes instead of one and an operator can see and navigate all of them using the scanning electron microscope located above the STM stage (Fig. 5).

UHV-Multiprobe is equipped with a high resolution SEM positioned vertically on top of the multiprobe stage. This has a GEMINI column with high lateral

resolution ($\sim$3 nm). This can be operated at low beam energy (100 eV–30 keV) and beam currents up to 50 nA. Advantage of this kind of SEM is that it can be operated at large working distance (10–15 mm) which is useful for multiprobe measurements. SEM is calibrated using Au/Carbon sample and Au/MoS2 sample. Multiprobe can be operated in a large temperature range from 440 to 30 K which gives a very good degree of freedom in the measurements. The sample can be cooled using liquid helium and temperature as low as 30 K. The tips are calibrated using Au (111) sample. We use standard sputtering technique using Ne+ ion beam and annealing up to 750 K resulting in atomically flat surface with large terraces.

The multiprobe chamber has a turbo pump, 2 ion pumps (one for the SEM column) with the base pressure of low -10 mbar.

One of the four STM tips is high resolution tip which can be used for both atomically resolved imaging and spectroscopy, whereas the other 3 tips can only image the surface. All four tips have one Matrix control unit which is usually connected to the high resolution probe and one manually controlled unit which is connected to one of the 3 standard probes. This limitation significantly complicates the process of the four probe measurements. In order to land all four tips on the substrate the standard tips have to be approached one by one by disconnecting the manually controlled unit from one tip to another. Taking into account that the multiprobe STM stage does not have additional vibration isolation unlike LT-STM part mechanical contact between the operator and the machine leads to the crash of the tips. In the case of contact measurements this situation is not as crucial as in the case of tunneling measurements. In order to solve this problem all tips must be controlled separately using 4 Matrix control units.

3 Experimental Results

Building of a single molecular device is a complicated process which involves different steps: surface preparation, nanoimprinting, atomic and cluster manipulation (device assembly), multi-tip spectroscopy and packaging.

Full and detailed description of the process can be found in the paper [1]. In this chapter a brief concept and realization on the specific interconnection machine (for moderate band gap surfaces) based in Singapore.

Hydrogen passivated Si(100) is used as a substrate. Surface preparation has been described in the previous section. Special attention should be paid to the size of the terraces because the whole molecular circuit has to be located in the same terrace, in contrast to work [10]. The size of the terraces can be controlled by direction of the current passing through the substrate with respect to the surface orientation [11].

The passivated substrate with long range terraces has been prepared in the preparation chamber and the sample has been transferred to the imprinting chamber in order to print gold clusters which will be used as electrodes of the molecular devices. These gold clusters are initially deposited on MoS_2 surface and

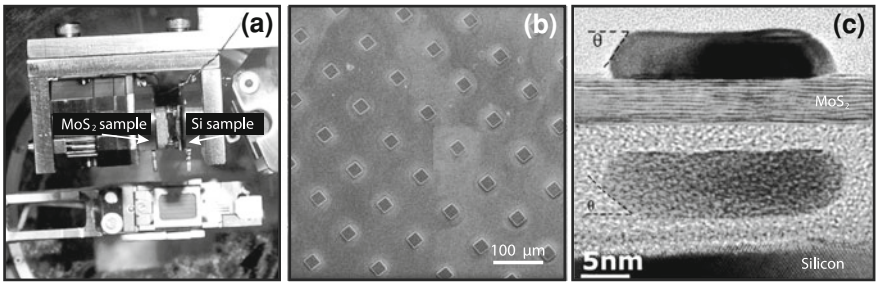

Fig. 6 **a** Inside view of the imprinting chamber: the piezo-driven part with MoS_2 sample is on the left; on the right side has Si sample; **b** SEM image of the MoS_2 pillars made by nanolithography method; **c** TEM image of the gold nanoislands transferred from the MoS_2 surface to Si surface

are known to form the islands of regular shape [12]. The height, shape and lateral dimensions of the islands depend on the MoS_2 surface temperature during deposition. At the substrate temperature of 400°C gold is the most uniformed and self-assembled into the triangular islands with a size of tens of nm.

After deposition of golden islands on MoS_2 the next step is to transfer them onto Si(100) surface using nanoimprinter (Fig. 6a). The nanoimprinter is based on the piezo-driven attocube positioning system which allows to get very high precision of the lateral movement of the stamps. The force applied to the indenter is the range of few Newton (maximum 5 N) which leads to the transfer of the Au islands only but not the MoS_2 sheets. In order to have a better contact between the two surfaces the MoS_2 surface is patterned with a help of nanolithography to have the pillars of square (25 by 25 μm) shape with a height of 8 μm (Fig. 6b).

The preliminary experiments show that the islands remain their truncated pyramid shape when transferred from one surface to another (Fig. 6c). These islands are mobile on MoS_2 surface [13] and can be manipulated with the STM tip. Similar behavior is expected on Si(100)H surface. Since the islands are not equally distributed on the surface (due to the patterning of the MoS_2) it is very difficult to find them with conventional STM with a scanning area of 1 by 1 μm. Therefore, the imprinted sample is transferred to the multiprobe which has the SEM for better tip navigation.

I(V) spectroscopy performed on the deposited islands and the bare silicon substrate reveals significant difference in their electronic properties. It also showed that in some cases there was MoS_2 sheets transferred together with the islands which can be avoided by better alignment and force control of the nanoimprinter.

When the electrodes made from the gold islands have been successfully made on the Si(100)-H surface the next step is to "wire" them to the functional group of the molecular device. The atomic wires are the dangling bonds of Si(100) which are formed by depassivation of individual Si dimmers. The STM tip is brought in close vicinity of the targeted hydrogen atom and the voltage pulse is applied leading to removal of the H atom from the surface [14]. These wires must be

relatively long in order to be able to land the 4 probes to the Au electrodes. Interatomic distance along the dimer rows on Si(100) is 3.84 Å and the minimum distance between the 2 tips which was reached is 50 nm which means that each atomic wire must be at least 35 nm long giving the number of around 90 atoms to be removed by the tip of the LT-STM. Such distance must be sufficient to avoid discrete electronic resonances [15].

The final step of a device assembling is introducing the functional group to the circuit [16]. As a functional group both organic molecules and inorganic structures can be used. Surface conformation, chemical and electronic properties of the molecule define the functional properties of the device. On the one hand large size of the single molecule shortens the length of the molecular wires needed. However, it makes more difficult to perform theoretical calculations for the large molecules. Moreover, the number of STM probes limits the number of electrodes which can be used simultaneously. Since the interconnection machine has 4 tips on the nanoprobe side in the ideal case the single molecule must have 4 wings. The preliminary experiments which were done on the Y-molecule on Au(111) surface [3] show the change of the electronic properties with attaching the Au adatoms to it. The trans–cis isomerization molecules [17] can also be the good candidates for the molecular electronics. However, the single molecule which will be used in a molecular device is not yet decided and the testing experiments and calculations are running.

Considering the inorganic components as the candidates to build the device one can think of the atomic circuit consisting of the lines of depassivated Si(100) dimers. The preliminary calculations reveal promising results for the variety of the logic gates such as OR, NOR and XOR.

In summary the Omicron atomic scale interconnection machine has been described. The test experiments reveal the minor problems of the machine (noise at the Multiprobe side, tip control); nevertheless, very good performance of the equipment can be achieved. The preliminary results toward building a single molecular device have been demonstrated and discussed.

References

1. Joachim, C., Martrou, D., Rezeq, M., Troadec, C., Deng, Jie., Chandrasekhar, N., Gauthier, S.: Multiple atomic scale solid surface interconnects for atom circuits and molecule logic gates. J. Phys. Cond. Matter **22**, 084025 (2010)
2. Duchemin, I., Renaud, N., Joachim, C.: An intramolecular digital 1/2 adder with tunneling current drive and read-outs. Chem. Phys. Lett. **452**, 269 (2008)
3. Soe, W.H., Manzano, C., De Sarkar, A., Ample, F., Chandrasekhar, N., Renaud, N., de Mendoza, P., Echavarren, A.M.: Hliwa, M., Joachim, C.: Demonstration of a NOR logic gate using a single molecule and two surface gold atoms to encode the logical input. Phys. Rev. B **83**, 155443 (2011)
4. Renaud, N., Hliwa, M., Joachim, C.: Single molecule logical devices. In: Topics in Current Chemistry, pp. 1–52. Springer, Berlin, Heidelberg (2011)
5. Rezeq, M., Joachim, C., Chandrasekhar, N.: Confinement of the field electron emission to atomic sites on ultra sharp tips. Surf. Sci. **603**, 697 (2009)

6. Bellec, A., Riedel, D., Dujardin, G.: Dihydride dimer structures on the Si(100): H surface studied by low-temperature scanning tunneling microscopy. Phys. Rev. B **78**, 165302 (2008)
7. Hla, S.-W., Braun, K.F., Iancu, V., Deshpande, A.: Single atom extraction by scanning tunneling microscope tip-crash and nanoscale surface engineering. Nano Lett. **4**, 1997 (2004)
8. Ramesh, T.: Surface Conductance Measurements on a MoS_2 Surface Using a UHV-Nanoprobe System. In this volume, (2012)
9. Cedric, T.: Solid State Nano Gears Manipulations. In this volume, (2012)
10. Ruess, F.J., Oberbeck, L., Simmons, M.Y., Goh, K.E.J., Hamilton, A.R., Hallam, T., Schofield, S.R., Curson, N.J., Clark, R.J.: Toward atomic-scale device fabrication in Silicon using scanning probe microscopy. Nano Lett. **4**(10), 1969–1973 (2004)
11. Latyshev, A.V., Aseev, A.L., Krasilnikov, A.B., Stenin, S.I.: Transformations on clean Si(111) stepped surface during sublimation. Surf. Sci. **213**, 1 (1988)
12. Deng, J., Troadec, C., Kim, H.H., Joachim, C.: Direct transfer of gold nanoislands from a MoS_2 stamp to a Si–H surface. J. Vac. Sci. Technol. B **28**, 3 (2010)
13. Yang, J., Deng, J., Chandrasekhar, N., Joachim, C.: UHV-STM manipulation of single flat gold nano-islands for constructing interconnection nanopads on MoS_2. J. Phys. Conf. Ser. **61**, 1288 (2007)
14. Soukiassian, L., Mayne, A.J., Carbone, M., Dujardin, G.: Atomic-scale desorption of H atoms from the Si.100.-2Ã1:H surface: Inelastic electron interactions. Phys. Rev. B **68**, 035303 (2003)
15. Doumergue, P., Pizzagalli, L., Joachim, C., Altibelli, A., Baratoff, A.: Conductance of a finite missing hydrogen atomic line on Si(001)-(2 × 1)-H. Phys. Rev. B **59**, 15910 (1999)
16. Nozaki, D., Cuniberti, G.: Silicon-based molecular switch junctions. Nano Res. **2**(8), 648–659 (2009)
17. Choi, B.-Y., Kahng, S.-Y., Kim, S., Kim, H., Kim, H.W., Song, Y.J., Ihm, J., Kuk, Y.: Conformational molecular switch of the Azobenzene molecule: A scanning tunneling microscopy study. Phys. Rev. Lett. **96**, 156106 (2006)

The DUF Project: A UHV Factory for Multi-Interconnection of a Molecule Logic Gates on Insulating Substrate

D. Martrou, L. Guiraud, R. Laloo, B. Pecassou, P. Abeilhou, O. Guillermet, E. Dujardin, S. Gauthier, J. Polesel Maris, M. Venegas, A. Hinault, A. Bodin, F. Chaumeton, A. Piednoir, H. Guo and T. Leoni

Abstract The scientific and technical challenges involved in the building of the planar electrical connection of an atomic scale circuit to N electrodes ($N > 2$) on insulating substrates are presented. In the Nanoscience group of Toulouse, the UHV factory has been developed since ten years in order to realize under UHV the five levels of interconnections on insulating substrate, to characterize by NC-AFM the different steps and to measure the electrical properties of the realized device.

1 Introduction

An UHV atomic scale interconnection machine is designed to follow *a dedicated interconnection sequence*. On an atomically clean well-prepared surface, an *atomic scale circuitry* is fabricated (A). This circuit must have a minimal lateral extension to make possible its connection to a large number N of *metallic nanopads* (B) positioned around it. In the example of Fig. 1, a molecule is connected to these nanopads by *atomic metallic wires*. These nanopads (B) have to be contacted by a series of N *nano-scale wires* (C) up to the point where *microelectrodes* (D) can be surface fabricated and contacted by N *micro-scale metallic cantilevers* (E) also from the top of the wafer.

For a large valence band-conduction band electronic surface gap (more than a few eV up to 12 eV for good insulators), SEM is difficult to use because the

D. Martrou (✉) · L. Guiraud · R. Laloo · B. Pecassou · P. Abeilhou · O. Guillermet
E. Dujardin · S. Gauthier · J. Polesel Maris · M. Venegas · A. Hinault · A. Bodin
F. Chaumeton · A. Piednoir · H. Guo · T. Leoni
Nanoscience Group, CEMES-CNRS, 29 Rue J Marvig, BP 94347,
31055 Toulouse Cedex, France
e-mail: martrou@cemes.fr

C. Joachim (ed.), *Atomic Scale Interconnection Machines*, Advances in Atom and Single Molecule Machines, DOI: 10.1007/978-3-642-28172-3_4,

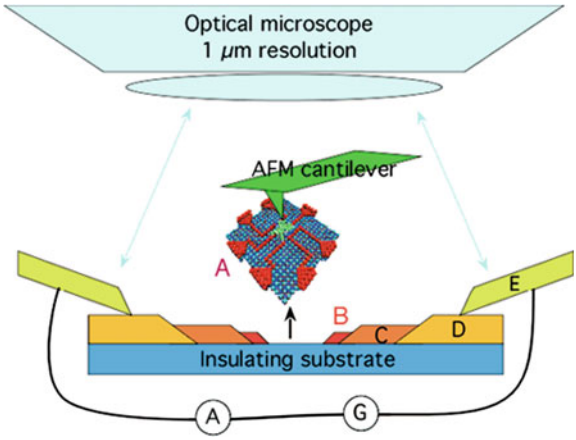

Fig. 1 Scheme of the atomic scale interconnection machines for wide surface band gap substrates. *A* The atomic scale circuitry embedded into the surface, *B* contacting metallic nanopads, *C* nanowires, *D* microelectrodes, *E* metallic microcantilevers

electron beam will charge the surface. In this case, an optical microscope must be used. This microscope determines the minimum length of metallic surface wiring that must be fabricated starting from the nano-pads (B) in Fig. 1 toward the next contact stage based on metallic microcantilevers. Fortunately, with a large surface gap, the surface area of those interconnects can be expanded laterally without significant leakage currents between the different electrodes. This is the basic of the UHV interconnection machine described in this chapter where a low temperature approach is not compulsory. As presented in Fig. 1, a large surface electronic gap for the material supporting the interconnection structure leads to five levels of interconnects. Levels (A) and (B) depend on our mastering of atomic scale surface science phenomena while level (C), (D) and (E) rely on mesoscopic scale surface phenomena like surface wetting, associated with developments in UHV instrumentation.

The starting point of a multi-access interconnection technology on a large electronic gap surface material is the careful selection and surface preparation of the supporting material.

2 Atomic Scale Circuitry (Level A)

2.1 Surface Selection and Preparation

For natural as well as for artificial mineral crystalline compounds, a wide band gap is more the rule than the exception. But, in this huge class of materials, only a few have been investigated in details by surface science techniques, mainly because of the inadequacy of techniques using electron beams to study them. Stringent conditions should be satisfied to make possible the construction of the first atomic scale level (A) of the interconnection sequence presented in Fig. 1: The surface

Table 1 Some of the most studied wide band gap semiconductors and insulators

Material	KBr	MgO	Al_2O_3	CaF_2	4H-SiC	2H-GaN	2H-AlN
Bulk band gap (eV)	6.6[a]	7.8[b]	8[c]	12.1[d]	3.07[e]	3.47[e]	6.28[e]

[a] [34]
[b] [35]
[c] [36]
[d] [37]
[e] [38]

should be (1) atomically clean, with a well-controlled stoichiometry, (2) atomically flat, with large enough terraces (3) should present few defects and (4) should allow the 2D growth of metal nanopads (B). In these conditions, a typical 50 nm × 50 nm "perfect" area, suitable to accommodate the atomic scale device, becomes readily accessible. A selection of wide band gap materials that have been studied in details, either for their simplicity or for their applications, and that satisfy these requirements, is presented in Table 1.

KBr is representative of the family of alkali halide, the archetype of ionic compounds. The most stable surface, prepared by cleavage, is the non-polar (001) surface. Large atomically clean terraces are easily obtained. MgO is one of the simpler ionic oxides, used for instance as a model catalyst. As for KBr, the most stable surface is the (001) surface. Cleavage allows getting a clean surface with the nominal stoichiometry of the material. The surfaces of the different phase of alumina have been studied for a long time, but despite their technological interest, their atomic structure remains largely unknown. They are difficult to prepare and present usually complex phase diagrams, where the surface stoichiometry plays a determining role. CaF_2 is an ionic insulator that has been considered for a long time as a good candidate for insulating material in microelectronics due to its small lattice mismatch with Si. The CaF_2(111) surface can be obtained by cleavage and it is atomically flat over large areas. SiC is one of the most studied wide band gap material, finding applications in such diverse area as power electronics, micro-electro-mechanical systems and as supporting material for graphene. It exists in different polytypes, which display a rich variety of surface reconstruction, some of which have been investigated in detail by STM [1]. More recently, group-III nitride semiconductors (GaN, AlN) have attracted much interest for their applications as short wavelength optical emitters and detectors as well as for high-speed electronics. A large variety of surface structures is obtained depending on the growth method and conditions. Some of these surfaces have been studied in detail, in particular by STM [2].

For all these materials, the *surface* band gap should be distinguished from the *bulk* band gap. For instance, at the MgO(001) surface, the band gap is reduced form the bulk value of 7.8 to 6.2 eV, due to an unoccupied surface state [3]. An extreme case is that of the metal-rich termination of GaN(0001) and AlN(00001) faces, which is metallic [2]. Among all these different insulating substrate, we have chosen to work on AlN(0001) surface. Indeed it is the only insulating substrate that

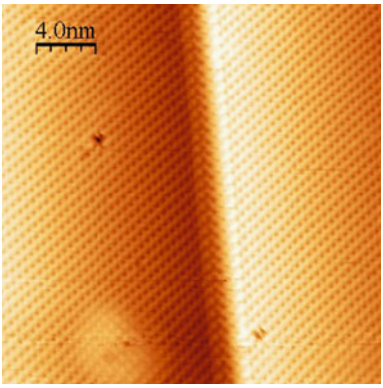

Fig. 2 Atomically resolved NC-AFM image of the KBr(001) surfaces showing a monoatomic step and atomic defects

would allow to fullfill the 4th criterium of 2D growth of metal nanopads as explained in the Sect. 1 "Atomic Scale Interconnection Machine".

2.2 Atomic Scale Imaging: NC-AFM

After the surface preparation, STM atomic scale surface imaging is practical only for SiC, GaN and the metal-rich faces of AlN, among the compounds listed in Table 1. Fortunately, recent progresses in AFM imaging with the so-called non-contact (NC) or frequency modulation (FM) mode [4, 5] have opened the way to atomic and molecular resolution on large gap and insulating surfaces. Notice that this NC-AFM can be efficiently combined with optical microscopy if suitable markers in the micron range are fabricated on the substrate as discussed at this end of this section.

In NC-AFM, the cantilever is embedded in a positive feedback loop that oscillates at the cantilever resonance frequency while another loop maintains its oscillation amplitude at a pre-set value. In contrast to the amplitude modulation (AM) or "Tapping" [6] method, where the frequency is externally fixed, the resonance frequency of the cantilever in the FM method varies under the influence of the tip-sample forces. A "topographic" image is obtained by scanning the surface while adjusting the tip-substrate distance required to maintain this frequency shift at a pre-set value. The specificity of this method is that very high quality factors force sensors, which lead to increased force sensitivity, can be used without penalizing the acquisition time, as in AM-AFM, as demonstrated in the founding paper of FM-AFM by Albrecht and co-workers [7].

True atomic resolution was first obtained in NC-AFM by Giessibl [8] and Kitamura and Iwatsuki [9] in 1995. It has now been achieved on a wide variety of surfaces (metals, covalent or ionic semiconductors, covalent or ionic insulators) and the technique, after been used in UHV for a long time, is now adapted to

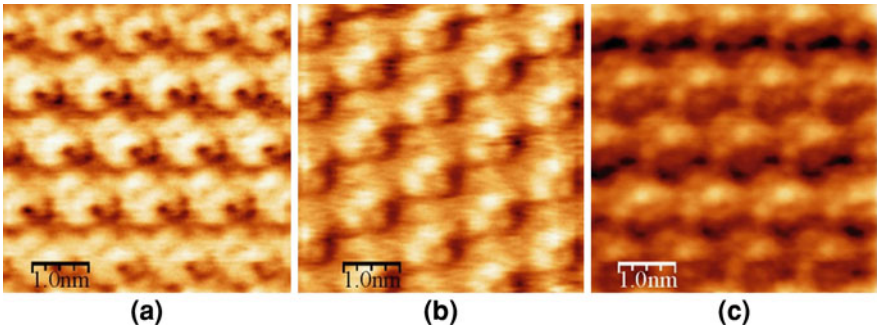

Fig. 3 High-resolution images of the top of type II islands, obtained on different samples with different cantilevers. Experimental conditions: **a** fo = 274 kHz, Δf = −150 Hz, A = 2 nm. **b** fo = 287 kHz, Δf = −80 Hz, A = 2 nm. **c** fo = 278 kHz, Δf = −285 Hz, A = 2 nm. The corrugation in these images is of the order of 0.1 nm

ambient conditions and to liquids, especially for applications in biology [10]. Referring to Table 1, true atomic resolution has been obtained on KBr(001) (Fig. 2) [11] and many other alkali halides [12], MgO(001) [13], Al_2O_3(0001) [14], CaF_2(111) [15] but not yet on SiC, GaN and AlN.

Even less is reported on the imaging of molecules on the surface of the materials of Table 1 by NC-AFM. Most of the reported work was performed on alkali halides surfaces, such as KBr(001) and at room temperature [16]. In these conditions, for low coverage, most molecules diffuse, due to their weak interaction with these surfaces, making the observation of single isolated molecules impossible, except when adsorbed on a defect, for instance a step edge. Using structured surfaces [17] allows more efficient trapping of the molecules [18]. For higher coverage, monolayer islands followed by multilayer 3D crystallites are often observed (PTCDA on NaCl(001) [19] and on KCl(001) [20]). Molecular lines are also formed in certain cases (DiMe-PTCDI/KBr(001) [21]). The observation of submolecular details on 2D layers of HMTP on KBr(001) can be achieved as shown in Fig. 3 [22]. The analysis of these topography images is not straightforward. The most probable reason is that the image is influenced by the structure of a non-symmetric tip. In these conditions, it is impossible to position a molecule on the image without further indications. Calculations, incorporating a realistic tip model are clearly needed to progress in the interpretation of this type of images.

It is clear that NC-AFM will boost this rapidly developing new domain of surface science. With the advent of low temperature NC-AFM heads, these problems of mobility of molecules on insulating surfaces will become less limiting. Nevertheless, a large effort is needed to synthesize molecules adapted to room temperature experiments in the longer term vision of devices that should ideally work at this temperature.

3 Atomic Scale Surface Interconnection Circuit

The next step in the interconnection strategy presented Fig. 1 is to build conductive atomic wires on the surface of the wide gap material to connect the atomic scale circuit to the metallic nanopads. Therefore, it is not enough to use for example surface step edges to self-stabilize metal atomic wires following a peculiar surface crystalline direction. These atomic wires have to converge toward a specific surface location whose lateral dimension will be around 10 nm and this is generally not compatible with surface crystallographic directions. Two strategies have been envisioned to construct these atomic wires: single atomic manipulation or a self-assembly process via molecular molding [23].

3.1 Metallic Nanopads Fabrication and Re-configuration (Level B)

The metallic nanopads (B) of the Fig. 1 interconnects have two functions: First, they serve to bridge the atomic scale circuit (A) to the next mesoscopic level of interconnection (C). Second, they provide the metallic density of states necessary in a decoherence like process to superpose the billions of through bond electron transfer per second that are occurring between a couple of voltage bias nanopads (B) through the atomic scale circuit (A). This superposition results in the tunneling current intensity which can be measured with a standard amperemeter [24]. The pads lateral dimension must be compatible with the actual precision of the dynamic nanostencil technique (described in Sect. 3.2.1), which is of the order of a few tens of nanometers. These nanopads should also be not too high (less than three monolayers) for the AFM tip to be able to image the surface where the central atomic scale circuit is located and crystalline to present well defined facets without which imaging a molecule becomes very difficult.

The first classification of growth modes of a deposit on a surface was proposed by Bauer [25] who distinguished three basic modes: (i) The Frank-van der Merwe two-dimensional growth, where atomic layers are formed one after each other, (ii) the island Volmer-Weber growth, where three-dimensional clusters are formed and (iii) the Stranski–Krastanov mode, where two-dimensional growth is followed by cluster formation.

It turns out that, in most cases, metals grow on the materials listed in Table 1 in the Volmer-Weber mode, that is in the form of low aspect ratio clusters. This is particularly the case for alkali halides and most oxides surfaces, while much less is known on the other materials. An example is shown in Fig. 4, where four monolayer (ML) of copper were deposited at room temperature on a $Al_2O_3(0001)$ surface and imaged with AFM: Compact islands with sizes ranging from 2 to 6 nm are observed. This general behavior can be traced back to the fact that the surface free energy of insulating materials is quite generally much lower than that of

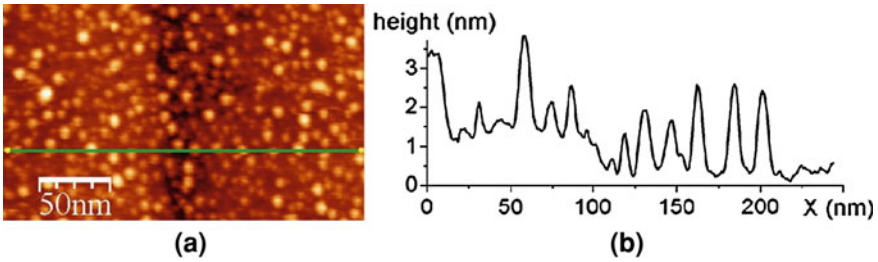

Fig. 4 **a** AFM image of an alumina surface where 4 ML of copper have been deposited at room temperature. **b** Profile corresponding to the line plotted on the image

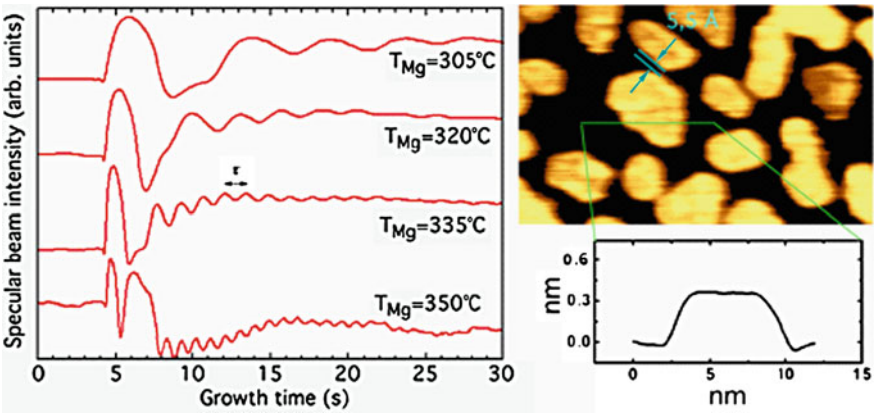

Fig. 5 Mg metallic nano-island growth on the GaN(0001) surface. (*Left*) the RHEED oscillations at different substrate temperatures during the growth. (*Right*) UHV STM image of a 0.6 ML deposit showing Mg monolayer islands with very small inter-island distances. Adapted from [27]

metals. Of course, many other parameters influence the growth mode, such as the lattice mismatch between the two materials or the nature of the interface (reactive or not) as well as the experimental conditions during the growth, which can drive the system far from thermodynamic equilibrium. We refer for a detailed description to the book of Noguera [26].

From a practical point of view, this behavior constitutes a serious problem to make suitable nano-pads. Fortunately, it was recently demonstrated that Mg grows on the N-rich face of GaN(0001) in the layer-by-layer mode [27], making this system promising for our purpose. Figure 5 shows the RHEED oscillations during the growth at different temperatures and a STM picture showing monolayer (height $\sim$ 0.3 nm) epitaxial islands. This behavior is favored by the small lattice parameter mismatch of 0.3% between the substrate and the deposit. Note that STM imaging can be practiced on GaN, due to its relatively small band gap (Table 1).

In contrast, studies to find a metal that would grow in the layer-by-layer mode on AlN, which has a larger gap (Table 1), require the use of NC-AFM.

Aside from continuing the exploration of the growth conditions of metal nano-islands on large gap semi-conducting and insulating surface for example by playing with kinetic effects to better adapt the metal nano-island shape, it is also important to consider how to arrange them on the surface. In Figs. 4 and 5, they are randomly distributed over the surface which may be very good to find two nano-pads contacts as indicated in Fig. 5 with sometimes very small inter nano-pads distances below 1 nm. Such small gaps are impossible to fabricate with conventional e-beam nanolithography techniques. For a larger number N of interconnects, the nanopads will have to be arranged in a specific order and orientation on the insulating surface. At present, the only way to construct such an interconnection structures with for example N nanopads converging in a circle toward the same surface spot is to manipulate them one by one using the tip of a NC-AFM. This puts forward the need to study manipulation by NC-AFM not only of single atoms or molecules but also of larger nano-objects made of millions of identical atoms. This had already been demonstrated on a small gap semiconductor surface with STM and is now required for larger electronic gap surfaces.

3.2 The Interconnections from Nano to Macro World (Levels C, D and E)

According to the interconnection scheme illustrated in Fig. 1 and after having fabricated well facetted metallic nano-islands (nanopads), the next steps are the realization of the three interconnection levels C, D and E with increasing width from the nanometer to the macroscopic scale. To realize these electrodes on the surface, it is not possible to use either a resist-based nano-lithography technique or a stamping technique because the atomic cleanness of the working area where the atomic scale circuitry A and the nanopads B should be built should be preserved. The only remaining possibility is to use different stencil techniques under UHV to grow the nanoscale wires (C) and the microelectrodes (D), and then to use metallic microcantilevers (E) to contact the microelectrodes. The order in which these different operations have to be performed does not follow the order in which they were presented, but depends on technical constraints related to the necessity of successive alignments of the different structures. The operations performed to realize the interconnection levels C, D and E, are combined with levels A and B according to the following sequence:

1. Surface preparation, for instance, growth of AlN.
2. Growth and possibly manipulation of the metallic nanopads (Level B).
3. Growth of the microelectrodes by static stenciling (Level D).
4. Nanostencil deposition of the nanowires between the metallic nanopads and the end of the microelectrodes (Level C).

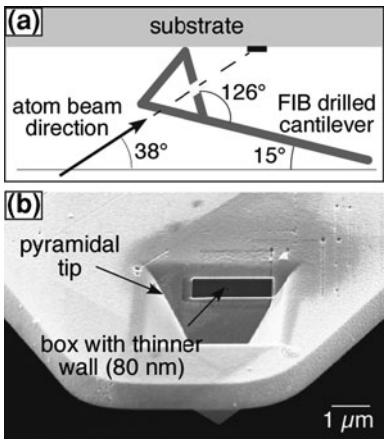

Fig. 6 **a** Schematic view of the geometrical configuration for the Toulouse AFM nanostencil machine. **b** Scanning electron microscopy (SEM) image showing a recessed box in the rear face of an AFM tip, which was first thinned down to 80 nm by FIB

5. Building of the atomic scale circuitry by NC-AFM (Level A).
6. Electrical measurement of the molecule properties with the help of the metallic microcantilevers (Level E).

3.2.1 The Stencil Techniques

Two main stencil techniques exist: the static technique, in which the mask is placed in contact with the substrate, and the pattern is directly evaporated on its surface, and the dynamic technique [28–32], in which the pattern is drawn on the substrate by moving the mask. This last mode is generally implemented on an AFM microscope. Indeed an AFM cantilever can be patterned using the focused ion beam (FIB) technique and used as the shadow mask. Figure 6a shows the principle of the nanostencil technique based on an AFM cantilever.

Figure 6a shows the geometrical configuration of the dynamic stencil on the Toulouse machine. Si_3N_4 cantilevers, with hollow tips, are used. The stencil pattern is made in the rear side of the tip, using a focused gallium ion beam. It should be positioned as close as possible to the substrate in order to minimize the geometrical enlargement of the deposited pattern, which varies as the ratio between the pattern-surface distance and the evaporation source-surface distance. To reach small mask pattern sizes, it is also necessary to thin down an area of the tip side from about 800 to 80 nm (the box shown in Fig. 6b) before drilling the patterns in this membrane.

The high positioning precision of the AFM combined to the nanometric size of the apertures made in the AFM cantilever allows to obtain nanowires. Dynamic nanostencil is a UHV in situ technique with the additional advantage of allowing to image the surface at the different stages of the fabrication process and therefore to directly align the mask relative to the nano-pads.

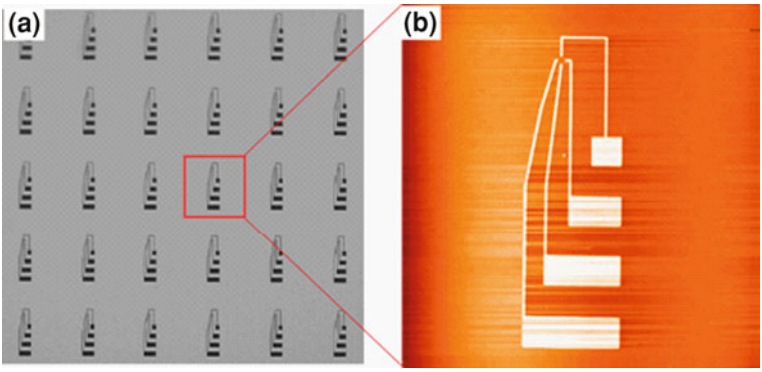

Fig. 7 **a** Optical microscope image of the microelectrodes aperture made in a static stencil membrane. **b** 75 × 75 μm AFM image in non-contact mode showing one device [32]

3.2.2 Growth of the Microelectrodes by the Static Stencil Technique

The microelectrodes are deposited in UHV by the static stencil technique. Specific microelectrodes were designed in such a way that they are protected by the shadow of the AFM cantilever used during the next steps to grow the nanowires.

Figure 7a shows the microelectrodes stencil mask, observed by optical microscopy. One microelectrodes device constitutes the bridge between the level C (1 μm) and E (10 μm): the pads used for the connection with the metallic microcantilevers are 6 μm in width separated by 6 μm. So the total device is 62 × 20 μm. It is easily seen with an optical microscope, but also with the wide scan range AFM available with the Micro Clean Room developed in Toulouse, described in Sect. 4.2. Figure 8b shows a 75 × 75 μm NC-AFM image of one device, made by depositing copper on SiO_2 [32].

3.2.3 Growth of the Nanoelectrodes by the Dynamic Nanostencil Technique

The nanopatterning of the inter-microelectrodes area by the nanostencil technique, described previously, relies on the precise determination of the actual location of the deposited nanopattern with respect to the nanostencil AFM tip. Consequently, a preliminary calibration step is needed for each new nanostencil AFM cantilever. In a typical calibration experiment, the cantilever is approached to a bare substrate in either non-contact or contact AFM mode. A deposit is then made using the dedicated effusion cell. Large-scale AFM images are then obtained by scanning the X–Y table and the relative position of the deposited pattern and the AFM tip can be precisely measured. Subsequently, the bare substrate is exchanged with the substrate with the deposited microelectrodes. Hence, knowing the location of one set of microelectrodes and the relative position of the deposit with respect to the AFM tip apex, the nanopositioning table is moved so as to deposit the nanopatterns

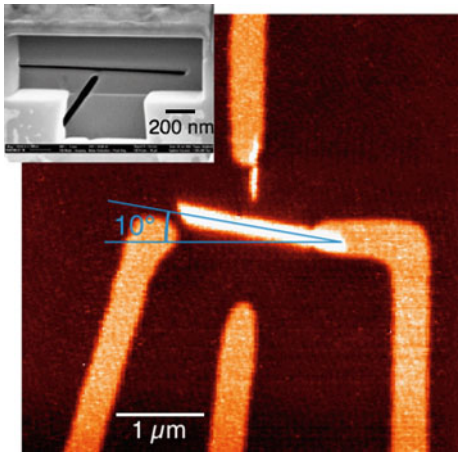

Fig. 8 Non-contact AFM image (4 × 4 μm) of Cu nanoelectrodes deposited between the Pd micro electrodes made by static stencil on Si substrate; (*inset*) SEM image of the FIB drilled pattern distorted to correct the geometrical distortions due to the evaporation geometry (from Ref. [31])

precisely between the microelectrodes. Figure 8 shows an NC-AFM image of 5 nm thick copper nanoelectrodes deposited between the four microelectrodes.

This example shows the difficulties met for precise alignment: the nanoelectrodes pattern is correctly aligned in y direction but has a misaligning of around 100 nm in *x* direction and a defect angle of 10°. The error in x and y direction is related to the mechanical drift of the piezo tube during the experiment. The angle error comes from addition of error angles during the FIB drilling and the gluing of the cantilever on its holder. We are confident that these errors can be minimized and plan to improve the overall accuracy to 20 nm, which is the limit imposed by our wide range (XY) table (see next section).

3.2.4 Electric Measurements with the Microcantilevers

The micropads at the end of the microelectrodes (Fig. 7) should be connected to the macroscopic world. Metallic microcantilevers mounted on a specific UHV compatible printed circuit board (PCB) connected to the outside of the UHV chamber are used for that purpose. They should have good mechanical and electrical properties in order to establish low resistance electrical contacts with the micropads. The first models of these metallic microcantilevers used in air were made entirely with gold and have shown bad mechanical properties: They are easily plastically deformed. In more recent designs, 1 μm thick SiC layers were used to support metallic wires. To avoid contact problems, it was also necessary to induce a curvature of several μm of the SiC cantilevers [33]. Furthermore, the size should be correctly chosen for the microcantilevers to be easily seen with the optical microscope. In the particular case of the Micro Clean Room, the size of the microcombs is 6 μm in width for SiC, 4 μm in width for each metallic wire, 100 μm in length and 24 μm of periodicity. Figure 9 shows one microcomb mounted on its dedicated PCB.

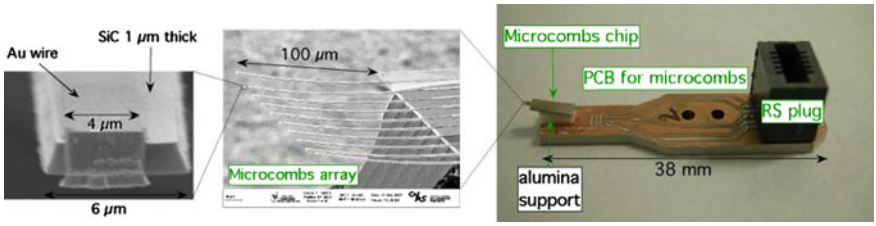

Fig. 9 (*Left*) SEM image of the end of a SiC-based cantilever with the Au wire; (*middle*) SEM image of the microcombs made of 10 SiC-based cantilever; (*right*) microcombs chip mounted on its specific PCB. The SiC-based microcombs were made by the LPN (CNRS UPR20) at Marcoussis during the DiNaMo project (French ANR founding No ANR-05-NANO-014)

4 The UHV Factory

To realize under UHV the five levels of interconnect described in Fig. 1, the deposition of molecules, their observation by NC-AFM and the measurement of their electrical properties, the GNS group has designed and realized a dedicated UHV equipment called DUF (DiNaMo UHV Factory). This equipment allows transferring samples under UHV between five complementary UHV chambers:

1. MBE growth dedicated to nitride semiconductors growth, metallic nanopads growth and stencil evaporation for microelectrodes.
2. Mass spectrometer transformed in a molecular ions source.
3. Preparation chamber for clean substrates, STM tips and AFM cantilevers.
4. Room Temperature AFM/STM for surface characterization by STM and NC-AFM.
5. The microclean room: AFM/STM modified for nanostenciling experiments and electrical measurements.

Figure 10 shows this equipment in its actual state.

4.1 The Nitride Dedicated MBE Chamber

The MBE chamber has mainly three objectives: (1) the growth of the AlN(0001) substrate, (2) the growth of the metal nanopads on AlN(0001) and (3) the growth of the microelectrodes described in Sect. 2. We have designed a specific MBE chamber with eight effusion cells at 45° of the normal axis of the substrate, and 1 effusion cell on the normal axis of the substrate to allow the growth of non-deformed microelectrodes by the static stencil technique. Furthermore, this MBE chamber is equipped with high temperature substrate manipulator (1400°C) and a NH3 gaz line for N precursor for AlN growth. The pumping is done by the way of a 2300 l/s turbopump and a 1200 l/s ionic pump. A 20 keV RHEED gun allows

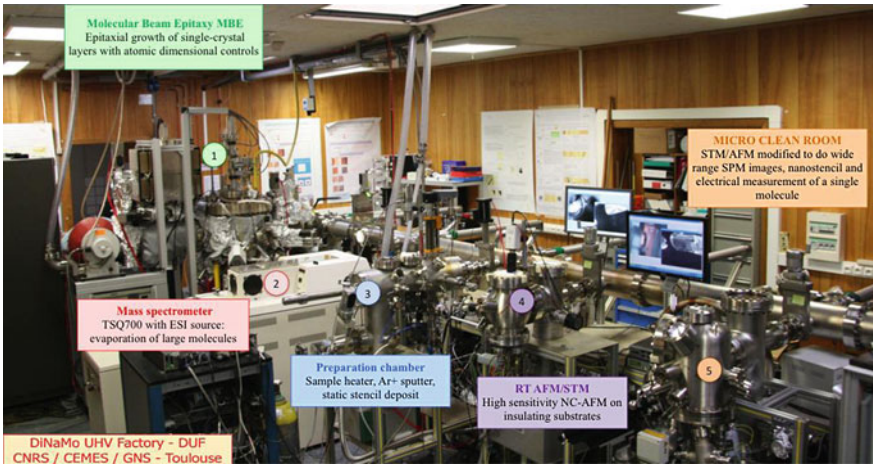

Fig. 10 The DUF (DiNaMo UHV Factory) equipment allows to transfer samples between five complementary UHV chambers in order to realize the five levels of interconnect on wide band gap semiconductors (GaN, AlN). The different chambers are described in the text

in situ RHEED acquisition. This specific MBE coupled under UHV to the RT AFM/STM will allow us to study the AlN(0001) surface which is actually not known.

4.2 The Microcleanroom

To realize the steps 4 and 6 described in the Sect. 3 "Atomic Scale Interconnection Machine, a UHV Omicron Nanotechnology VT STM/AFM head has been modified to accommodate different tools, namely [32]:

1. A flexural-hinge guided (XY) piezoceramics driven nanopositioner stage (100 × 100 µm, repeatability 5 nm) with a closed loop control based on capacitive sensors.
2. An evaporation system highly collimated on the cantilever to perform nanostencil deposition.
3. A (XYZ) piezo table for positioning the metallic microcombs.
4. An optical microscope to control the positioning of the microcombs.

These modifications were designed by the mechanical department of the laboratory. Figure 11 shows a scheme (a) and a picture (b) of the modified AFM.

The main advantage of using a commercial UHV AFM/STM is to benefit from its good characteristics for SPM imaging. But the piezoelectric tube used to scan has a range of a few µm only. The addition of a XY table to move the sample offers the possibility to perform wide range scanning, up to 80 µm SPM images,

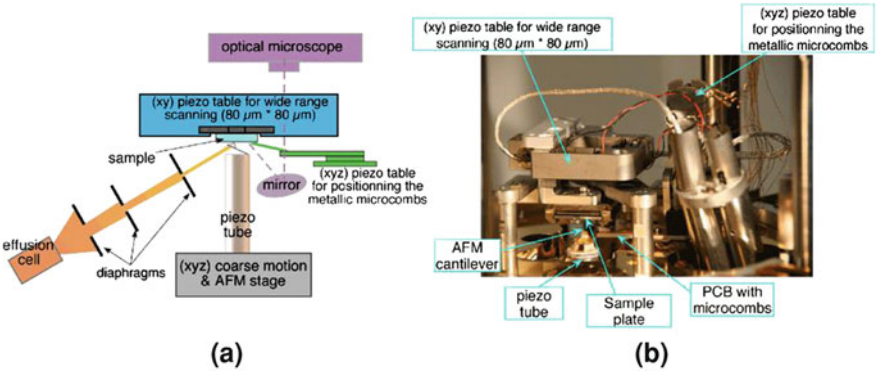

Fig. 11 **a** Schematic view of the functionalities implemented inside the Micro Clean Room, and **b** the modified AFM/STM head

while keeping the possibility to realize atomic scale imaging with the piezoelectric tube.

One of the disadvantages is the small accessible space around the SPM head. Indeed, it is not possible to place an optical microscope with normal incidence with respect to the substrate, and an atomic source for the nanostencil experiments with normal incidence with respect to the AFM cantilever. In our case, the image obtained by the optical microscope is reflected by a mirror that makes an angle of 30° with the substrate plane. This gives distorted images, with a loss of resolution: only 3 μm instead of 1 μm in normal incidence. The effusion cell is fixed on a port of the UHV chamber at an angle of 33° with the horizontal plane, and another angle of 28° between the two vertical planes passing through the evaporation beam and the central axis of the cantilever (Fig. 6a). This orientation of the atom beam induces distortion, which should be taken into account in the design of the nanopattern to be drilled into the pyramidal tip of the cantilever (Fig. 8) [32].

4.3 The Modified Mass Spectrometer TSQ700

To evaporate molecule on a surface, the usual technique is thermal evaporation. This technique allows the sublimation of molecules if the needed temperature is not too high. Indeed for fragile molecules, at too high temperature breakdown of molecules can occur leading to the evaporation of molecule pieces. To sustain to this problem, one solution is to use soft ionization of molecules. The electrospray ionization (ESI) was developed for proteins studies. The electrospray ionization involves the introduction of a sample solution, consisting of an analyte: the molecule to analyze, dissolved in a solvent, through a stainless steel needle into the ion source. The solution is pumped through a narrow stainless steel capillary into the electrospray needle. A high voltage of 3 or 4 kV is applied to the tip of the

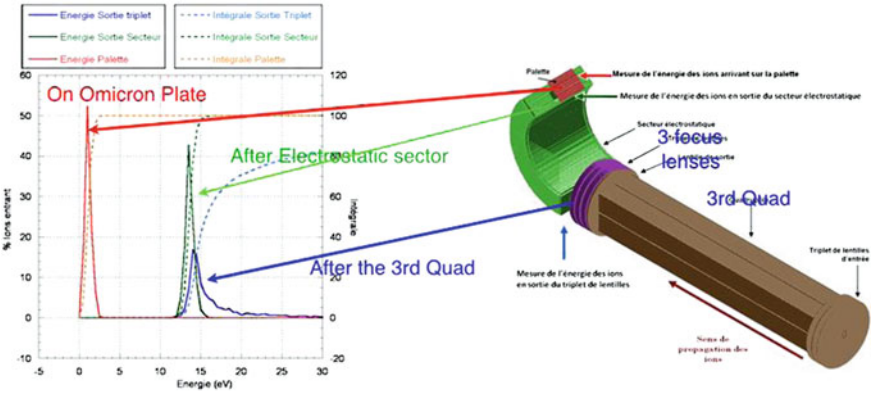

Fig. 12 (*Right*) Model of the last quad (*brown*), the collimator lenses (*purple*), the 127° electrostatic sector (*green*) and susbtrate (*red*); (*left*) energy histogram of ions getting outside of the quad (*blue curve*), after the electrostatic sector (*green curve*) and then on the substrate with 12 V applied voltage (*red curve*)

capillary. As a consequence, a strong electric field is created and when the solution emerges from the tip of the electrospray needle, its surface becomes charged, and the solution is dispersed into a fine spray of highly charged liquid droplets. The surface's charge generates Coulomb repulsion forces that disrupt the surface of the solution, prompting the formation of highly charged liquid droplets. In order to direct the spray emerging from the end of the capillary tip of the electrospray needle toward the ionization room, a counter current drying gas is used. This gas, usually nitrogen, is heated around 60°C. It is used to help to direct the spray and also to evaporate the solvent present in the solution. So the dispersed droplets contain solvent molecules and positive and negative analyte molecules. In consequence of the voltage applied on cylindrical electrodes, there are a majority of negative or positive analyte ions depending on the polarity of this voltage.

In the TSQ700, the ionized molecules enter into a series of three quadrupoles allowing the selection of ionized molecules with respect to their mass under charge ratio (m/z). The three quadrupoles are designed to reject the neutral molecules and X-rays. To not destroy the molecules when landing into the substrate, their energy should be lower than 5 eV. We have studied the energy of ions flying through a quadrupole using the software SIMION which allows to calculate electrical fields and trajectory of ions in those fields. We have shown that the ions getting outside of a quadrupole have sprayed energy. Around 50% of them have high energy more than 50 eV, which is incompatible with soft landing. In order to remove these high energy ions, we have designed an electrostatic sector of 127° with collimator electrostatic lenses. With this added electrostatic system at the end of the last quadrupole, the ions energy shows a peak with FWHM of 2 eV, as shown in Fig. 12. By applying the good voltage on the substrate, the ions energy is decreased below 5 eV.

This study allows us to find the dimensions of the different parts. The design and modifications of the TSQ700 was already done. Actually, the experimental tests are on the way to characterize the energy of the ions.

5 Conclusion

The experimental measurement of the electronic properties of a single molecule logic gate on insulating substrate is a world challenge. Ten years of design and fabrication was necessary to assemble the unique UHV experimental setup which will allow the realization under UHV of all the electrical interconnection steps necessary to connect the molecule with the macroscopic world. Meanwhile a lot of knowledge and know-how on the different techniques used inside this UHV factory has been acquired, such as static stencil and nanostencil techniques, non-contact atomic force microscopy (NC-AFM) on molecules and insulating substrates at the atomic level, energy filtering of ions beam getting out of a quadrupole, etc.…

Nevertheless one scientific bottleneck should be broken through in the future: It is first, the growth and the characterization at the atomic level of AlN(0001) insulating surfaces, and second the growth of flat metallic nanopads on this surface and their electrical characterization by the mean of different technique such as Kelvin probe force microscopy (KPFM). Once this study is done, the knowledge of all the scientific and technologic blocks will allow us to realize the single molecule device in a planar configuration.

Acknowledgments The design and the realization of the UHV factory and the studies made with it was supported by European fundings : AtMol project "Atomic Scale and single Molecule Logic gate Technologies" (Contract No ICT-2009.8.7-270028), Artist project « Alternative routes toward information storage and transport at the atomic and molecular scale » (Contract No ICT-2007.8.0-243421), Pico-Inside project « Computing Inside a Single Molecule Using Atomic Scale Technologies » (Contract No IST-2004-2.3.4.2-15847), NaPa project "Emerging Nano-patterning Methods" (Contract No NMP4-CT-2003-500120), CHIC project "Consortium for Hamiltonian Intramolecular Computing" (Contract No IST-2001-33578), and French national funding : *CPER* 2007-2013 Campus *Gaston Dupouy* "Des nanomatériaux aux nanosciences moléculaires. et aux picotechnologies", NanoSens (Contract No ANR-08-NANO-017), MolSiC (Contract No ANR-08-NANO-030), DiNaMo (Contract No ANR-05-NANO-014), CPER 2002-2007 "Nanosciences, Nanotechnologies et Nanomatériaux".

References

1. Heinz, K., Bernhardt, J., Schardt, J., Starke, U.: Functional surface reconstructions of hexagonal SiC. J. Phys. Condens. Matter **16**, S1705 (2004)
2. Feenstraa, R.M., Dong, Y., Lee, D.C.: Recent developments in surface studies of GaN and AlN. J. Vac. Sci. Technol. B **23**, 1174 (2005)

3. Schönberger, U., Aryasetiawan, F.: Bulk and surface electronic structures of MgO. Phys. Rev. B **52**, 8788–8793 (1995)
4. Giessibl, F.J.: Advances in atomic force microscopy. Rev. Mod. Phys. **75,** 949 (2003)
5. Morita, S., Wiesendanger, R., Meyer, E.: Noncontact Atomic Force Microscopy. Noncontact Atomic Force Microscopy. Springer, Berlin (2002)
6. Zhong, Q., Innis, D., Kjoller, K., Ellings, V.B.: Fractured polymer/silica fiber surface studied by tapping mode atomic force microscopy. Surf. Sci. **290**, L688 (1993)
7. Albrecht, T.R., Grutter, P., Horne, H.K., Rugar, D.: Frequency modulation detection using high-Q cantilevers for enhanced force microscope sensitivity. J. Appl. Phys. **69**, 668 (1991)
8. Giessibl, F.: Atomic resolution of the silicon (111)-(7 × 7) surface by atomic force microscopy. J. Sci. **267**, 68 (1995)
9. Kitamura, S., Iwatsuki, M.: Observation of 7 × 7 reconstructed structure on the Silicon (111) surface using ultrahigh vacuum noncontact atomic force microscopy. Jpn. J. Appl. Phys. Part 2 **34**, L145 (1995)
10. Fukuma, T., Higgins, M.J., Jarvis, S.: Direct imaging of Lipid-Ion network formation under physiological conditions by frequency modulation atomic force microscopy. Phys. Rev. Lett. **98**, 106101 (2007)
11. Venegas de la Cerda, M.A., Abad, J., Madgavkar, A., Martrou, D., Gauthier, S.: Step-induced tip polarity reversal investigated by dynamic force microscopy on KBr(001). Nanotechnology **19**, 045503 (2008). doi:10.1088/0957-4484/19/04/045503
12. Bammerlin, M., Lüthi, R., Meyer, E., Baratoff, A., Lü, J., Guggisberg, M., Loppacher, C., Gerber, C., Güntherodt, H.: Dynamic SFM with true atomic resolution on alkali halide surfaces. J. Appl. Phys. A **66**, S293 (1998)
13. Barth, C., Henry, C. R.: Atomic resolution imaging of the (001) surface of UHV cleaved MgO by dynamic scanning force microscopy. Phys. Rev. Lett. **91**, 196102 (2003)
14. Barth, C., Reichling, M.: Imaging the atomic arrangements on the high-temperature reconstructed alpha-Al2O3(0001) surface. Nature **414**, 54 (2001)
15. Barth, C., Foster, A.S., Reichling, M., Shluger, A.L.: Contrast formation in atomic resolution scanning force microscopy on CaF2(111): experiment and theory. J. Phys. Condens. Matter **13**, 2061 (2001)
16. Pfeiffer, O., Gnecco, E., Zimmerli, L., Maier, S., Meyer, E., Nony, L., Bennewitz, R., Diedrich, F., Fang, H., Bonifazi, D.: Force microscopy on insulators: imaging of organic molecules. J. Phys.: Conf. Ser. **19**, 166 (2005)
17. Bennewitz, R.: Structured surfaces of wide band gap insulators as templates for overgrowth of adsorbates. J. Phys. Condens. Matter **18**, R417 (2006)
18. Nony, L., Gnecco, E., Baratoff, A., Alkauskas, A., Bennewitz, R., Pfeiffer, O., Maier, S., Wetzel, A., Meyer, E., Gerber, C.: Observation of individual molecules trapped on a nanostructured insulator. Nano Lett. **11**, 2185–2189 (2004)
19. Burke, S.A., Ji, W., Mativetsky, J.M., Topple, J.M., Fostner, S., Gao, H.-J., Guo, H., Grütter, P.: Strain induced dewetting of a molecular system: bimodal growth of PTCDA on NaCl. Phys. Rev. Lett. **100**, 186104 (2008)
20. Dienel, T., Loppacher, C., Mannsfeld, S.C.B., Forker, R., Fritz, T.: Growth-mode-induced narrowing of optical spectra of an organic adlayer. Adv. Mat. **20**, 959 (2008)
21. Fendrich, M., Kunstmann, T.: Organic molecular nanowires: N,N′-dimethylperylene-3,4,9,10-bis(dicarboximide) on KBr(001). Appl. Phys. Lett. **91**, 023101 (2007)
22. Hinaut, A., Lekhal, K., Aivazian, G., Bataille, S., Gourdon, A., Martrou, D., Gauthier, S.: NC-AFM study of the adsorption of Hexamethoxytriphenylene on KBr(001). J. Phys. Chem **115**(27), 13338–13342 (2011). doi:10.1021/jp202873f
23. Joachim, C., Martrou, D., Rezeq, M., Troadec, C., Jie, D., Chandrasekhar, N., Gauthier, S.: Multiple atomic scale solid surface interconnects for atom circuits and molecule logic gates. J. Phys. Condens. Matter **22**(8), 084025 (2010). doi 10.1088/0953-8984/22/8/084025
24. Joachim, C., Ratner, M.A.: Molecular electronics: some views on transport junctions and beyond. PNAS **102**, 8801 (2005)

25. Bauer, E.: Phänomenologische Theorie der Kristallabscheidung an Oberflächen. I. Zeit. Kristall. **110**, 372 (1958)
26. Noguera, C.: Physics and Chemistry at Oxide Surfaces. Cambridge University Press, Cambridge (1996)
27. Pezzagna, S., Vézian, S., Brault, J., Massies, J.: Layer-by-layer epitaxial growth of Mg on GaN(0001). Appl. Phys. Lett. **92**, 233111(2008)
28. Lüthi, R., Schittler, R.R., Brugger, J., Vettiger, P., Welland, M.E., Gimzewski, J.K.: Parallel nanodevice fabrication using a combination of shadow mask and scanning probe methods. Appl. Phys. Lett. **75**, 1314 (1999)
29. Zahl, P., Bammerlin, M., Meyer, G., Schlittler, R.R.: All-in-one static and dynamic nanostencil atomic force microscopy/scanning tunneling microscopy system. Rev. Sci. Instrum. **76**, 023707 (2005)
30. Egger, S., Llie, A., Fu, T., Chongsathien, J., Kang, D., Welland, M.E.: Dynamic shadow mask technique: a universal tool for nanoscience. Nano Lett. **5**, 15 (2005)
31. Guo, H., Martrou, D., Zambelli, T., Polesel-Maris, J., Piednoir, A., Dujardin, E., Gauthier, S., van den Boogaart, M.A.F., Doeswijk, L.M., Brugger, J.: Nanostenciling for fabrication and interconnection of nanopatterns and microelectrodes. Appl. Phys. Lett. **90**, 093113 (2007). doi: 10.1063/1.2710473
32. Guo, H., Martrou, D., Zambelli, T., Dujardin, E., Gauthier, S.: Development of UHV dynamic nanostencil for surface patterning. Rev. Sci. Instrum. **79**, 103904 (2008). doi:10.1063/1.2999547
33. Coutrot, A.-L., Roblin, C., Lafosse, X., David, C., Madouri, A., Laloo, R., Martrou, D.: New SiC microcantilever electric connection array for single molecule electrical investigation. Microelectron. Eng. **86**, 119 (2009). doi:10.1016/j.mee.2009.01.069
34. Mei, W.N., Boyer, L.L., Ossowski, M.M., Stokes, H.T.: Phys. Rev. B **61**, 11425 (2000)
35. Roessler, D.M., Walker, W.C.: Phys. Rev. **159**, 733–738 (1967)
36. French, R.H.: J. Am. Ceram. Soc. **73**, 477 (1990)
37. Rubloff, G.W.: Phys. Rev. B **5**, 662 (1972)
38. Cimalla, V., Pezoldt, J., Ambacher, O.: J. Phys. D: Appl. Phys. **40**, 6386 (2007)

Challenges and Advances in Instrumentation of UHV LT Multi-Probe SPM System

Zhouhang Wang

Abstract The progress of nanoscience and nanotechnology can be realized only through continued advances and utilization of instruments and techniques for characterizing material properties and manipulating material and device at nanoscale. The UHV LT Multi-Probe SPM system with high resolution SEM has been developed to meet such challenges. This integrated instrument bridges dimensions from the centimeter to atomic scale, and provides an unprecedented platform for local, non-destructive transport measurements and for building, manipulating and function-testing complex nanoelectronics and nanoscale machineries. It also enables combining many different techniques for characterizing sample conductance, topography, chemical, optical or magnetic properties with complementary information at the same position or on the same nanodevice. Design and development of such complex systems pose many issues and challenges. This chapter will discuss some of the issues faced, solutions reached and advances made. Examples include: (1) Disturbance by magnetic material and magnetic field of SEM imaging and coordination of SEM/SPM position, and their influence on and disturbance of SAM spectra and SAM mapping. The design and use of non-magnetic motors for multi-probe modules will be presented and discussed. (2) Tip holder and sample holder design for easy handling, better mechanical stability over the temperature range and better thermal contact and the versatility of the sample holder with multiple contacts. (3) Use of optical fiber as one of the probe modules, and positioning of the fiber probe. CL spectra and CL mapping results will be presented.

Z. Wang (✉)
RHK Technology, Inc, 1050 East Maple Road, Troy, MI 48083, USA
e-mail: Wang@RHK-Tech.Com

C. Joachim (ed.), *Atomic Scale Interconnection Machines*, Advances in Atom and Single Molecule Machines, DOI: 10.1007/978-3-642-28172-3_5,

1 Challenges

RHK has been fortunate to work with LT Multi-Probe STM system from its early stage; we worked with our customers and industry partners to overcome many issues. These challenges are the ones every system manufacture and users have to face. These include the following:

High resolution SEM is the most important part of such instrument; it is used to locate the feature on the sample and to position the probes. But if the positioning motors are magnetic, there will be difficulties in positioning, namely image shifting. The same magnetic field will also influence the operation of the SAM.

For atomic resolution imaging in SPM mode, we need high mechanical stability, especially for the exchangeable components, such as probe holder and sample holder. We also need to ensure good thermal contact of the exchangeable holders to ensure low temperature at sample and tip.

For study electro-optical property of the sample, since we have electron source from both SEM and STM, we introduced Cathode Luminescence.

A four probe transport measurement using STM probes is basically a DC measurement, see Fig. 1. For testing today's nanodevices and nanoelectronics, we need high frequency signal to each of the probes so we have to introduce high frequency signal channeled to all four probes.

And we also see a future for a seamlessly integrated instrument, from centimeter scale to atomic scale, which certainly calls for a unified controller from Optical imaging to SEM imaging to SPM imaging.

In the following, we will present each of the challenges and RHK's solutions and advances.

2 Effects of Magnets and Magnetic Materials

2.1 ORNL System

The first Multi-Probe SPM system RHK constructed is the UHV LT 4 Probe STM/SEM/SAM system in CNMS at Oak Ridge National Lab [1], see Fig. 2. It is a system with low temperature (LT, below 10 K) operation, with high resolution SEM, high resolution SAM, and has four independent STMs, each capable of atomic resolution imaging and stable STS at low temperature.

Figure 3a shows atomic resolution STM image on HOPG at 300 K. Figure 3b shows STM image of Ag/Si(111)-($\sqrt{3} \times \sqrt{3}$) at 84 K and Fig. 3c shows STM image of Gd/Si(100)-(2 × 7) at 8 K. The images (b and c) are showing atomic structures at low temperature with LN and LHe cooling, respectively.

Figure 4 shows high resolution SEM image of gold particles on carbon. This is a standard sample for high resolution SEM test. The resolution showing as the rising edge of a gold particle is 12 nm as illustrated.

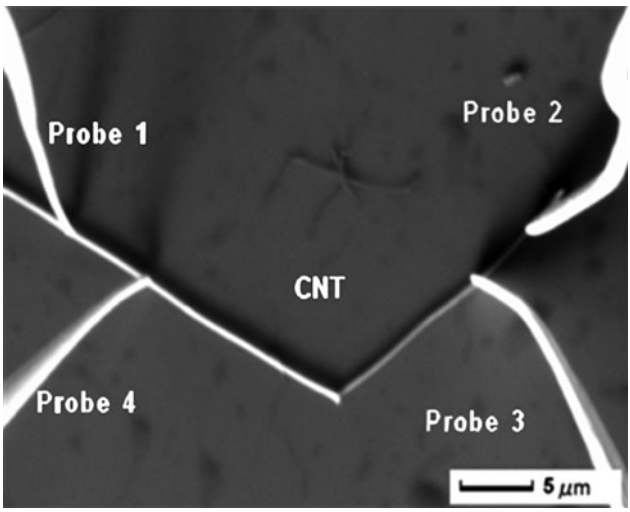

Fig. 1 Probe positioning and four probe transport measurement on CNT. Image courtesy of An-Ping Li and Tae-Hwan Kim of CNMS, Oak Ridge National Laboratory

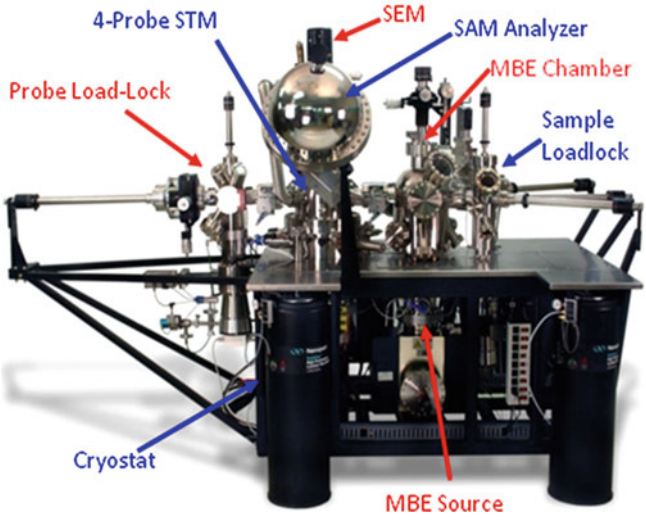

Fig. 2 UHV LT 4 Probe STM/SEM/SAM System at CNMS, Oak Ridge National Laboratory. RHK Technology, Inc.

With high resolution SEM column and energy analyzer, high resolution Scanning Auger Microscope and Auger Spectroscopy can be performed. Figure 5 shows SEM image and SAM image/mapping of two adjacent Ag islands on Si (100) taken simultaneously.

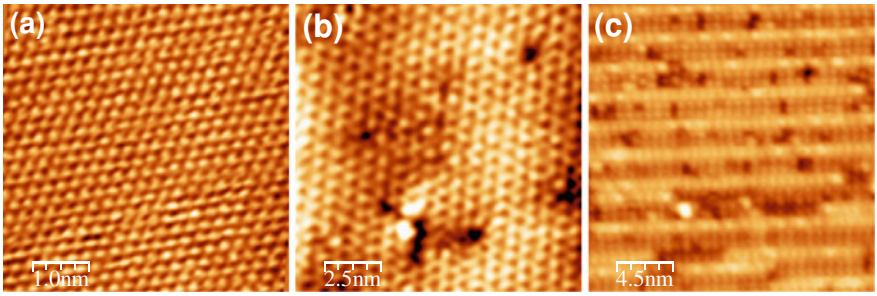

Fig. 3 **a** STM image on HOPG at 300 K; **b** STM image of Ag/Si(111)-($\sqrt{3} \times \sqrt{3}$) at 84 K; **c** STM image of Gd/Si(100)-(2 × 7) at 8 K. (**a**) and (**b**): Image courtesy of An-Ping Li and Tae-Hwan Kim of CNMS, Oak Ridge National Laboratory; (**c**): adopted from Kim et al. [2]

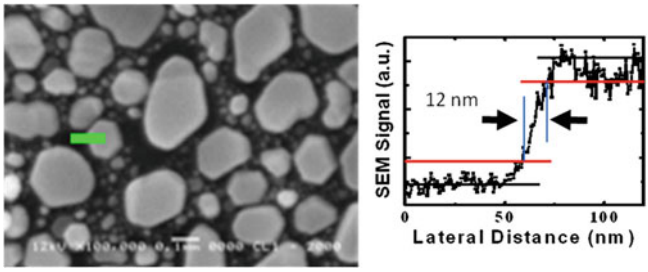

Fig. 4 SEM image of gold particles on carbon. Image adopted from Kim et al. [1]

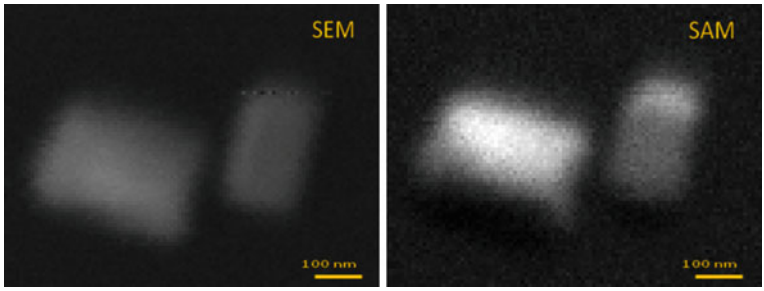

Fig. 5 SAM mapping of Ag island on Si(100) with related SEM image taken simultaneously. Image Adopted from Kim et al. [1]

The instrument is capable of four probe transport measurement as shown in Fig. 6. The tips are positioned with SEM to be in contact with the fiber in various positions along the fiber. Once the tips are positioned and in contact with the fiber, the connections to the tips are switched to a Keithley constant current source and voltage meter for four probe transport measurement. A constant current is applied

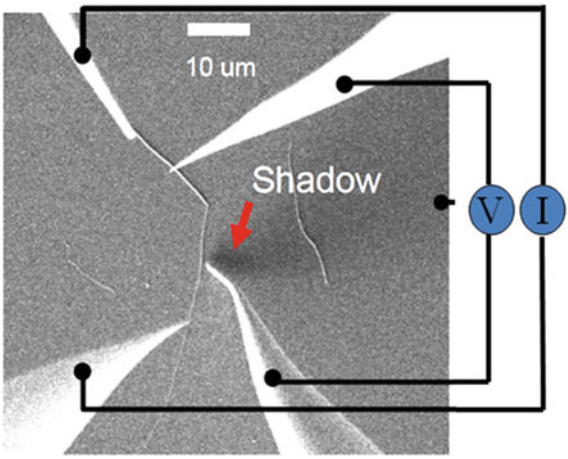

Fig. 6 Four Probe transport measurements. Image Adopted from Kim et al. [1]

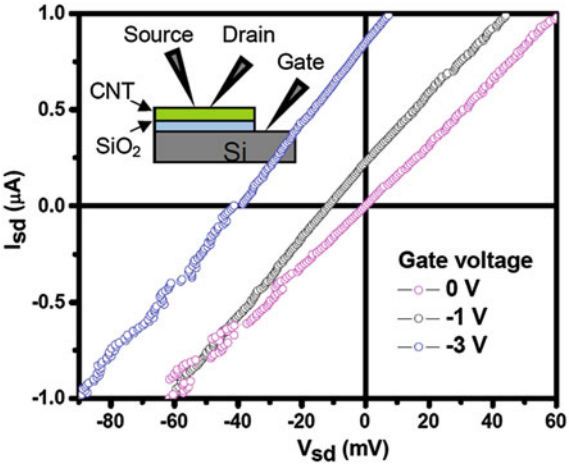

Fig. 7 Carbon nanotube transistor test. Image adopted from Kim et al. [1]

through the two tips positioned far apart along the fiber, and the voltage between the two tips is measured.

Similar tip positioning and measurement can be done as Nanodevice test, such as for this carbon nanotube transistor in Fig. 7. One tip is in touch with the Si base for applying Gate voltage. Two tips touch two places on the carbon nanotube as Source and Drain. Source-Drain current is measured versus Source-Drain voltage while using Gate voltage as a control. As shown in Fig. 7, the Source-Drain current depends on Gate voltage.

The four probe instrument can also work for Nonomanipulation & Nanomachining since the four (4) STM probes are independently operational and positionable, so operations such as pushing/bending, slicing, burning and cutting of objects such as carbon nanofiber can be performed.

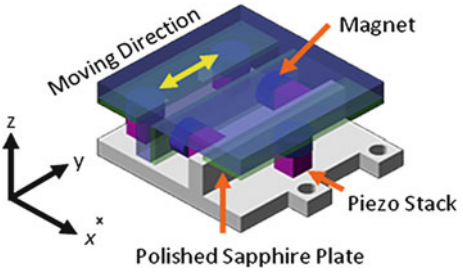

Fig. 8 Piezo motor made with magnets and magnetic materials. Image adopted from Kim et al. [1]

2.2 Magnets and Magnetic Materials on Piezo Motors

Many successful piezo motor designs, which are used for UHV and UHV LT SPM system, use magnets and magnetic materials for construction of the motor (see Fig. 8). The magnetic force between the magnets, which is on the base or on the piezo stacks, and the moving carrier, which is made of magnetic materials, holds the moving parts in position. The advantage of using magnetic force is obvious. The motor is easy to manufacture and assemble. There is no need of force adjustment and there is no change in the holding force with the change of temperature so there will be no dramatic change of motor performance when operating at low temperatures. The disadvantages are strong magnetic field and low resonance frequency due to heavy magnetic materials.

2.3 Influence of Magnetic Field on SEM Image

The magnetic field will influence on the electrons in travel. When moving a magnet or moving magnetic material, the magnetic field will change and the electron beam will be shifted. For SEM imaging, this will image frame shift.

In Fig. 9, when probe 2 (the probe at up-left corner) is lifted (in + Z direction) from near the sample surface to far away (about 2.5 to 3 mm), the image frame shifted about 56 μm in X direction and 22 μm in Y direction, which is very significant.

In Fig. 10, probe 2 is moving in the +Y direction, from close to the image center to far away (about 3 mm), the SEM image frame shifted about −6 μm in X direction and −40 μm in Y direction. These are the motions of Z motor and Y motor of Probe 2. Z motor is closer to the e-beam in the center with its relative height. The Y motor is the motor at the bottom of the motor stack so it is further away from the e-beam.

When moving sample stage X motor in +X direction for 500 um, the image frame shifted in −Y direction for 114 μm (see Fig. 11). Similarly, when moving sample stage Y motor in +Y direction for 1029 μm in SEM image, the image frame shifted in −X direction for 143 μm. The sample stage motors are much closer to the e-beam than the motors of a Probe module so they have bigger

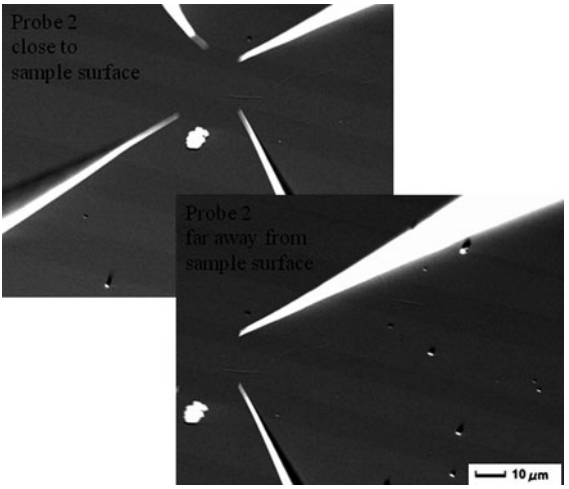

Fig. 9 SEM image shift when Probe 2 moves far away in +Z direction. Image frame shift: X: 56 μm; Y: 22 μm. Image courtesy of An-Ping Li and Shengyong Qin of CNMS, Oak Ridge National Laboratory

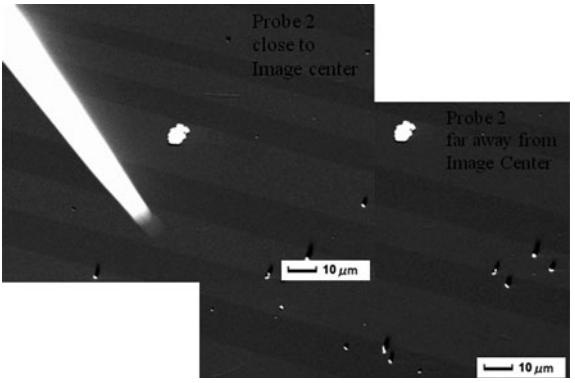

Fig. 10 SEM image shift when moving Probe 2 in +Y direction. Image frame shift: X: 6 μm; Y: −40 μm. Image courtesy of An-Ping Li and Shengyong Qin of CNMS, Oak Ridge National Laboratory

influences. Also, because they moved the sample, so the total motion is a combination of the real motor motion and the motion caused by e-beam shift. And as showing in the image, there is an XY motion coupling. The motion coupling cannot be explained by the misorientation between the sample stage XY direction and the SEM scanning XY direction. If that is the case, the cross movement angle should be the same, but it is not in the above case (12.9° when move in +X direction versus 7.8 degree when move in +Y direction).

2.4 Influence of Magnetic Material on SEM Image

Motion of any magnetic material in the vicinity of the e-beam in magnetic field generated from those magnets on the motors will also cause the shift of the e-beam, therefore the shift of the SEM imaging frame.

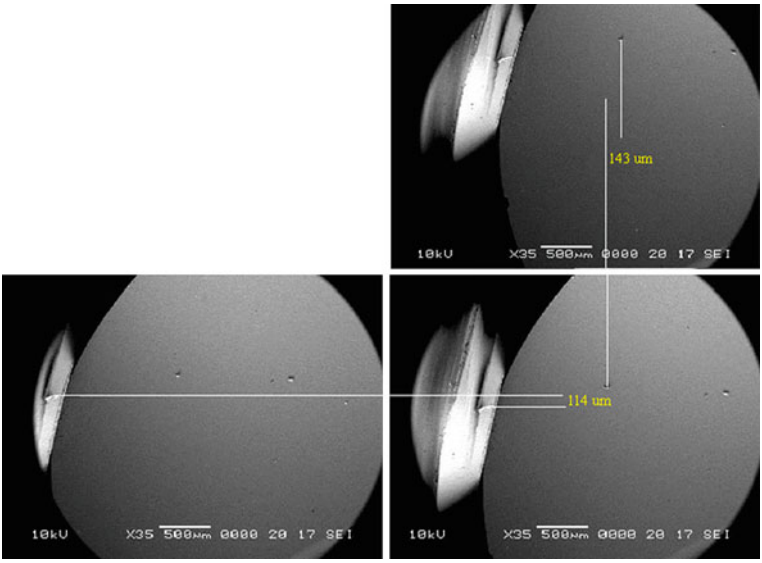

Fig. 11 SEM image shift when moving sample stage X and Y motors

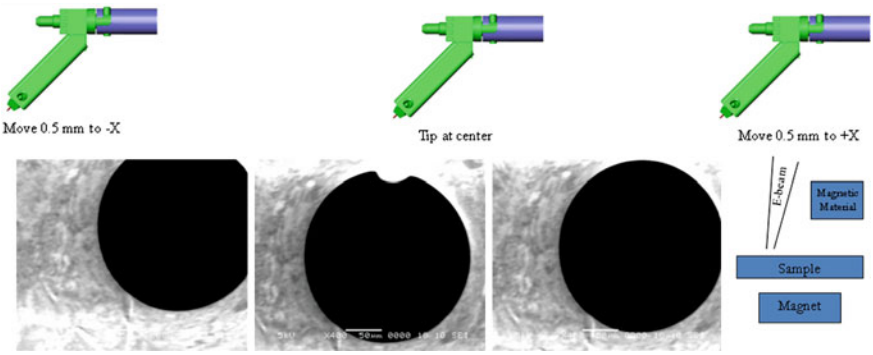

Fig. 12 SEM image shift when moving magnetic material

As shown in Fig. 12, a tip holder with a Stainless Steel 0−80 size screw, which is slightly magnetic, is placed on the end of transfer arm and moved to the center to point at the center of the sample (showing as a 200 μm diameter hole as an entrance of a Faraday Cup). In this case, there is no motor therefore no single magnet is moved. Moving the tip holder away from the sample center by 0.5 mm in +X or −X direction will cause the SEM image to shift dozens of micrometers. The scale bar in the SEM image is 50 μm, which gives a sense of scale.

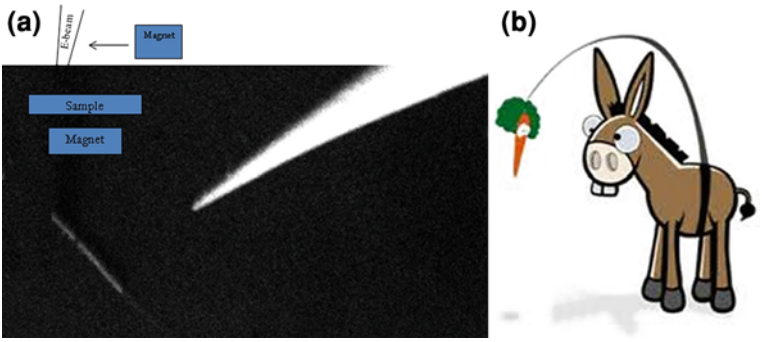

Fig. 13 Chasing moving object in SEM image. **a** Image courtesy of An-Ping Li and Shengyong Qin of CNMS, Oak Ridge National Laboratory

Fig. 14 Influence of magnetic field on SAM image

The above demonstrated situations are like a donkey and a carrot, which is hanging over the donkey's head. When the STM probe is moving to an object (e.g. a nanowire) in the guidance of SEM image, the object is moving as well (in the SEM image), so the donkey may never reach the carrot, or at least have some difficulty, which is in the case of STM probe, see Fig. 13.

2.5 Influence of Magnetic Field on SAM Image

In the case of Scanning Auger Microscope and Auger Spectroscope, the situation also exists.

As show in Fig. 14, the Auger electrons collected is not from the area in the center of the image where determined by the acceptance angle of the analyzer, but from an area away from the center due to the influence of the magnets and magnetic materials to the low energy Auger electron.

If any motor of a probe module moved, the Auger electron path will be affected. The Auger electrons collected by the analyzer could be changed to be from a different area. See Fig. 15. That is because if a magnet is moved, the magnetic

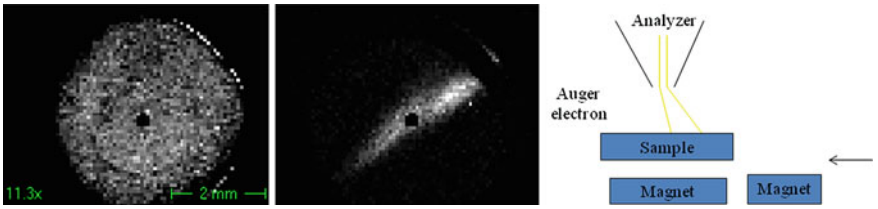

Fig. 15 Influence of magnetic field on SAM image due to motion of magnetic motors

field around the area will be changed so the collectable electrons are from a different area now.

3 Non-Magnetic Piezo Motors

Based on above experience and the issues we saw, we think it is desirable to design and build piezo motors which *DOES NOT* use any magnets and magnetic materials, and which are only mechanically held together with high resonance frequency.

We list the following criteria's for the design of the new motor for multi-probe SPM system:

(1) Use only non-magnetic materials.
(2) Use light material as main components for high resonance frequency.
(3) Working from 4 to 300 K while keeping the rigidity.
(4) XYZ motors stackable, without degrading too much of their rigidity and resonance frequency.

The most successful UHV LT, non-magnetic piezo motor design is the Pan Motor [3]. Most Pan style STM scan head only use the Pan Motor as Z coarse motion without XY coarse motion. For the SPM scan head using Pan Motor and also has XY coarse motion, the XY coarse motion is realized with a symmetric, compact, non-stacked XY motor on the sample side to move the sample holder. The motion of XY is not decoupled. The successful configuration is a symmetric setup with non-stacked motors, see Fig. 16.

Stack XYZ motor on each other and using them in a non-symmetric setup such as a four probe SPM for an all mechanical motor assemble is a challenge, see Fig. 17. The non-symmetric loading and the weight of the motor(s) on top of the motor(s) below will dramatically reduce the resonance frequency and causing instability of lower motor(s). In four probe SPM setup, the probe holder is cantilevered out to reach the sample at the center; this will reduce the resonance frequency and causing instability of all the motors. For LT four probe system with all mechanical motors which use mechanical spring force to hold moving parts, when the temperature changes the structure will change due to thermal contraction/expansion, so the spring force will change, which will change the motors

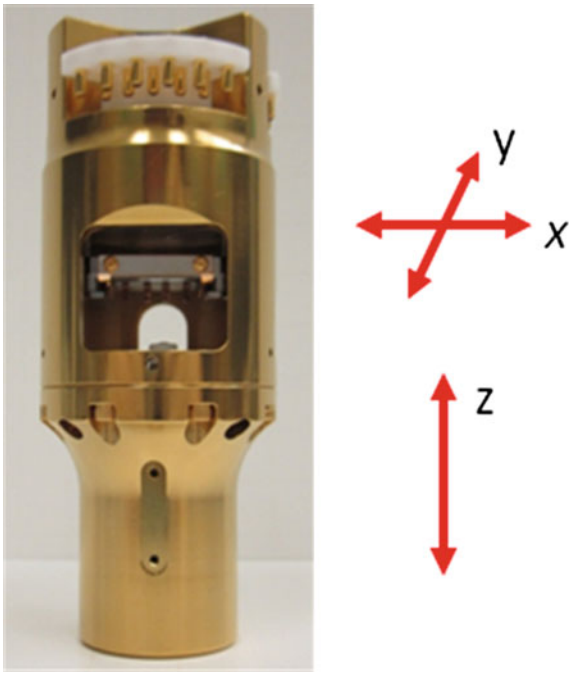

Fig. 16 SPM scan head constructed with one Pan Motor and one non-stacked XY motor. RHK Technology, Inc.

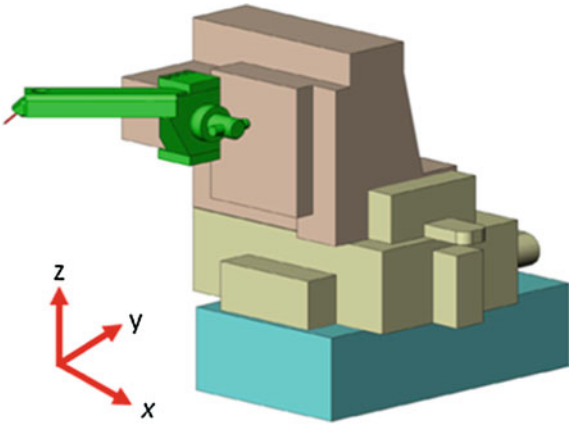

Fig. 17 SPM scan head constructed with stacked XYZ motors

driving behavior. So it is necessary to balance the spring force to cover the whole temperature range within available driving voltage, while keeping high resonance frequency and rigidity of the XYZ motor assemble.

RHK Technology took such a challenge, designed and built nonmagnetic, all mechanical piezo motors for multi-probe system.

As shown in Fig. 18, each probe module has XYZ motors stacked as a probing unit for probe positioning. The XY motors are used for probe coarse and fine positioning. They can also be used for probe XY scanning.

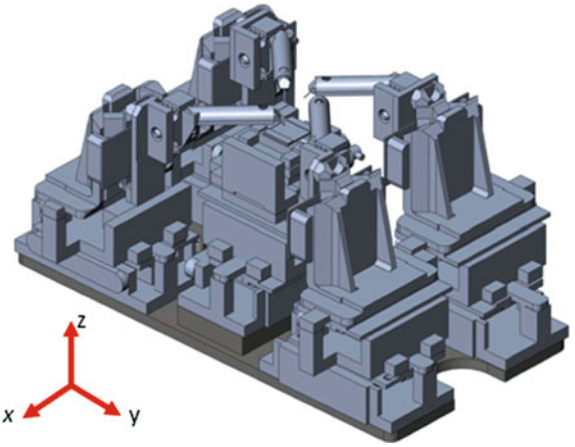

Fig. 18 Multi-Probe SPM system using nonmagnetic, all mechanical motors

The sample stage has XY motors stacked to provide sample motion and coarse and fine positioning. They can also be used for sample XY scanning.

The mechanical and thermal stability of the motor design and the multi-probe setup has been tested/verified and demonstrated by STM atomic resolution imaging on Si(111) and HOPG in UHV at RT and 80 K (with LN cooling which will be more noisy due to bubbling of LN) of all probes, see Fig. 19. In Fig. 19, the particular multi-probe system used in the test has two STM probes and an optical fiber probe (see below). For simplicity and consistence with a full four probe system, we still named the STM probes as Probe 2 and Probe 4 according to their relative positions in a full four probe system setup. The optical fiber probe therefore is named probe 1.

4 Cathode Luminescence

The new non-magnetic motor design leads to RHK's second generation UHV LT Multi-Probe SPM system, which uses those non-magnetic motors and achieves STM atomic resolution imaging on all probes. Besides high resolution SEM and STM, we introduced another complimentary technique for study Electro-optical properties of the sample, the Cathode Luminescence (CL). Since we have the e-beam from SEM and/or STM, CL is a nature extension for the system. What we need is effective and efficient light collection.

A light collection mirror/lens system, such as the ones used in a conventional SEM system for CL light collection, is not feasible for such LT multi-probe UHV system since the LT system have double thermal shields. Introducing a big mirror/lens system with mechanical XYZ positioning will be too much thermal disturbance to the sample and probes. The space inside the thermal shields and the STM probes and STM operation also does not allow a mirror/lens system. We

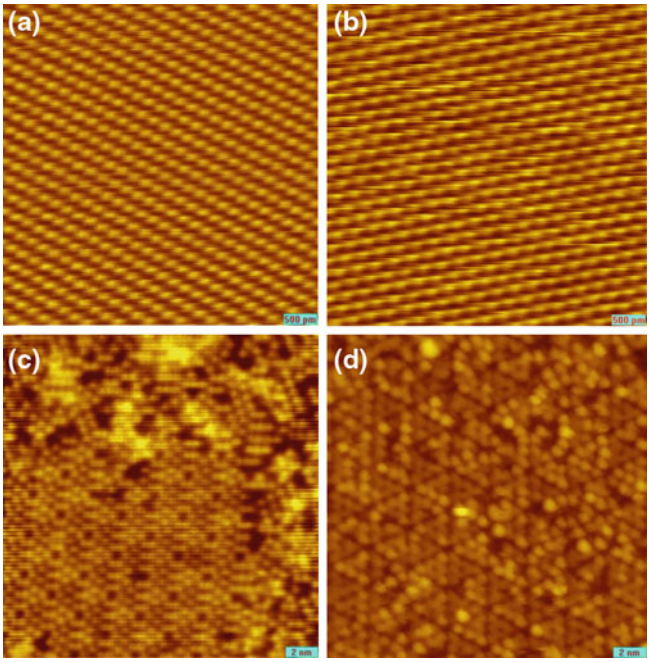

Fig. 19 STM atomic resolution images of Multi-Probe STM system. **a** on HOPG in UHV at RT with Probe 2; **b** on HOPG in UHV at RT with Probe 4; **c** on Si(111) in UHV at 80 K with Probe 2; **d** on Si(111) in UHV at RT with Probe 4. **c**: Image courtesy of Junyong Kang and Kongyi Li of Department of Physics, Xiamen University, China

introduced optical fiber as a probe which is independently positionable just like a STM probe. With high precision monochromator and photon counting, the fiber probe can effectively and efficiently collect CL signal for CL spectra and CL mapping.

We constructed this system for Xiamen University in China with two STM probes and one optical fiber probe (see Fig. 20). This system uses high resolution electron beam as electron source for cathode luminescence. The high resolution SEM is capable of 10 nm SEM resolution at a working distance of 20 mm, see Fig. 21. This long working distance is due to the LT multi-probe SPM stage with double thermal shields.

We introduced a Multi-Mode optical fiber (see up-left insert in Fig. 22) into the UHV chamber using UHV fiber feedthrough. The optical fiber is 200 μm in diameter and used as a probe module for light collection. The fiber is mounted on one XYZ piezo motor probe stage (see *lower-left insert* in Fig. 22) just like a STM probe module. The motor stage is used for XYZ positioning of the fiber under CCD and SEM guidance. The final positioning of the fiber is done by adjusting the position of the fiber while monitoring and optimizing the CL signal to reach maximum signal on a peak of the CL spectra when the e-beam is at a fix spot.

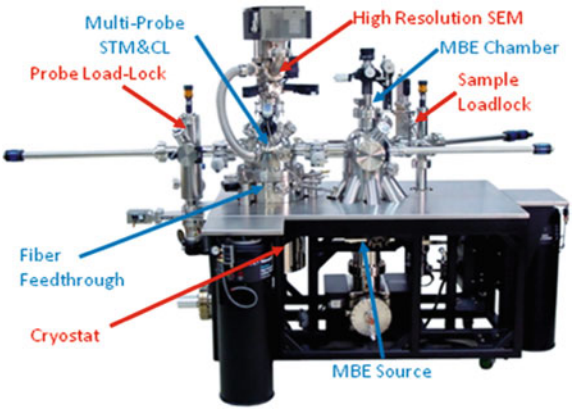

Fig. 20 UHV LT Multi-Probe STM/SEM/CL System at Department of Physics, Xiamen University, China. RHK Technology, Inc.

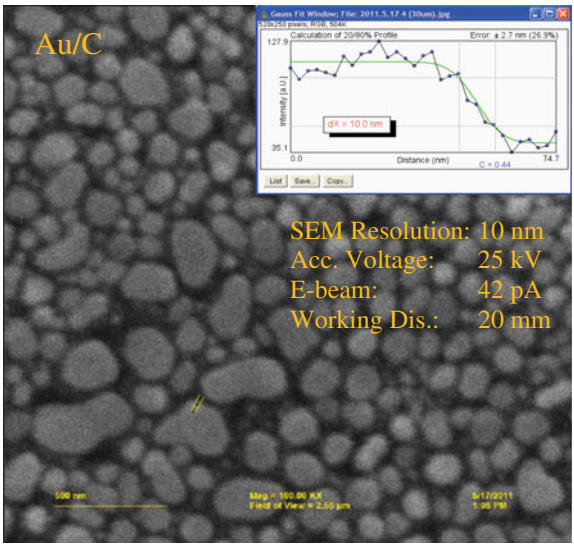

Fig. 21 High resolution SEM image of Au particles on carbon

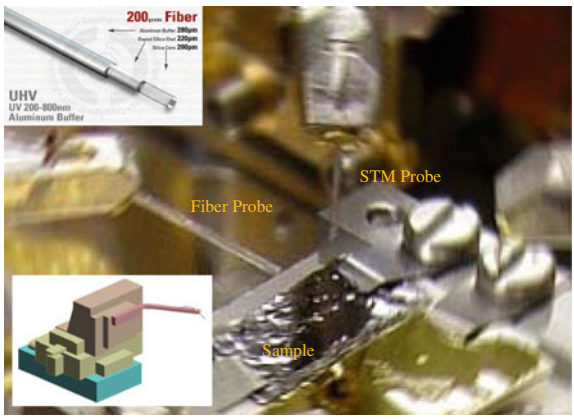

Fig. 22 Optical fiber and fiber probe module with XYZ positioning

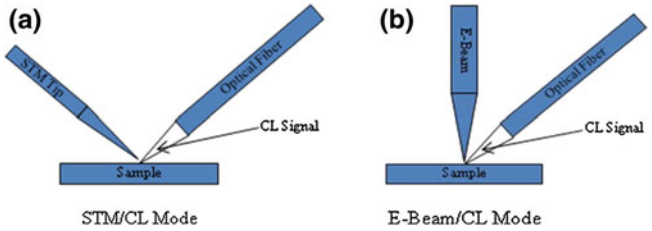

Fig. 23 Cathode luminescence using STM (**a**) or SEM (**b**) as e-Beam source

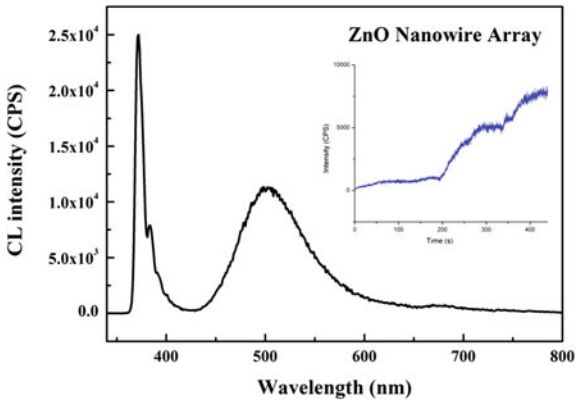

Fig. 24 CL spectrum of ZnO nanowire array, The insertion shows the process of fiber position optimization. E-beam energy is 25 kV and the e-beam current is 700 pA. The photon counting integration time is 0.5 s. Image courtesy of Junyong Kang and Kongyi Li of Department of Physics, Xiamen University, China

CL point spectrum and CL surface mapping could work with either the SEM e-beam or e-beam from STM as electron source, see Fig. 23. Using STM will theoretically reach higher spatial resolution on CL mapping but usually the CL signal will be weak so S/N ratio will be low, and STM will only work on somewhat conductive samples.

The light collected by the fiber probe is coupled into a precision Monochromator for wavelength selection and for CL spectrum. Photon counting with chilled PMT is used for the weak CL signal detection.

Figure 24 is an example of CL spectrum on a customer ZnO nanowire array sample. The insertion shows the optimization of the fiber probe positioning. The spectrum was taken at 80 K which shows the low temperature operation capability of the instrument for CL measurement. With a relatively low electron current (700 pA), the collected CL signal is relatively strong and the signal to noise ratio is pretty good. This spectrum demonstrates how well it works using an optical fiber for CL signal collection.

Figure 25 is an example of CL mapping. If we fix the wave number at one of the peak of the CL spectrum (385 nm), while we scan the electron beam, we will get SEM image and corresponding CL image simultaneously. Figure 25 shows the SEM image and related CL image at 385 nm taken together. The CL image shows

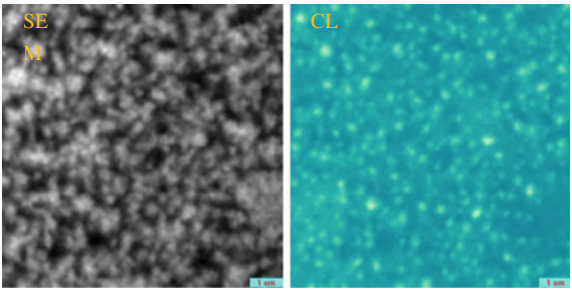

Fig. 25 SEM image and CL mapping image of ZnO nanowire array taken simultaneously. E-beam energy: 25 kV; E-beam current: 700 pA; Image magnification: 30,000X; Field of view: 8.57 μm; Wavelength 385 nm; Photon counting integration time is 10 ms. Image courtesy of Junyong Kang and Kongyi Li of Department of Physics, Xiamen University, China

different contrast and pattern than the SEM image. The CL image only shows the structure and nanowires which are CL active.

The same optical fiber can also be used in a reverse way for light illumination, introducing light into the tip/sample surface area for CCD camera observation or for tip and sample surface light excitation. In Fig. 26, the optical fiber is positioned to shine external light right at the tip/sample junction of Probe 2. This introduced light can be used for localized illumination without much scattered light so the contrast of the optical image from the CCD camera will show more details. Or the introduced light can be wavelength selected for tip and/or sample surface excitation, such as light assisted tunneling or Tip Enhanced Raman Spectroscopy (TERS).

5 Probe Holder and Sample Holder Design

One of the challenges for LT UHV multi-probe SPM system is the tip holder and sample holder design and mounting mechanism. The design has the following requirements.

(1) Exchangeable in UHV at LT.
(2) Do not need very accurate alignment with the exchange tool used.
(3) Good thermal contact with probe or sample stages.
(4) Good mechanical stability.
(5) Mechanical and thermal contact does not change with temperature.
(6) Multiple electronic contacts for multiple signal access.
(7) No excessive force to probe or sample stage and motor stack during probe and sample exchange.
(8) Have small opening and intrusion to double thermal shields.
(9) Have less thermal disturbance to the cold stage and other cold components.

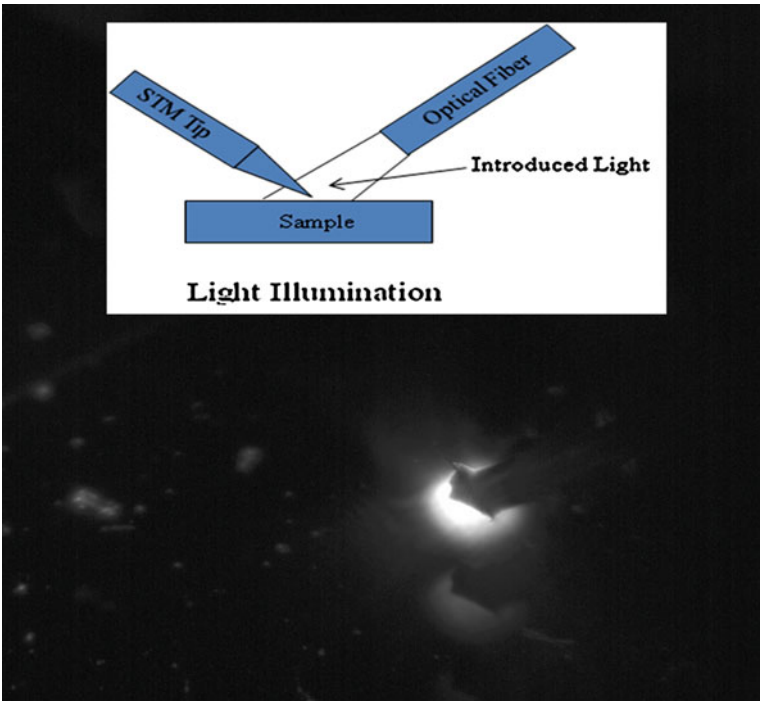

Fig. 26 Light illumination and/or excitation with the positionable optical fiber

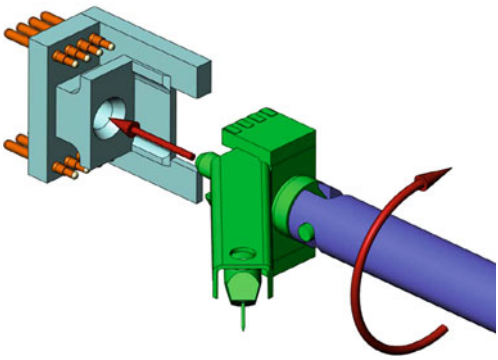

Fig. 27 Probe holder mounting mechanism with simple linear and rotation motion

RHK has this tip holder and sample holder design, with mounting and handling mechanism, which uses single, simple and same transfer arm operation across the whole system, with only linear and rotational motion, see Fig. 27. The mounting/driving pin on the tip/sample holder has threads like a screw with tamped leading front. The hole on the tip/sample stage is a mating tapped hole with large opening. So it does not need very precise alignment between the tip/sample holder and the

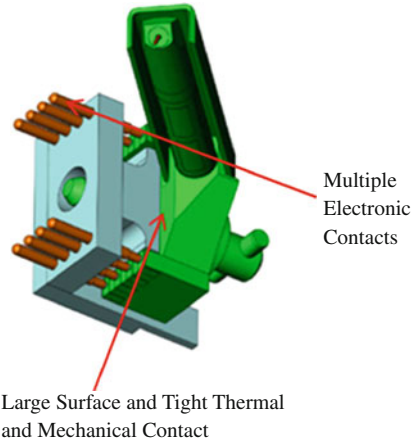

Fig. 28 Probe holder mounted with large surface contact

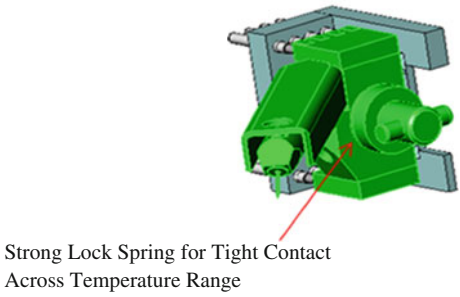

Fig. 29 Probe holder mounted with strong lock spring

tip/sample stage. There is no linear friction resistance like a spring force to overcome. With easy rotational operation using the magnetically coupled transfer arm, it is easy to tighten the pin to make good surface to surface contact, see Fig. 28. The screw operation does not need much force to tighten but will generate large force so strong spring washer with large spring force can be used to make good and secure spring loaded contact, see Fig. 29.

The large, spring loaded contact surface means good thermal contact with probe or sample stage for cooling the tip and sample holder during LT operation to ensure the tip and sample reach low temperature fast and stable. This also ensures good mechanical stability for SPM and SEM operation.

The mechanical and thermal contact does not get loose with the change of temperature due to the large spring force loading which secure the contact firmly.

The simple operation can easily be done in UHV at LT since there is no linear friction force to overcome which may change with temperature.

There is no excessive force to probe or sample stage and motor stack during probe and sample exchange since only a small force is applied to tighten the screw/pin. Furthermore, force breaker/limiter can be placed on transfer arm linkage to the chuck to limit the force which could be applied.

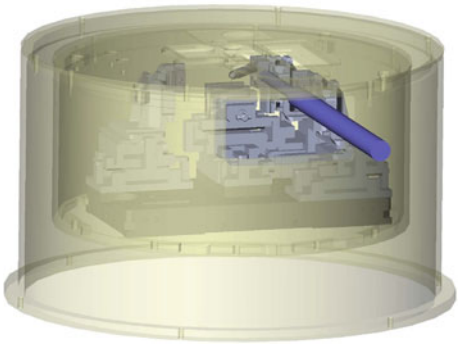

Fig. 30 Small opening on double thermal shields

For both tip and sample holder, there are multiple electronic contacts for multiple signal access and SPM scanning and other versatile use. Those contacts are all spring loaded pins and they go directly against the screw tightening. The large tightening force of the screw will easily overcome those spring loaded contactors to make good and secure spring loaded electronic contacts.

This tip and sample holder design and transfer mechanism also ensures small opening and small intrusion to the double thermal shields. And have less thermal disturbance to the cold probe and sample stage and other cold components.

The openings on the thermal shields just need to be big enough for the size of the tip and sample holder, see Fig. 30.

This is like a Laparoscopic surgery, with minimum intrusion, in comparison to "open heart" surgery, which may use a wobble stick to open the shields and making the operation in multiple dimension motions.

6 Versatile Sample Holder

The sample holder uses exactly same handling and mounting mechanism as the tip holder.

Besides good thermal and stable mechanical contact with the sample stage, there are multiple electronic contacts for multiple signal access and other versatile use, see Fig. 31.

There are two large contacts capable of high current for heating filament or direct current heating of the sample.

There are contacts for temperature measuring on sample holder; this is a direct measurement of sample temperature.

There are also contacts for bias or other electronic connections, which will be useful when the sample gets to the nanodevice and nanoelectronics level when multiple electronic connections to the sample are desirable.

There is an integrated filament for radiative and/or e-beam heating.

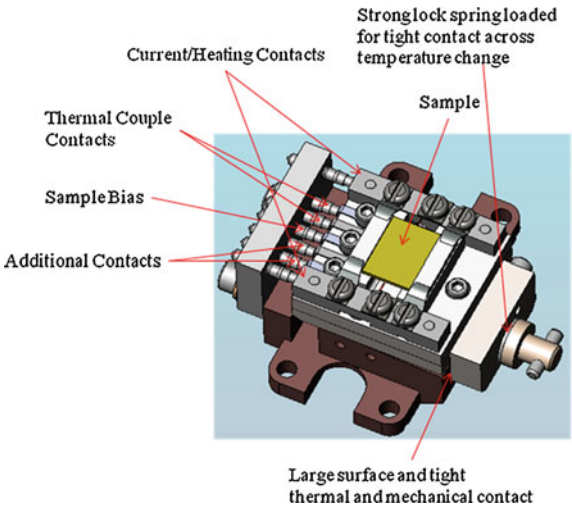

Fig. 31 Versatile sample holder with multiple electronic contacts

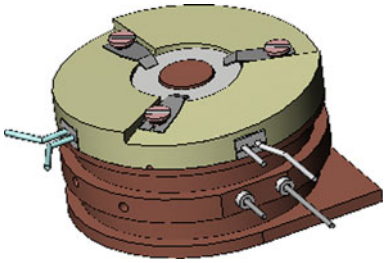

Fig. 32 RHK "Walker" type SPM sample holder with six contacts

The size of the sample holder will allow other structures and devices to be mounted on sample holder for different purposes and measurements.

This sample holder follows the same concept as the RHK standard "walker" type SPM sample holder, with multiple contacts and built-in filament and temperature sensing, see Fig. 32.

Figure 33 shows some examples of various configurations of the versatile sample holder.

The standard sample holder has built-in tungsten filament for radiative and/or e-beam heating of the sample. Without the filament, the sample holder can be used for room temperature and low temperature operation.

For direct current heating of a sample, the tungsten filament and its holding ceramics are removed and the sample is in direct contact with the two high current carry contacts so the applied current will go through the sample. For STM operation, the sample bias will also be applied through one of the current carry contacts in this situation.

For sample fracture/cleaving, the sample is mounted on the sample holder mechanically (clamped) or glued. With or without prescribed line at desired cleaving position, the up part of the sample is pushed over by end of transfer arm

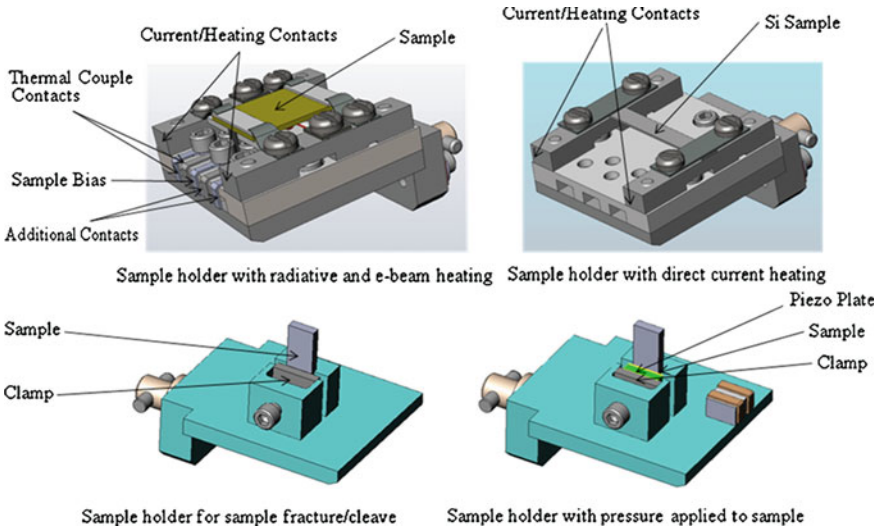

Fig. 33 Versatile sample holders with various configurations

or a special wobble stick in the cleaving station which is usually in the sample storage area in UHV. The sample is then transferred to the multi-probe sample stage under UHV.

If a piezo plate is glued or clamped on the sample holder, it can apply pressure/stress to sample which is glued or clamped on the sample holder. The sample can be a fracture/cleaving sample or a non-cleaving sample. The additional electronic contacts on the sample holder can be used for activating the piezo plate. The pressure/stress generated by the piezo plate can be applied to the sample during SPM or SEM imaging.

Figure 34 shows the example of using a cleaving sample holder. The $Sr_3Ru_2O_7$ sample is mounted on the cleaving sample holder and introduced into the UHV system through load lock. After the sample cleaving under UHV to obtain a clean surface insider the storage chamber, the sample holder was transferred into the SPM chamber on the sample stage. STM imaging is performed, the topography image and a scan line of a step on the surface is shown.

An example of using sample holder which can apply pressure/stress to the sample is illustrated in Fig. 35. The $Sr_3(Ru_{1-x}Mn_x)_2O_7$ single crystal sample with $x = 0$ and 0.2 is mounted in the sample holder which has the piezo plate to apply the pressure/stress to the sample. The sample was cleaved under UHV and transferred to STM/SEM sample stage. At temperature of 81 K, SEM image reveals contrast between different domains on the surface, due to charging in the insulating domains, which shows as bright area in compare to metallic domains. When pressure/stress is applied across the sample, the domain pattern in the SEM image change with time, which showing a domain evolution under pressure/stress.

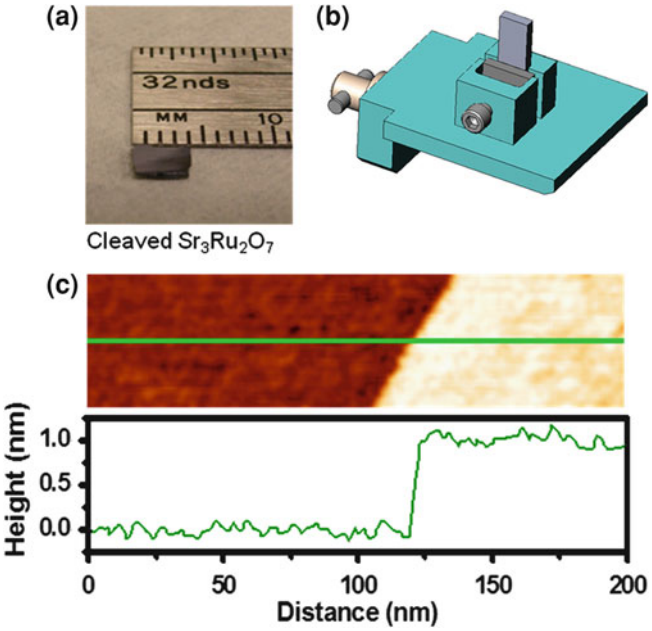

Fig. 34 STM image of cleaved $Sr_3Ru_2O_7$ sample. **a** and **c**: Image adopted from Kim et al. [4]

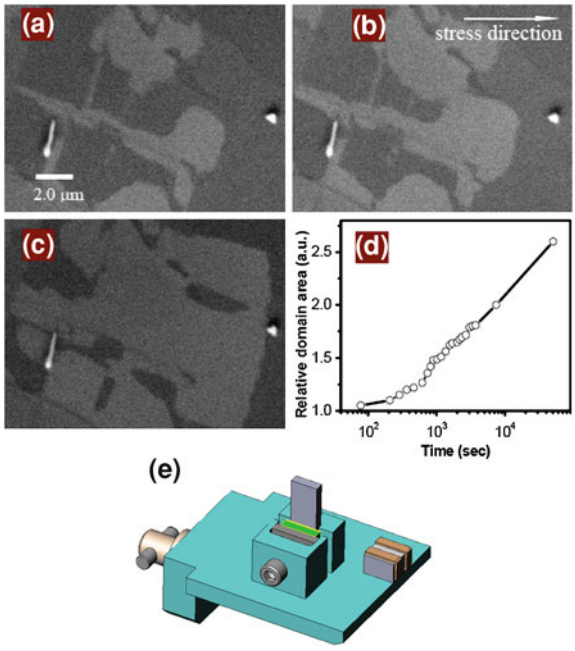

Fig. 35 Time laps SEM images of strain induced phase transition. **a** domain image before stress; **b** After compressive stress being applied for some time; **c** After the stress being applied for long time (14 h); **d** Domain Area (compared to total area in SEM image) change with time. **a** to **d**: Image adopted from Kim et al. [4]

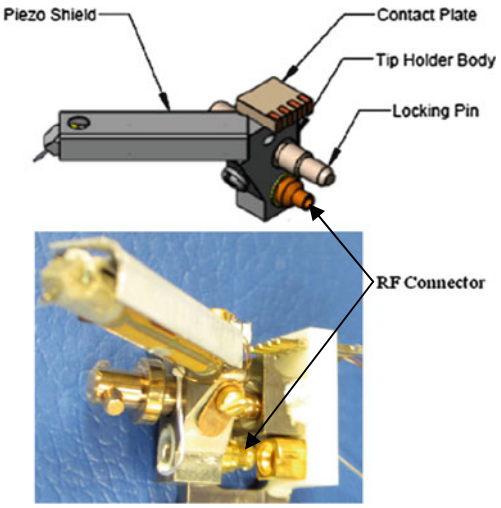

Fig. 36 RF compatible tip holder for high frequency signal

7 RF Compatible Tip Holder for High Frequency Signal

Four probe transport measurement using four STM tips with normal STM tunneling current wiring is basically a DC measurement. Today's electronics and electronic components are all running at very high frequency. For real-life test of nanodevices and nanoelectronics at high frequency, High Frequency RF signal has to be channeled to all four probes.

RHK is making high frequency compatible STM probe holder for next four probe STM/SEM system. The system under construction will have high frequency channeled to all four probes and will be capable doing high frequency testing on Nanodevices and nanoelectronic components.

Starting from high frequency UHV Feedthrough, semi-rigid high frequency coax cable is used for connection inside UHV chamber. The semi-rigid cable is thermally anchored to heat exchange plate to be precooled during low temperature operation. The coax connection is terminated with a UHV compatible RF connector on probe holder stage of each probe station/module. There is a mating RF connector on each probe holder to make high frequency connection when the probe holder is mounted on the probe holder stage, see Fig. 36. There is a short coax connection on each probe holder to STM tip or RF probe to deliver or measure RF signal. This mating RF connector pair allows the probe holder to be exchangeable in UHV and ensures a true RF connection for high frequency signal. The tunneling current of STM operation and high frequency signal for high frequency transport measurement or nanodevice test are using the same high frequency signal path.

The mating RF connectors need good position alignment and large force for insertion to make secure RF connection. The design and structure of the RHK multi-probe system's probe holder and the way how it is mounted is perfect for this

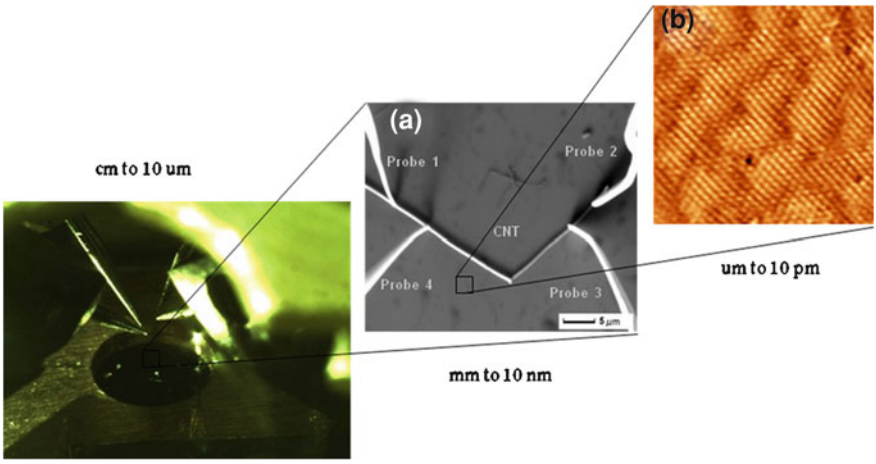

Fig. 37 Seamless imaging from centimeter scale to atomic scale. **a** Image courtesy of An-Ping Li and Tae-Hwan Kim of CNMS, Oak Ridge National Laboratory. **b** Image Adopted from Kim et al. [2]

requirement. The leading edge of the locking pin (mounting screw) will first engage to guide the alignment of the mating RF connectors and the screw operation of the locking pin will provide the needed large force to insert the RF connector.

8 Seamless Integration with Unified Controller

We are seeing a future of a seamlessly integrated LT Multi-Probe SPM/SEM instrument, from centimeter scale to atomic scale. This seamlessly integrated instrument certainly calls for a unified controller from optical imaging to SEM imaging to SPM imaging, see Fig. 37.

In the seamless integration, every piezo motor of the multi-probe SPM system have calibrated position sensor. There is a unified controller for controlling SPM, SEM and optical microscope and all the position sensors with one integrated user interface. Optical (CCD camera) image scale is calibrated. The SEM image is calibrated. The SPM image is calibrated. The calibrations and all positions are indexed and interconnected so interested feature can be chosen from optical image, SEM image or SPM image.

In this case, one can click and zoom in an optical image to the next level with SEM image and zoom into a SEM image to directly start taking SPM image on interested feature, just like one will do within each individual imaging techniques along. Such seamlessly integrated system has been realized these days with some integrated XPS system and large scale ambient SPM systems.

Fig. 38 RHK's QuadraProbe controller

For this seamless integration to work, if we recall from early sections of this chapter, we cannot have magnets or magnetic materials for construction of any piezo motors or any moving parts on the multi-probe stage. If the SEM image shifts uncontrollable and unquantified, we will lose this coordination since the SEM image is the interconnecting bridge for all those coordination from centimeter scale to atomic scale.

The first step for such seamless integration is a unified multi-probe STM controller for uniformly controlling of all the probes and sample stage with single user interface. RHK Technology was a pioneer in the field of unified multi-probe system controller. At a very early stage of multi-probe system, RHK build this QuadraProbe SPM Controller (see Fig. 38) for ORNL's UHV LT 4 Probe STM/SEM/SAM System which RHK delivered in 2006.

This integrated four probe SPM controller is all digital; it has four fully digital SPM feedbacks for controlling the four STM probes independently. It also controls the sample stage for scanning besides probe scanning. The controller uses single computer, with single user interface. It displays the four probe STM modules and the sample stage as they are in their physical relative positions. The XYZ coordination of all four STM modules and the sample stage are all coordinated/aligned, as well as with the XY coordination of the SEM scanning and the CCD camera image. This gives the operator of the system a direct visualization of the four STM modules and the sample stage in their relative physical positions when move each of them in different directions, see Fig. 39. This also gives the relative directional coordination between optical image, SEM image and STM image. The controller has the SW control of the four independent preamplifiers for gain and bandwidth. And it also controls the switch box between STM operation and transport measurement, which route the connection of all four probes to external transport measurement equipments.

RHK is developing a next generation unified multi-probe system controller, the new R9 Multi-Probe SPM/SEM System Controller, see Fig. 40. The new controller is fully digital. It is ultra integrated for multiple SPM control as well as SEM and other related instrument control. The new controller has ultra low noise on analog output, with high speed DAC. It uses ultra high speed ADC with a sampling rate of 100 MS per second, which will be well suited for SEM operation. The controller has multiple I/O for other input, output and control, such as position

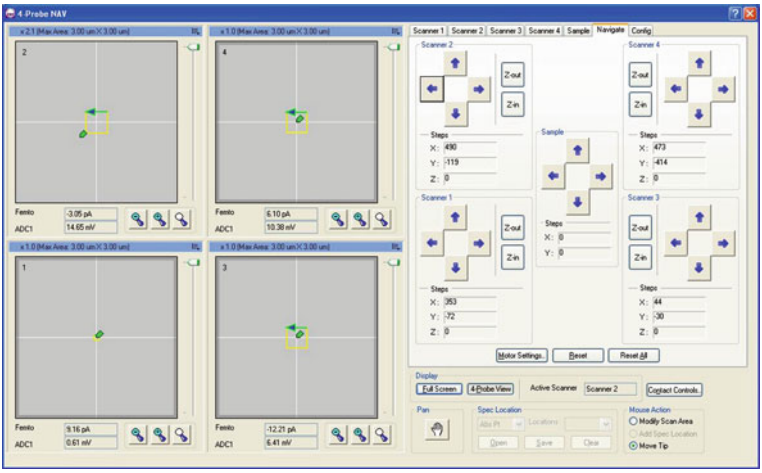

Fig. 39 Unified single user interface of QuadraProbe controller

Fig. 40 RHK's R9 Multi-Probe SPM/SEM system controller

sensors on each motor. The controller is completely software or user configurable, featuring IHDL, the "Iconic Hardware Description Language", which Drag-and-Drop icons for hardware, firmware and experimental procedures configuration. So users can configure or modify the controller according to their experimental needs. This could make the controller a purposely built controller tailored for different experiment and research without actually changing the hardware. The new controller uses single computer with single user interface. The new controller follows the continued development of RHK's QuadraProbe controller and it will have all

the multi-probe functions RHK developed with QuadraProbe controller as we discussed above.

Acknowledgments The author would like to thank academy and industry partners for their collaboration at various stages of the instrument development. They are CNMS at Oak Ridge National Lab of USA; Department of Physics, Xiamen University of China; SPECS Surface Nano Analyses GmbH of Germany; and UNISOKU Co., Ltd. of Japan. A portion of the research was conducted at the Center for Nanophase Materials Sciences, which is sponsored at Oak Ridge National Laboratory by the Office of Basic Energy Sciences, U.S. Department of Energy. The author would like to specially thank Dr. An-Ping Li of CNMS, ORNL for his cooperation and support. The author would like to thank Prof. Junyong Kang of Department of Physics, Xiamen University, China for his cooperation and support. The author also would like to thank the people who worked on various projects at RHK Technology, Inc. Dr. Sergii Priadkin, a staff scientist, who worked at the initial stage of non-magnetic motor design; Gennady Royzenblat and Emanuel Chirila, the mechanical engineers, who worked on the motor and systems design and drawings; and Xun Pan, the senior technician, who assembled and did all the initial test of those motors.

References

1. Kim, T.-H., Wang, Z., Wendelken, J.F., Weitering, H., Li, W., Li, A.-P.: A cryogenic QuadraProbe scanning tunneling microscope system with fabrication capability for nano-transport research. Rev. Sci. Instrum. **78**, 123701–123707 (2007). doi:10.1063/1.2821610
2. Kim, T.-H., Wendelken, J.F., Li, A.P.: Probing electron transport and structural properties of nanostructures on Si with a Quadra-probe scanning tunneling microscope. In: Advanced Metallization Conference 2007, Materials Research Society Conference Proceedings, vol. 23, pp. 653−659 (2008)
3. Shuheng, P.: European Patent Application WO 93/19494 (1993)
4. Kim, T.-H., Angst, M., Hu, B., Jin, R., Zhang, X.G., Wendelken, J.F., Plummer, E.W., Li, A.-P.: Imaging and manipulation of the competing electronic phases near the Mott Metal-Insulator transition. PNAS **107**, 5272–5275 (2010). doi:10.1073/pnas.1000655107

On the Road to Multi-Probe Non-Contact AFM

T. Vančura, S. Schmitt, V. Friedli, S. Torbrügge and O. Schaff

Abstract This contribution highlights some important aspects that have to be considered when building a multi-probe non-contact AFM. Specifically the requirements on the control system for such applications are considered.

Keywords Multi-probe microscopy · Multi-probe control system · Non-contact AFM · SPECS · Nanonis · Length extension resonator · LER · KolibriSensor · LabVIEW · SPM control system · Programming interface

1 Introduction

The possibility of probing a sub-micrometer small area of a sample with multiple probes simultaneously has become a very promising field of research in the past years. The main challenges in building a multi-probe microscope lie in the following fields:

- *Scan Head:* the size constraints that have to be met in order to get multiple tips into close proximity of each other are substantial, especially if atomic resolution should be achieved with each tip.
- *Probe:* the first instruments using multiple tips relied on the tunneling current for feedback. In order to do more involved experiments new sensors capable of doing non-contact AFM will be required to open the road to new experiments.
- *Control System:* once the difficulties of the mechanics have been overcome the control system operating the tips and sample should be aware of the multiple probes, rather than working as multiple copies of a single probe system.

T. Vančura (✉) · S. Schmitt · V. Friedli · S. Torbrügge · O. Schaff
SPECS Surface Nano Analysis GmbH, Voltastrasse 5,
13355 Berlin, Germany
e-mail: t.vancura@specs.com

C. Joachim (ed.), *Atomic Scale Interconnection Machines*, Advances in Atom and Single Molecule Machines, DOI: 10.1007/978-3-642-28172-3_6,

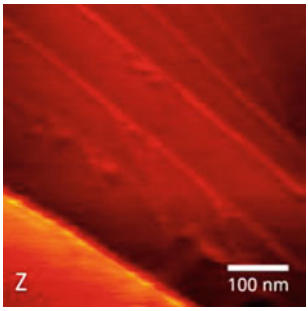

Fig. 1 Atomic steps measured in non-contact AFM in frequency-modulation mode with Akiyama sensor

- *Visual Observation*: a short working distance of a few millimeter between the SEM or optical microscope head and the sample and probes is very important in order to have a good understanding of the mutual positions of tips and sample.

Today most commercial suppliers of multi-probe systems focus on *scan head* and sometimes *probe* when building a multi-probe SPM. Typically only a minor focus is put on the control system running the system. In this contribution we will focus on control system and probe and shine some light onto why it is essential to think of the control system just as much as on the hardware it operates.

2 Piezoelectric Force Sensors

Piezoelectric force sensors are very promising in the field of multi-probe microscopy. Piezoelectric sensors like the Akiyama probe [1], tuning fork sensors [2], Qplus^{TM} sensor [3] or SPECS' KolibriSensor^{TM} [4] will most likely be the first candidates to achieve atomic resolution in non-contact AFM mode on multiple tips.

Due to the fully electrical detection and control of these sensors there is no need for any optical beam/detector alignment. This enables the design of very compact multi-probe systems with STM and NC-AFM functionality. SPECS' new Curlew^{TM} scan head is an extendable platform for building up a multi-probe microscope with up to four tips working on the same sample. The head fully supports piezoelectric force sensors like the Akiyama probe as well as the KolibriSensor^{TM} for combined STM and NC-AFM operation. We have recently resolved atomic steps in air and UHV with an Akiyama probe by frequency-modulation AFM (FM-AFM) (see Fig. 1).

The KolibriSensor^{TM} has been used to achieve atomic resolution FM-AFM imaging on various samples [4]. Beyond this particularly the measurement of surface potentials via Kelvin Probe force microscopy is of interest in multi-probe systems (see Fig. 3). To study the capabilities of the KolibriSensor^{TM} in multiple imaging modes a heterogeneous sample system was chosen: graphene grown on Ru(0001) [5]. To further elucidate the properties of this fascinating material,

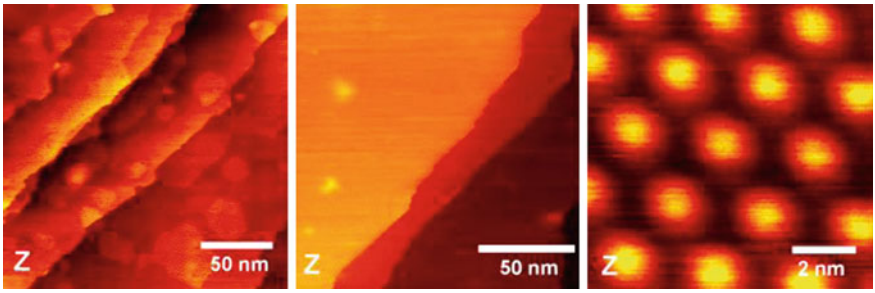

Fig. 2 Topographic (Z) NC-AFM images of single layer graphene on Ru(0001) at room temperature. The graphene monolayer shows the characteristic buckling resulting in a hexagonal reconstruction as shown in detail in the *right* image. By varying the growth conditions the total coverage and shape of the graphene islands can be tuned ranging from partial coverage (*left*) to full monolayer coverage (*center*)

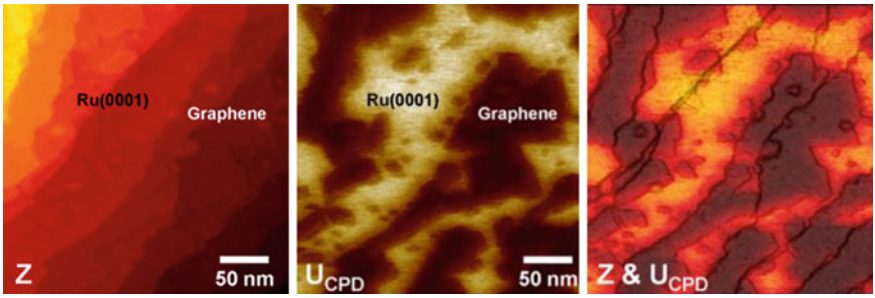

Fig. 3 FM-KPFM image of graphene islands on Ru(0001). *Left*: topographic image (Z), *Center*: simultaneously recorded image of contact potential difference (UCPD). *Right*: superposition of topography and contact potential difference. Bright areas in the contact potential map UCPD correspond to the metal substrate

complementary studies of the electronic and geometrical structure of single layer graphene on Ru(0001) (g/Ru) using STM, non-contact atomic force microscopy (NC-AFM) (see Fig. 2), and frequency-modulation Kelvin probe force microscopy (FM-KPFM) (see Fig. 3) were applied. These experiments were carried out with a commercial SPM 150 Aarhus equipped with the piezoelectric KolibriSensor [4] in ultra-high vacuum.

3 Multi-Probe Control System

The control system used to operate any multi-probe setup, be it in STM or in NC-AFM mode, is crucial to the experiment. As multi-probe scanning is still a relatively young field with very few research groups working on it there is not yet

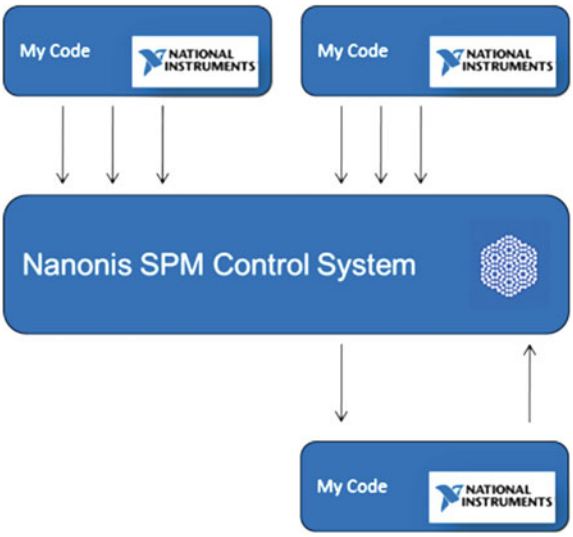

Fig. 4 Model of the programming interface. The control system can call and be called by user-defined LabView routines

any established method how multiple tips should work together, and how they should be controlled and operated. Adding to this the multitude of mechanical setups (individual tips scanning, sample scanning, individual tips on separate bias, bias over the sample, …), it becomes obvious that so far not one single approach will fit everybody's needs. Therefore, SPECS has chosen to make its multi-probe control system as flexible as possible.

Adding multi-probe functionality to a control system will induce a wealth of difficult design decisions which will ultimately lead to a less flexible system. For example, adding multi-probe functionality to the seemingly simple spectroscopy modules opens questions like How do I select the tip on which to run the curve, What should happen to the other tips during this time (voltage? feedback? position?), How do I make sure the user does not accidentally run the wrong tip?

Therefore, SPECS has opted to use a different approach and give each tip its own fully operational control system. The approach that makes it different from other solutions is that the LabVIEW programming interface available for the Nanonis control system allows the operation, integration, data exchange and to some extent synchronization of the control systems.

Figures 4 and 5 display the philosophy of the programming interface for the Nanonis control system. With over 350 individual functions readily available within LabVIEW^{TM} it is possible to call functions of the Nanonis control system from individual pieces of LabVIEW^{TM} code just as well as call user-defined LabVIEW^{TM} code from with the controls system. An example for the former is a procedure which uses the atom tracking module to adjust the position of the tip on top of an atom after each spectroscopy experiment. With this it was possible for a customer to automatically collect spectroscopy data on the same atom over several

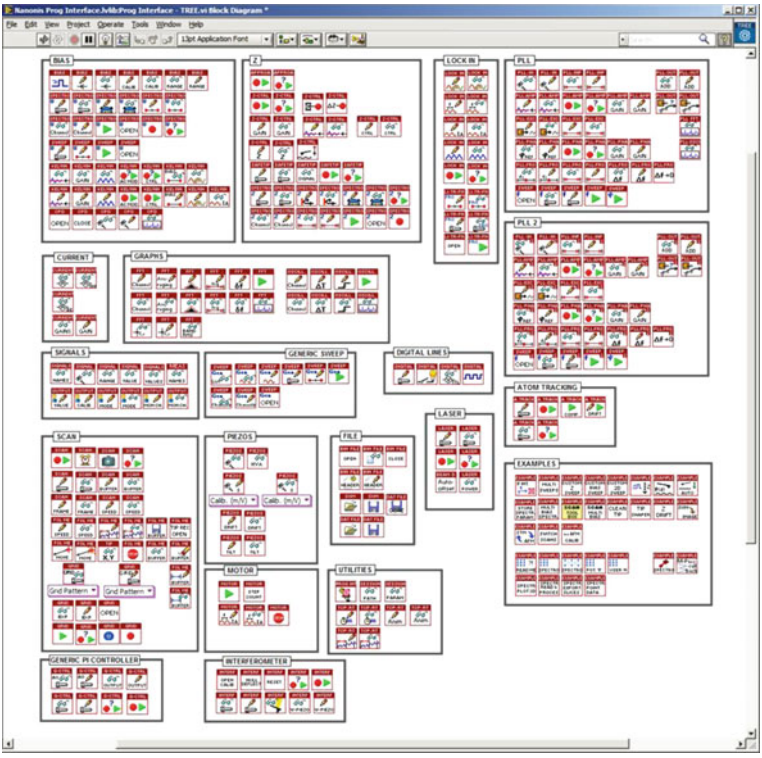

Fig. 5 Over 350 functions are available and integrated into LabVIEW to operate the Nanonis control system

days. An example for the latter would be to implement a new type of spectroscopy and call this routine on every point of a grid defined within the control system environment. There is no limitation to the complexity of the code, it can be debugged with LabVIEW^{TM}'s internal debugger, and integrated with other external equipment.

The user interface can be designed using standard LabVIEW^{TM} controls and indicators including graphs, sliders and buttons. Figure 6 shows a code example of a very simple piece of code running a bias spectroscopy experiment first on Tip 1 and then on Tip 2, while the bias is kept fixed at the other two tips. A list of examples of user-contributed code can be found here [6].

The diagram in Fig. 7 shows the systematic of a multi-probe setup using the Nanonis control system. Each control system is operated by a personal computer, of which one acts as the master control PC, i.e. the cockpit from which the user operates all other systems remotely. The master control PC is equipped with multiple screens, typically one for each tip, while the slave PCs do not have a user interface. If necessary an adaptation kit interfaces each control system with the electrical connection to the microscope head.

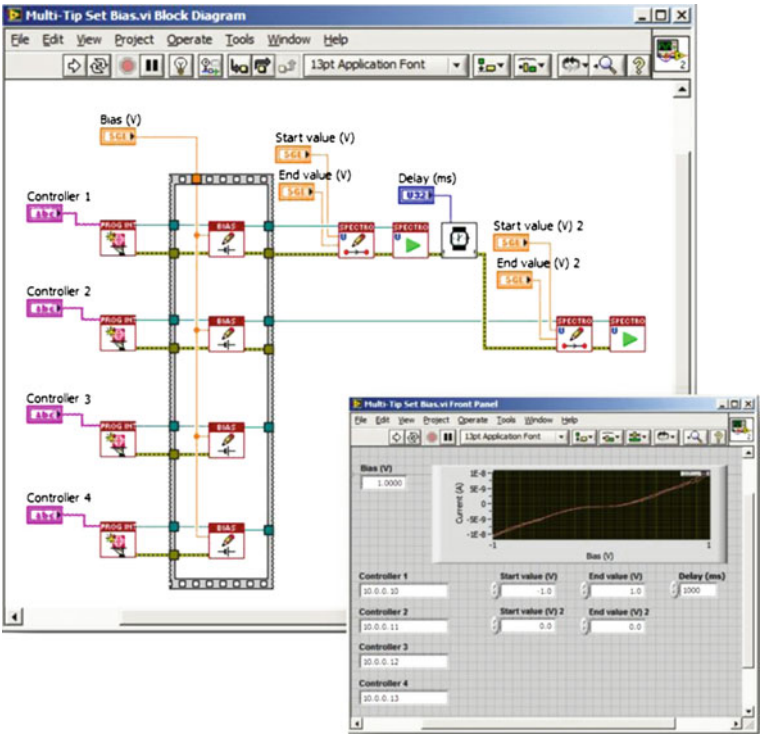

Fig. 6 Multiple instances of the code interact with four control systems, each in charge of another scanning tip

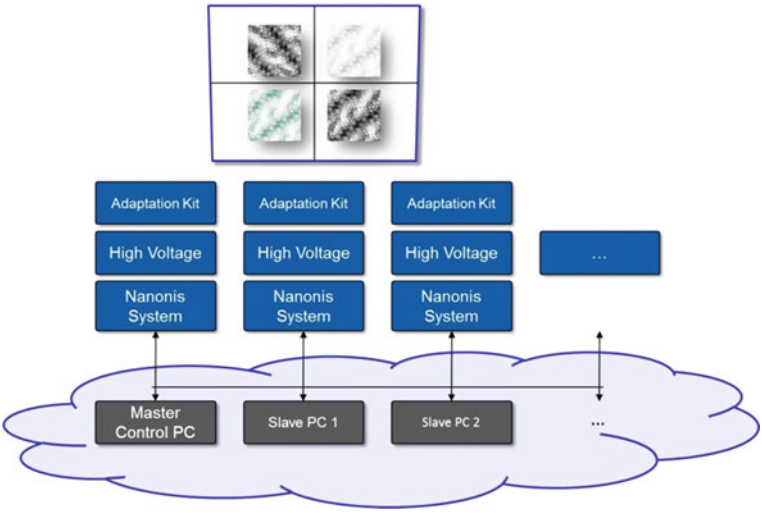

Fig. 7 Four control systems talking to each other over TCP/IP using the LabVIEW programming interface

4 Summary

In conclusion we have shown a possible setup for controlling a multi-probe control system. The approach is very flexible and does not rely on a pre-defined setup for scanning unit, probe mechanics or operation mode. The system is flexible enough to operate most commercially available multi-probe systems as well as home-built setups.

The results achieved with the KolibriSensor™ make it a promising candidate for a multi-probe non-contact AFM microscope.

References

1. Akiyama, T., Staufer, U., Rooij, N.F.: Self-sensing and self-actuating probe based on quartz tuning fork combined with microfabricated cantilever for dynamic mode atomic force microscopy. Appl. Surf. Sci. **210**, 18–21 (2003). doi:10.1016/S0169-4332(02)01471-X
2. Karrai, K., Grober, R.D.: Piezoelectric tip-sample distance control for near field optical microscope. Appl. Phys. Lett. **66**, 1842 (1995). doi:10.1063/1.113340
3. Giessibl, F.J.: Atomic resolution on Si(111)-(7 × 7) by noncontact atomic force microscopy with a force sensor based on a quartz tuning fork. Appl. Phys. Lett. **76**, 1470 (2000). doi:10.1063/1.126067
4. Torbrügge, S., Schaff, O., Rychen, J.: Application of the KolibriSensor® to combined atomic-resolution scanning tunneling microscopy and noncontact atomic-force microscopy imaging. J. Vac. Sci. Technol. B **28**, C4E12 (2010). doi:10.1116/1.3430544
5. Günther, S., Dänhardt, S., Wang, B., Bocquet, M.-L., Schmitt, S., Wintterlin, J.: Single terrace growth of graphene on a metal surface. Nano Lett. **11**, 1895–1900 (2011). doi:10.1021/nl103947x
6. SPECS Zurich: Programming interface example gallery. http://www.specs-zurich.com/en/programming_interface_gallery_content—1–1501.html (2011). Accessed 1 Nov 2011

Atomically Precise Manufacturing: The Opportunity, Challenges, and Impact

John N. Randall, James R. Von Ehr, Joshua Ballard, James Owen, Rahul Saini, Ehud Fuchs, Hai Xu and Shi Chen

Abstract Fifty years ago, Richard Feynman famously stated that "I am not afraid to consider the final question as to whether, ultimately—in the great future—we can arrange the atoms the way we want" (Feynman, "There's Plenty of Room at the Bottom", speech on December 29th 1959 at the annual meeting of the American Physical Society at the California Institute of Technology). Twenty years ago, Don Eigler of IBM, did arrange atoms the way he wanted (Eigler and Schweizer, Nature 344:524, 1990). We contend that in the very near future, that arranging atoms the way we want will become a manufacturing technology. This technology will start small, very small, in making practical and profitable products, and from there scale-up to a wide range of products and applications with very large economic and societal impacts. We will explain some of the details of the path that we are on to achieve Atomically Precise Manufacturing (APM), some of the challenges we must overcome to succeed, and the surprising number of applications that we have identified that are waiting for us to exploit.

Keywords Atomically precise manufacturing · Scanning tunneling microscope · Digital lithography · Atomic layer epitaxy · Precision

J. N. Randall (✉) · J. R. Von Ehr · J. Ballard · J. Owen · R. Saini · E. Fuchs
Zyvex Labs LLC, Richardson TX 75081, USA
e-mail: jrandall@zyvexlabs.com

H. Xu · S. Chen
Zyvex Asia Pte Ltd, 3 Research Link, Singapore 117602, Singapore

C. Joachim (ed.), *Atomic Scale Interconnection Machines*, Advances in Atom and Single Molecule Machines, DOI: 10.1007/978-3-642-28172-3_7,

1 Nanotechnology and Atomic Precision Manufacturing

The term nanotechnology [3] was first used by Norio Tanaguchi a Japanese industrialist who tracked and predicted trends in manufacturing precision from the early 1900s to the year 2000. His predicted trend lines have proven to be fairly accurate if somewhat conservative. For instance if his ultra precision manufacturing trend is extrapolated beyond the year 2000, it suggests that precision of 0.3 nm "atomic lattice" would be expected around 2015. In fact, thin film deposition precision at that level has been available through atomic layer deposition [4] for more than a decade. There has been a tendency to separate nanotechnology into two camps, bottom-up and top-down. Bottom-up nanotechnology typically takes advantage of some form of "self-assembly" to make large numbers of nanoscale objects with no direct control of the process imposed other than the design of the process. Self-assembly is driven by thermodynamics to the minimum energy configuration of the nanoscale object. Thus a given self-assembly process will result in a single outcome that is in its minimum energy configuration. Top-down nanotechnology exerts some control through directed energy (e-beam lithography) or through a created pattern (photo lithography or nanoimprint) to allow the same process to create a much wider range of products and ones that are not in minimum energy configurations. We are interested in developing a manufacturing technology that has top-down control and will allow us to use the same process to make many different size and shape features (that are not required to be in a minimum energy configuration) with the same process. It is this sort of manufacturing process that can have a wide impact because the same tool can be used to make a wide variety of structures.

We are interested in a top-down nano-manufacturing process that has the additional attribute of atomic precision. We need to be more specific about what we mean when we refer to "atomic precision", because we mean something different than building something with precision in some dimension that is precise to within plus or minus the size of a single atom. When we refer to an atomically precise manufacturing process, what we really mean is a process that has zero tolerance and absolute accuracy in all three dimensions and in placement of the structure. What we mean is that we want to be in control of where every atom goes in what we are building. Additionally, for structural stability and robustness, we seek to create covalently bonded structures.

There are a number of processes both bottom-up and top-down that achieve a subset of what we are aiming for. Seeman [5] and Rothemund [6] use DNA and Schafmeister [7] uses custom peptide building blocks to create three and two dimensional structures that in-principle control where every atom goes, but cannot control placement of their structures. Eigler [2], Hla [8], Ho [9], and others can create two dimensional structures of atoms and molecules where there is absolute control of the position of each atom or molecule. None of these processes can be considered a manufacturing process. Automated DNA sequencing however, is a manufacturing process that produces (with some restrictions on length) any DNA

sequence which is essentially absolute control (at least in terms of relative position) of atom placement.

2 Our Approach to Atomically Precise Manufacturing

We are attempting to create an APM process that uses the same tool that Eigler used for his seminal demonstration of atomic precision, the scanning tunneling microscope (STM). While Eigler used direct manipulation of atoms on a metal surface with the STM tip, we are using electron stimulated desorption of H atoms from a Si surface, in a process referred to H depassivation lithography [10, 11]. With a set-point current of several nA and sample bias of 2–5 V, H atoms can be removed from the surface (depassivated) and allow specific H atoms to be targeted and removed. This has been done by Lyding [10], Hersam [12], Schofield [13], Wolkow [14] and others. In other words, a patterning process that is capable of removing the specific atoms from a specific location is potentially available. Another part of this process is a version of Atomic Layer Epitaxy (ALE). There are several Si ALE processes [15, 16] that are essentially cyclic chemical vapor deposition (CVD) processes that deposit a monolayer, or a well-defined fraction of a monolayer, per cycle. Several of these use H as the mechanism that self-limits the deposition. For instance, Si ALE process would start with a clean (depassivated) Si surface, and introduce a precursor molecule that contains Si and H. The molecule sticks to the clean surface and dissociates depositing both Si and H atoms on the surface. Once all available surface covalent bonds are satisfied with either H atoms or Si atoms that are themselves H passivated, then the surface is saturated and no more deposition takes place because the precursor molecules will not stick to the passivated surface. The ALE cycle proceeds by using a process to remove all surface H. This can be simply done by raising the temperature to thermally desorb the H or use high energy photons to remove the H. Instead of this global removal of all H from the surface, our process would remove the H atoms in a designed pattern so that Si atoms could be deposited exactly where we want them. This process is shown schematically in Fig. 1. While we have not yet fully demonstrated this process, we have made significant progress in overcoming the challenges that must be overcome to realize an APM technology. We will discuss the challenges and some of our progress in the following sections.

2.1 Absolute Precision Patterning

H depassivation lithography with an STM is essentially e-beam lithography using the limit of a self developing resist: a monolayer of H. We do this lithography on a Si(100) 2×1 reconstructed surface that has been H passivated. In this state, every surface Si atom has all four of its covalent bonds satisfied, two back bonds to the Si

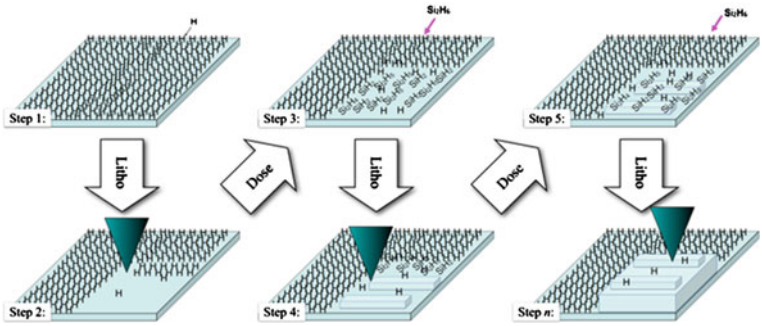

Fig. 1 Schematic diagram of the APM process. A H-terminated Si(001) surface is prepared (Step 1). A pattern is drawn using suitable lithographic conditions (Step 2). Disilane is dosed into this pattern, to saturation (Step 3). The adsorbed disilane is exposed to a second lithography step, removing the H, and allowing the Si adatoms to arrange into islands (Step 4). This pattern is again exposed to disilane (Step 5). Iteration of Steps 4 and 5, gradually build up a block of silicon (Step n)

lattice, one bond to a neighboring surface atom formed during the surface reconstruction, and one bond to the H atom. The depassivation, or electron stimulated desorption, of the H atom from the Si surface, is accomplished by electrons from the tip depositing enough energy to break the Si–H bond. There are two regimes of H depassivation lithography: a low bias regime 2–6 V where the depassivation process is presumed to be a multi-electron process because there is a current dependence for the depassivation efficiency (atoms removed per incident electron) and a high bias regime 7–50 V where there is enough energy transferred from a single electron for depassivation and the depassivation efficiency is higher than the low bias regime and not current dependant. These two regimes are also roughly the regimes of electron tunneling (low bias) and field emission (high bias).

The depassivation process is fairly inefficient, even in the high bias regime, requiring significantly higher doses per unit area than conventional high resolution e-beam lithography. This inefficiency is particularly acute in the low bias regime which is required to do atomic precision patterning. This patterning inefficiency is mitigated somewhat by the extremely large current densities possible with STM-based e-beam lithography. To do sub 5 nm lithography [17], ultra high resolution e-beam tools typically are limited to beam currents less than 1 nA. Lyding's group has shown that sub 1 nm lithography can be done with currents up to 60 nA [18]. Further mitigating the poor patterning efficiency of the STM lithography process at atomic resolution is the variable spot size approach used in conventional e-beam lithography.

Similar to conventional e-beam lithography, H depassivation lithography can be operated with variable spot sizes. In this way only the very small features and the edges of larger features are done with the low bias mode, and the much more efficient larger spot high bias mode can be used to expose the interior of larger features. Previously, it was believed that the depassivation efficiency was constant above 7 V [19], but most STM systems are limited to a 10 V sample bias. We have

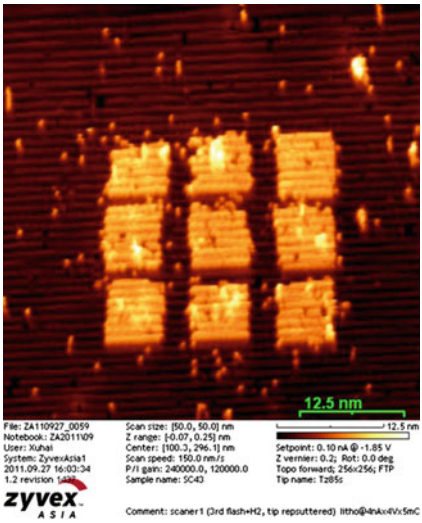

Fig. 2 An STM image of nine nominally 5 × 5 nm squares patterned by low bias H depassivation lithography using 4 nA, 4 V, and a line dose of 5 mC/cm

discovered that there is at least one order of magnitude higher efficiency by raising the voltage to 40 V where the spot size is on the order of 15 nm. We should be clear that the patterning speed of STM-based H depassivation lithography is still much lower than conventional e-beam lithography [17] which is already much too slow to do direct write of integrated circuits. We are not proposing that this technology will have any direct impact on integrated circuit manufacturing.

However, we are not interested in manufacturing ICs, and though slower than conventional e-beam lithography, STM-based H depassivation lithography can do something that no other lithographic process can do: it can make perfect lithographic patterns. While we have demonstrated the proof of principle of perfect patterns, significant challenges remain in the path of automated high reliability and high yield atomic precision patterning. In Fig. 2 we demonstrate the ability to make very small (5 × 5 nm) patterns with good edge acuity. This was done with dead reckoning rather than alignment to the crystal lattice, which will improve the fidelity and placement of the patterns.

2.2 Closed Loop Lithography

There is something else that STM-based H depassivation lithography can do that e-beam lithography cannot. It can write, inspect, do metrology on its patterning result and correct a pattern that has unexposed parts. This is something that Michel Dupont of IBM Zurich calls “Closed Loop Lithography”. There are three reasons for this powerful combination of capabilities. One, there is a large difference between imaging and lithography modes. Two, the resist is self developing.

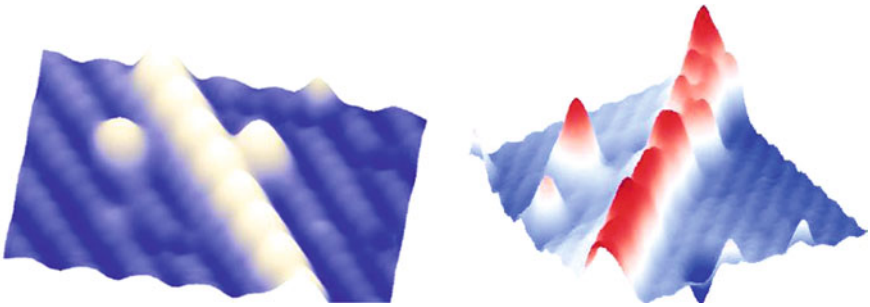

Fig. 3 At *left*, a row of H atoms from one side of a single dimer row have been removed, exposing a line of Si dangling bonds. At *right*, Gallium has been adsorbed onto the dangling bonds, creating a metallic nanowire. Images courtesy of T. Hashizume, of Hitachi ARL, Saitama, Japan

Three, the Si lattice can be used as a global fiducial grid to align the pattern before exposure and to do metrology afterwards. The manufacturing advantages of combining these functions into a single tool cannot be overemphasized. This will be a significant advantage in developing atomically precise manufacturing.

2.3 Digital Lithography

In addition to the possibility of closed loop lithography, H depassivation lithography has the opportunity to be the first "digital lithography". It is digital in virtually all aspects. The resist is spatially quantized into pixels that are surface Si atoms. The atoms sit on an addressable grid that is the Si 2 × 1 (100) surface lattice. The exposure/self-development process is absolutely digital process: the H atoms are either removed or not. There is no possibility for a partially exposed pixel. This quantization both spatially and with respect to the exposure/development will provide a significant opportunity to do process control for a reliable automated lithography process. We point out that in addition to our APM technology, that progress in H depassivation lithography will be very useful in a wide variety of fields. In Fig. 3, for instance, researches in Japan are using H depassivation lithography to make dangling bond wires and are using the dangling bonds to get patterned deposition of metals [20].

2.4 Tip Technology

In continuing our analogy of H depassivation lithography with conventional e-beam lithography, we emphasize the importance of the electron source. Focused electron beam systems are designed around the capabilities of their source.

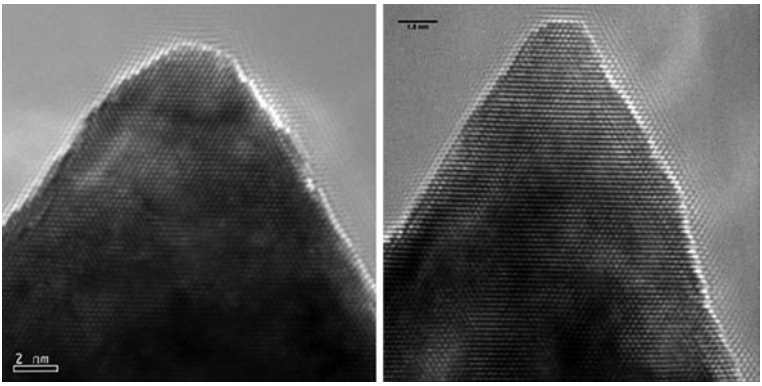

Fig. 4 Transmission Electron Micrographs (TEM) of two W STM tips prepared by electrochemical etching followed by two different sputter sharpening techniques. On the *left* the tip was formed by the Field Directed Sputter Sharpening technique. On the *right* the tip was formed in a Focused Ion Beam (FIB) tool. In both cases the apex radius is 2 nm or less and the tips show no amorphization due to ion damage. Note that both tips have been exposed to atmosphere for many minutes and show no oxidation. TEMs courtesy of Maia Bischof of UNT. FIB work courtesy of David Jaeger of UNT

Since the invention of the STM, attempts have been made to improve STM tips, but these have not made a large impact on STM operation to date. Electrochemically etched tungsten tips with poor control of tip radius and PtIr tips cut with scissors or pliers are still the two predominant tips used in STMs today. We believe that this lack of progress in improving tip technology is due primarily to two factors. One, when imaging an atomically flat surface, the shape of the tip at the micro or even nanoscale is not very important. Two, the size and shape of a tip at the apex is frequently changed during normal STM operation.

However, for H depassivation lithography, particularly in the high bias mode where the tip is a field emitter, the size and shape of a tip does make a significant difference. We have investigated several methods of preparing more reproducible and robust STM tips for both imaging and lithography. For instance in Fig. 4 we show two tungsten tips which have been produced by electrochemical etching followed by two different methods of sputter sharpening, Field Directed Sputter Sharpening (FDSS) [21, 22] and Focused Ion Beam (FIB) sharpening. Note that both are still crystalline in spite of some damage from the ions used in the sputtering process and both have a small radius of curvature of 3 nm or less. We can routinely control the radius of curvature with both processes to be 2–3 nm.

Further, we have discovered that we can preserve these tips to maintain their size, shape, and surface cleanliness for long periods of time in storage and transport and exposures to ambient. One precaution is to handle the tips with precautions to avoid electrostatic discharge (ESD) using the same techniques as used to handle ESD sensitive CMOS chips [23]. If these precautions are not taken, the tips suffer ESD events at their apex which results in a small amount of metal being vaporized and quickly condensing into a low density nanocrystalline “fuzz”

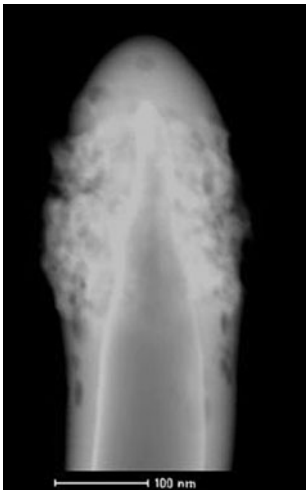

Fig. 5 TEM of etched W tip after ESD event has created nanocrystalline W "fuzz" at the apex. TEM courtesy of Maia Bischof of UNT

at the apex such as is shown in Fig. 5. By handling the tips as if they are ESD sensitive, and storing them in metal containers (as opposed to plastic which is often the case) we can prevent this type of tip degradation. To prevent oxidation of the tungsten tips, we assumed that they would need to be prepared in situ and kept in the ultra high vacuum (UHV) chamber. We have discovered, much to our surprise, that these extremely sharp W tips can survive long periods of time (days) in ambient with no oxidation. We do not understand why the tips are not oxidizing. We have explored leaving the tips grounded or ungrounded, exposed to light or in the dark, initial venting with O_2 or N_2 after sharpening in UHV, and in mild electrical fields or in no fields. All of these variations seem to have no effect, the tips simply do not oxidize in ambient for a period of days. Even though we do not understand this lack of oxidation, we can make use of this situation to prepare tips outside of the UHV STM chamber, store them in metal containers built for tips storage where they are pumped out (rough vacuum) and backfilled with N_2, if we wish, ship them anywhere in the world.

On the other hand, we have yet to solve the problem that results in frequent tip changes while the tip is in use in the STM. While there are a number of processes that can change a tips ability to image well or do lithography consistently, we are currently considering the feedback loop that monitors the tunneling current and adjust the tip's height above the surface to maintain the set-point current selected by the operator. The majority of STM feedback loops are proportional-integral-derivative (PID) controllers with the Derivative coefficient set at zero. A large percentage of the time, the control loop carries out its principle mission, minimizing the set-point current errors, and in doing so, also manages to avoid tip changing interactions with the surface. The small percentage of the time that tips do interact with the surface and change their imaging properties are manageable if one is doing science with the STM and has the time to employ methods to "process" the tip to regain adequate imaging capabilities. For manufacturing

purposes however, this is an unacceptable situation. To meet this challenge, we plan on attempting to develop a feedback loop and scanning method whose primary function is to avoid tip altering encounters with the surface and whose secondary function is to provide high quality topographical information about the surface.

2.5 Atomic Layer Epitaxy of Si

Our goal is to use this H depassivation lithography to determine where Si atoms will be added epitaxially to a Si surface, and to do so repeatedly with absolute precision to create three dimensional structures. This could be considered spatially controlled deprotection.

We are working with disilane (Si_2H_6) which has been used in several Si ALE processes. Disilane has several advantages. It is readily available in high purity. It has a high sticking coefficient on unpassivated Si surfaces. There is a wealth of literature on disilane-based Si chemical vapor deposition (ALE) epitaxy. ALE is a cyclic CVD process that starts with unpassivated Si, introduces a precursor gas (disilane) which sticks to the surface and dissociates with the process continuing until all available unsatisfied Si surface bonds are occupied either with H atoms or H passivated Si atoms. At this point the deposition process is self-limiting where in disilane's case 1/3–1/2 of a monolayer of Si atoms are deposited per cycle. The precursor gas is then pumped from the chamber and some process is used to remove all of the H from the surface. This process can be simply raising the temperature until all H desorbs thermally or using high energy photons to break the Si H bonds. The deposited Si atoms now free of H have the mobility to move into epitaxial positions. The surface is again depassivated and the ALE cycle is repeated.

In the process we are developing, instead of removing the H globally from the Si surface, we intend to remove H in desired patterns with H depassivation lithography. There are several consequences of adopting this approach. For one it makes a constant temperature process viable since the H removal does not require any additional thermal energy. This is indeed an advantage when attempting to pattern with atomic resolution since any change in temperature would likely require significant time to allow the sample to stabilize after the temperature change. However, this approach will also limit the temperature of the process to approximately 300°C or lower because of the mobility of the H on the Si surfaces would cause the carefully written pattern edges to diffuse and defeat the goal of atomic precision. This is a relatively low temperature for Si epitaxy which is usually carried out 200–300°C higher. However, very low temperatures have been reported for solid source Si epitaxy [24]. And while we are essentially doing gas source epitaxy, we are removing the H from the surface after the Si has been deposited from gas precursor molecules. Shown in Fig. 6 is the patterned area and patterned epitaxial growth carried out at less than 300°C where dimer row

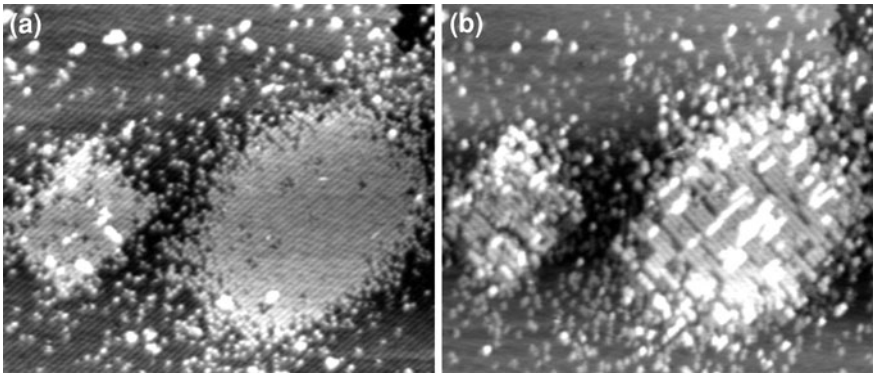

Fig. 6 STM Lithography and Patterned Epitaxy of 1 monolayer of Si(001); Ts = 275°C. **a** The surface after the initial patterning. On the *left*, a pattern drawn using the low-V mode, at 4.5 V, 6 nA, and an electron dose of 16 mC/cm. On the right, a high-V mode pattern, at 8 V, 6 nA, 1 mC/cm. **b** The same pattern after four cycles of disilane deposition (1 × 10−6 Torr × 10 s), and lithography, showing growth of around 1 ML of Si(001). Some large second-layer islands are also forming in the right-hand pattern

formation in the growth area is visible and is a clear indication of epitaxial growth. While in Fig. 6 we have only grown the first monolayer with the second monolayer just starting, we have also grown approximately 18 monolayers (2 nm thickness) of Si in an area that is roughly 20 × 20 nm.

The next step is to improve our lithography process to be able to do automated atomically precise patterning on significant topography in order to make three dimensional atomically precise, top-down controlled Si structures. This will involve overcoming some significant challenges which include doing the H depassivation lithography on surfaces that are not 2 × 1 reconstructed. The lithography part of the cycle is carried out after deposition and the deposited Si atoms are deposited in a disordered fashion and do not join the crystal lattice until the H atoms are removed. Since only 1/2–1/3 of a monolayer (depending on deposition conditions) is deposited on the surface per cycle, at best we will have an atomically flat terrace every other cycle and getting the Si atoms in every position that we want them has not yet been demonstrated.

2.6 Surface Protection

If we create atomically precise Si structures, they must be able to maintain their dimensions in the environment that they will be used in. While there are a limited number of applications in vacuum, preventing oxidation of the Si is a desirable goal. H passivation can forestall oxidation for a short time, but a longer lasting passivation would be beneficial. A robust monolayer passivation would be ideal, though for a number of applications an atomic layer deposition of ∼1 nm of Al_2O_3 or other durable material would be acceptable.

2.7 Extension to Other Material Systems

We have described the APM technology that we are developing as patterned atomic layer epitaxy of Si using H depassivation lithography. This implies that we are restricted to building Si structures. If we instead think of this technology spatially controlled desorption, where the desorption mechanism is electron stimulated desorption, then this can be considered a more general fabrication approach. At one point in time, the atomically precise removal of H from Si surfaces was suspected of being a process viable only with Si and H. Hersam [25] and Wolkow [26] have demonstrated that a variety of species may be desorbed from Si surfaces. There are many atomic layer epitaxial and atomic layer deposition [4] processes that use a specific species of atom or molecule as a protection layer to achieve the self-limiting deposition that makes layer by layer deposition possible. We believe that a subset of these will be adaptable to our APM approach.

3 If We Succeed in Realizing APM Technology, So What?

If we are successful in creating a technology where with programmable top-down control, would this be anything more than a laboratory curiosity, is a question that must be asked of a process that is going to initially have a very limited throughput capability; therefore, there is a requirement for a useful structure to have an extremely small volume of atomically precise material. We have identified a number of applications and products that, we believe, more than justify our efforts. We will list a subset here.

3.1 Nanometrology Standards

A wall of single crystal Si that is uniformly a countable number of atomic layers tall and wide would have great value as an atomically precise metrology standard. We are already working with the National Institute of Standards and Technologies on the possibility of creating such standards.

3.2 NanoBio: DNA Nanopores

If surfaces can be sculpted with atomic precision this brings up a host of possibilities to create surfaces for specific designed molecular interaction. This could include chiral structures for enantiomer separation, molecular binding sites for specific chemical sensors, enzymatic catalysts, and many others. One almost trivial structure with potentially enormous impact that could be realized with a nanoscopic

quantity of atomically precise material would be a nanopore with integrated electrodes for DNA sequencing. While there are interesting possibilities with protein channels in lipid membranes, these are fragile structures and a solid state membrane would be preferable. While a number of researchers have produced solid state nanopores with the requisite 2 nm pore diameter, the fabrication methods lack the precision to control the size and shape of the nanopore so that the DNA will move in an orderly fashion through the pore allowing the bases to be read as they pass the integrated electrode. If we successfully develop our technology we would be able to create nanopores that would be successful in this application. A relatively small number of such nanopores (~ 100) would be all that is required for extremely high speed DNA sequencing [27].

3.3 NEMS

Micro Electro Mechanical Systems (MEMS) have seen a wide range of valuable applications. Nano Electro Mechanical Systems (NEMS) could extend these capabilities into many more applications. A key feature of APM is that in addition to being able to make very small structures, it should be able to make these small structures with unprecedented precision. A relatively simple NEMS oscillator would operate at extremely high frequencies and the control of the resonant frequency would be extremely good. These NEMS oscillators could be used for high frequency filtering for very low power radios, or for extremely sensitive sensors.

3.4 Quantum Dots

The value of Quantum Dots is that they contain electronic states that are different from the electronic states in the same material in bulk form. These electronic states, which are controlled by the size of the quantum dots, can lead to a wide variety of optical and electronic applications. For instance by making quantum dots of different sizes, they can be made to fluoresce at different wavelengths providing specific tags that can be used in medical imaging. They can also be used in single electron or resonant tunneling electronic devices. In many of these applications, the utility of the quantum dots is directly affected by the degree of control of the energy level of the quantum dots which directly determined by the control of the dimensions of the quantum dots. Top-down fabrication methods adopted from semiconductor processing have poor relative precision which results in $\pm 5\%$ control of the size of the quantum dots. Chemical synthesis methods are not any better. If we can create quantum dots with absolute size and shape control, we will have much better control of the energy levels of the quantum dots allowing more effective use in a variety of applications. If we can simultaneously control

their placement with respect to each other, we can control their interactions more effectively.

3.5 Qubits

While there are a fairly wide variety of proposals for realizing qubits for quantum computation, one of the most promising is the P in Si which utilizes the long lived nuclear spin of P. Simmons at the University of New South Wales is using atomically precise H depassivation lithography to position P atoms in Si for the purpose of making Qubits for a scalable quantum computing technology [28, 29]. This sort of lithography is also used to pattern delta-doped layers of P in Si which will form the electrodes used to control the interactions of the qubits and their readout. We are collaborating with the UNSW to develop more automated and reliable lithography process.

3.6 Nanoimprint Templates

One of the most cost effective methods of getting nanoscale patterning done is nanoimprint. To date, the resolution of nanoimprint seems to be template limited and there are a number of applications already identified that would benefit from sub-10 nm resolution. The principle tool for template making, e-beam lithography, is capable of sub-10 nm resolution, but the relative precision is very poor. As is discussed below, the throughput in the near term would preclude making integrated circuit masks, APM could make nanoimprint master templates with extremely high absolute as well as relative precision that is simply not available in any other technology. This will allow very cost effective nanoscale patterning. We are actively working with Molecular Imprints Inc. one of the leading nanoimprint companies in the world.

3.7 Initial Cost of Production

While the atomically precise patterned Atomic Layer Epitaxy process has not yet been fully demonstrated, we have learned enough about the process to make some estimations of the cost of production. The model used was a cost of ownership model including labor (operators and engineer), cost of factory space, five year depreciation, and a production tool that cost 5 M USD and has 10 tips operating in parallel. The cost varies with the amount of patterning required in the low bias, small-spot, atomic-resolution mode versus the high bias large-spot mode and ranges from about 500–3,000 $(USD) per cubic micrometer of atomically precise

Table 1 The production cost versus product sizes

X (nm)	Y (nm)	Z (nm)	μm^3	LR (%)	$/$\mu m^3$	Product component	Cost/ unit	Units	Total
1000	1000	10	1.0E-02	90	$476	DNA nanopore	$4.76	200	$952.00
1000	20	20	4.0E-04	0	$2,970	CD metrology standard	$1.19	10	$11.88
10	10	4	4.0E-07	0	$2,970	NEMS resonator	$0.001	10	$0.01

Si structures. While this is a very high cost for producing material at the micro scale, several of the applications listed above could be produced cost-effectively even at this relatively high price per unit volume because the applications only require a nanoscopic quantity of material. In the Table 1 we list three possible products, their dimensions and nominal volume, the percentage of patterning in low resolution mode (LR%), unit costs, number of units for a useful product, and the total production cost for the atomically precise portion of the product. We already have an order placed for 10,000 of the NEMS resonators [30].

4 Scaling Up

We would expect the production tool to be based on MEMS closed loop X, Y, Z scanners rather than on piezo tube scanners. While still being developed, the MEMS scanner technology should provide substantial benefits over the established piezo tube scanner technology. Neil Sarkar of Integrated Circuit Scanning Probe Instruments Corporation is developing XYZ MEMS scanners which will include closed loop positioning and initial designs have a very small footprint (200 $\times$ 200 μm), allowing many tips to be operating on a small sample area. We anticipate the technology to include local circuitry for driving the MEMS actuators, closing the positional feedback loop, including a preamplifier for the tunneling current, and possibly a microcontroller to allow the scanner to perform simple patterning functions semiautonomously. This architecture will allow the scanners to operate independently allowing arbitrary patterns to be created and stitched together. It will also simplify the interconnection of the array, requiring only ground, power, a serial communication line for instructions, and a tunneling current signal line per scanner versus the separate actuator drive and sense signals per axis required with out the local circuitry. We anticipate that these scanners will have small scan ranges (<1 μm) which can be traded off for the $\sim$0.1 nm positioning resolution required. A global high resolution nanopositioning stage will be used to allow the scan fields to overlap.

While initial production tools will start with modest levels of parallelism (10 tips for example), we anticipate scaling to much larger numbers of tips to increase productivity and allow a much larger range of products to be made. The semi-autonomous MEMS scanners will allow many tips to be placed on a sample (2,500 per square cm for a 200 $\times$ 200 μm pitch) with a tractable number of

electrical connections. In light of the analogy that we have made with conventional e-beam lithography, it is worthwhile to look at the challenges that have been faced by attempts to make parallel arrays of e-beams for lithography.

To start with, electron optical columns are complex and expensive, requiring high voltage, many optical elements, and the control of many potentials or currents (for electrostatic or magnetic lenses or deflectors). While an array of columns is a possible approach, most efforts, REBL [31] and MAPPER [32], for instance have taken the one column, many beamlet approach. Attempts to parallelize anything will have a linear component of complexity which increases proportionally with the level of parallelism. However, when there is unwanted interaction between the units being parallelized, the complexity increases with an exponential component as well. The problem of unwanted interaction with parallelizing electron beams is space charge. Electrons are charged particles that repel each other and limit the performance of e-beam systems even in single columns. In a parallel array of beamlets in a single column this interaction can be minimized by using smaller currents and/or larger spacing of the beamlets. Unfortunately, both of these factors reduce the productivity of the parallel array of electron beams in a conventional system. In principle, much of the space charge interaction can modeled and compensated for with clever optics and corrections to the deflection of the beamlets. These corrections however are pattern dependent and because electrostatic interactions are long range the complexity of these corrections increases exponentially with the number of individual beams.

In comparison our STM-based version of e-beam lithography has much a much simpler and less expensive electron optical system. The maximum voltage is 50 V and the entire electron optics consists of two elements, the cathode (tip) and anode (sample). And while electron beam interaction in a parallel array of STM tips is not eliminated, the extremely short path of electrons in free space which is 1–100 nm (depending on the writing conditions), the shielding geometry of the tip and sample, and the relatively large spacing of the tips render any space charge interaction negligible.

Another significant advantage of our tip-based lithography approach is its closed loop nature and ability to use the crystal lattice as an addressable grid. These attributes will lessen considerably the difficulty in producing accurate placement of patterns and the stitching of fields, which are two of the more challenging aspects of high resolution lithography and particularly challenging for multi-beam (tip) approaches.

Based on the simplicity of the electron optics, the small footprint and favorable interconnectivity of the semi-autonomous MEMS scanners, and the lack of interaction of the separate array elements, we believe that the scale-up to high levels of parallelism of H depassivation lithography will be a significantly less costly and complicated path to scaling up through parallelism compared to conventional e-beam lithography. Note that we are not suggesting that H depassivation lithography will compete with e-beam lithography to pattern integrated circuits. We are simply indicating that if there is an economic drive to scale-up the throughput capacity of atomically precise manufacturing, that there is a tractable path for many

orders of magnitude increase in throughput over a technology that should be able to produce, cost-effectively, valuable products in the near future.

5 Conclusions

Atomically Precise Manufacturing technology is being pursued via scanning tunneling microscope-based patterning and atomic layer epitaxy. This technology should permit top-down controlled fabrication of arbitrary three dimensional Si structures where we are in control of the placement of every atom. Significant progress toward realizing this technology has been made such as the proof of principle of atomically precise patterning and patterned epitaxial growth in the available temperature window. We believe that this technology will be demonstrated in the near future, that it will enable the manufacturing of high valued products in the near term, and that it is amenable to scaling up productivity by many orders of magnitude permitting a much wider range of products to be manufactured. Numerous challenges remain such as more reliable tip technology, the development of closed loop MEMS scanners, and a suitably robust surface protection technology that will preserve the atomically precise nature of the manufactured structures in the environment that they must operate.

Acknowledgments This material is based upon work supported by the Defense Advanced Research Project Agency (DARPA) and Space and Naval Warfare Center, San Diego (SPAWARSYSCEN-SD) under contract N66001-08-C-2040. It is also supported by a grant from the Emerging Technology Fund of the State of Texas to the Atomically Precise Manufacturing Consortium. The authors would also like to acknowledge the excellent support of Maia Bischof and David Jaeger of the University of North Texas for Transmission Electron Microscopy and Focused Ion Beam work respectively, and many useful discussions with Richard Silver and Jason Gorman of NIST, Joseph Lyding of the University of Illinois, Neil Sarkar of ICSPI, Rick Reidy of the University of North Texas, S.V. Sreenivasan at the University of Texas at Austin, Brian Gorman of Colorado School of Mines, and Bob Wallace, Yves Chabal, and K.J. Cho of the University of Texas at Dallas.

References

1. Feynman, R.: “There’s Plenty of Room at the Bottom”, Speech on December 29th 1959 at the annual meeting of the American Physical Society at the California Institute of Technology
2. Eigler, D.M., Schweizer, E.K.: Positioning single atoms with a scanning tunneling microscope. Nature **344**, 524 (1990). doi:10.1038/344524a0
3. Taniguchi, N.: On the basic concept of ‘nano-technology’. In: Proceedings of the International Conference on Production Engineering, Tokyo, Part II (Japan Society of Precision Engineering) (1974)
4. Ritala, M., Leskelä, M.: Atomic layer epitaxy—a valuable tool for nanotechnology? Nanotechnology **10**(1): 19–24 (1999). doi:10.1088/0957-4484/10/1/005

5. Zheng, J., Birktoft, J.J., Chen, Y., Wang, T., Sha, R., Constantinou, P.E., Ginell, S.L., Mao, C., Seeman, N.C.: From molecular to macroscopic via the rational design of a self-assembled 3D DNA crystal. Nature **461**, 74–77 (2009). doi:10.1038/nature08274
6. Rothemund, P.W.K.: Folding DNA to create nanoscale shapes and patterns. Nature **441**, 298–302 (2006). doi:10.1038/nature04586
7. Levins, C.G., Schafmeister, C.E.: The synthesis of functionalized nanoscale molecular rods of defined length. J. Am. Chem. Soc. **125**, 4703–4704 (2003). doi:10.1021/ja0293958
8. Hla, S.-W.: STM single atom/molecule manipulation and its application to nanoscience and technology. J. Vac. Sci. Technol. B **23**, 1351–1360 (2005).doi:10.1116/1.1990161
9. Hahn, J.R., Ho, W.: Oxidation of a single carbon monoxide molecule manipulated and induced with a scanning tunneling microscope. Phys. Rev. Lett. **87**, 166102 (2001). doi:10.1103/PhysRevLett.87.166102
10. Lyding, J.W., Shen, T.-C., Hubacek, J.S., Tucker, J.R., Abeln, G.C.: Nanoscale patterning and oxidation of H-passivated Si(100)-2x1 surfaces with an ultrahigh vacuum scanning tunneling microscope. Appl. Phys. Lett. **64**, 2010 (1994). doi:10.1063/1.111722
11. Randall, J.N., Ballard, J.B., Lyding, J.W., Schmucker, S., Von Ehr, J.R., Saini, R., Xu, H., Ding, Y.: Atomic precision patterning on Si: an opportunity for a digitized process. Microelectron. Eng. **87**, 955–958 (2010). doi:10.1016/j.mee.2009.11.143
12. Hersam, M.C., Guisinger, N.P., Lee, J., Cheng, K., Lyding, J.W.: Variable temperature study of the passivation of dangling bonds at Si(100)-2 × 1 reconstructed surfaces with H and D. Appl. Phys. Lett. **80**, 201 (2002). doi:10.1063/1.1431689
13. Schofield, S.R., Curson, N.J., Simmons, M.Y., Ruess, F.J., Hallam, T., Oberbeck, L., Clark, R.G.: Atomically precise placement of single dopants in Si. Phys. Rev. Lett. **91**, 136104 (2003) doi:10.1103/PhysRevLett.91.136104
14. Tong, X., Wolkow, R.A.: Electron-induced H atom desorption patterns created with a scanning tunneling microscope: implications for controlled atomic-scale patterning on H-Si(1 0 0). Surf. Sci. Lett. **600**, L199–L203 (2006). doi:10.1016/j.susc.2006.06.038
15. Bedair, S.M: Atomic layer epitaxy deposition processes. J. Vac. Sci. Technol. B **12**, 179–185 (1994) doi:10.1116/1.587179
16. Suda, Y., Misato, Y., Shiratori, D.: Si atomic-layer epitaxy using thermally cracked Si_2H_6. Jpn. J. Appl. Phys. **38**, 2390–2392 (1999) doi:10.1143/JJAP.38.2390
17. Yang, J.K.W., Cord, B., Berggren, K.K.: Understanding of hydrogen silsesquioxane electron resist for sub-5-nm-half-pitch lithography. J. Vac. Sci. Tech. B **27**, 2622–2627 (2009). doi:10.1116/1.3253652
18. Private communication with Joe Lyding University of Illinois
19. Shen, T.-C., Wang, C., Abeln, G.C., Tucker, J.R., Lyding, J.W., Avouris, Ph, Walkup, R.E.: Atomic-scale desorption through electronic and vibrational excitation mechanisms. Science **268**, 1590 (1995). doi:10.1126/science.268.5217.1590
20. Hashizume, T., Heike, S., Lutwyche, M.I., Watanabe, S., Nakajima, K., Nishi, T., Wada, Y.: Jpn. J. Appl. Phys. Pt. 2 35, L1085–L1088 (1996). doi:10.1143/JJAP.35.L1085
21. Schmucker, S.W., Kumar, N., Abelson, J.R., Daly, S.R., Girolami, G.S., Lyding, J.W.: Field-directed sputter sharpening for tailored probe materials and atomic-scale lithography. submitted for publication
22. Lyding, J.W., Schmucker, S.W.: Nanometer-scale sharpening of conductor tips. U.S. Patent Application No. 11/740, 678, Filed April 26, 2007
23. http://www.evaluationengineering.com/archives/articles/1102esd.htm
24. Zandvliet, H.J.W., Zoethout, E., Wulfhekel, W., Poelsema, B.: Origin of roughening in epitaxial growth of silicon on Si(001) and Ge(001) surfaces. Surf. Sci. **482–485**, 391–395 (2001). doi:10.1016/S0039-6028(01)00807-X
25. Yoder, N.L., Fakonas, J.S., Hersam, M.C.: Control and characterization of cyclopentene unimolecular dissociation on Si(100) with scanning tunneling microscopy. J. Am. Chem. Soc. **131**, 10059 (2009). doi:10.1021/ja9010546

26. Wolkow, R.A.: Controlled molecular adsorption on silicon: laying a foundation for molecular devices. Annu. Rev. Phys. Chem. **50**, 413–441 (1999). doi:10.1146/annurev.physchem.50.1.413
27. Branton, D., Deamer, D.W., Marziali, A., Bayley, H., Benner, S.A., Butler, T., Di Ventra, M., Garaj, S., Hibbs, A., Huang, X., Jovanovich, S.B., Krstic, P.S., Lindsay, S., Ling, X.S., Mastrangelo, C.H., Meller, A., Oliver, J.S., Pershin, Y.V., Ramsey, J.M., Riehn, R., Soni, G.V., Tabard-Cossa, V., Wanunu, M., Wiggin, M., Schloss, J.A.: The potential and challenges of nanopore sequencing. Nat. Biotechnol. **26**, 1146–1153 (2008). doi:10.1038/nbt.1495
28. O'Brien, J.L., Schofield, S.R., Simmons, M.Y., Clark, R.G., Dzurak, A.S., Curson, N.J., Kane, B.E., McAlpine, N.S., Hawley, M.E., Brown, G.W.: Towards the fabrication of phosphorus qubits for a silicon quantum computer. Phys. Rev. B **64**, 161401-04(R) (2001). doi:10.1103/PhysRevB.64.161401
29. Simmons, M.Y., Schofield, S.R., O'Brien, J.L., Curson, N.J., Oberbeck, L., Hallam, T., Clark, R.G.: Towards the atomic-scale fabrication of a silicon-based solid state quantum computer. Surf. Sci. **532–535**, 1209–1218 (2003). doi:10.1016/S0039-6028(03)00485-0
30. Tom Kenny of Stanford placed an order for 10, 000 NEMS resonators during the Technologies for Future Micro-Nano Manufacturing Workshop August 8–10, 2011
31. Petric, P., Bevis, C., Carroll, A., Percy, H., Zywno, M., Standiford, K., Brodie, A., Bareket, N., Grella, L.: REBL: a novel approach to high speed maskless electron beam direct write lithography. JVST-B **27**, 161–166 (2009). doi:10.1116/1.3054281
32. Wieland, M.J., de Boer, G., ten Berge, G.F., van Kervinck, M., Jager, R., Peijster, J.J.M., Slot, E., Steenbrink, S.W.H.K., Teepen, T.F., Kampherbeek, B.J.: MAPPER: high-throughput maskless lithography. Proc. SPIE **7637**, 76370F (2010). doi:10.1117/12.849480

Combined STM and Four-Probe Resistivity Measurements on Single Semiconductor Nanowires

M. Berthe, C. Durand, T. Xu, J. P. Nys, P. Caroff and B. Grandidier

Abstract Transport measurements on free-standing nanostructures with clean and reconstructed facets require an instrumentation based on electrical probes that scan materials at the atomic scale with fine tuning in the establishment of the electrical contact. We describe a multiple probe tunneling microscope that operates under a scanning electron microscope in ultra-high vacuum and fulfills these requirements thanks to a unique control system. We show how this instrument is well adapted to study the resistivity of semiconductor nanowires.

1 Introduction

Scaling of electronic device dimensions into the ultimate regime of a few nanometers has been the bottom line of the semiconductor industry for nearly 30 years. Emerging technologies based on quantum confinement, nanomagnetism, molecular electronics, superconductivity, place increasingly stringent requirements on metrology, that encompass accurate measurements of dimensions, characterization of materials and reliable electrical performances of structures and devices.

Among the current nanomaterials, nanowires have attracted a lot of interests with the demonstration of numerous applications in various fields such as sensing (virus [1], gas [2]), optoelectronics (light detection [3], light emission [4]) and microelectronics [5]. Based on top-down [6] or bottom-up [7] approaches, nanowire devices can be made of different materials: molecules [8], metals [9], semiconductors [4] in any combination. They all have in common:

M. Berthe (✉) · C. Durand · T. Xu · J. P. Nys · P. Caroff · B. Grandidier
IEMN—UMR 8520, Avenue Poincaré, BP 60069, 59652 Villeneuve d'Ascq Cedex, France
e-mail: maxime.berthe@isen.fr

C. Joachim (ed.), *Atomic Scale Interconnection Machines*, Advances in Atom and Single Molecule Machines, DOI: 10.1007/978-3-642-28172-3_8,

- A nanoscale radius that makes it difficult to connect with conventional methods like technological processing and metal deposition.
- An electrical or thermal conduction that is governed by quantum confinement, correlation or surface effects, rather than the conductivity of the bulk materials.
- A high impedance that gives rise to parasitic effects when they are connected with micrometer-scale probes.

These properties preclude their accurate characterization, unless multi-physical analyzes can be performed in the same experimental system. A multiprobe scanning tunneling microscope (STM) that works under the supervision of a scanning electron microscope (SEM) in ultra-high vacuum (UHV) has a considerable potential, because structural analyzes can be simultaneously obtained with the electrical characterizations of a single nanowire. In principle, this instrument should be able to address key questions regarding the dependence of the transport measurements with the surface properties of the nanowire or its environment [1, 2]. Such a system exists at the Institute of Electronics, Microelectronics, and Nanotechnology (IEMN, France). Thanks to specific characteristics, that are described in the first section of this chapter, the instrument has the ability to probe the DC conductivity of semiconductor nanowires, with a precise knowledge of their surface structure, as shown in the second section of the chapter.

2 Instrumentation

The system installed at IEMN is called Nanoprobe (Omicron Nanotechnology GmbH), where particular attention has been drawn to precisely control the STM tips that are brought into contact with a nanostructure. The evolutive preparation chamber and the analysis chamber of the Nanoprobe make it ideal for the preparation and the study of semiconductor nanowires by SEM and STM.

2.1 The Scanning Electron Microscope

Thanks to its practical magnification range, SEM is traditionally used to localize nanoscale structures on macroscopic samples, and then to investigate their size, shape and more [10]. As the intensity of the secondary electrons collected in a SEM is very sensitive to the sample surface potential, the SEM also allows identifying regions consisting of different semiconductor materials or performing dopant profiling with semiconductor samples [11]. At best, the microscope can reach a resolution of the order of one nanometer, but in that case, it requires the highest focalization of the electron beam, corresponding to small working distances, typically 2 mm.

In the Nanoprobe, where four STM tips have to be brought in contact with a nanostructure, the bias tube of the Zeiss Gemini column is kept further from the sample. Typical working distances are between 12 and 15 mm. In addition,

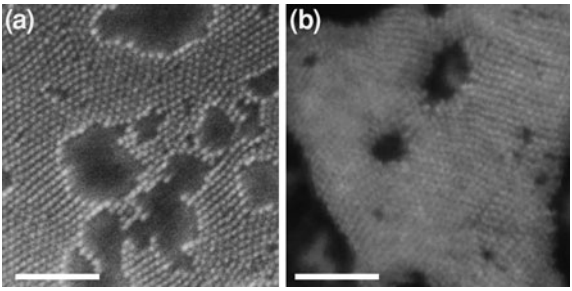

Fig. 1 SEM images of PbSe nanocrystals with a mean diameter of 8 nm, deposited on a SiO_2 surface by drop casting. **a** Image acquired with a regular Gemini SEM, at a working distance of 2.7 mm. **b** Image acquired with a UHV-Gemini SEM on the nanoprobe at a working distance of 14.6 mm. Scalebars: 100 nm

because the multiple STM stage has to be rigidly maintained to the SEM in order to avoid any resolution loss due to external vibrations, no tilt of the sample is allowed. As a result, SEM images are always acquired from the top of the sample.

In order to highlight the performance of the microscope, we compare, in Fig. 1, two images that were acquired with identical Carl Zeiss Gemini-based SEMs, the first corresponding to a conventional system and the second to the SEM of the Nanoprobe. The sample consists of a submonolayer of PbSe nanocrystals that have been deposited on a SiO_2 surface by drop casting. With the conventional SEM (Fig. 1a), the array of nanocrystals is clearly visible and each nanocrystal is well resolved. In that case the working distance was 2.7 mm and measurements of the mean size of the nanocrystal yield 8 nm, consistent with the nanocrystal diameter found by additional TEM characterization. When the sample is imaged in the Nanoprobe (Fig. 1b), the working distance was set at 14.6 mm. The SEM image is then slightly blurred in some regions, but the nanocrystals are still resolved. Such observation allows a statistical count of the nanocrystals and still gives relevant information on the morphology of the array.

Despite the lower resolution caused by the large working distance and the lack of sample tilt, the Nanoprobe has a double advantage over conventional SEMs:

- It is operated in a UHV environment that prevents the adsorption of carbon contaminants provided that the sample is clean.
- It is compatible with the operation of STM, that can acquire images of the sample down to the atomic resolution; the SEM being rather used as a localization tool.

2.2 Multiple Probe Scanning Tunneling Microscopes

The Nanoprobe contains four independent STM scanners. Due to the requirement to mechanically bind the SEM with the STM stage in order to keep the SEM resolution high enough, and the need for tips that must be long enough to be

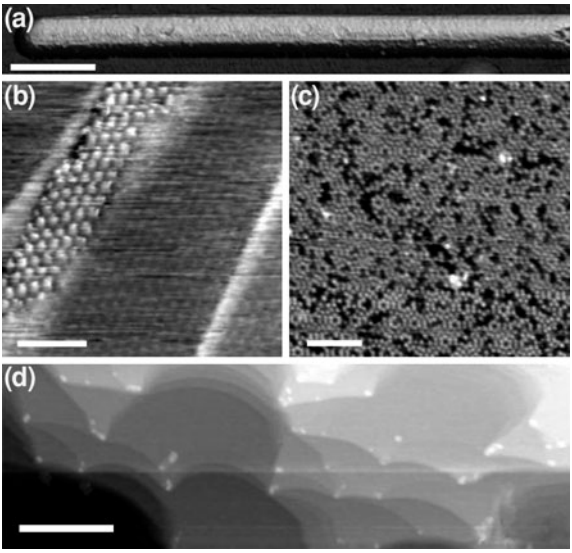

Fig. 2 **a** Large scale 3D STM image ($V = -470$ mV; $I = 3$ nA) of a InAs nanowire, scale bar: 200 nm. **b** STM image ($V = 80$ mV; $I = 115$ pA) of PbSe nanocrystals deposited on a graphite substrate, scale bar: 100 nm. **c** High resolution STM image ($V = 1.5$ V; $I = 400$ pA) of a Si(111)-(7 × 7) surface, scale bar: 2 nm. **d** Large scale STM image ($V = 2$ V; $I = 200$ pA) of a Si(111) surface, where atomic steps are clearly seen, scale bar: 500 nm. All images were acquired at $T = 295$ K, with the high resolution probe in (**a**), (**b**) and (**c**) and one of the three low resolution tips in (**d**)

positioned under the SEM, while the scanners are kept far away from the sample, the tunneling junctions usually suffer from a low vibration damping. In order to increase the stability of the STM tip, the tip length can be reduced by making the scanner more compact and closer to the sample stage. But, in the current configuration, only one of such scanners can be built due to space requirements. As a result, the Nanoprobe system hosts three "low resolution" STM tips, that are able to resolve atomic steps, and a "high resolution" STM tip, that images surfaces with the atomic resolution. Figure 2 shows a few examples of STM images acquired with the both types of scanners.

Figure 2a–c were recorded with the high resolution scanner. This scanner is capable of large scale imaging, like in Fig. 2a that shows an InAs nanowire. Its compactness also ensures a good stability of the tunneling junction. Indeed the tip does not seem to disrupt the array of PbSe nanocrystals, seen in Fig. 2b, when the tip scans over the array, damages that could happen for too strong vibration instabilities. Moreover, the tip is able to resolve the typical atomic reconstruction of the Si(111)-(7 × 7) surface, as shown in Fig. 2c. Conversely, Fig. 2d was acquired with the low resolution scanner. It shows a large scale STM image of a Si(111) surface. Although the external vibrations hinder the observation of the atomic resolution on the terraces, the scanner allows for a high vertical resolution showing single atomic step between adjacent terraces.

Thanks to this combination of high resolution STM and SEM, the localization and structural characterization of nanowires (Fig. 2a) becomes feasible. The small diameter of such structures is no more an obstacle and the STM tips may contact a nanostructure to be used as electrical probes. The combination of microscopy with the electrical measurement is a subject of prime importance that is described in the following section.

2.3 A Unique Control System

To take full advantage of the equipment, one needs to be able to simultaneously operate the SEM and all four STM tips. Moreover, the STM tips can work in two different modes, either in the tunneling regime, where they are used to observe a sample and to perform tunneling spectroscopic measurements, or in the contact regime, where they are used in a source/measure configuration to perform DC electrical measurements. Due to the complexity that can occur when multiple probes are operated at the same time by a single person, a powerful human–machine interface (HMI) that allows all types of experiments has to be built. For such purpose, the SPM control system consists of a Nanonis control system (SPECS-Zürich GmbH) that has been replicated four times.

In Fig. 3a, the blue, white and red boxes compose the four SPM units. They are connected to the STM current/voltage preamplifiers (Omicron SPM PRE 4E) on one side and to a master control PC running the user interface on the other side. Figure 3b gives an overview of this computer interface that allows handling any of the STM tips independently, with only one keyboard and one mouse: one operator can monitor and program all the STM parameters without switching constantly to another system. Thanks to the multiple hardware units, it is therefore possible to run four feedback loops to acquire up to four STM images at the same time. Synchronization and recording of the analog and digital signals coming from the different control units can easily be done by software or by hands through the front panel of the controller (Fig. 3a).

As measurements of the conductivity of a nanostructure require to bring the tips into contact, each feedback loop has to be disabled and such a condition is achieved by placing between each high-gain transimpedance preamplifier and the UHV electrical feedthroughs a switch unit (Omicron CSW4-G), that is software-controlled. The switch unit provides an alternative output to the system that can be connected to other preamplifiers, voltage or current sources, electrical measurement devices, function generators, etc. In order to measure the resistivity of a nanostructure using a four point probe method, a software interface has been designed to control the low current Source Measure Units (Keithley 2636) that are shown in Fig. 3c. These units are used for simple biasing (Fig. 3d) and for DC electrical measurements with a specified number of probes in any combination (Fig. 3e).

The software control of the switch units allows opening the feedback loop once the tip has been positioned in a region of interest on the sample thanks to the SEM

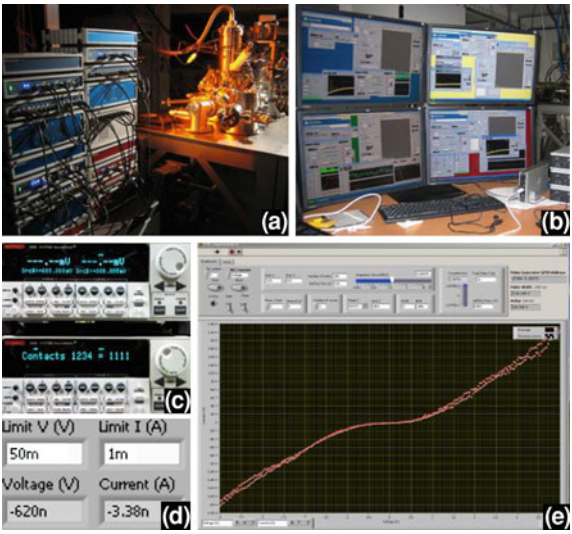

Fig. 3 Pictures of the nanoprobe control system for scanning tunneling microscopy and transport measurements. **a** Quadruple Nanonis SPM control system for independently operating each probe; **b** controller interface with four screens, one keyboard and one mouse allowing one operator to control the whole system; **c** switchbox-controlled source measure units (KEITHLEY 2636) for low current transport measurements; **d** zoom on the computer interface for the SMU. It is possible to directly set and read the current and voltage for simple biasing; **e** Transport measurement interface

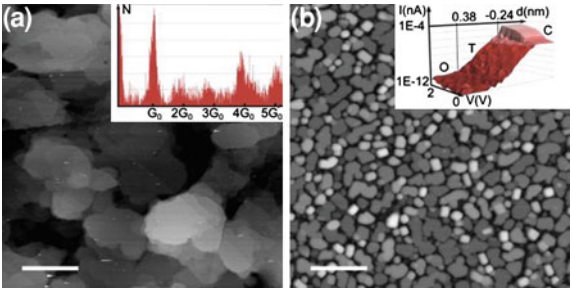

Fig. 4 Examples of the behavior of the STM tip while approaching/retracting from a surface. **a** STM image of a Au(111) surface (scalebar: 400 nm) and graph displaying the quantum steps of conductance while retracting the tip from the surface after gentle approach. **b** STM image of Al nanodots on silicon (scalebar: 40 nm) and I(Z, V) graph (logarithmic vertical scale) showing the different electronic regimes as a function of the distance: open circuit (O), tunneling (T) and contact (C)

and/or the STM. Since the thickness of the investigated nanostructure is quite small (sometimes smaller than a few nanometers), great care must be taken to bring the tip in contact while the feedback loop is opened. As a result, the current intensity is monitored through the SMUs when the tip is approached toward the sample. Figure 4a and b show examples of such manipulations performed with a

single probe and different samples, that demonstrates the precision of the tip displacement to reach the electrical contact.

In Fig. 4a, a Au(111) surface was first imaged with STM. The tip was immobilized on a flat terrace and the feedback loop open. Then the current was derivated to another amplifier with a lower gain (Keithley 428) and series of approach-retract curves were performed. While approach curves (not displayed) only show an exponential increase of the current followed by a saturation when the contact is established, retracting the tip reveals sharp jumps associated to atomic-size channels of conductance breaking one after the other [12]. The graph displayed in Fig. 4a corresponds to the statistical plot of the value of the conductance that was measured. The equidistant peaks materialize the occurrence of transport through multiples of the quantum of conductance. After the experiment, the signal was switched back to the tunnel mode.

In Fig. 4b, Al dots were grown on a Si(111) surface [13]. The tip was immobilized over a single dot and the signal switched to a low current SMU (Keithley 2636) to record the different regimes of conductance as a function of the distance between tip and sample. The graph (vertical logarithmic scale) reports three regimes depending on the tip-sample distance:

- At large distances, when the tip is retracted from the sample, no current flows: $I = 1E - 12$ A for $d = +1$ nm to +0.38 nm, for any value of the voltage V.
- At smaller distances (0.38 nm $> d > -0.24$ nm), the tunnel regime is revealed by a straight line on the logarithmic scale, implying that the current varies exponentially as a function of the tip-sample distance [14].
- For short tip-sample distance ($d < -0.24$ nm), the current reaches saturation, corresponding to a contact regime. In this regime, if the tip-sample distance is kept constant, a rectifier-shaped I(V) curve is measured when the bias varies. This behavior is caused by the formation of the Schottky barrier between the Si surface and the Al dot.

Such results demonstrate the potential of every probe with both spatial and electrical precision. They can also be combined for manipulation and contact of nanowires as described in the next section.

3 Contacting Single Semiconductor Nanowires and Measuring Their Conductance

Intensive research activities focus on the fabrication and characterization of one-dimensional (1D) nanostructures because the anisotropy of (1D) systems provides unique properties and phases to the materials. For example, they should exhibit density of states singularities and allow to carry either spin or charges [15, 16]. In addition, they are expected to play an important role as both interconnects [17] and functional units in electronic devices [18, 19]. Concomitant with the emergence

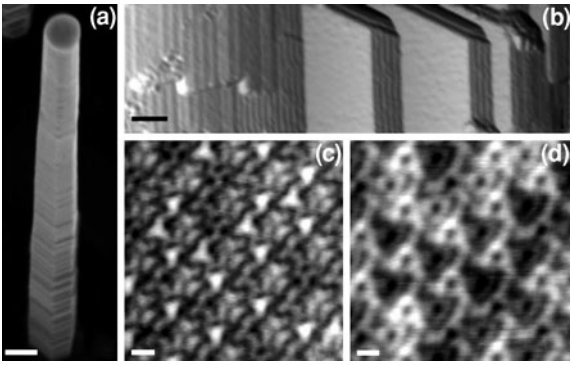

Fig. 5 SEM images of different structures based on nanowires contacted with the nanoprobe: **a** MEMS resonator involving a Si beam; **b** Si nanowire deposited on a SiO_2 surface and contacted with two tips; **c** freestanding InAs nanowires contacted with four tips; **d** Si nanowire lifted from the substrate and connected with four tips. (**a**) scalebar: 100 μm; (**b**), (**c**), (**d**) scalebar: 1 μm

of such nanostructures are the practical challenges for their efficient location/registration and their contact to electrodes.

Figure 5 illustrates how the multiprobe scanning tunneling microscope under the operation of the SEM allows the arbitray arrangement of the probe electrodes onto (a) a MEMS structure containing a single vibrating silicon beam or directly onto a single nanowire, that is either (b) deposited on a substrate, (c) standing free upward on a substrate or (d) fully suspended between the four STM tips. As the studies of the nanowire conductivity requires precise control over the nanowire surface structure and its environment to accurately determine the contribution of the surface to the electronic transport, new methods for the surface preparation of 1D nanostructrures are highly desirable. Indeed, removal of the oxyde layer that usually covers the surface of semiconductor nanowires and W tips is of particular importance in order to achieve a good electrical contact. As an example, Fig. 6a shows the SEM image of an upward Si nanowire grown by chemical vapor deposition along the ⟨111⟩ direction. Before the cleavage of the nanowire, for its observation by STM, the initial sample is briefly heated in UHV around 800°C to desorb the thin oxide layer. The SEM ensures that heating does not change the overall morphology of the nanowire. Then STM provides a direct observation of the facet orientations on the Si nanowire ⟨112⟩-oriented sidewalls (Fig. 6b), as well as the atomic reconstructions of the different facets. In the case of the (111) facets, a typical 6×6 phase, that appears to be voltage dependent (Fig. 6c and d), are obtained and demonstrates the presence of Au due its diffusion from the Au seed particle, seen on top of the wire in Fig. 6a [20].

Careful procedures are also required to ensure that the sidewalls of III–V semiconductor nanowires are oxide-free; the nanowires illustrated here were grown at IEMN under UHV by molecular beam epitaxy, see [21] for growth details. If successful, then the I(V) curves measured between a single tip and an InAsSb nanowire in contact with the Si(111) substrate, that is held at ground, has an ohmic behavior. Thanks to the precision of the STM scanners, four tips can be

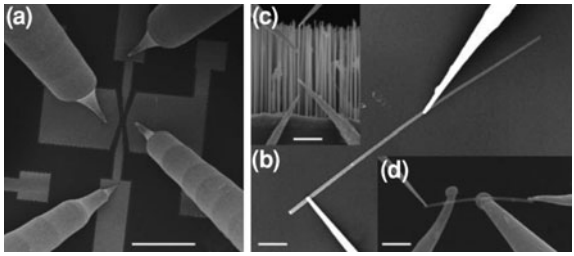

Fig. 6 **a** SEM image of a Si nanowire grown in the [111] direction from a gold island that was synthesized on a Si(111) surface. Scalebar: 200 nm; **b** large scale STM image of the surface of a silicon nanowire deposited on a silicon substrate. The average diameter of the nanowire is 120 nm. Scalebar: 10 nm, Vbias = + 2.0 V, Itunnel = 100 pA; (**c**) and (**d**) atomic resolution filled and empty state images of a (111) facet of a Si nanowire showing a 6 × 6 phase. Scalebar: 1 nm. (**c**) Vbias = −1.3 V, Itunnel = 100 pA; (**d**) Vbias = 1.3 V, Itunnel = 100 pA

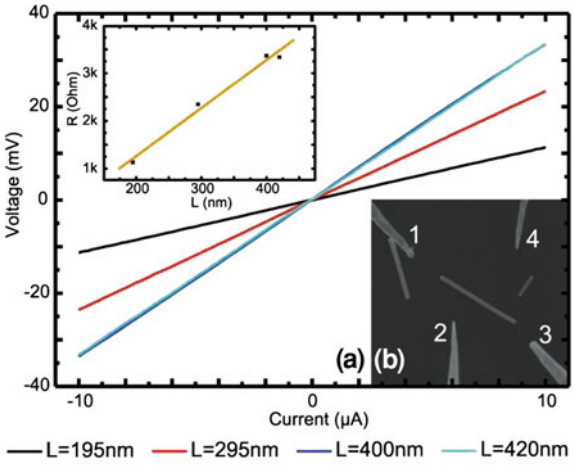

Fig. 7 **a** V–I curves measured as a function of the inter-probe distance measured by the collinear four-probe method on an $InAs_{0.95}Sb_{0.05}$ nanowire. Inset: plot of the resistance values compared to the inter-probe distance; **b** SEM image of the four probes, labeled 1–4, ready to be connected to a nanowire deposited on a Si(111) substrate. The inter-probe distance will be measured between the two inner probes (2 and 4)

brought into electrical contacts with an InAsSb nanowire such as the one visible in the center of the SEM image of Fig. 7a. Tips 1 and 3 are connected, respectively, to the gold catalyst and to the base of the wire and used as source and drain electrodes for driving the current through the wire. Tips 2 and 4 are the potential probes. When a current is passed through the wire, the potential drop measured between the inner probes is found to be linearly proportional to the current intensity as shown in Fig. 7b. The gradient of the curves yields the resistance of

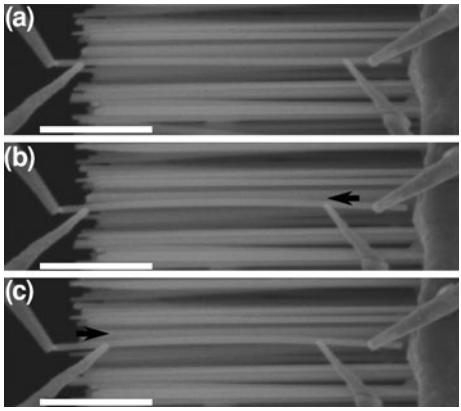

Fig. 8 SEM images of a single InAs nanowire, that has been detached from the substrate and is fully suspended between four tips. While the outer tips are always in mechanical contact with the nanowire, the inner tips are moved along the nanowire between successive transport measurements. The lateral shift of the inner STM tips is achieved thanks to the precise control of the system in tip-positioning. Scalebars: 1 μm

the nanowires for a given separation between the inner probes. By changing the position of the tips 2 and 4, a set of $V(I)$ characteristics were acquired for different separations between the inner probes. From these $V(I)$ curves, we obtain the resistance R_{NW} that is found to linearly increase with the tip separation L, as shown in the inset of Fig. 7b. The slope yields a resistance per unit length R_{NW}/L of 7.6 kΩ/μm for an $InAs_{0.95}Sb_{0.05}$ nanowire with a diameter of 100 nm.

In order to separate the surface effects from geometrical considerations, the nanowires can also be characterized in a free-standing position as shown in Fig. 8, where an InAs nanowire has been directly contacted on its original substrate. After an electrical contact has been made with the tip located at the bottom of the nanowire, a gentle manipulation can be exerted to detach it from the substrate. Such configuration allows performing transport measurements with a nanowire fully suspended that can also be bent to characterize its transport properties under mechanical strain (Fig. 8b and c).

4 Conclusion

We have shown that Scanning Electron Microscopy, Scanning Tunneling Microscopy and four point DC electrical measurements can be combined in a unique platform in UHV to study the structural and electrical properties of nanostructures. To reach that scheme, the control system is a key component of the instrument for the successful localization of nanometer-sized objects like single semiconductor nanowire and the characterization of their atomic scale topography and nanoscale electrical properties.

Compared to the commonly used methods for contacting single nanostructures, the measurements performed with the Nanoprobe allow faster and cheaper characterization of nanometer-sized electronic devices. Moreover, the absence of air exposure between measurements and the UHV chamber provide the best controlled atmosphere for characterization.

This technique not only gives the opportunity of a full characterization of nanostructures, but the four tips may be thought as manipulators for controlled strain characterization or direct assembly of nanosized blocks.

References

1. Cui, Y., Wei, Q., Park, H., Lieber, C.M.: Nanowire nanosensors for highly sensitive and selective detection of biological and chemical species. Science **293**, 1289–1292 (2001)
2. Wan, Q., Li, Q.H., Chen, Y.J., Wang, T.H., He, X.L., Li, J.P., Lin, C.L.: Fabrication and ethanol sensing characteristics of ZnO nanowire gas sensors. Appl. Phys. Lett. **84**, 3654–3656 (2004)
3. Wang, J., Gudiksen, M.S., Duan, X., Cui, Y., Lieber, C.M.: Highly polarized photoluminescence and photodetection from single indium phosphide nanowires. Science **293**, 1455–1457 (2001)
4. Haraguchi, K., Katsuyama, T., Hiruma, K., Ogawa, K.: GaAs pn junction formed in quantum wire crystals. Appl. Phys. Lett. **60**, 745–747 (1992)
5. Cui, Y., Lieber, C.M.: Functional nanoscale electronic devices assembled using silicon nanowire building blocks. Science **291**, 851–853 (2001)
6. Stern, E., Klemic, J.F., Routenberg, D.A., Wyrembak, P.N., Turner-Evans, D.B., Hamilton, A.D., LaVan, D.A., Fahmy, T.M., Reed, M.A.: Label-free immunodetection with CMOS-compatible semiconducting nanowires. Nature **445**, 519–522 (2007)
7. Minot, E.D., Kelkensberg, F., van Kouwen, M., van Dam, J.A., Kouwenhoven, L.P., Zwiller, V., Borgström, M.T., Wunnicke, O., Verheijen, M.A., Bakkers, E.P.A.M.: Single quantum dot nanowire LEDs. Nano Lett. **7**, 367–371 (2007)
8. Tans, S.J., Verschueren, A.R.M., Dekker, C.: Room-temperature transistor based on a single carbon nanotube. Nature **393**, 49–52 (1998)
9. Dobrev, D., Vetter, J., Angert, N., Neumann, R.: Electrochemical growth of copper single crystals in pores of polymer ion-track membranes. Appl. Phys. A Mater. **69**, 233–237 (1999)
10. Zhou, W., Wang, Z.L.: Scanning Microscopy for Nanotechnology, Techniques and Applications. Springer, New York (2007)
11. Elliott, S.L., Broom, R.F., Humphreys, C.J.: Dopant profiling with the scanning electron microscope: a study of Si. J. Appl. Phys. **91**, 9116–9122 (2002)
12. Olesen, L., Laegsgaard, E., Stensgaard, I., Besenbacher, F., Schiøtz, J., Stoltze, P., Jacobsen, K.W., Nørskov, J.K.: Quantized conductance in an atom-sized point contact. Phys. Rev. Lett. **72**, 2251–2254 (1994)
13. Liu, H., Zhang, Y., Wang, D., Pan, M., Jia, J., Xue, Q.: Two-dimensional growth of Al films on Si(111)-7 $\times$ 7 at low-temperature. Surf. Sci. **571**, 5–11 (2004)
14. Binnig, G., Rohrer, H., Gerber, C., Weibel, E.: Tunneling through a controllable vacuum gap. Appl. Phys. Lett. **40**, 178–180 (1982)
15. Wildöer, J.W.G., Venema, L.C., Rinzler, A.G., Smalley, R.E., Dekker, C.: Electronic structure of atomically resolved carbon nanotubes. Nature **391**, 59–62 (1998)
16. Auslaender, O.M., Steinberg, H., Yacoby, A., Tserkovnyak, Y., Halperin, B.I., Baldwin, K.W., Pfeiffer, L.N., West, K.W.: Spin-charge separation and localization in one dimension. Science **308**, 88 (2005)

17. Dong, L., Bush, J., Chirayos, V., Solanki, R., Jiao, J., Ono, Y., Conley Jr, J.F., Ulrich, B.D.: Dielectrophoretically controlled fabrication of single-crystal nickel silicide nanowire interconnects. Nano Lett. **5**, 2112 (2005)
18. Patolsky, F., Lieber, C.M.: Nanowire nanosensors. Mater. Today **8**, 20 (2005)
19. Thelander, C., Agarwal, P., Brongersma, S., Eymery, J., Feiner, L.F., Forchel, A., Scheffler, M., Riess, W., Ohlsson, B.J., Gösele, U., Samuelson, L.: Nanowire-based one-dimensional electronics. Mater. Today **9**, 28 (2006)
20. Xu, T., Nys, J.P., Addad, A., Lebedev, O.I., Urbieta, A., Salhi, B., Berthe, M., Grandidier, B., Stiévenard, D.: Faceted sidewalls of silicon nanowires: Au-induced structural reconstructions and electronic properties. Phys. Rev. B **81**, 115403 (2010)
21. Thelander, C., Caroff, P., Plissard, S., Dey, A., Dick, K.: Effects of crystal phase mixing on the electrical properties of InAs nanowires. Nano Lett. **11**, 2424–2429 (2011)

Probing Electronic Transport of Individual Nanostructures with Atomic Precision

Shengyong Qin and An-Ping Li

Abstract Accessing individual nanostructures with atomic precision is an important process in the bottom-up fabrication and characterization of electronic nanodevices. Local electrical contacts, namely nanoelectrodes, are often fabricated by using top-down lithography and chemical etching techniques. These processes however lack atomic precision and introduce the possibility of contamination. Here, we review recent reports on the application of a field-induced emission process in the fabrication of local contacts onto individual nanowires and nanotubes with atomic spatial precision. In this method, gold nanoislands are deposited onto nanostructures precisely by using a scanning tunneling microscope tip, which provides a clean and controllable process to ensure both electrically conductive and mechanically reliable contacts. The applicability of the technique has been demonstrated in a wide variety of nanostructures, including silicide atomic wires, carbon nanotubes, and copper nanowires. These local contacts bridge the nanostructures and the transport probes, allowing for the measurements of both electrical transport and scanning tunneling microscopy on the same nanostructures in situ. The direct correlation between electronic and transport properties and atomic structures can be explored on individual nanostructures at the unprecedented atomic level.

Keywords Electronic transport · Nanowire · Nanotube · Atomic wire · Nano contact · Four probe measurement · Scanning tunneling microscope

S. Qin · A.-P. Li (✉)
Oak Ridge National Laboratory, Center for Nanophase Materials Sciences,
Oak Ridge TN 37831, USA
e-mail: apli@ornl.gov

C. Joachim (ed.), *Atomic Scale Interconnection Machines*, Advances in Atom and Single Molecule Machines, DOI: 10.1007/978-3-642-28172-3_9,

1 Introduction

A major challenge in nanoscience and nanotechnology is electrical interfacing of individual nanoobjects to the macroscopic world. The reliable methods of accessing individual nanoobjects electrically are demanded in testing their electronic properties with nanoscopic to atomic positioning precision. Many nanofabrication processes have been developed using a range of self-assembly and nanomanipulation methods, which enabled the creation of organized structures composed of individual nanoobjects such as nanowires, nanotubes, nanodots, nanorods, and nanoribbons with the size down to a few nanometers [1–6]. The feature sizes of these nanoobjects are often orders of magnitude smaller than conventional electronic probes. A key challenge for contacting these nanoobjects is the formation of local electrical contacts whose size can be tailored and the location can be controlled to create the desired link to mesoscopic transport probes.

To address this great challenge, many groups have developed contacting methods suitable for individual nanoobjects. Those methods include e-beam lithography, ion beam deposition of material [7], direct deposition from organometallic gases, [8] local crystallization or melting of amorphous materials, and scanning probe microscopy-based surface modification techniques [9]. Successful local oxidation and metal deposition from tips in close proximity with the surface of a nanostructure has been performed by using either a scanning tunneling microscope (STM) or an atomic force microscope (AFM). Here we focus on the recent reports on utilizing a field-induced material transfer method to fabricate nanocontacts with STM probes. This method promises formation of electrically conducting junctions, with inherent cleanliness, flexibility, and high spatial precision. In particular, this contacting method has enabled the measurements of both the electron transport behavior and local structural and electronic properties of a variety of nanostructures with a four probe STM in situ [10–12].

2 Formation of Gold Nanocontacts with Atomic Resolution

Experiments of fabricating nanocontact can be performed with either an STM or an AFM. A field-induced material transfer process, first reported by Mamin, Guethner, and Rugar, [13] was used. Since then, reproducible formations for gold nanodot with STM and AFM have been reported by a number of research groups [14–18]. And the application of this method in fabricating electrical contacts that can bridge nanoscopic structures and mesoscopic transport electrodes has been demonstrated recently [10, 11].

The fabrication process of nanocontacts by the field emission process is illustrated in the schematic of Fig. 1. Sharp tungsten tips coated with gold can be used to map out the size and location of nanostructures ($GdSi_2$ nanowires on Si(100) in

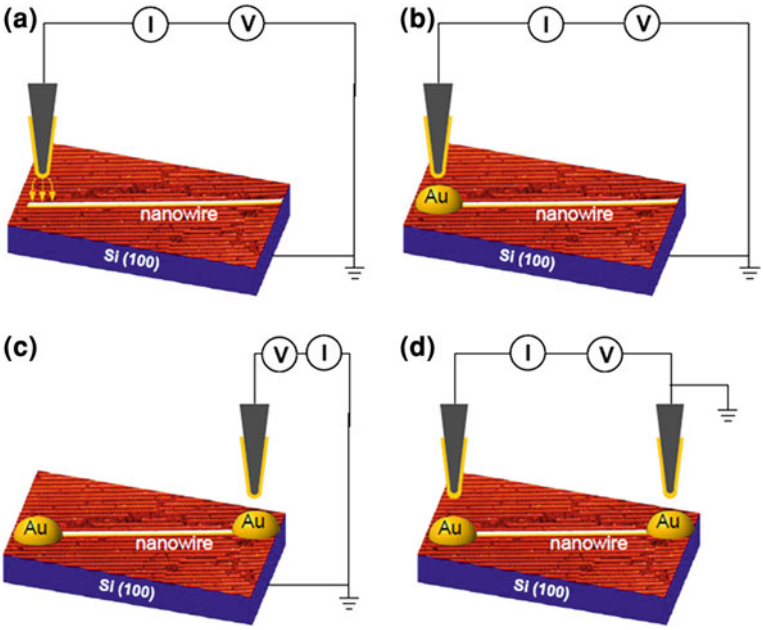

Fig. 1 Schematic of the nanocontact fabrication and transport measurement procedures. **a** The Au-coated STM tip is held above one end of $GdSi_2$ nanowire with a voltage applied between tip and sample. A $GdSi_2$ nanowire is shown on a Si(100)-Gd 2×7 surface with a STM image size of 77×48 nm^2. **b** Au atom emission occurs by bringing the tip close to the sample till the current reaches 100 nA. **c** Au-coated tip is moved to the other end of the nanowire in STM scanning mode and then the feedback is switched off and atom emission occurs by bringing the tip close to the sample. **d** Transport measurement along the $GdSi_2$ nanowire made by contacting two probes using the nanocontacts. (Adapted from [10])

this case) by STM topography imaging. After locating the nanowire, the STM tip is positioned about 200 nm above the end of the $GdSi_2$ nanowire. The STM controller feedback is then disabled, and the tip is slowly lowered toward the nanowire surface with a -15 V bias applied to the tip with respect to the sample. When the tip-sample distance is close enough, the tunneling current suddenly jumps to above ~ 100 nA, which usually happens at a thresh-old field of ~ 3.5 V/Å. The current pulse leads to the formation of an Au nanocontact with size of 50–200 nm in diameter onto the end of the nanowire via a field-induced atomic emission process. The precision of contact location can be controlled down to the atomic scale, depending on the STM lateral spatial resolution.

This process can be repeated multiple times on different locations of the nanowire to create multiple local contacts. The local contacts are large enough to identify under conventional scanning electron microscope (SEM) or even some optical microscope. In our setup, the deposited Au nanocontacts are then contacted by two STM tips guided by a SEM integrated in the four probe STM system for electrical characterizations [12].

The physical mechanisms of dot formation in this process have been studied by many groups [10, 13, 18–20]. Two basic models have been widely discussed, with one involving direct contact between the tip and the sample due to Joule heating and thermal expansion [20], and the second involving field evaporation [13, 19]. It was shown that both these processes can create well-defined nanodots of metal [18]. In the field-evaporated material transfer process, positive gold ions are transferred in the direction of the electric field. At the same time, material can also be transferred due to direct tip-substrate contact. The direction of this mechanical contact transfer is determined by materials and geometry of the involved sample and tip, which can then create either mounts or pits on the sample surface.

3 Application of Nanocontacting Technique in Electron Transport

3.1 Fabrication of Nanocontacts on $GdSi_2$ Nanowires

This nanocontacting technique was first applied to the formation of local contacts on a $GdSi_2$ nanowire. And the measurement of its electrical conductivity was performed by using the local contacts in situ in a multi-probe STM system. $GdSi_2$ nanowires were grown on the Si(100) 2 × 1 surface by depositing Gd at 600°C with a deposition rate of 0.1–0.2 ml/min [11, 21, 22]. The growth of $GdSi_2$ on Si(100) 2 × 1 proceeds with the formation of a wetting layer, followed by the growth of well-ordered and uniformly-oriented array of $GdSi_2$ nanowires. Figure 2b shows an STM image with two nanowires separated by a Si(100)-Gd 2 × 7 surface layer insulating on Si. The anisotropic growth can be rationalized by considering the asymmetric lattice mismatches in the two orthogonal crystallographic directions of the $GdSi_2$ and Si: the lattice mismatch in the $[0001]_{GdSi_2}/[1\bar{1}0]_{Si}$ direction is +8.6% and in the $[11[11\bar{2}0]_{GdSi_2}/[110]_{Si}$ direction is +0.8%, thus giving rise to the nanowire growth direction of along $[110]_{Si}$. The narrowest nanowire has a width of 1.7 nm and a height of 4 Å, as shown in Fig. 2c. The length of the nanowires can be up to several micrometers, as shown in Fig. 2a. Clearly, the width of these $GdSi_2$ nanowires is beyond the spatial resolution of conventional transport measurement technique.

By using the filed-emission nanocontacting method, we have fabricated Au nanoislands on both ends of the $GdSi_2$ nanowires. The Au nanoislands can be seen with SEM and thus can serve as electrical terminals for in situ transport measurements. Figure 2d shows an SEM image of a $GdSi_2$ nanowire with two Au nanocontacts. Two STM tips were then brought into contact with the nanoislands under SEM for transport measurements of the $GdSi_2$ nanowire in situ. Figure 2e shows the transport I(V) curve measured along a $GdSi_2$ nanowire with a size of 6.55 nm × 0.4 nm × 0.79 μm. At a temperature of 60 K, the wires have linear I(V) characteristics. This indicates that the Au/$GdSi_2$ contact is ohmic and that the

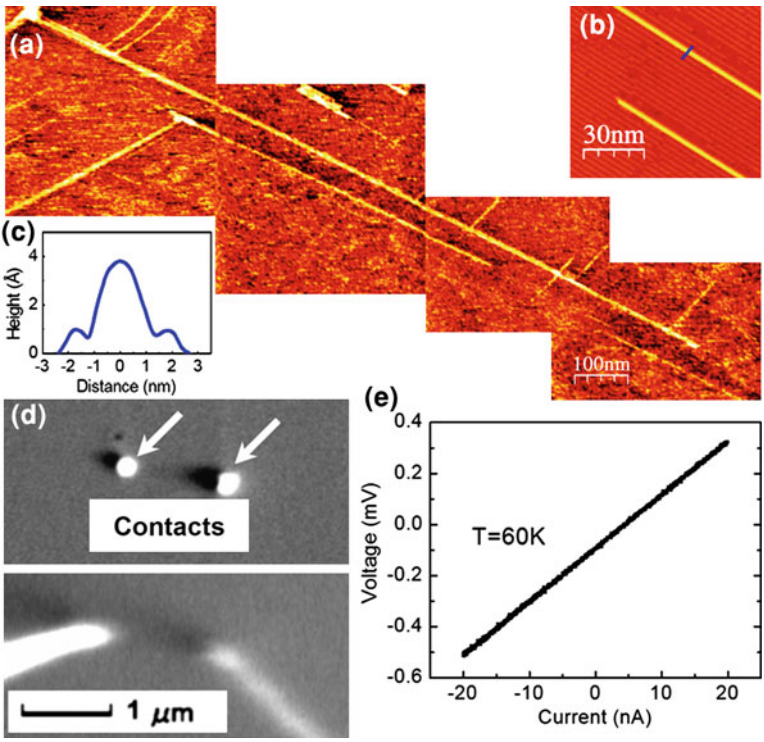

Fig. 2 **a** A series of STM images showing a $GdSi_2$ nanowire with length of 1.2 μm. **b** High resolution STM image of a narrow $GdSi_2$ nanowire. **c** Cross-sectional line profile showing the dimensions of a narrow nanowire. **d** SEM images showing Au nanocontacts on a $GdSi_2$ nanowire (*top panel*) and STM probes on Au nanocontacts (*bottom panel*). The $GdSi_2$ nanowire could not be resolved in the SEM. **e** I(V) curve of $GdSi_2$ nanowire at T = 60 K. (Adapted from [10])

wires themselves have metallic conductance. The resistivity of the $GdSi_2$ nanowire at 60 K is calculated to be 6.9 μΩ cm based on the nanowire dimensions.

Besides direct measurement of the electrical transport on NWs of only a few nm wide, this local contact provides us an unprecedentedly opportunity to study the correlation between the transport and local structures down to the atomic scale by performing both STM and nanotransport measurements on the same nanowires. In the following, we summarize the reports [11] on the effects of atomic defects and interwire coupling on the transport properties of self-assembled $GdSi_2$ nanowires.

3.2 Direct Measurements of Transport Properties of $GdSi_2$

The formation of both "isolated" nanowires and bundles of two or more $GdSi_2$ nanowires with atomic spacing provides the opportunity to study the effects of interwire coupling on the Si(100) surface. The representative STM images of a

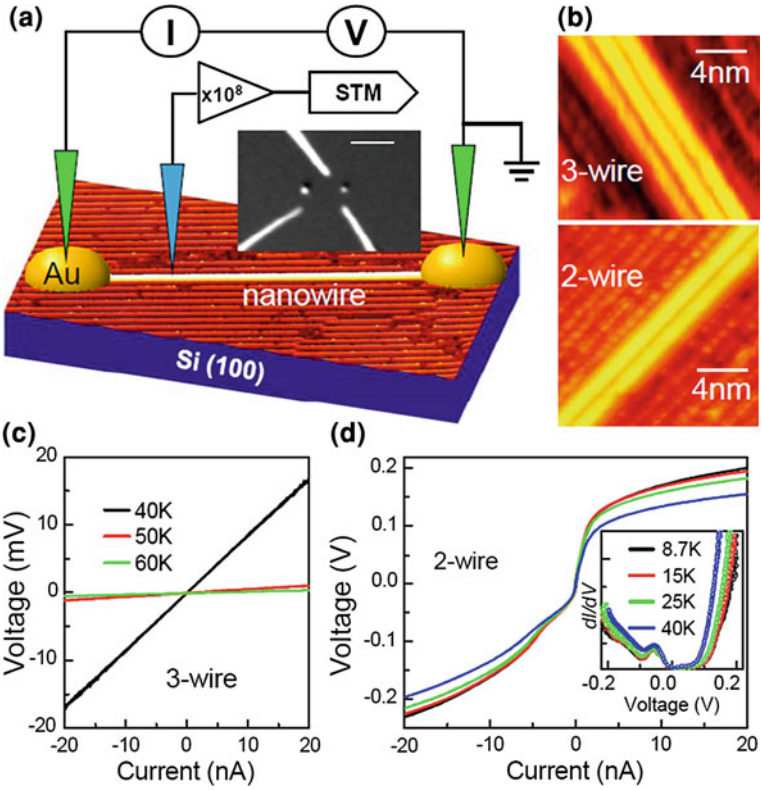

Fig. 3 Electrical conductance of individual $GdSi_2$ nanowires from nano-transport measurements. **a** Schematic illustration of the measurement configurations for in situ electrical transport and local density of states on a single nanowire. Inset: SEM image of local Au contacts and Au-coated STM tip above a $GdSi_2$ nanowire. Scale bar: 1 μm. **b** STM images of 2- and 3-wire bundles. **c** Transport I(V) curves for a 3-wire bundle. **d** Transport I(V) curves for a 2-wire bundle. Insets: numerical transport dI/dV of the 2-wire bundle. (Adapted from [11])

single nanowire and two- or three-wire bundles are shown in Figs. 3a and b. Here, the above fabrication method was utilized to deposit gold nanoislands in situ as local electrical contacts on nanowires.

Single and bundled $GdSi_2$ nanowires display dramatically different transport characteristics. At room temperature, both the single wires and wire bundles exhibit linear I(V) in transport measurements, indicative of a metallic conductance and the Ohmic nature of the Au/$GdSi_2$ contacts. At lower temperatures, below 50 K, the linear I(V) behavior and the metallic conductance only persist for nanowire bundles that consist of three or more nanowires, as shown in Fig. 3c for a three-wire bundle. In contrast, I(V) curves of single nanowire and two-wire bundle become nonlinear at low temperatures. As an example, the numerical dI/dV curves of a two-wire bundle in Fig. 3d display a clear conductance gap of $\sim$95 mV,

indicating an insulating state at low temperature. A metal–insulator transition is confirmed by measurements of nanowire resistance as a function of temperature, which reveal a MIT in a two-wire bundle at about 50 K. To rule out the possible role of substrate conductance, we measured the transport I(V) curves on the (2 × 7) reconstructed Gd/Si(001) surface without a nanowire. We find that the surface layer is insulating with a resistance that is in an order of magnitude higher than that of the nanowires. Consequently, the substrate conductance is negligible and does not affect our measurements of the wire transport.

3.3 Correlations Between Transport and Local Density of States

STS measurements on single and bundle nanowires at 80 and 6 K are shown in Figs. 4a and b, respectively. At 80 K, both single and bundle nanowires show finite DOS near the Fermi level (E_F), confirming their metallic nature. At 6 K, the DOS of a single nanowire shows a small gap, consistent with the transport (Fig. 3d) results. The DOS of a bundled wire however remains finite near E_F at 6 K, confirming the previous ARPES reports for the bundle wires [23]. At both temperatures, the DOS in the middle of the bundle wire is significantly higher than that at the edge. To better understand the origin of the MIT for a single nanowire, we map the spatial distributions of STS along the single nanowire in the inset of Fig. 4b, which shows an n-type band structure. Strong spatial variations of the pseudo-band gap can be found in the defect regions as highlighted by the blue color. We find larger modifications at band edges and wider band gap near defects, as marked with white vertical dash lines in the inset of Fig. 4b. It is clear that a single $GdSi_2$ nanowire has a strongly disordered energy band at low temperature, which is also confirmed by DFT calculations. The evolution from semiconducting single nanowire and relatively conducting wire bundle at the edge, to the robust metallic state in the middle of a wire bundle is well correlated with the interwire coupling-induced suppressions of adatoms and superstructures. For a wire bundle consisting of only two wires, the interwire coupling is overwhelmed by the edge states, and metallic states are only stable when three or more wires are coupled.

3.4 Application of Nanocontracting in Cu Nanowires

In this experiment, the Cu nanowires were grown with an electroplating method and then dispersed onto SiO_2/Si substrate. The Cu nanowires have typical dimensions of 65 nm in diameter and 2–4 μm in length. The study of electrical properties of Cu wires has largely been driven by its extensive application in

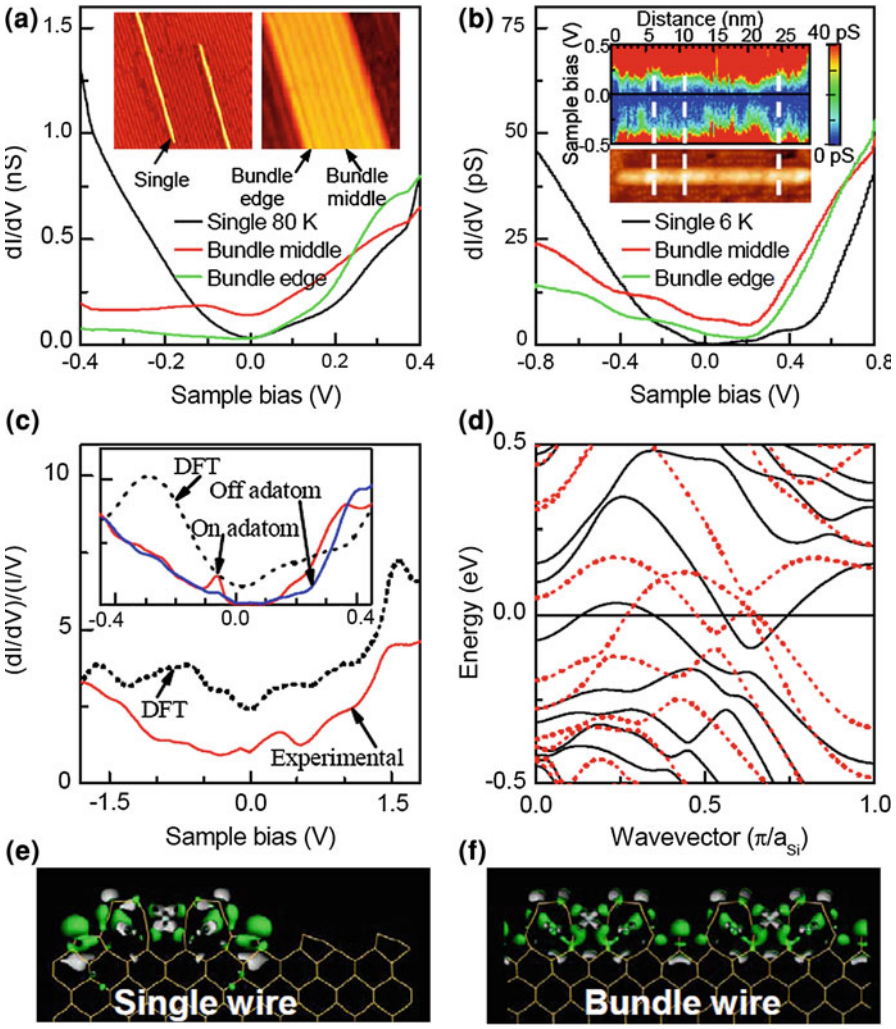

Fig. 4 Electronic structure of single nanowire and wire bundle from STS and DFT. **a** dI/dV spectra at 80 K on $GdSi_2$ single nanowire (*black*), bundle center (*red*), and bundle edge (*green*). Inset: STM images of the single wire and bundle wire. **b** dI/dV spectra at 6 K on $GdSi_2$ single nanowire (*black*), bundle center (*red*), and bundle edge (*green*). Insets: the spatial variations of dI/dV spectra as a function of energy along a single nanowire. White dashed lines mark the locations of adatoms. **c** Comparison of the measured (dI/dV)/(I/V) spectrum at 10 K and the calculated DOS projected to a region 3 Å above the bundle wire. Inset: (dI/dV)/(I/V) spectra of a single wire measured at 10 K on an adatom and 2 nm away from the adatom defect, and the calculated DOS without adatoms. **d** Calculated band diagram of $GdSi_2$ single wire along the wire (Γ-X) for majority (*solid black*) and minority spins (*dashed red*). **e** Cross-sectional view of the calculated wave function distributions for states around the Fermi level of single, and **f** for bundle nanowires. *Green* and *gray* represent outer and inner sides of the isosurfaces. (Adapted from [11])

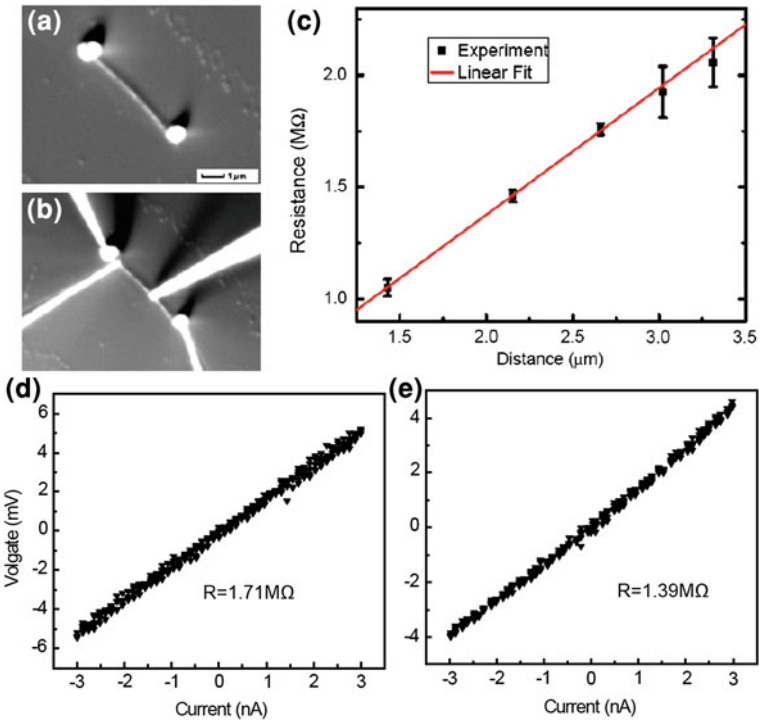

Fig. 5 **a** SEM image of a Cu nanowire with Au nanocontacts made at the ends. **b** SEM image of four probe transport measurement with movable inner probes. **c** Resistance of Cu nanowire as function of probe spacing. **d** and **e**, Two and four-point measurements of the resistance of the same Cu nanowire, respectively. (Adapted from [10])

microelectronics. Cu is the current choice of the interconnect metal in integrated circuits due to its higher electrical conductivity and improved electromigration reliability in comparison with aluminum. However, as the interconnect width narrows, and especially when the interconnect width is approaching a mean free path of the conduction electrons ($\sim$40 nm at 300 K for copper), the resistance of copper interconnects increases dramatically. Therefore, there has been an intense research interest in characterizing the electrical conductance of Cu nanowires [24]. Figure 5a shows SEM image of a Cu nanowire with nanocontacts made at both ends. In order to eliminate the contact resistance and minimize measurement errors, a four-point measurement was also employed at different inner-probe spacing (Fig. 5b). The resistance versus inner probe distance was plotted in Fig. 5c as a function of probe spacing. The slope of the resistance-probe spacing curve provides accurate measure of the linear resistivity of the nanowire. The resistivity of the Cu nanowire was then calculated based on the nanowire dimensions (diameter $\sim$63 nm) to be 0.0563 Ω cm. The much larger resistivity of Cu nanowire in comparison with that of pure metal is due to the surface oxide layer of Cu

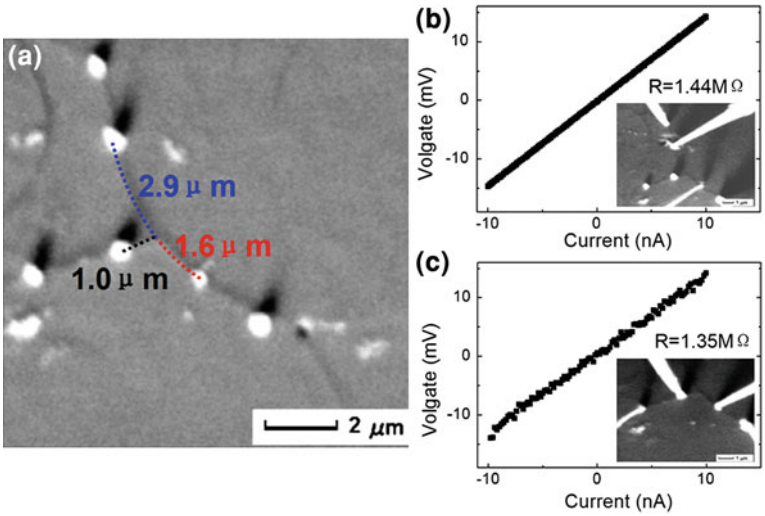

Fig. 6 **a** SEM image of carbon nanotube bundles (CNTB) with Au nanocontacts made on different branches, which enables four probe transport measurement on the same CNTB or across different bundles. Dashed lines indicate the locations of CNTBs with lengths of each segment labeled. **b** I–V curve along CNTB, inset: SEM image of four probe transport measurement along a CNTB by using STM probes and the nano-contacts from (**a**). **c** I–V curve across two CNTBs, inset: SEM image of four probe transport measurement across two CNTBs. (Adapted from [10])

nanowire that was formed by air exposure for a long time (weeks) [25]. By making the nanocontacts at the end of Cu nanowires, we can also conveniently eliminate the influence of contact resistance on the measurements. Figure 5d and e are the Voltage versus Current curve on the nanowires for the two- and four-point measurements, respectively. From the difference between the two, we can extrapolate the contact resistance of between tips and the Cu nanowire to be 320 kΩ.

3.5 Application of Nanocontracting in Carbon Nanofibers

The local contacting technique was also demonstrated on individual bundles and junctions in a network of single-walled carbon nanotubes (CNTs). In this experiment, arc-discharged CNTs were first purified and sonicated in chloroform solution to form CNT bundles (CNTB) [26]. CNT bundles were dispersed via spin coating onto a Si substrate with native oxide to form a CNT bundle network. The density of the bundle network was controlled so that isolated CNT bundles and bundle junctions could easily be found with SEM. A sample SEM image (Fig. 6a) shows CNT bundles with Au nanocontacts made on different branches of a CNT network. Compared to four probe measurements without nanocontacts, contact fabrication greatly improved measurement stability and reproducibility.

Figure 6b and c show four probe measurements made by using pre-fabricated nanocontacts along different branches of a CNTB. The diameters of the CNTBs are around 200 nm, meaning they consist hundreds of single tubes. If we assume a constant CNTB linear resistivity, from the measured resistance in Fig. 6b and c we can calculate that the linear resistivity of CNTB at 140 K is 370 kΩ/μm while the contact resistance across different CNTBs is 390 kΩ.

3.6 Summary

We have summarized the recent reports on the application of a field emission process in fabricating nanocontacts for bridging nanostructures and mesoscopic transport probes. The high spatial resolution nanocontacting method provides a controllable and reliable approach for electrically accessing <100 nm nanowires and other one-dimensional nanoobjects with the help of STM probes and SEM images. The whole nanocontacting process using STM probes is clean, simple, quick, controllable, and reliable. The process can be applied to a range of metallic and semiconducting materials. As the field evaporation-induced Au dot formation has also been demonstrated on the surface of SiO_2/Si by using an Au-coated AFM probe [15], this nanocontacting method can also be applied to insulating samples. Precise engineering of nanocontact by this technique that allows contacting to arbitrarily any nanostructures with high spatial resolution should result in additional research applications including fabrications of nanosersors and nanoelectronics, and repair of interconnects and failed nanoscale electronics.

Acknowledgments This research was conducted at the Center for Nanophase Materials Sciences, which is sponsored at Oak Ridge National Laboratory by the Division of Scientific User Facilities, U. S. Department of Energy.

References

1. de Jonge, N., Lamy, Y., Kaiser, M.: Controlled mounting of individual multiwalled carbon nanotubes on support tips. Nano Lett. **3**, 1621–1624 (2003)
2. Decossas, S., et al.: Nanomanipulation by atomic force microscopy of carbon nanotubes on a nanostructured surface. Surf. Sci. **543**, 57–62 (2003)
3. Duan, X., Zhang, J., Ling, X., Liu, Z.: Nano-welding by scanning probe microscope. J. Am. Chem. Soc. **127**, 8268–8269 (2005)
4. Grill, L., et al.: Nano-architectures by covalent assembly of molecular building blocks. Nat. Nanotech. **2**, 687–691 (2007)
5. Wang, Y. G., et al.: Ohmic contact junction of carbon nanotubes fabricated by in situ electron beam deposition. Nanotechnology **17**, 6011 (2006)
6. Wilms, M., Conrad, J., Vasilev, K., Kreiter, M., Wegner, G.: Manipulation and conductivity measurements of gold nanowires. Appl. Surf. Sci. **238**, 490–494 (2004)

7. Matsui, S., et al.: Three-dimensional nanostructure fabrication by focused-ion-beam chemical vapor deposition. J. Vac. Sci. Technol. **B 18**, 3181 (2000)
8. Kent, A.D., Shaw, T.M., von Molnar, S., Awschalom, D.D.: Growth of high aspect ratio nanometer-scale magnets with chemical vapor deposition and scanning tunneling microscopy. Science **262**, 1249–1252 (1993)
9. Sato, A., Tsukamoto, Y.: Nanometre-scale recording and erasing with the scanning tunnelling microscope. Nature **363**, 431–432 (1993)
10. Qin, S., et al.: Contacting nanowires and nanotubes with atomic precision for electronic transport. Appl. Phys. Lett. **100**, 103103 (2012)
11. Qin, S., et al.: Correlating electronic transport to atomic structures in self-assembled quantum wires. Nano. Lett. **12**, 938–942 (2012). doi: 10.1021/nl24003s
12. Kim, T.-H., et al.: A cryogenic quadraprobe scanning tunneling microscope system with fabrication capability for nanotransport research. Rev. Sci. Instrum. **78**, 123701 (2007)
13. Mamin, H.J., Guethner, P.H., Rugar, D.: Atomic emission from a gold scanning-tunneling-microscope tip. Phys. Rev. Lett. **65**, 2418 (1990)
14. Bessho, K., Hashimoto, S.: Fabricating nanoscale structures on Au surface with scanning tunneling microscope. Appl. Phys. Lett. **65**, 2142–2144 (1994)
15. Koyanagi, H., Hosaka, S., Imura, R., Shirai, M.: Field evaporation of gold atoms onto a silicon dioxide film by using an atomic force microscope. Appl. Phys. Lett. **67**, 2609–2611 (1995)
16. Park, J.Y., Phaneuf, R.J.: Polarity dependence in pulsed scanning tunneling microscopy fabrication and modification of metal nanodots on silicon. J. Appl. Phys. **92**, 2139–2143 (2002)
17. Pumarol, M. E. et al. Controlled deposition of gold nanodots using non-contact atomic force microscopy. Nanotechnology **16**, 1083 (2005)
18. Yang, Z., Hoffmann, S., Lichtenwalner, D.J., Krim, J., Kingon, A.I.: Resolution of the transfer direction of field-evaporated gold atoms for nanofabrication and microelectromechanical system applications. Appl. Phys. Lett. **98**, 044102 (2011)
19. Chang, C.S., Su, W.B., Tsong, T.T.: Field evaporation between a gold tip and a gold surface in the scanning tunneling microscope configuration. Phys. Rev. Lett. **72**, 574 (1994)
20. Pascual, J.I., et al.: Quantum contact in gold nanostructures by scanning tunneling microscopy. Phys. Rev. Lett. **71**, 1852 (1993)
21. Harrison, B.C., Ryan, P., Boland, J.J.: STM and DFT study of the Gd wetting layer reconstructions on the Si(0 0 1)-2 × 1 surface. Surf. Sci. **582**, 79–89 (2005)
22. Liu, B.Z., Nogami, J.: An STM study of the Si(0 0 1) (2 × 7)-Gd. Dy surface. Surf. Sci. **540**, 136–144 (2003)
23. Yeom, H.W., Kim, Y.K., Lee, E.Y., Ryang, K.D., Kang, P.G.: Robust one-dimensional metallic band structure of silicide nanowires. Phys. Rev. Lett. **95**, 205504 (2005)
24. Kim, T.-H., et al.: Large discrete resistance jump at grain boundary in copper nanowire. Nano Lett. **10**, 3096–3100 (2010)
25. Rathmell, A.R., Bergin, S.M., Hua, Y.-L., Li, Z.-Y., Wiley, B.J.: The growth mechanism of copper nanowires and their properties in flexible transparent conducting films. Adv. Mater. **22**, 3558–3563 (2010)
26. Hellstrom, S.L., Lee, H.W., Bao, Z.: Polymer-assisted direct deposition of uniform carbon nanotube bundle networks for high performance transparent electrodes. ACS Nano **3**, 1423–1430 (2009)

Surface Conductance Measurements on a MoS_2 Surface Using a UHV-Nanoprobe System

R. Thamankar, O. A. Neucheva, T. L. Yap and C. Joachim

Abstract We present detailed information about the first experiments performed on the A*STAR UHV-Nanoprobe system in Singapore. As a model system, naturally occurring MoS_2 surface was considered for those measurements. This surface is interesting as it is easy to prepare and shows a surface band gap of about 1.3 eV close to that of a Si(100)H surface. Two tip surface I–V measurements were performed by varying the inter-tip distance down to 100 nm. A transition from nonlinear to linear I–V characteristics are seen when the 2 tip separation is below 1 μm.

Keywords UHV-Nanoprobe · Scanning electron microscope (SEM) · Conductivity · MoS_2 · Molecular electronics

R. Thamankar (✉) · O. A. Neucheva · T. L. Yap · C. Joachim
IMRE, A*STAR (Agency for Science, Technology and Research),
3 Research Link, Singapore 117602, Singapore
e-mail: thamankarrm@imre.a-star.edu.sg

C. Joachim
CEMES and MANA Satellite, CNRS, 29 rue J. Marvig,
31055 Toulouse Cedex, France

T. L. Yap
GLOBALFOUNDRIES Singapore Pte Ltd, 60 Woodlands
Industrial Park D Street 2, Singapore 738406, Singapore

T. L. Yap
Department of Physics, National University of Singapore,
Singapore 117542, Singapore

C. Joachim (ed.), *Atomic Scale Interconnection Machines*, Advances in Atom and Single Molecule Machines, DOI: 10.1007/978-3-642-28172-3_10,

1 Introduction

Electronic properties of materials are very important to master the nano-electronics applications especially when the size of the devices reduces to such an extent that quantum size effects come into play, for example, when the device sizes are in the range of electron mean free path (∼few tens of nanometers). They become even more fascinating when the size of the device is of atomic dimensions. In this later case, it becomes more and more difficult to use conventional nanolithographic techniques to fabricate electronic elements at the atomic scale. Therefore, the bottom-up approach to fabricate nano-devices using single molecule is becoming more and more interesting to the researchers.

Molecular electronics involving single molecule(s) as active element is an area of research wherein both physicists and chemists combine their efforts together to design and synthesize the molecules for designed device performance. Designing such molecules is intended toward getting the desired logic operation. Already in 1971, Mann and Kuhn had explored the conductance measurements of tunnel junction whose basic material was long and large HOMO-LUMO gap molecular chains. They have found an exponential decay of the junction conductance versus thickness as predicted by the tunnel theory [1] After the seminal work by Aviram and Ratner on single molecular rectifiers, the design and usage of single molecules to construct molecular devices became of much more interest [2–5]. Furthermore, specially designed molecule and molecule/substrate combination are very important to study electron-vibration (electron–phonon) interaction, electron–electron interaction (Coulomb blockade) and spin–spin interaction (Kondo effects).

To accurately determine the intrinsic transport properties of these molecular devices, four-probe measurements are a priori required [6–8]. In the four-probe measurements, two probes serve as current source and the other two independent probes measure the potential difference between well-defined distances. This way, the contribution from the probe-surface resistance (or contact resistance) can be eliminated. To be able to construct a single molecule device and to measure its electronic characteristics, the A*STAR Institute of Materials Research and Engineering Singapore (IMRE) has recently assembled together a cluster of UHV low temperature equipments all interconnected together via a UHV low temperature linkage (Interconnection Machine).

To test this interconnection machine and before bringing on the surface the single molecule logic gates, we have selected the MoS_2 surface. There are many advantages in using two-dimensional materials for UHV atomic scale device studies. First, it is easy to UHV prepare a graphene or MoS_2 surface. Second, such surfaces exhibit rich physics coming from the high mobility of the carriers. For surface conductance experiments where a surface gap is required, MoS_2 makes much more important member in this sense because of its intrinsic band gap close to that of the Si(100)H surface, while pristine graphene is a gapless material.

MoS_2 is one of member of the metal chalcogenide group which finds application in many areas. The structure of MoS_2 has been solved many decades back [9].

The bulk crystals of MoS_2 have stacks of Suphur and Molebdenum layers, respectively. Each pair of Mo and S layers is bonded by Van der Waal forces just like in Highly Oriented Pyrolytic Graphite (HOPG). The crystallographically determined structure shows a triangular pyramid of sulfur atoms and within that one Mo atoms is situated. A clean surface of MoS_2 can be obtained by micromechanical cleavage technique using a scotch tape. By doing this, we obtain a Sulfur (S) terminated surface [10, 11]. Importantly the sulfur terminated MoS_2 is very stable at room temperature.

Recently MoS_2 single layers have been used to fabricate the field effect transistors [12–14]. It is shown that all the characteristics such as current on/off ratio, room temperature mobility are comparable to the corresponding FET's using thin films of silicon and graphene ribbons. These investigations show clearly the possible usage of layered materials in the low power electronic device applications in future.

The band gap of MoS_2 is shown to depend on the numbers of layers considered. The optical spectroscopic studies on MoS_2 with increasing number of monolayers clearly show a transition from an indirect to direct band gap material [14]. Recent photoluminescence studies have also shown that a strong luminescence emerges when MoS_2 is thinned down to monolayer thickness, thus indicating a transition from being indirect to direct band gap material [15].

It is also shown that STM-like field evaporation of single sulfur atoms take place at much lesser tip—sample voltage than the W field evaporation of the STM tip apex. Additionally the cleaved MoS_2 surface is suitable for this experiment as the surface defect induced by the extraction of a single sulfur atom is stable at room temperature. Hosaka et al. have successfully extracted sulfur atoms from the cleaved MoS_2, showing that indeed the atomic fabrication is possible on the MoS_2 surface [16, 17]. Interestingly the introduction of a defect by extraction of a sulfur atom introduces a few electronic states within the band gap of MoS_2. Recent experimental investigations of Kodama et al. clearly show that the I–V measured on the single sulfur vacancy show metallic behavior compared to the semiconducting I–V measured elsewhere [18]. Therefore, if a straight line of sulfur single atom vacancies is created, it can produce a non zero-local density of states within the bulk band gap. Since the atomic wire created by sulfur vacancies is stable at room temperature, it can be used for electronic transport and to construct surface atomic scale devices. It has been shown that due to the remaining three dangling bonds occurring when a sulfur atom is extracted, a localized electronic energy band is formed when a line of sulfur atoms is constructed [19, 20].

2 Experiments and Results

2.1 Interconnection Machine

The IMRE's interconnection machine is a cluster of equipments specifically designed for the construction, packaging and measurements of the surface

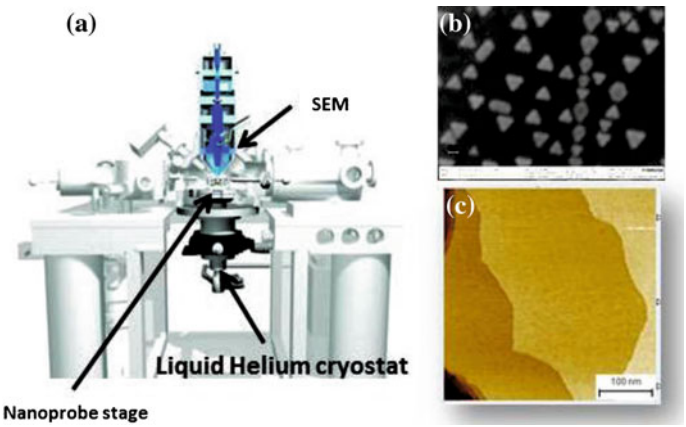

Fig. 1 **a** Schematic diagram of the UHV-Nanoprobe (*Courtesy* Omicron GmbH, Germany) of the A*STAR IMRE interconnection machine. It can be operated at a wide range of temperature from 440 to 30 K. The sample can be cooled to 30 K using liquid helium using a continuous flow cryostat. **b** An SEM image taken on an Au/MoS_2 sample. (9 kV/100 pA, working distance ~12.8 mm). **c** An STM image of an Au(111) UHV prepared surface taken at 300 K. Scanning parameters are +0.1 V/1000 pA, scanning area is 400 × 400 nm

transport of single molecule devices in the UHV. This is detailed in the Chap. 3 of this book. In this chapter a detailed account of the first experiments performed on UHV-Nanoprobe of this interconnection machine is given.

Figure 1 shows the schematic diagram of the UHV-Nanoprobe part of our interconnection machine. This consists of a Scanning Electron Microscope positioned vertically above the sample stage. The sample stage can be cooled to cryogenic temperature using liquid helium. The scanning electron microscope attached in this Nanoprobe is calibrated using Au/Carbon and Au/MoS_2 samples. Triangular islands of Au can be grown on MoS_2 as shown in the Fig. 1b. The Nanoprobe stage also hosts four scanners individually holding a tip. Normally all the scanners are calibrated with tips. We use electrochemically etched W tips followed by flashing in UHV by passing large current (~5–7 Amps for short duration) through the apex of the tip. Normally the etched tips having apex diameter ~50–100 nm are selected for the surface conductance measurements.

2.2 Calibration of the Interconnection Machine

We use an Au(111) surface for the calibration of the Nanoprobe. As a standard procedure, Au(111) was prepared using a sequence of sputtering/annealing to get large terraces STM imaged as presented in Fig. 1c.

Figure 2 shows the typical I–V curve on Au(111) surface taken at room temperature. This I–V curve clearly shows that the tip-sample junction is very well

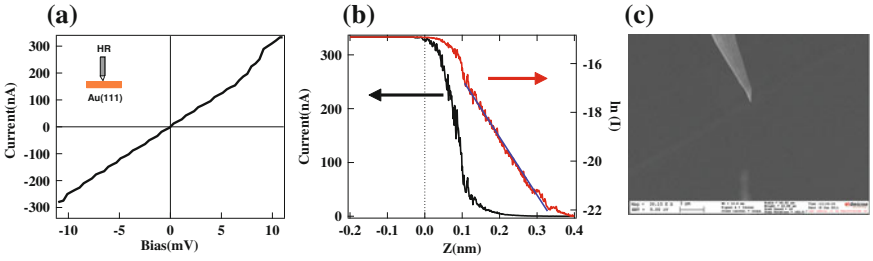

Fig. 2 Spectroscopic measurements on Au(111) using high resolution (HR) scanner in the Nanoprobe. **a** I–V curve showing a linear behavior indicating a good ohmic contact. The slope of this curve gives a resistance ∼39.4 kOhms. **b** Typical I–Z curve obtained (*black*) and in the ln(I) versus Z curve, a jump-to-contact can be clearly seen (*Red*). **c** The SEM image of the tip used in the spectroscopic investigation

controlled with ohmic contact. I–V curves are obtained with low bias setting for the tip. The slope of the I–V curve gives us a resistance of 39.4 kOhms which indicates a very good ohmic contact with the surface. It should be noted that a 20 kOhms series resistance was included in the feedback control circuit to limit the current, thus giving rise to actual resistance of ∼19.4 kOhms in the junction. Figure 2b shows the I–Z curves obtained at room temperature with the same tip. The work function of the Au(111) substrate is calculated by measuring the slope of the ln(I)–Z curve. From our measurements we obtain a value 6.05 eV which agrees fairly well with the known values for the work function on a Au(111) surface. This suggests a very good control over the tip-sample junction distance. This curve also shows a jump-to-contact, showing also a very good control over the tip-sample junction atomic scale structure [21, 22]. This procedure is repeated whenever a new tip is used. Once the tip is characterized this way, it is further used in the measuring in the surface conductivity experiments.

MoS_2 surface was prepared by cutting a small piece from the naturally occurring rock obtained from Australian mines. After cutting, it is glued on to molybdenum sample plate and introduced into the UHV system. The surface is not subjected to any further cleaning procedure, just a little thermal annealing. MoS_2 is a layered material similar to *highly ordered pyrolytic graphite* (HOPG) with indirect (direct) band gaps of 1.29 (1.78) eV [23]. This small band gap makes it very useful for the study on surface atomic scale devices and it can be compared to the band gap of the Si(100)H surface.

2.3 Measurements on MoS_2

As mentioned earlier, the MoS_2 surface band gap depends on its thickness. To check the electronic band gap of our MoS_2 sample, we have performed single tip measurement at room temperature and at 30 K. Since the selected MoS_2 sample

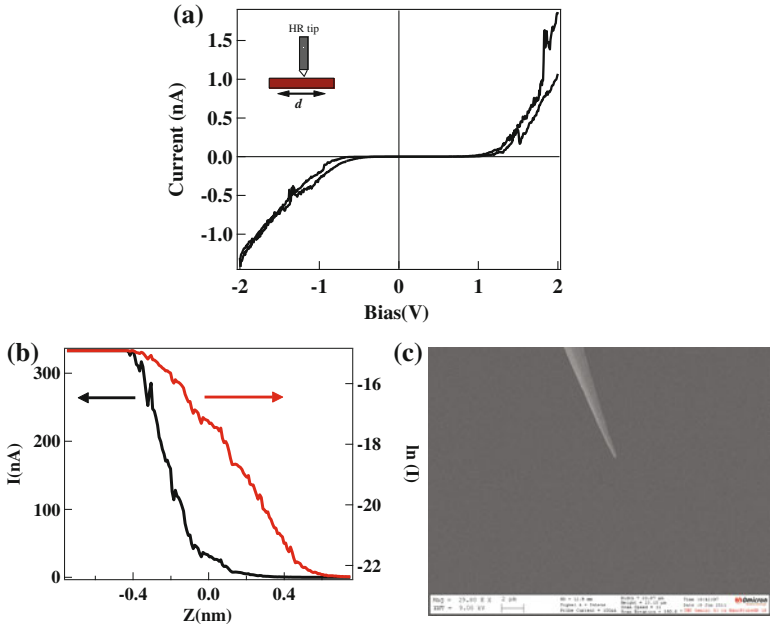

Fig. 3 Spectroscopic measurements on an MoS_2 surface using high resolution (HR) scanner in the Nanoprobe. **a** Typical I–V curve taken on MoS_2 with single tip. **b** Typical I–Z curve obtained (*Black curve*) and ln(I) versus Z curve (*Red*). **c** The scanning electron microscope image of the tip used for the measurements

was fairly thick, we expect a bulk band gap of $\sim$1.3 eV. The Fig. 3a shows a typical I–V curve at room temperature. One should note that single tip measurements do give a lot of scatter in the I–V curves. Thus very precise measurements are required to exactly determine the bulk band gap of MoS_2. Also there is a need for knowing exact thickness of the MoS_2 sample taken. To determine the work function, an I–Z curve was obtained and Fig. 3b shows I–Z curve obtained at room temperature. As mentioned earlier the slope of ln(I)–Z gives the work function and from the slope of this curve, a value of 5 eV obtained. This agrees very well with the known values of the work function for MoS_2 [23]. Similar experiments should be done with other tips available in the NanoProbe to get I–V and I–Z curves. This gives us a clear understanding of the tip apex structure. Once the apex from all the tips are characterized this way, a multi probe experiment can be performed.

The clear understanding of the electronic structure of the tip apex is especially important when the transport characteristics of single molecule or atomic wire are to be determined. In this scenario, it is necessary to have single channel conduction via the molecule or the atomic wire which enables us to understand the transport in a full quantum regime. The requirement of point contact is due to the fact that in a quantum regime of conductance, it is assumed that conduction takes place via a few quantum channels (or less in a tunneling regime) especially in the low bias regime.

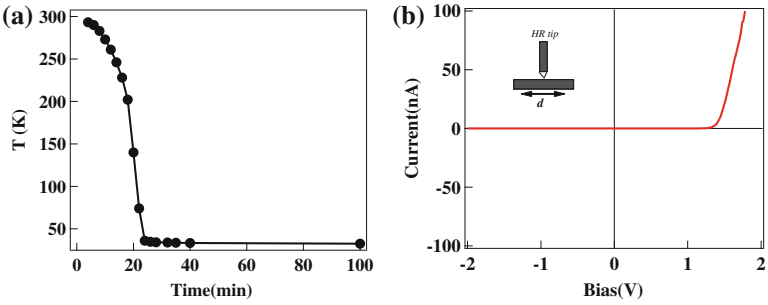

Fig. 4 **a** Cooling curve of the MoS_2 sample on the Nanoprobe. The minimum temperature reached is 30 K. **b** A typical single tip measurement of I–V on MoS_2 at 30 K

Similar experiments were done at 30 K by cooling the sample using liquid helium. In our experimental set up, only the sample is cooled via liquid helium, whereas the tip is always at room temperature. The I–V curves using a single tip like measurement show a completely different behavior compared to room temperature I–V curves shown in the Fig. 4b. Notice that there is almost zero current passing through the MoS_2 sample in the complete negative bias range scanned. This kind of I–V was observed with various MoS_2 samples. Further measurements are needed to understand the change in the I–V curves due to the cooling down of the sample.

We have seen that the I–V and I–Z curves differ from tip to tip even though the tips have similar apex diameter. Thus all the tips need to be characterized very carefully and it is important to have all the tips in the same position along the I–Z in order to measure transport in the quantum regime. With this in mind and for the two tip measurements, we have used the I–Z curves of individual tips as reference. Proper *Z*-offsets are given to individual tips to reach the same I setting for both tips. Since the UHV-Nanoprobe is attached to a high resolution scanning electron microscope, it enables us to determine exactly the tip apex diameter and to position them at a required distance of separation. In our experiments, the distance between the tips has been varied systematically and the two tip I–V measurements were done.

Once the tips were calibrated individually, surface transport measurements can be performed. In this case, the scanning electron microscope was used to determine the distance of tip separation precisely. By keeping one of the tips stationary, second tip was moved systematically thus varying the distance of separation. Figure 5a shows a SEM image of tips while doing the surface transport measurements. In this image, the distance of separation is about 3.3 μm. Figure 5b shows two probe measurements done at a distance of 2.395 μm. It clearly shows a nonlinear I–V curve. The inset in Fig. 5b shows the actual tunnel conditions applied to the two tips. The transverse resistance can be determined by taking the slope at zero current. Note that the position of zero current is taken as origin in the I–V curve during the two probe measurements.

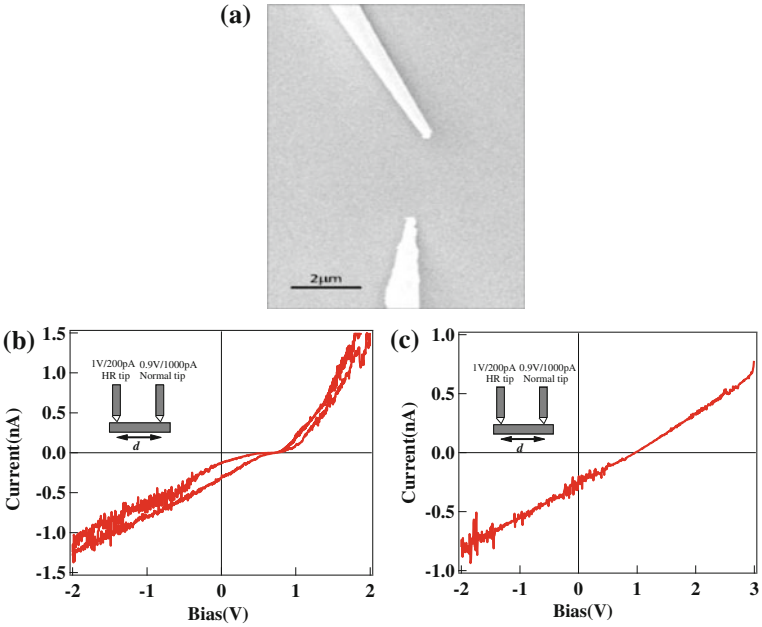

Fig. 5 Surface transport measurements using two tips. Measurements are done at 30 K. **a** Scanning electron microscope image of two tips used for surface transport measurements. The distance of separation is 3.3 m. **b** I–V curve showing the nonlinear behavior. The distance of separation here is 2.395 m. **c** A linear I–V curve for the two tip measurements with tip separation ~335 nm

In our measurements, the voltage is changed on the high resolution tip, thus the zero current location is depending on the bias voltage of the second tip, depicted as 'normal tip' in the inset. We can clearly see that the I–V curves show an offset corresponding to the bias setting of the "normal tip". We change the distance of separation by moving the high resolution tip under the electron microscope. Once the proper distance is selected, two tip surface transport measurements are conducted. Once the distance of separation is less than 1 μm, the I–V shows linear behavior. Again the offset is due to the bias setting of the second tip (Fig. 5c).

3 Conclusion

To summarize, the distance-dependent surface conductance was measured using two tips on a UHV-Nanoprobe system. The distances have been precisely changed by imaging the surface with a scanning electron microscope within the Nanoprobe. The key features of a two tip measurements are (i) for tip separation more than 1 μm, the I–V shows a nonlinear behavior. (ii) By decreasing the tip separation less than 1 μm, the I–V becomes linear and shows distance-dependent resistance.

Acknowledgments The authors wish to thank the A*STAR VIP "Atom Technology" project under project no. 1021100972 and the European AtMol Integrated Project funding under the contract no. 270028.

References

1. Mann, B., Kuhn, H.: Tunneling through fatty acid salt monolayers. J. Appl. Phys. **42**, 4398 (1971)
2. Aviram, A., Ratner, M.: Molecular rectifier. Chem. Phys. Lett. **29**, 277 (1974)
3. Metzger, R.M.: Unimolecular electronics. J. Mater. Chem. **18**, 4364 (2008)
4. Joachim, C., Ratner, M.: Molecular electronics: some views on transport junctions and beyond. Proc. Natl. Acad. Sci. **102**(25), 8801–8808 (2005)
5. Joachim, C., Gimzewski, J.K., Aviram, A.: Electronics using hybrid-molecular and mono-molecular devices. Nature **408**, 541–548 (2000)
6. Higuchi, S., Osamu Kubo, O., Kuramochi, H., Aono, M., Nakayama, T.: A quadruple-scanning-probe force microscope for electrical property measurements of microscopic materials. Nanotechnology **22**, 285205 (2011)
7. Hasegawa, S., Ichiro Shiraki, I., Tanikawa, T., Petersen, C.L., Hansen, T.M., Boggild, P., Grey, F.: Direct measurement of surface-state conductance by microscopic four-point probe method. J. Phys.: Condens. Matter **14**, 8379–8392 (2002)
8. Hasegawa, S.: François grey, electronic transport at semiconductor surfaces—from point-contact transistor to micro-four-point probes. Surf. Sci. **500**(1–3), 84 (2002)
9. Dickinson, R.G., Pauling, L.: The crystal structure of molybdenite. J. Am. Chem. Soc. **45**(6), 1466–1471 (1923)
10. Hosoki, S., Hosaka, S., Hasegawa, S.: Surface modifications of MoS_2 using an STM. Appl. Surf. Sci. **60/61**, 643 (1992)
11. Qin, X.R., Yang, D., Frindt, R.F., Irwin, J.C.: Real-space imaging of single-layer MoS_2 by scanning tunneling microscopy. Phys. Rev. B **44**, 3490–3493 (1991)
12. Radisavljevic, B., Radenovic, A., Brivio, J., Giacometti, V., Kis, A.: Single layer MoS_2 transistors. Nat. Nanotechnol. **6**, 147 (2011)
13. Yoon, Y., Ganapathi, K., Salahuddin, S.: How good can monolayer MoS_2 transistors be? Nano Lett. **11**(9), 3768–3773 (2011)
14. Splendiani, A., Sun, L., Zhang, Y., Li, T., Kim, J., Chim, C.-Y., Galli, G., Wang, F.: Emerging photoluminescence in monolayer MoS_2. Nano Lett. **10**(4), 1271–1275 (2010)
15. Mak, K.F., Lee, C., Hone, J., Shan, J., Heinz, T.F.: Atomically thin MoS_2: a new direct-gap semiconductor. Phys. Rev. Lett. **105**, 136805 (2010)
16. Hosaka, S., Hosoki, S., Hasegawa, T., Koyanagi, H., Shintani, T., Miyamoto, M.: Fabrication of nanostructures using scanning probe microscopes. J. Vac. Sci. Technol. (B) **13**, 2813 (1995)
17. Stupain, G.W., Leung, M.S.: Imaging of MoS_2 by scanning tunneling microscopy. Appl. Phys. Lett. **51**, 1560 (1987)
18. Kodama, N., Hasegawa, T., Okawa, Y., Tsuruoka, T., Joachim, C., Aono, M.: Electronic states of sulfur vacancies formed on a MoS_2 surface Japanese. J. App. Phys. **49**, 08LB01 (2010)
19. Yong, K.S., Otalvaro, D.M., Duchemin, I., Saeys, M., Joachim, C.: Calculation of the conductance of a finite atomic line of sulfur vacancies created on a molybdenum disulfide surface. Phys. Rev. B **77**, 205429 (2008)
20. Fuhr, J.D., Saúl, A., Sofo, J.O.: Scanning tunneling microscopy chemical signature of point defects on the MoS_2(0001) surface. Phys. Rev. Lett. **92**(2), 026802 (2004)
21. Gimzewski, J.K., Möller, R.: Transition from the tunneling regime to point con tact studied using scanning tunneling microscopy. Phys. Rev. B **36**, 1284 (1987)

22. Gimzewski, J.K., Möller, R., Pohl, D.W., Schlittler, R.R.: Transition from tunneling to point contact investigated by scanning tunneling microscopy and spectroscopy. Surf. Sci. **189–190**, 15–23 (1987)
23. Böker, Th., Severin, R., Müller, A., Janowitz, C., Manzke, R., Voß, D., Krüger, P., Mazur, A., Pollmann, J.: Band structure of MoS_2, $MoSe_2$, and α-$MoTe_2$: angle-resolved photoelectron spectroscopy and ab initio calculations. Phys. Rev. B **64**, 235305 (2001)

Multi-Probe Characterization of 1D and 2D Nanostructures Assembled on Ge(001) Surface by Gold Atom Deposition and Annealing

M. Wojtaszek, M. Kolmer, S. Godlewski, J. Budzioch, B. Such, F. Krok and M. Szymonski

Abstract The demand to discover new, alternative solutions in future electronics has currently focused the attention on the possible use of single atomic wires and conductive mesa pads as components in electronic circuits. For such applications, we need a good knowledge of structural and electronic properties of 1D and 2D conductive nanostructures fabricated on large and/or moderate band gap semiconductor surfaces. This chapter is reporting on case studies invoking preparation of well organized atomic wires and 2D conductive pads by self-assembly of gold atoms on clean, reconstructed Ge(001) surface. Structural characterization of the fabricated nanostructures was performed with atomic resolution on low temperature scanning tunneling microscope (LT-STM) and multi-probe STM designed by Omicron Nanotechnology GmbH. Using the far field, high resolution scanning electron microscope (SEM), the pre-prepared nanostructures were identified after an UHV transfer into a multi-probe station of the system, and their surface conductance was measured with two STM probes. The conductance dependence as a function of the inter-probe distance confirmed 2D (surface) character of the Au rich nanostructures assembled on Ge(001).

Keywords Ge(001) · Gold nanowires · Self-assembly · Surface conductance · Multi-probe STM · Scanning tunneling microscope · Scanning electron microscopy

M. Wojtaszek · M. Kolmer · S. Godlewski · J. Budzioch · B. Such · F. Krok · M. Szymonski (✉)
Faculty of Physics, Astronomy, and Applied Computer Science,
Research Center for Nanometer-Scale Science and Advanced Materials, NANOSAM,
Jagiellonian University, Krakow, Poland
e-mail: ufszymon@cyf-kr.edu.pl

C. Joachim (ed.), *Atomic Scale Interconnection Machines*, Advances in Atom and Single Molecule Machines, DOI: 10.1007/978-3-642-28172-3_11,

1 Introduction

Recent concepts in nanoscale electronics often explore molecular devices for which a single molecule, or a molecular circuit is connected to external environment by a set of conductive nanopads (nano-electrodes) interconnected by a network of atomic and/or molecular wires able to make an Ohmic contact directly with the molecules. Therefore, in order to facilitate essential fabrication steps in technology of such molecular electronic devices, surface resistance of conductive 2D nanopads fabricated on semiconductor surfaces have to be known/characterized as a function of the inter nanopad distance down to a nanometer range. One approach to accomplish such a goal is to use top STM-like contacts of the multiprobe STM system navigated by a high resolution scanning electron microscope.

Deposition and self-assembling of noble metals on semiconductor surfaces have been frequently studied for almost 3 decades. In spite of that, many aspects of such interfaces, including quantum electronic properties of self-assembled metallic nanowires are only recently explored. A spectacular example of such a system is Au on Ge(001) which after first publication in 1988 [1], and some others in 2004, and 2005 [2, 3] was not in a main stream of research until recent letter by Schaefer and co-workers [4] in which formation of 1D electron liquid in self-organized gold chains on Ge(001) was described. Although detail understanding and theoretical modelling of geometrical and electronic structure of the Au chains on Ge(001) are still under discussions [4–13], gold on Ge(001) seems to be an ideal system for measuring surface conductance because of clear indications of the 1D and/or 2D confinement in the nanostructures [13, 14]. Moreover, simultaneous appearance of the gold-induced chain domains and clean Ge(001) reconstruction areas on the same surface [3] create the opportunity to use such conductive wires as interconnects to structures build on clean or hydrogen passivated Ge(001). Also molecules evaporated on Au/Ge(001) system [15], connected to the wires, seem to offer a way to develop a new type of interconnects between individual molecules and micro size devices. The challenging task of charge transport characterization for 1D and 2D surface nanostructures could be accomplished with multi-probe STM tips capable of forming well-defined, Ohmic contacts by controlled approach to the nanometer size objects. In this work we describe the first attempt to measure surface conductance of the gold deposition-induced nanostructures on a clean, reconstructed Ge(001) by means of the two-probe STM device navigated with a high resolution SEM microscope. The results of the conductance versus inter-probe distance measurements indicate its surface character for Au-induced nanowire domains.

2 Experimental

The experiments are carried out in a commercial four-nanoprobe UHV System made by Omicron Nanotechnology GmbH incorporating a high resolution Gemini Column from Carl Zeiss, Germany. The system is equipped with three UHV

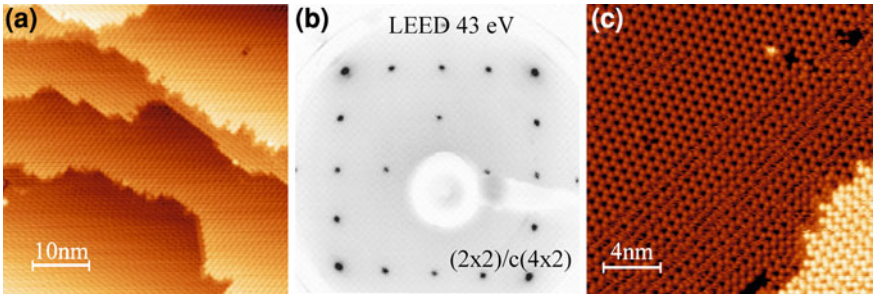

Fig. 1 Clean Ge(001) as prepared by 600 eV Ar^+ ion sputtering and thermal annealing at 1040 K. **a** STM image taken at room temperature (STM parameters: sample bias voltage: −2 V and tunneling current: 0.5 nA); **b** LEED pattern showing mixed (2 × 2)/c(4 × 2) surface reconstruction at room temperature; **c** LT-STM image of clean Ge(001) surface taken at 77 K (STM parameters: sample bias voltage: −2 V and tunneling current: 0.3 nA)

interconnected chambers with the base pressure in the low 10^{-10} mbar range, or better. In addition to the four-probe STM unit, the system also consists of a low energy electron diffraction (LEED) optics, a low temperature scanning tunneling microscope (LT-STM), and a hemispherical electron energy analyzer allowing, in combination with the Gemini column, for an Auger electron spectroscopy (AES) analysis, as well as for scanning Auger microscopy (SAM). All conductance measurements are done at room temperature.

The substrate is cut from a wafer of undoped *n*-type Ge(001) crystal with a resistivity of about 30 Ω · cm. The cleaning procedure consists of few cycles of 600 eV Ar^+ ion sputtering at sample temperature of 1040 K (as measured by a pyrometer). After this procedure the Ge(001) surface exhibits a mixed (2 × 2)/c(4 × 2) − 2 domain pattern as seen in Fig. 1.

3 Conductive Pads and Nanowires by Gold Deposition on Ge(001)

Surface nanostructures are obtained by deposition of 6 monolayers (MLs) of Au on the reconstructed Ge(001) from a resistively heated tungsten crucible. The deposition rate of 0.2 ML/min is monitored by a quartz crystal microbalance and the substrate temperature is kept at 150 K. This procedure of sample preparation is different from the one applied by other groups [4, 5] who focused their work on measuring the structure and properties of nanostructures formed at Au deposition of 1 ML or less. Our goal, however, is focused on obtaining a more complex system of well separated gold islands interconnected by conductive 2D wire domains.

In order to accomplish this goal we perform metal deposition at low temperature so that the thermal diffusion range of Au atoms is limited and Ge(001)

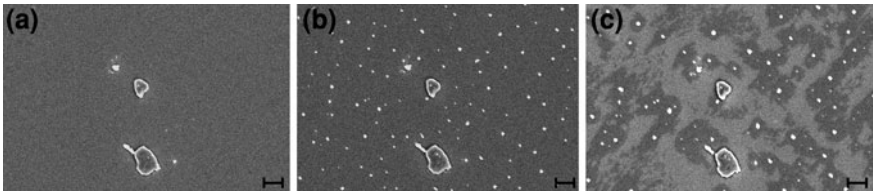

Fig. 2 SEM images of gold on germanium surface (black bars indicate 1 μm). The topographic defects are shown to compare the differences between subsequent steps of sample preparation. Panel (**a**) shows the surface covered with gold after deposition and before annealing. Image (**b**) shows the surface after annealing at 720 K for 15 minutes, which produces the surface fully covered with reconstructed gold wires and gold islands with diameter of 150 nm visible as bright spots. After annealing to 770 K for 15 min gold islands become bigger and a dark "halo" surrounding islands appears indicating surface covered with well reconstructed gold chains (panel (**c**)). Light gray shows areas where the gold atoms disappear leading to exposure of defected Ge(001) surface

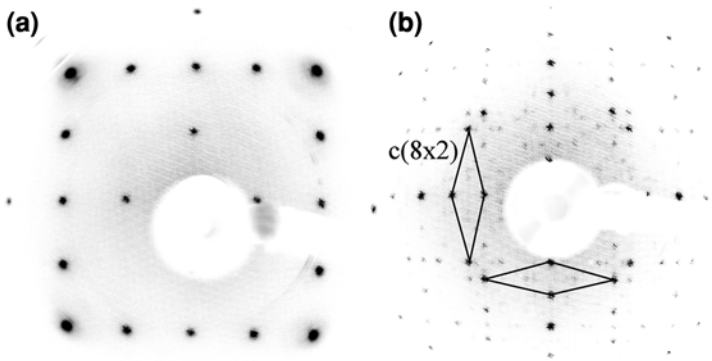

Fig. 3 LEED patterns (**a**) of clean Ge(001) and (**b**) of Ge(001) after Au deposition and annealing at 720 K (electron energy of 43 eV). Additional spots show 4 × 2 and c(8 × 2) reconstructions with dual domains

surface is randomly covered with gold clusters, neither showing any well-defined LEED spots, nor any specific topographic pattern under SEM imaging conditions (see Fig. 2a). However, subsequent thermal annealing of the Au clusters/Ge system leads to development of a mixed crystallographic structure of flat gold islands distributed over well-ordered wire domains. For example, if the sample temperature is increased and kept at 720 K for 15 minutes, islands with an average diameter of 150 nm are found on the surface uniformly covered with well-defined and oriented wires as seen in Fig. 2b. LEED image (see Fig. 3) taken after heating shows different structure from that obtained for clean germanium. Additional spots indicate c(8 × 2) structure symmetry with dual domains [9] but also some 8× spots are seen in Fig. 3b. Spots exhibiting additional 8× reconstruction, below 1.2 ML deposition, and 16×, above 1.2 ML deposition, were previously reported

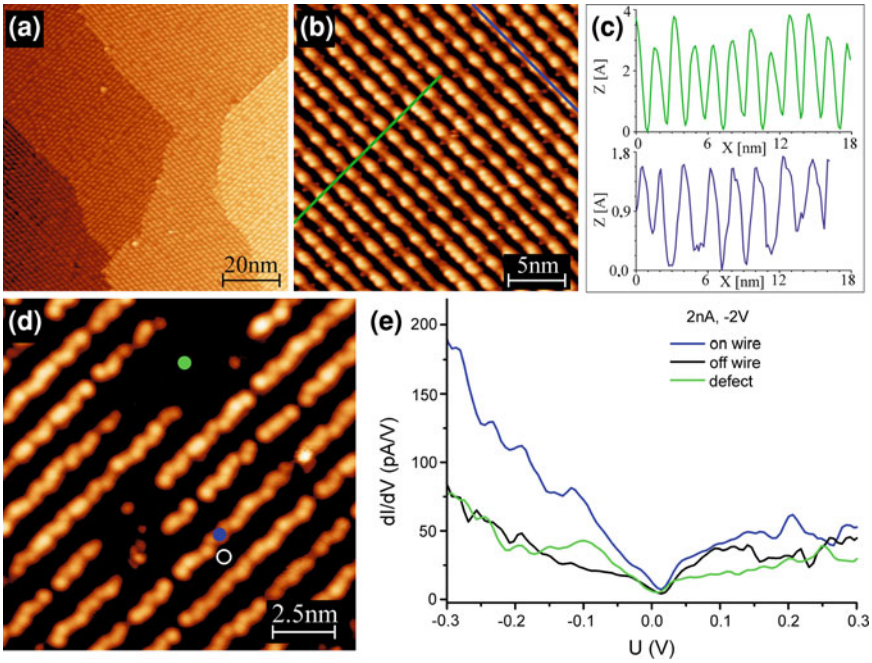

Fig. 4 **a** and **b** STM images of gold-induced nanowires on germanium surface after annealing at 720 K for 15 min. Sample bias voltage: −2 V; tunneling current: 0.2 nA. **c** Cross-cut profiles along the lines indicated in panel **b**. **d** High resolution STM image of the nanowires taken at liquid helium (LHe) temperature. **e** Scanning tunneling spectroscopy (*dI/dU*) at various locations indicated in image **d**

in this system by other authors [6, 12]. Repeated cycles of heating at the same temperature do not change neither SEM, nor LEED images.

STM imaging of the areas between gold islands reveals a regular structure of 1D wires assembled on Ge(001) as seen in Fig. 4. The adjacent terraces (Fig. 4a) covered with regularly spaced structure of anisotropic wires are separated with single steps. The sharp terrace edges aligned to the wires indicate that the terraces are newly formed upon the annealing process. The wire structures on the adjacent terraces are rotated by 90 degrees with respect to each other due to the reconstruction of the substrate surface. The wires are not uniform along their length and exhibit bright features with the average separation of approximately 2 nm (Fig. 4b). The wire orientation follows the direction of Ge(001) reconstruction rows with the spacing of 1.6 nm (see the upper cross-cut profile in Fig. 4c). Scanning tunneling spectroscopy (*dI/dU*) taken at various locations on the wire covered area (Fig. 4e) reveals that there is no gap in the band structure of the surface domains containing the wires.

In Fig. 5 STM topographies of the neighboring domains of the regular wire structure and that of the bright contrast in SEM image are shown. The high resolution STM imaging of the bright contrast areas (Fig. 5b and c) reveals the structure of highly defected Ge(001) [3].

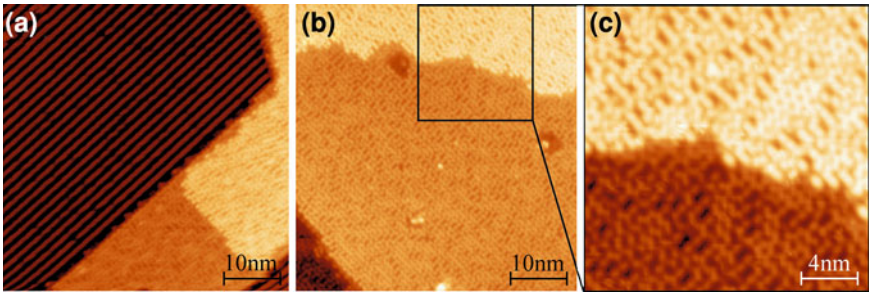

Fig. 5 High resolution STM images of the Au/Ge(001) sample after annealing at 770 K (**a**), and 820 K (**b**, **c**). Tunneling parameters: sample bias voltage: −2 V; tunneling current: 0.2 nA

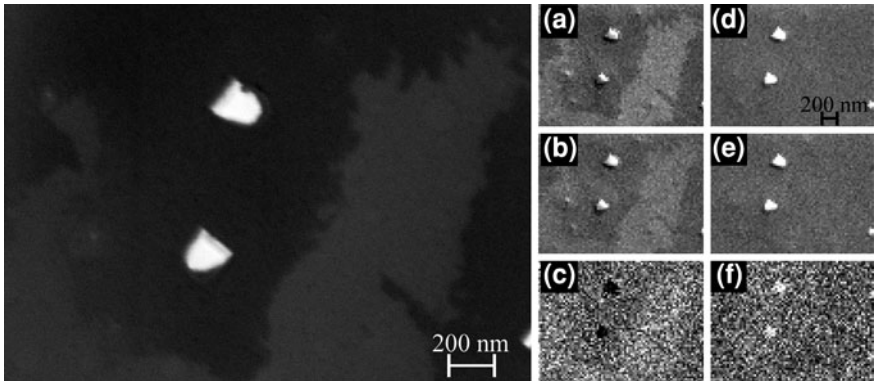

Fig. 6 SEM image on the *left* and a set of SAM images on the *right* taken at the same area of the Au/Ge(001) surface (brighter data points correspond to higher signal). Image (**a**) was obtained for the energy corresponding to Ge Auger transition (1145 eV), image (**b**) shows the background of Auger spectrum in the vicinity of Ge line, and image (**c**) is given by $c = \frac{a-b}{a+b}$. Images (**d**–**f**) are obtained by the same procedure taken for Auger transition of Au (2015 eV)

The distribution of the system components (Au and Ge) over the surface can be examined "in situ" by scanning Auger microscope (SAM) utilizing the Gemini column as a primary electron source (Fig. 6). The left scan in Fig. 6 shows SEM image of islands surrounded by the dark "halo" next to the light gray area. Figures 6a and d show SAM maps of the same area obtained for electron energy analyzer set at the Auger transition for Ge (1145 eV, Fig. 6a), and for Au (2015 eV, Fig. 6d). Figure 6b and e are taken at energies corresponding to the background signals in the vicinity of Ge and Au peaks respectively. A map obtained by subtracting signal acquired at the Auger transition energy and the background signal and dividing the result by the sum of the two signals is shown in Fig. 6c for Ge ($c = \frac{a-b}{a+b}$) and in Fig. 6f for Au ($f = \frac{d-e}{d+e}$). A comparison of the resulting maps (c) and (f) indicates that the islands seen in the SEM image are built with gold and surrounded by dark "halo", which is enriched in gold in comparison to the light areas.

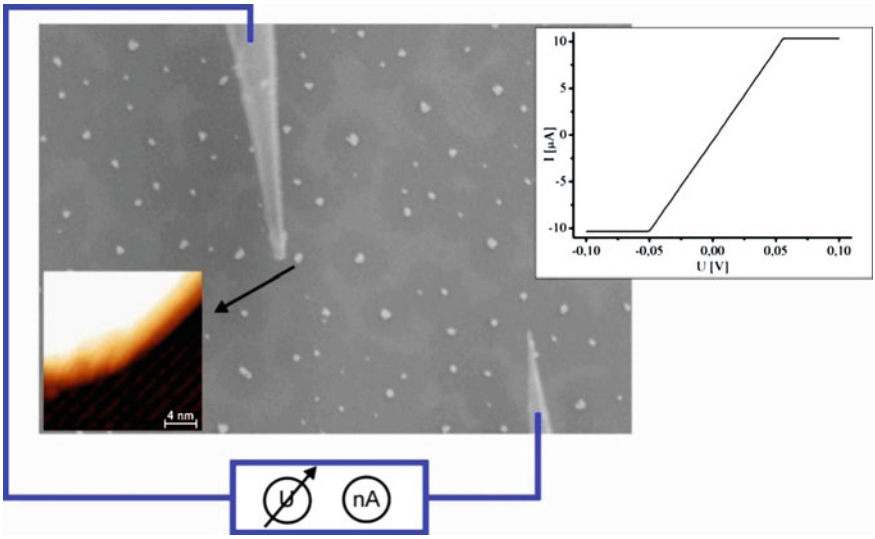

Fig. 7 A schematic view of the two-probe surface conductance measurements. The SEM image shows 2 STM tips of the instrument approaching Au islands at selected inter-probe distance. For each combination of the island pairs $I(U)$ dependence is measured as visualized in the plot at the upper right corner. Lower left corner of the drawing shows a high resolution STM image of gold island on top of the well-defined nanowires assembled by Au deposition and thermal annealing at 770 K (tunneling parameters: sample bias voltage: −2 V; tunneling current: 20 pA)

After a few subsequent cycles of annealing at higher temperatures (from 770 to 820 K) the overall structure of gold islands and both dark and light contrast surface areas remain almost unchanged, with the exception of the light ones which are slightly less defected showing recognizable Ge(001) reconstruction. Comparing our results to previous studies by Wang et al. [3], one could imply that at our annealing conditions gold atoms are diffusing not only over the surface toward gold islands, which are growing during annealing, but also into the bulk of the germanium substrate, making the uncovered surface areas sufficiently clean for undergoing the reconstruction characteristic for pure germanium.

4 Two-Probe Surface Conductance Measurements

Taking the advantage of the above described preparation procedure we could perform surface conductance measurements as a function of the inter-probe distance using multiple Au nano-islands which provide stable Ohmic contacts between the probe tips and the surface. A schematic outline of the experiment is shown in Fig. 7.

Depending on the annealing conditions two different interfaces on the surface can be obtained. The first, in which the gold islands are connected by gold

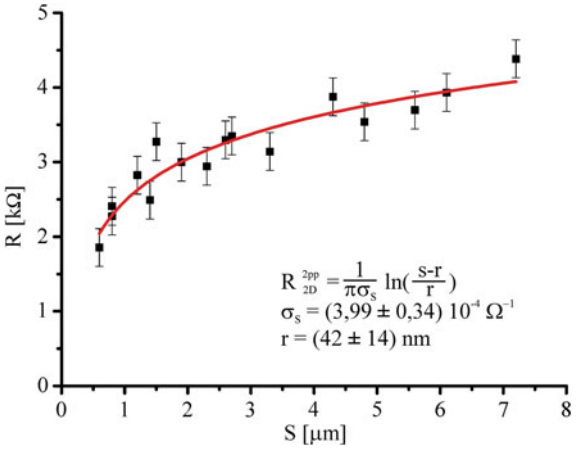

Fig. 8 Two-probe resistance measurements as a function of the probe separation for Au/Ge(001) system annealed at 720 K. Au probe islands are interconnected by the surface network of well reconstructed nanowires

nanostructures on the Ge(001) surface, and the second, in which the gold islands are surrounded by the gold wire "halo" but different island/wire domains are separated by defected Ge(001) areas with partial reconstruction. Therefore, we could measure the surface conductance between islands either connected, or not connected by the gold wires. Measurements are based on direct contact between the W-tip probes and Au islands of 150 nm ÷ 500 nm in size. This allows to decrease the 3D bulk resistance in measurements and to remove uncertainty connected with resistance of the contacting tip. The resistance for each island separation was extracted from the slope of $I(U)$ dependence taken within the voltage range from −0.5 V to +0.5 V.

4.1 Two-Probe Measurements of Au/Ge(001): Uniform Nanowire Coverage Between the Au Island Contacts

The two probes are at first approached to the surface using tunneling current feedback and placed over the selected gold islands, then the tips are manually driven to the islands till the $I(U)$ characteristics between each tip and the sample satisfies the Ohm dependence. When connections between tips and sample are satisfactory, the sample grounding is cut-off and the $I(U)$ dependence between the two tips is collected. The whole process is repeated for various inter-probe distances. The results are shown in Fig. 8.

Following the work by Hofmann & Wells [14] and Jaschinsky et al. [16] two-point probe (2pp) sample resistance could be approximated by solution of the Poisson equation written for an idealized situation, such as for a homogeneous 2D or 3D conductor, zero resistance of the probes and spherical/cylindrical contact shapes. In such a case the measured resistance U/I is related to 2D sample conductivity σ_s in the following way:

$$R_{2D}^{2pp} = \frac{U}{I} = \frac{1}{\pi\sigma_s}\ln\left(\frac{s-r}{r}\right)$$

where s is the spacing between contacting tips, and r is the radius of the contacts (in this case the size of Au islands). In reality it is difficult to separate this 2D part of the resistance from the measured one because of the second significant part which is related to bulk (3D) resistance [14]:

$$R_{3D}^{2pp} = \frac{U}{I} = \frac{1}{\pi\sigma_b}\left(\frac{1}{r} - \frac{1}{s-r}\right)$$

where σ_b is the 3D sample conductivity. For realistic conditions of our experiment the radius of contact (the size of Au islands) is always significantly smaller than the inter-probe spacing (of the order of hundreds of nm), so $r \ll s$ and from the above equations we can approximate that R stays constant for 3D case, and grows slowly as $\sim ln(s)$ for 2D surface conductor. It is clear from Fig. 8 that the resistance measured by two-probe STM tips in the range of 500 nm–10 μm for the case of uniform nanowire coverage has a logarithmic dependence which is in good agreement with theoretical predictions of the model [14, 16] and consistent with a concept of a one-dimensional electron liquid system formed in Au/Ge(001) as proposed by Schaefer et al. [4, 13]. Also fitted values of the model parameters r and σ_s are quite realistic in the context of our experimental conditions.

4.2 Two-Probe Measurements of Au/Ge(001): Nanowire Domains Separated

The same experimental procedure as described in Sect. 4.1 is also used for surface conductance measurements for the second surface of Au/Ge(001) system prepared by annealing at 770 K. The results are presented in Fig. 9 together with the fit of the R dependence on the inter-probe spacing. Also in this case a reasonable fit of the experimental data to the logarithmic dependence is clear, although the scattering of the data points is much larger than in the case of uniform nanowire coverage. This effect is to be expected, since the separation of the nanowire "halos" by the defected areas of partially reconstructed Ge(001) is not controlled in this experiment, and is characterized by a wide random distribution. Also the wire orientation with respect to surface terrace steps is random. Therefore, one of the important assumptions of the model of 2D conductor: presence of uniformly conductive pads is not fulfilled. On the other hand, the values of model parameters r and σ_s obtained by fitting procedures are quite realistic again. The Au islands size (related to the probe size r) is definitely larger in the case of higher temperature annealing (as confirmed by SEM and STM measurements), and σ_s is expected to be smaller (experimentally obtained value is smaller by a factor of 2) than in the previous case of uniform 1D wire coverage.

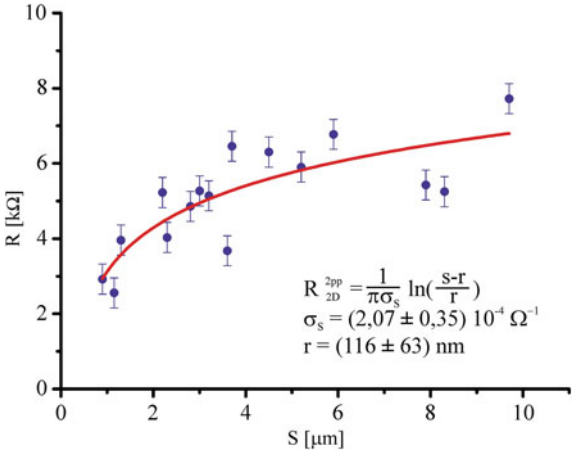

Fig. 9 Two-probe resistance measurements as a function of the probe separation for Au/Ge(001) system annealed at 770 K. Au probe islands surrounded by nanowires are separated by defected Ge(001) domains

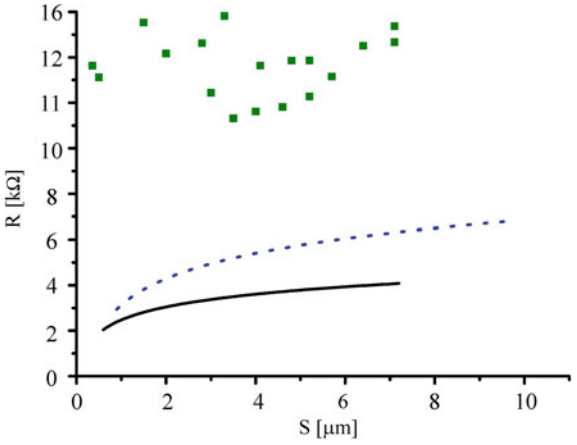

Fig. 10 Comparison of the two-probe resistance measurements as a function of the probe separation for Au/Ge(001) system self-assembled by annealing at 720 K (*solid line*—resistance dependence fitted to the experimental points from Fig. 8), at 770 K (*broken line*—resistance dependence fitted to the experimental points from Fig. 9), all data points for clean reconstructed Ge(001) surface are plotted as *squares*

4.3 Two-Probe Conductance Measurements of Clean Reconstructed Ge(001)

In case of clean, reconstructed Ge(001) surface the measurements are performed using a direct STM tip crash-contact with the sample. This approach unavoidably leads to an increased contribution of the 3D bulk resistance in the measurements and to uncertainty connected with resistance of the contacting tips. Our goal, however, is to compare the resistance versus probe separation dependence for the system anyhow dominated by 3D bulk conductance with the 1D/2D nanostructure covered surfaces described in the previous sections. The comparison is presented in Fig. 10. It is seen that R is considerably higher for clean Ge(001) with no significant dependence on the inter-probe separation s, as it is be expected for 3D

conductor. Since the tip probes are directly penetrating the sample in an uncontrolled way, some additional resistance of the tip contacts can contribute to R and significantly increase spreading of the data points. Nevertheless, clear difference in character of R versus s dependence between clean Ge(001) sample and the two cases of Au/Ge(001) interface is apparent.

5 Conclusions

In this work we have demonstrated that assembling of nanoscopic, atomically structured conductive pads on Ge(001) semiconductor surface could be obtained by gold deposition on Ge(001) at low temperature and subsequent thermal annealing of the Au/Ge(001) system at temperatures above 720 K. The pads consist of regularly spaced structure of anisotropic wires aligned along the direction of Ge(001) reconstruction rows with the inter-wire spacing of 1.6 nm. Unique properties of the system, i.e. co-existence of Au islands distributed within nanowire domains seem to offer good Ohmic contacts for multi-probe conductance measurements. Tunneling current spectroscopy measurements reveal that there is no gap in the surface band structure of the wires and the two-probe conductance measurements indicate a 2D character of the surface resistance dependence on the inter-probe separation.

Our results confirm that two-point probe sample resistance measurements could be adequately described by solution of the Poisson equation written for a homogeneous 2D or 3D conductor as proposed in the work by Hofmann & Wells [14] and Jaschinsky et al. [16].

Acknowledgments Founding for this research has been provided by EC under Large-scale Integrating Project in FET Proactive of the 7th FP entitled "Atomic scale and single molecule logic gate technologies, AtMol". The research was carried out with the equipment purchased thanks to the financial support of the European Regional Development Fund in the framework of the Polish Innovation Economy Operational Program (contract no. POIG.02.01.00-12-023/08). S.G. acknowledges financial support received from the Foundation for Polish Science within START program (2010 and 2011).

References

1. Benson, J.A., Hansen, J.C., McEllistrem, M.T., Clendening, W.D., Tobin, J.G.: An investigation of the Au/Ge(001) interface. Surf. Sci. **193**, 37–46 (1988)
2. Wang, J., Li, M., Altman, E.I.: Scanning tunneling microscopy study of self-organized Au atomic chain growth on Ge(001). Phys. Rev. B **70**, 233312 (2004)
3. Wang, J., Li, M., Altman, E.I.: Scanning tunneling microscopy study of Au growth on Ge(001): bulk migration, self-organization, and clustering. Surf. Sci. **596**, 126–143 (2005)
4. Schaefer, J., Blumenstein, C., Meyer, S., Wisniewski, M., Claessen, R.: New model system for a one-dimensional electron liquid: self-organized atomic gold chains on Ge(001). Phys. Rev. Lett. **101**, 236802 (2008)

5. van Houselt, A., Fischer, M., Poelsema, B., Zandvliet, H.J.W.: Giant missing row reconstruction of Au on Ge(001). Phys. Rev. B **78**, 233410 (2008)
6. Nakatsuji, K., Niikura, R., Shibata, Y., Yamada, M., Iimori, T., Komori, F.: Anisotropic two-dimensional metallic state of Ge(001) c(8 × 2)-Au surfaces: an angle-resolved photoelectron spectroscopy. Phys. Rev. B **80**, 081406(R) (2009)
7. Sauer, S., Fuchs, F., Bechstedt, F., Blumenstein, C., Schaefer, J.: First-principles studies of Au-induced nanowires on Ge(001). Phys. Rev. B **81**, 075412 (2010)
8. Lopez-Moreno, S., Romero, A. H., Munoz, A., Schwingenschloegl, U.: First-principles description of atomic gold chains on Ge(001). Phys. Rev. B **81**, 041415 (2010)
9. Niikura, R., Nakatsuji, K., Komori, F.: Local atomic and electronic structure of Au-adsorbed Ge(001) surfaces: scanning tunneling microscopy and x-ray photoemission spectroscopy. Phys. Rev. B **83**, 035311 (2011)
10. Meyer, S., Schaefer, J., Blumenstein, C., Hoepfner, P., Bostwick, A., McChesney, J. L., Rotenberg, E., Claessen, R.: Strictly one-dimensional electron system in Au chains on Ge(001) revealed by photoelectron k-space mapping. Phys. Rev. B **83**, 121411(R) (2011)
11. Nakatsuji, K., Motomura, Y., Niikura, R., Komori, F.: Shape of metallic band at single-domain Au-adsorbed Ge(001) surface studied by angle-resolved photoemission spectroscopy. Phys. Rev. B **84**, 115411 (2011)
12. Blumenstein, C., Schaefer, J., Morresi, M., Mietke, S., Matzdorf, R., Claessen, R.: Symmetry-breaking phase transition without a peierls instability in conducting monoatomic chains. Phys. Rev. Lett. **107**, 165702 (2011)
13. Blumenstein, C., Schaefer, J., Mietke, S., Meyer, S., Dollinger, A., Lochner, M., Cui, X.Y., Patthey, L., Matzdorf, R., Claessen, R.: Atomically controlled quantum chains hosting a Tomonaga-Luttinger liquid. Nat. Phys. **7**, 776–780 (2011)
14. Hofmann, P., Wells, J.W.: Surface-sensitive conductance measurements. J. Phys.: Condens. Matter **21**, 013003 (2009)
15. Berkelaar, R. P., Sode, H., Mocking, T. F., Kumar, A., Poelsema, B., Zandvliet, H. J. W.: Molecular Bridges. J. Phys. Chem. C **115**, 2268–2272 (2011)
16. Jaschinsky, P., Wensorra, J., Lepsa, M. I., Myslivecek, J., Voigtlaender, B.: Nanoscale charge transport measurements using a double-tip scanning tunneling microscope. J. Appl. Phys. **104**, 094307 (2008)

Nanometer-Scale Four-Point Probe Resistance Measurements of Individual Nanowires by Four-Tip STM

S. Hasegawa, T. Hirahara, Y. Kitaoka, S. Yoshimoto, T. Tono and T. Ohba

Abstract We present a review of our recent results about transport properties of nanowires measured by a four-tip scanning tunneling microscope (STM) installed with metal-coated carbon nanotube (CNT) tips. We first present our custom-made apparatus (with UNISOKU Co.) as well as CNT tips, and then some case studies with two different samples, Co-silicide nanowires self-assembled on Si(110) surface and Cu nanowires made by damascene processes used in LSI industry. It is shown that the four-tip STM with CNT tips is versatile and powerful for measuring the conductivity of individual nanostructures.

1 Introduction

Conductivity measurements in sub-micron or nanometer scale are of great interest in nanoscience and nanotechnology. For example, nanoelectronics such as semiconductor devices requires low and stable electrical resistance of interconnects to maintain device performance. Several kinds of methods to measure the conductivity at nanoscales have been developed including fixed electrodes made by microlithography techniques. A method which adopts tips of scanning tunneling

S. Hasegawa (✉) · T. Hirahara · Y. Kitaoka · S. Yoshimoto · T. Tono
Department of Physics, School of Science, University of Tokyo, 7-3-1, Hongo, Bunkyo-ku, Tokyo 113-0033, Japan
e-mail: shuji@surface.phys.s.u-tokyo.ac.jp

T. Ohba
School of Engineering, University of Tokyo, Tokyo 113-0033, Japan

S. Yoshimoto
Institute of Solid State Physics, University of Tokyo, Kashiwa 277-8581, Japan

C. Joachim (ed.), *Atomic Scale Interconnection Machines*, Advances in Atom and Single Molecule Machines, DOI: 10.1007/978-3-642-28172-3_12,

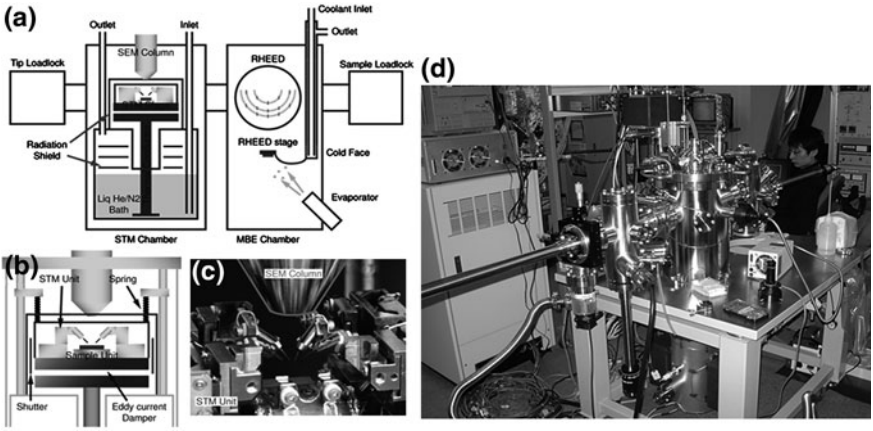

Fig. 1 Schematic drawings of the whole system of low-temperature four-tip STM (**a**) and around the STM stage (**b**) [14]. **c** A close-up photo of the STM stage without radiation shields. **d** The photo of the whole system

microscope (STM) as electrodes, however, has great advantages in positioning of the probes in arbitrary configurations as well as in high spatial resolution of measurements. But single-tip STM is not enough for versatile measurements of transport properties at various kinds of nanostructures: we need source, drain, and gate electrodes. For this reason, several groups [1–10] including companies [11] and our group [12–14] have developed four-tip STM, in which four independent STM tips are operated in an organic manner with aid of a SEM or optical one, and they are used as electrodes for microscopic two- or four-point probe (μ4PP) conductance measurements. In this article, we show our apparatuses including installation of carbon nanotube tips [15–17] and some results of resistance measurements of nanowires obtained in our group.

2 Four-Tip STM System

Figures 1a, b show schematic drawings of our new version of four-tip STM system [14], consisting of a main (STM) chamber, a sample preparation molecular beam epitaxy (MBE) chamber, and two load-lock chambers for sample and tip exchanges, all of which are UHV compatible. The STM tips can be installed into the main chamber from the tip load-lock chamber where a hot W filament is installed for out-gassing of the tips. The sample is introduced from the MBE chamber where cleaning of the sample, deposition of materials and reflection-high-energy electron diffraction (RHEED) observation can be done. The sample can be heated by direct current heating and cooled down to about 30 K by continuous-flow type cryostat in the MBE chamber. These capabilities are necessary for

preparing aimed surface superstructures, epitaxial thin films, nanodots, nanowires, and for making in situ measurements.

The STM stage is mounted on the thermal conducting Cu rod which is soaked in the coolant of the bath cryostat below. The STM stage including the sample and four sets of actuator units is wholly surrounded with two-fold radiation shields and movable shutters. The photo of Fig. 1c is the stage without the radiation shields, and Fig. 1d shows the whole system. The sample and tips can be cooled down to 7 K and can be kept for 23 h with liquid He as coolant. In the case of liquid N_2, the minimum temperature is 80 K and the preserved time is longer than three days.

The SEM column (APCO Mini-EOC) is mounted above the STM stage. The working distance of SEM is about 25 mm. The electron beam is irradiated from SEM column through a 1 mm diameter hole in the radiation shields. A multi-channel plate for the secondary electron detection for SEM imaging is placed on the inside wall the outer shield. The SEM image is obtained from the secondary electron signal or beam induced current signal electron-beam-induced current image (EBIC). The resolution of the SEM is about 20 nm for both signals.

A spring vibration isolator and an eddy-current damper are built between the thermal conductor and the STM stage to avoid vibration of STM stage. The spring isolator decoupled the STM stage from other components. However, during SEM observation, tip/sample exchanges, and cooling the stage, the STM stage is fixed to the thermal conductor (Cu rod) and therefore the isolator and damper are disabled. When we fix the STM stage, the Cu plate works as a thermal conductor and enlarges the contact area for good thermal connection. When we float the STM stage by the springs, this plate makes eddy-current damper. Since alternative arrangements of the small magnets make closed magnetic paths, the magnetization does not affect the SEM beam.

Four sets of tip actuator units are mounted at the corner of the square STM stage, and a sample actuator unit is placed at the center. The actuator units consist of stacked piezo ceramics supported by sapphire plates. For fine positioning or scanning in nanometer or sub-nanometer range, tips and samples are driven by conventional piezoelectric effect of the ceramics by DC voltage. The maximum positioning range by this method is about 2 μm to each direction. For coarse positioning, the actuators are driven by stick–slip mechanism in 5 mm travel distance in XY directions and 2.5 mm in Z direction at accuracy of about 100 nm. In addition to these three- or two-dimensional-motion actuators, the tip actuators also contain small piezo ceramics near the tips for fast STM feedback.

Figure 2 shows a series of SEM images of the four tips arranged in various configurations [12, 13, 18]. The tips are chemically etched W wires. The probe spacing can be changed from 1 mm to ca. 200 nm in Figs. 2a–c. They can be arranged on a line equidistantly (linear μ4PP method) (c, d) in arbitrary directions, or in square arrangement (square-μ4PP method) Figs. 2e–h. The square can be rotated with respect to the sample surface (rotational square-μ4PP method) by re-positioning each tip under computer control. This is useful to measure anisotropic surface conductivity in which the conductivity is different depending on the crystal orientation.

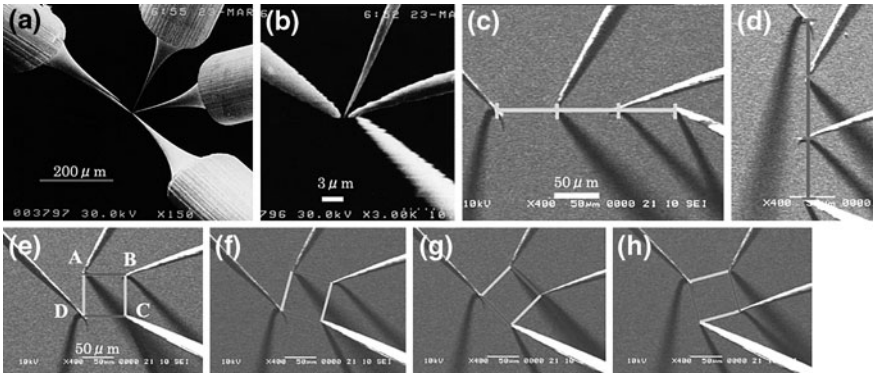

Fig. 2 SEM images of the four W tips in various arrangements in the four-tip STM [12, 13, 18]

3 Metal-Coated Carbon Nanotube Tips

An important issue for the four-tip STM is the probe spacing; the probe spacing should be in the order of 10 nm to measure various kinds of nanostructures. At the present the minimum probe spacing in the multi-tip STM is approximately 100 nm when W tips are used. This is due to the radius of tip apex of electrochemically etched W tips. This probe spacing is not small enough for observing ballistic transport and quantum interference effects because the coherence length of conduction carriers is shorter than 100 nm in many cases. For this reason, continuous efforts are made to shorten the probe spacing down to ca. 10 nm. To make the probe spacing shorter, carbon nanotube tips have been developed in which a carbon nanotube is glued at the end of W tip [19–22]. Since the radius of the (multi-walled) carbon nanotubes is usually ca. 10 nm and the aspect ratio is much higher than usual W tips, two carbon nanotube tips can be brought together into approximately 10 nm spacing. Another feature of the carbon nanotube tip is its mechanical flexibility which can reduce damage to delicate samples such as organic and biological molecules, and make the tips withstand numerous direct contacts to the samples. These properties are quite convenient for the transport measurements by multi-tip STM at nanometer scales. However, there have been problems in the carbon nanotube tips; high contact resistance between the supporting metal tip and the attached carbon nanotube strongly disturbs electron transport at the STM/STS measurements. Moreover, adsorbates contained in the carbon nanotube degrade the surface cleanness of the specimen under STM operation.

A novel technique for overcoming these difficulties has been developed; the carbon nanotube together with the supporting metal tip is wholly coated with a thin metal layer [15]. Figures 3a,b show TEM images of a W-coated carbon nanotube tip glued on a W supporting tip. The W layer of ca. 3 nm thick was deposited by pulsed laser deposition (PLD) method. The W layer fully covers the tip even at the

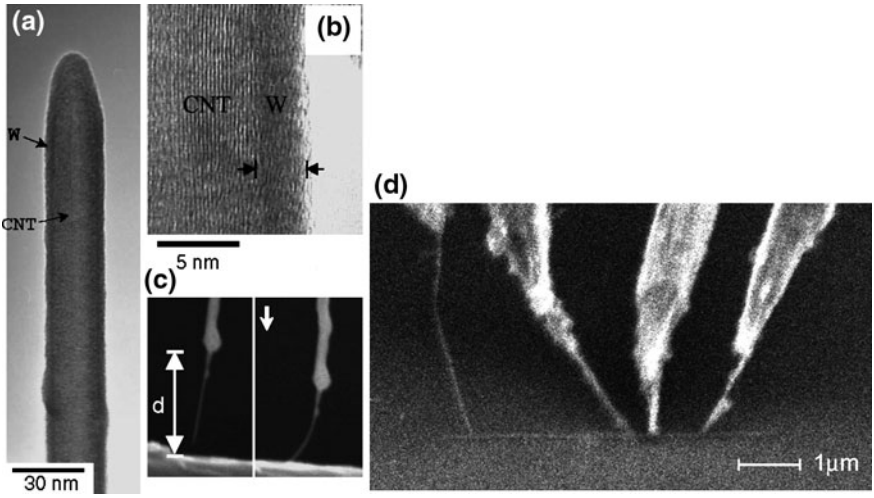

Fig. 3 **a** TEM image and **b** high-resolution TEM image of a W-coated carbon nanotube tip coated by pulsed laser deposition method. **c** SEM images of the W-coated carbon nanotube tip, directly contacting to a sample surface. Reproduced from Ref. [15]. **d** A SEM image showing four carbon nanotube tips contacting a Co-silicide nanowire grown on a Si substrate [23]

end. Figure 3c shows flexibility and robustness of the W-coated carbon nanotube tip upon the direct contact to a sample surface. Figure 3d is a SEM image showing four CNT tips contacting a Co-silicide nanowire grown on a Si substrate [23]. We have also confirmed that the electrical resistance at the glued point between the carbon nanotube and supporting W tip is stably reduced by the metal coating; especially PtIr coating is the most efficient for this purpose [16]. Atomic-resolution STM imaging and STS spectra were acquired with the W-coated carbon nanotube tip at the first attempt [15]. With this metal-coated carbon nanotube tips, we have succeeded in bringing the two tips together into less than 30 nm [17, 23, 24]. Since the resolution of SEM is not enough for observing a smaller probe spacing, we believe that the minimum spacing can be reduced to ca. 20 nm, similar to the diameter of CNT itself.

4 Measuring Co-Silicide Nanowires

$CoSi_2$ nanowires are known to grow self-assembly by depositing high-purity cobalt on a Si(110) clean surface held at 750–850°C in UHV, as shown in Figs. 4a–c [25]. The nanowires become longer and thinner with lowering the substrate temperature during the Co deposition. The wires are single-crystalline, half of which is embedded in the Si substrate as observed by a cross-sectional TEM image of Fig. 4d [25]. The $CoSi_2$ is known to be highly conductive metallic

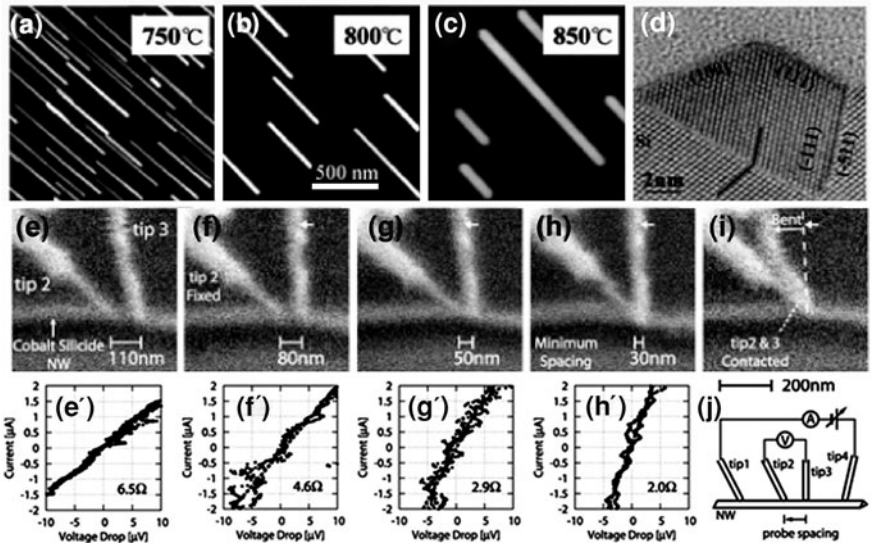

Fig. 4 **a**–**c** Atomic force microscopy images of $CoSi_2$ nanowires formed by depositing Co on the heated Si(110) substrate at different temperatures reproduced [25]. **d** A cross-sectional TEM image of the nanowire from Ref. [25]. **e**–**h** SEM images of the inner pair of CNT tips (tip 2 and tip 3 in (j)), with different probe spacings, contacting one of the nanowires during the resistance measurements in the four-tip STM [23]. The current probes (tip 1 and tip 4) are about 1 μm away from these voltage probes. **e′**–**h′** Four-terminal current–voltage curves measured at the tip configuration shown in **e**–**h**, respectively [23]. The four-terminal resistance R_4t decreased with reducing the probe spacing. **i** The voltage probes contacted each other, and the tip 3 was bent. **j** A schematic showing the four-terminal current–voltage measurements

and its resistivity is 31 ± 9 μΩ cm for the nanowire [26] and ∼15 μΩ cm for the films [27] at 300 K.

As shown in Fig. 3d, the four CNT tips were made contact onto one of the nanowires under SEM observation. The tips were made approach beyond the point of tunneling until the contact resistances became less than 1 MΩ, corresponding to direct contact. At the current–voltage (I–V) measurement, the STM feedback loops were cut. Even if the tip physically contacted the NW, the contact resistance between the tip and sample was higher than 50 kΩ. It was difficult to reduce this resistance because of the nanometer-sized contact area. This is much larger than the resistance of the nanowire itself, which is less than 1 kΩ with probe spacing smaller than 1 μm [26]. Therefore, by two-terminal I–V measurements, the resistance did not depend on the probe spacing due to the large contact resistance at the probe contacts: four-point measurements are indispensable at nanometer scale.

Four-terminal I–V measurements were done by sweeping the bias voltage between tip 1 and tip 4 with recording the current I and the voltage drop V between tip 2 and tip 3, with changing the spacing between tip 2 and tip 3 as shown in Figs. 4e–h. The SEM beam was stopped at the I–V measurements to avoid possible influence on

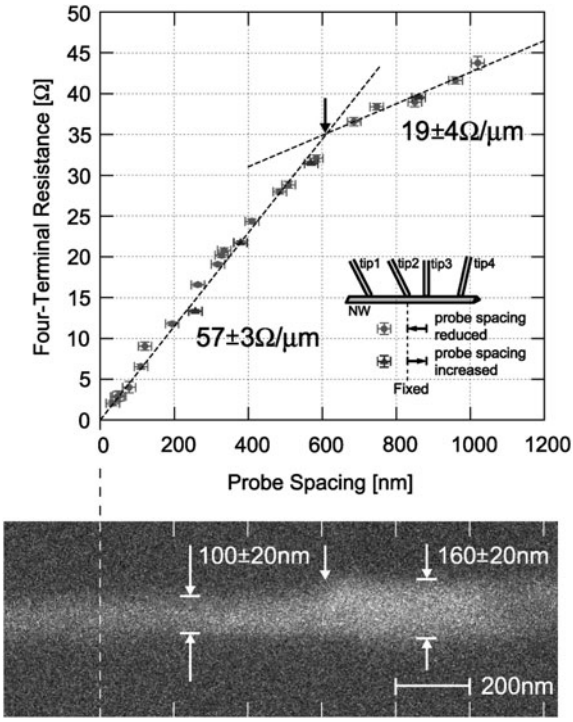

Fig. 5 The measured four-terminal resistance R_4t as a function of the spacing between the voltage probes, and SEM image of the nanowire under measurement (*top view*). The *black arrow* around 600 nm in the graph and the *white arrow* in the SEM image indicate the position where the nanowire width changes, resulting in a change of the resistivity [23]

the resistance caused by high-energy electron beam (10 kV). Figures 4e–h show a series of SEM images around the voltage probes (tip 2 and tip 3) touching on the nanowire, and corresponding four-terminal I–V curves are shown in (e′–h′). We reduced the probe spacing between the voltage probes during taking the I–V characteristics. The positions of the two current probes (tip 1 and tip 4) and one of the voltage probes (tip 2) were fixed in the measurements, and only tip 3 was shifted. All I–V curves were linear. The four-terminal resistance $R_4t = \mathrm{dV/dI}$ around $\mathrm{I} = 0$ decreased with shortening the probe spacing. They are several Ω, much smaller than the contact resistance. A voltage amplifier was introduced at the STM pre-amplifiers to detect small voltage drops resulted from the small resistance. Finally tip 3 bent as shown in Fig. 4i, and R_4t became 0 Ω because of direct contact between the voltage probes. The minimum probe spacing achieved here was 30 ± 20 nm as shown in Fig. 4h. This was limited by the diameter of the CNT tip apex we used, 30 nm (20 nm diameter of CNT + 5 nm thick PtIr layer). The error bar in the probe spacing is determined by the radii of the apexes in tip 2 and tip 3.

We plot the measured four-terminal resistance R_4t as a function of the spacing between the contact points of the voltage probes on the nanowire in Fig. 5. The linear proportional relation in the range 30–600 nm means diffusive transport, and the fit line gives one-dimensional resistivity $\rho_{1D} = 57 \pm 3$ Ω/μm. By extrapolating the data points, there seems to be no residual resistance at zero probe

Table 1 Probe spacing L dependence of the four-terminal resistance R_4t in various conduction mechanisms

Conduction mechanism	1D Ohmic	2D Ohmic	3D Ohmic	1D strong localization	1D weak localization	Ballistic
L-dependence of R_4t	$\propto L^1$	$\propto L^0$ (constant)	$\propto L^{-1}$	$\propto \exp\left(\frac{L}{L_0}\right)$	$\propto \frac{L}{L_0-L}$	$\propto L^0$ (with fluctuation)

L_0 is the localization length

spacing, which is owing to the four-point probe configuration. The gradient decreased to 19 ± 4 Ω/μm above 600 nm probe spacing. This is due to an increase of the nanowire width from 100 ± 20 to 160 ± 20 nm as shown in the SEM image in Fig. 5. By checking the reproducibility we found that the physical contacts of the CNT tips did not cause any significant damage to the nanowire.

We now discuss the transport property of the NW. Table 1 shows a list of the probe spacing L dependence of the four-terminal resistance in various conduction mechanism. The probe spacing dependence of resistance in $CoSi_2$ nanowire showed a linear one-dimensional Ohmic feature ($R_4t \propto$ L). This behavior is due to a one-dimensional conduction path through the nanowire without leakage of current to the underlying three-dimensional substrate or to the two-dimensional substrate surface. This is because a Schottky barrier between the nanowire and the Si substrate confines the current [26]. The mean free path of the electrons in $CoSi_2$ is around 6 nm at room temperature [28], which is much smaller than the width and height of our nanowire as well as the probe spacing. Therefore, our result of diffusive conduction is reasonable. The three-dimensional resistivity of the nanowire can be calculated. The width of the nanowire is determined by SEM image, and the height can be determined by the transmission electron microscope image [25]. We obtain the three-dimensional resistivity 22 ± 4 μΩ cm. In the same way, we obtain 19 ± 4 μΩ cm for the region larger than 600 nm. These values are comparable to the previous results (31 ± 9 μΩ cm) in which similar $CoSi_2$ NWs were measured with W tips in larger probe spacing range [26].

In the ballistic transport regime, two-terminal and four-terminal resistances (R_2t and R_4t) do not depend on the probe spacing. They depend only on the total transmission probability T23 of electron wavefunction between the voltage probes, tip 2 and tip 3 (which are also the current probes in the two-terminal measurement). A remarkable feature of the ballistic transport is that R_4t takes any value between $-R_2t$ and $+R_2t$, meaning that R_4t can be negative by quantum interference effects [21]. At liquid-He temperature, the mean free path of conduction electrons in a $CoSi_2$ film with the thickness of 110 nm becomes ca. 100 nm [27]. Therefore, at low temperatures, we can possibly observe quantum interference effects in resistance at probe spacing we achieved here by using the PtIr-coated CNT tips. The probe spacing dependence of R_4t in the present experiment also excludes observable effects of carrier localization.

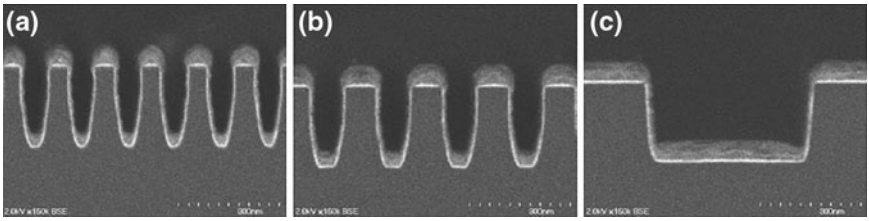

Fig. 6 Cross-sectional SEM image of damascene trenches. The trench widths are **a** 70 nm **b** 100 nm, and **c** 500 nm, respectively [29]

5 Measuring Cu Nanowires

Copper (Cu) wires are now widely used for interconnects in semiconductor devises. But, as the wire width reaches down to the sub-micrometer scale, which is comparable to the mean free path of conduction electrons in the wires, a significant increase in the resistivity has been observed. This is speculated as due to the increased surface and grain boundary scatterings. As the wire width scales down, electrons will undergo reflections more frequently at the surfaces/interfaces, so the collisions with the surfaces/interfaces will become a significant fraction of the total number of collisions. In addition, grain boundaries in polycrystalline wires may act like partially reflecting planes for electron waves, so they also contribute to the increase of resistivity. To investigate these effects directly, the conductivity measurements by the four-tip STM at nanometer scales is very useful [29].

Cu wires having the width between 70 nm and 1 μm were prepared using a Cu/Low-k damascene processes which are now very common in semiconductor industry. Figure 6 shows the cross-sectional SEM images of the damascene structure made in SiO_2 layer. Tantalum (Ta) was used as a barrier metal (BM) in this experiment. Cu damascene lines were formed using conventional Cu process such as seed Cu, electrochemical plating (ECP) Cu for trench filling, and chemical–mechanical polishing. The Cu nanowires are not single-crystalline; they are consisted of small gains. By the electron back-scatter diffraction (EBSD) method, such grains are visualized along the Cu damascene lines [29]. The average grain size was measured to be about 100 nm at 70 nm wide Cu nanowires, which did not change so much with the width, because the grain size is thought to be determined by the height when the width is smaller than the height.

The four-tip STM was used to measure the resistance of individual wires as shown in Fig. 7. By using Pt-coated CNT tips, the probe spacing can be reduced down to the order of several ten nm routinely [23]. When the Pt-coated CNT tips were used, the contact resistance between the tip and sample could not be smaller than 50 kΩ because of its very small contact area. This means that it is impossible to measure conductive materials whose resistance is less than 50 kΩ by the two-point probe method. Only with the four-point probe method, resistances much smaller than the contact resistance (as small as 0.1Ω in the present case) can be measured. Therefore, the combination of the CNT tips and the four-tip STM is very powerful for studies in nanoscale measurements.

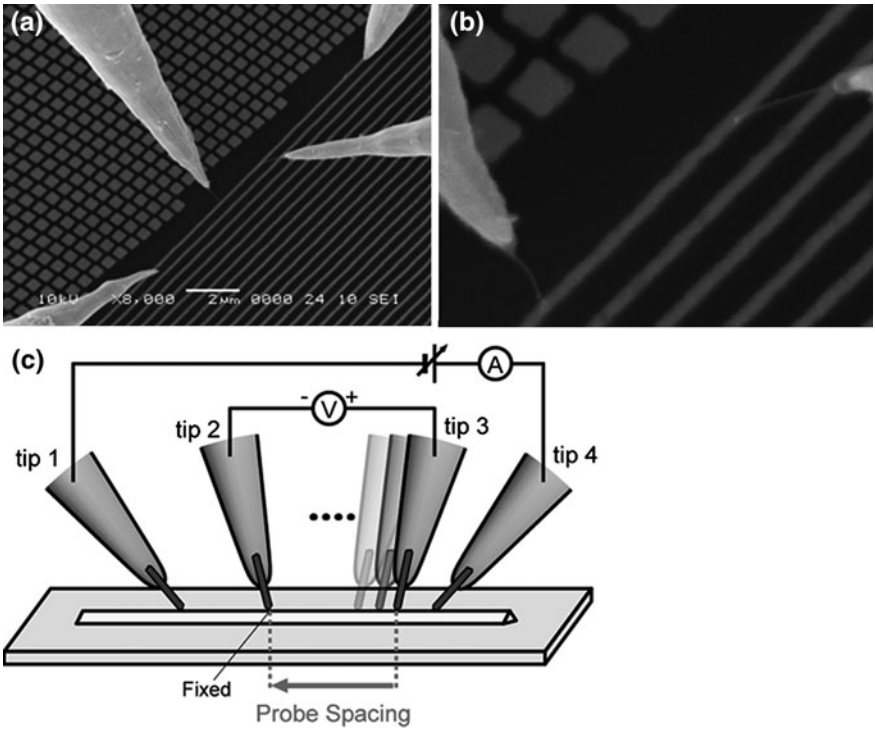

Fig. 7 **a** An SEM image of the Cu wire being contacted with the four probes [29]. **b** The enlargement of the area of rectangle in (**a**). **c** The illustration of the four-terminal I–V measurement

Four-terminal I–V measurements were performed by sweeping the bias voltage between the outer pair of tips and recording the current I and the voltage drop V between the inner pair of tips (Fig. 7c). The probe spacing between the voltage probes was reduced while measuring the I–V characteristics. The two current probes (tip 1 and tip 4) and one of the voltage probes (tip 2) were fixed during the measurements, and only tip 3 was moved between tip 2 and tip 4 (Fig. 7c).

The measured values of four-terminal resistance as a function of the probe spacing between the contact points of the voltage probes on the Cu wires are shown in Figs. 8 and 9. For all of them, the probe spacing dependence of resistance basically showed a linear one-dimensional feature, meaning a diffusive transport. By multiplying the gradient of the fitted straight lines and the cross section of Cu wires (which was estimated from SEM image in Fig. 6), the three-dimensional resistivity was calculated as 4.6, 3.7, and 3.4 Ω cm, for the 70, 50 nm, and 1 μm wide Cu wires, respectively. The resistivity of Cu increased as the line width decreased as shown in Fig. 9b. This result is understood by the Fuchs–Sondheimer theory for the surface-scattering effect and the Mayadas–Shatzkes model for the grain boundary effect [29]. No change in the measured resistance

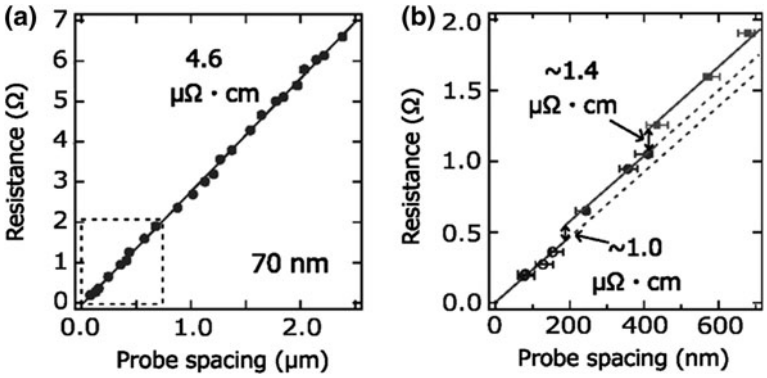

Fig. 8 **a** The measured resistances of the 70 nm wide Cu wire are shown as a function of probe spacing. **b** The enlargement of the area under 600 nm of probe spacing [29]

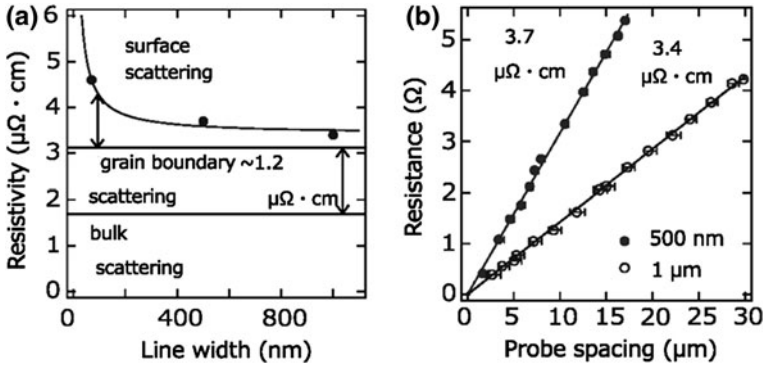

Fig. 9 **a** The measured resistances of Cu wires are shown as a function of probe spacing for the 500 nm and 1 μm wide wires. **b** Plot of the resistivity versus Cu line width [29]. The resistivity coming from the grain boundary scattering is assumed to be constant because the gran size is roughly independent of the line with in our samples

was found in each measurement before and after repeated contacts of CNT tips. It means no significant damage on the sample by the probe contacts.

In this experiment, the probe spacing was reduced to the scale which is comparable with the grain size. Therefore, it can be expected that there will be some change in the resistance when the probe spacing becomes so short that electrons do not undergo grain boundary scattering. This has been indeed observed. Figure 8b shows the enlarged view of the data shown in Fig. 8a for the probe spacing smaller than 600 nm. There is a slight jump in resistance when the probe spacing is shorter than 200 nm. This directly corresponds to the grain boundary scattering where additional resistance occurs at the grain boundary due to the reflection of electron wave there.

6 Concluding Remarks

Electrical measurements using metal-coated CNT tips in the four-tip STM have been demonstrated for the $CoSi_2$ nanowires and Cu damascene wires. Since the apex of CNT tips is around 10 nm and the aspect ratio is so large, it is able to measure the resistance at nanoscale surface areas. The minimum probe spacing in the four-point probe resistance measurement was reduced to a few 10 nm, which is similar or less than the grain size of polycrystalline wires and even the carrier mean free path. The resistance along the wires present here increased linearly with the measured length, meaning classical diffusive transport. But very recently, we have found quasi-ballistic transport in semiconducting $FeSi_2$ nanowires at room temperature where the carrier mean free path is much longer than that of the metallic wires. The details will be reported elsewhere. In the case of Cu damascene wires, the resistivity increased as the wire width decreased. This is due to the surface/interface scattering of carrier. We have evaluated the surface/interface scattering quantitatively to obtain the specularity factor in Fuchs-Sondheimer theory. At the very narrow probe spacing which was comparable to the grain size, the resistance jump due to a single grain boundary was clearly observed. As demonstrated by the measurements presented here, the four-tip STM with CNT tips is a very useful tool for transport physics at nanoscale as well as industrial purposes.

Acknowledgments The present work was done in collaboration with UNISOKU Co., Ltd. in construction of the four-tip STM and Prof. M. Katayama in fabricating CNT tips. It was fully supported by the SENTAN Program of the Japan Science and Technology Agency (JST), and also by Grants-in-Aid for Scientific Research and A3 Foresight Program from the Japanese Society for the Promotion of Science (JSPS).

References

1. Kubo, O., Shingaya, Y., Nakayama, M., Aono, M., Nakayama, T.: Epitaxially grown WOx nanorod probes for sub-100 nm multiple-scanning-probe measurement. Appl. Phys. Lett. **88**, 254101 (2006)
2. Tsukamoto, S., Siu, B., Nakagiri, N.: Twin-probe scanning tunneling microcope. Rev. Sci. Instrum. **62**, 1767 (1991)
3. Okamoto, H., Chen, D. M.: An ultrahigh vacuum dual-tip scanning tunneling microscope operating at 4.2 K. Rev. Sci. Instr. **72**, 4398 (2001)
4. Watanabe, H., Manabe, C., Shigematsu, T., Shimizu, M.: Single molecule DNA device measured with triple-probe atomic force microscope. Appl. Phys. Lett. **78**, 2928 (2001); **79**, 2462 (2001)
5. Lin, X., He, X.B., Yang, T.Z., Guo, W., Shi, D.X., Gao, H.-J., Ma, D.D.D., Lee, S.T., Liu, F., Xie, X.C.: Intrinsic current-voltage properties of nanowires with four-probe scanning tunneling microscopy: A conductance transition of ZnO nanowire. Appl. Phys. Lett. **89**, 043103 (2006)
6. Guise, O., Marbach, H., Yates Jr, J.T., Jung, M.-C., Levy, J.: Development and performance of the nanoworkbench: A four tip STM for conductivity measurements down to submicrometer scales. Rev. Sci. Instr. **76**, 045107 (2005)
7. Ishikawa, M., Yoshimura, M., Ueda, K.: Development of four-probe microscopy for electric conductivity measurement. Jpn. J. Appl. Phys. **44**, 1502 (2005)

8. Takami, K., Akai-Kasaya, M., Saito, A., Aono, M., Kuwahara, Y.: Construction of independently driven double-tip scanning tunneling microscope. Jpn. J. Appl. Phys. **44**, L120 (2005)
9. Grube, H., Harrison, B.C., Jia, J.F., Boland, J.J.: Stability, resolution, and tip–tip imaging by a dual-probe scanning tunneling microscope. Rev. Sci. Instr. **72**, 4388 (2001)
10. Bannani, A., Bobisch, C.A., Möller, R.: Local potentiometry using a multiprobe scanning tunneling microscope. Rev. Sci. Instrum. **79**, 083704 (2008)
11. Omicron Nano Technology GmbH (http://www.omicron.de/), MultiProbe, Inc (http://www.multiprobe.com/), Zyvex Co. (http://www.zyvex.com/)
12. Shiraki, I., Tanabe, F., Hobara, R., Nagao, T., Hasegawa, S.: Independently driven four-tip probes for conductivity measurements in ultlahigh vacuum. Surf. Sci. **493**, 633 (2001)
13. Hasegawa, S., Shiraki, I., Tanabe, F., Hobara, R.: Transport at surface nanostructures measured by four-tip STM. Current Appl. Phys. **2**, 465 (2002)
14. Hobara, R., Nagamura, N., Hasegawa, S., Matsuda, I., Yamamoto, Y., Ishikawa, K., Nagamura, T.: Variable-temperature independently-driven four-tip scanning tunneling microscope. Rev. Sci. Inst. **78**, 053705 (2007)
15. Ikuno, T., Katayama, M., Kishida, M., Kamada, K., Murata, Y., Yasuda, T., Honda, S., Lee, J.-G., Mori, H., Oura, K.: Metal-coated carbon nanotube tip for scanning tunneling microscope. Jpn. J. Appl. Phys. **43**, L644 (2004)
16. Yoshimoto, S., Murata, Y., Hobara, R., Matsuda, I., Kishida, M., Konishi, H., Ikuno, T., Maeda, D., Yasuda, T., Honda, S., Okado, H., Oura, K., Katayama, M., Hasegawa, S.: Electrical characterization of metal-coated carbon-nanotube tips. Jpn. J. Appl. Phys. **44**, L1563 (2005)
17. Konishi, H., Murata, Y., Wongwiriyapan, W., Kishida, M., Tomita, K., Motoyoshi, K., Honda, S., Katayama, M., Yoshimoto, S., Kubo, K., Hobara, R., Matsuda, I., Ha-segawa, S., Yoshimura, M., Lee, J.-G., Mori, H.: High-yield synthesis of conductive carbon nanotube tips for multiprobe scanning tunneling microscope. Rev. Sci. Instr. **78**, 013703 (2007)
18. Kanagawa, T., Hobara, R., Matsuda, I., Tanikawa, T., Natori, A., Hasegawa, S.: Anisotropy in conductance of a quasi-one-dimensional metallic surface state measured by square micro-four-point probe method. Phys. Rev. Lett. **91**, 036805 (2003)
19. Shingaya, Y., et al.: Carbon nanotube tip for scanning tunneling microscopy. Phys. B **323**, 153 (2002)
20. Ishikawa, M., et al.: Simultaneous measurement of topography and contact current by contact mode atomic force microscopy with carbon nanotube probe. Jpn. J. Appl. Phys. **41**, 4908 (2002)
21. Ueda, K., Yoshimura, M., Nagamura, T.: A fabrication method tips for scanning probe microscopes and its apparatus, Japan Patent 2004, No. 3557589
22. Tang, J., Gao, B., Geng, H., Velev, O.D., Qin, L.-C., Zhou, O.: Assembly of ID nanostructures into sub-micrometer diameter fibrils with controlled and variable length by dielectrophoresis. Adv. Mater. **15**, 1352 (2003)
23. Yoshimoto, S., Murata, Y., Hobara, R., Matsuda, I., Kishida, M., Konishi, H., Ikuno, T., Maeda, D., Yasuda, T., Honda, S., Okado, H., Oura, K., Katayama, M., Hasegawa, S.: Four-point probe resistance measurements using ptIr-coated carbon nanotube tips. Nano Lett. **7**, 956 (2007)
24. Murata, Y., Yoshimoto, S., Kishida, M., Maeda, D., Yasuda, T., Ikuno, T., Honda, S., Okado, H., Hobara, R., Matsuda, I., Hasegawa, S., Oura, K., Katayama, M.: Exploiting metal coating of carbon nanotubes for scanning tunneling microscopy probes. Jpn. J. Appl. Phys. **44**, 5336 (2005)
25. He, Z., Smith, D.J., Bennett, P.A.: Endotaxial silicide nanowires. Phys. Rev. Lett. **93**, 256102 (2004)
26. Okino, H., Matsuda, I., Hobara, R., Hosomura, Y., Hasegawa, S., Bennett, P.A.: In situ resistance measurements of epitaxial cobalt silicide nanowires on Si(110). Appl. Phys. Lett. **86**, 233108 (2005)
27. Hensel, J.C., Tung, R.T., Poate, J.M., Unterwald, F.C.: Specular boundary scattering and electrical transport in single-crystal thin films of $CoSi_2$. Phys. Rev. Lett. **54**, 1840 (1985)
28. Allen, P.B., Schulz, W.W.: Bloch-Boltzmann analysis of electron transport in intermetallic compounds - ReO_3, $BaPbO_3$, $CoSi_2$, and Pd_2Si. Phys. Rev. B **47**, 14434 (1993)
29. Kitaoka, Y., Tono, T., Yoshimoto, S., Hirahara, T., Hasegawa, S., Ohba, T.: Direct detection of grain boundary scattering in damascene Cu wires by nanometer-scale four-point probe resistance measurements. Appl. Phys. Lett. **95**, 052110 (2009)

Silicon Surface Conductance Investigated Using a Multiple-Probe Scanning Tunneling Microscope

Janik Zikovsky, Mark H. Salomons, Stanislav A. Dogel and Robert A. Wolkow

Abstract A custom-built multiple probe scanning tunneling microscope (STM) was used to perform measurements of the surface conductivity of Si(111)-7 × 7 and H–Si(111)-1 × 1 surfaces. Metallic contacts with points spaced <1 μm, deposited via electron-beam lithography, were used as contact points for two probes, while a central STM tip imaged the region between the contacts. A novel imaging method measuring the fraction of the tunneling current flowing to each contact was used to image surface conductivity with nanometer resolution. Si(111)-7 × 7 was shown to be significantly more conductive than H–Si(111)-1 × 1. Additionally, the resistance of single atomic steps on the Si(111)-7 × 7 was imaged using this method.

1 Introduction

Studies of nanoscale entities that might one day be deployed within non-CMOS architectures to address the shortcomings of that near mature technology remain topical and challenging. Most exploratory nanoscale electronic schemes, including molecular electronics, have failed to achieve, or often to consider, the key issue of connections to the passive or active nanoentity of interest. Independent of the degree of self-assembly or forced assembly that will be employed in future

J. Zikovsky · R. A. Wolkow (✉)
Department of Physics, University of Alberta,
Edmonton AB T6G 2G7, Canada
e-mail: rwolkow@ualberta.ca

M. H. Salomons · S. A. Dogel · R. A. Wolkow
National Institute for Nanotechnology, 11421 Saskatchewan Drive,
Edmonton AB T6G 2M9, Canada

C. Joachim (ed.), *Atomic Scale Interconnection Machines*, Advances in Atom and Single Molecule Machines, DOI: 10.1007/978-3-642-28172-3_13,

devices, a substantial number of well controlled connections to relatively large electrodes will be required. In our own work we favor explorations of nanoentities based on and of silicon [1]. Emerging control over the charge state of single dangling bonds [2], will allow ultra-efficient (with respect to gate charge) FET-like molecular transistors [3–5]. Moreover, artificial molecules and quantum-dot cellar automata-like structures formed of atomic silicon quantum dots can enable room temperature functioning nanoelectronic devices of extreme lower power consumption [6, 7]. While we have a leaning toward the above areas of study, the techniques described in this paper may be deployed to assist in the electrical characterization of a great variety of nanoscale entities.

Scanned probe microscopes can, within limits, image, manipulate and electrically connect to surface bound entities. But electrical characterization with single probe instruments is limited and as a result many investigators have been attempting to build multi-probe instruments. Several home-made and commercial instruments now exist and more will become available soon. While multiple probes might be very useful in some preliminary studies, ultimately a surface fabricated connector(s)-nanostructure assemblage is required to fully characterize a system of interest and then to eventually deploy it in a practical way. For these reasons we pursue both lithographic contact and multi-probe scanned probe connection strategies simultaneously.

In this chapter, we focus on investigating the properties of surface conductance of two silicon surfaces, Si(111)-7 $\times$ 7 and H–Si(111)-1 $\times$ 1, using a custom-built multiple probe scanning tunneling microscope (STM) operating in ultra-high vacuum (UHV) as well as nanofabricated metal contacts.

2 Methods

2.1 Description of the Multiple Probe UHV Scanning Tunneling Microscope

Our experiments were performed using a custom-built multiple probe scanning tunneling microscope capable of ultra-high vacuum ($<10^{-9}$ Torr base pressure). The heart of the instrument consists of 3 STM scanners on a suspended vibration isolation table. The central STM scanner consists of a tripod of single-crystal piezoelectric elements, offering excellent stability, low piezo "creep" and low cross-talk between scan directions. This scanner is used as our main STM and is routinely capable of atomic resolution. The left and right scanners are referred to as "probes" and consist of traditional tube scanners, except that they are mounted horizontally. These two probes have larger ranges of motion, making it easier to locate and contact features, but are less mechanically stable, making atomic-resolution imaging more difficult. The main STM scanner is controlled using a Nanonis controller and software, whereas the probes use two Createc controllers and custom software.

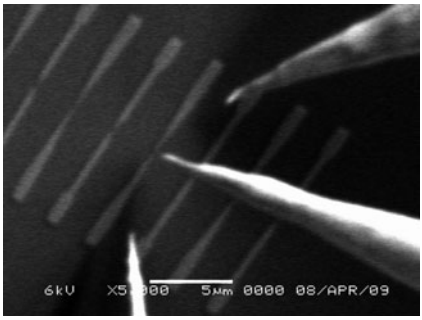

Fig. 1 SEM images of three STM tips brought in close proximity, over a pattern of metal pads. The spacing between the tips can easily be reduced to below one micron

In addition to the micron-range level of motion of the piezoelectric tube of the probes, they are mounted on stick-slip UHV coarse movers capable of multi-millimeter motion in all three directions. The main STM tip is mounted on a coarse mover capable of only vertical motion (for tip approach). Finally, the sample is mounted with several millimeters of motion in the X–Y horizontal plane. This combination of nine coarse movers means that all three tips can be brought in arbitrarily close to each other (within <1 μm), and close to any point on the sample's surface. The nine degrees of freedom of the piezoelectric elements then allows the tips to come into tunneling distance to the surface and to be placed within nanometers of each other.

The tip and sample handling system of the instrument is unusual, in that no holders are used. Instead, bare tungsten wires and bare samples are used. Custom-built UHV pliers are used to move samples and tips from load-locks to their use positions. The tips are held in the scanners with metal clips, and samples are held on a ceramic plate with foil springs.

Avoiding the use of holders has a significant advantage in increasing the throughput of the instrument: by minimizing the amount of matter that is exposed to atmosphere before entering the UHV chamber, degassing of tips and samples is significantly faster. The UHV pliers act as electrical connections that allow us to run a current through the tip wire or through the Si sample crystal, which quickly degasses due to its small surface area. Since the pliers are only rarely exposed to atmosphere, there is no need to degas the sample holder, a task that typically takes several hours in a traditional STM. Using bare tips and wires, only minutes are required to prepare a sample or tip for use.

A JEOL UHV scanning electron microscope (SEM) is installed on the instrument and affords us a direct view of the three STM tips (see Fig. 1). Using the SEM and the coarse movers for the sample and probes allows the user to align all three probes to a range that is close enough to use the piezoelectric scanners.

2.2 Metal Contacts and Surface Preparation

As mentioned in the previous section, the use of piezoelectric scanners allows us to bring the three probe tips arbitrarily close to each other, and indeed it is possible to touch the three tips together. However, the radius of the tips limits the distance at

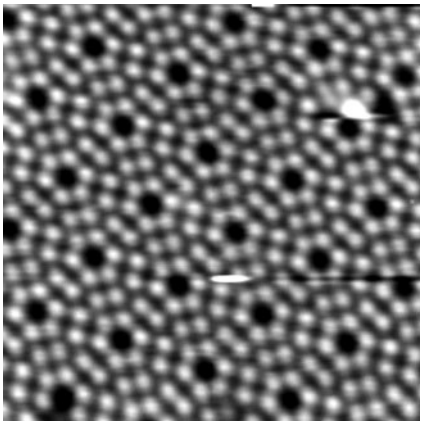

Fig. 2 STM image of a high-quality Si(111)-7 × 7 surface (10 nm wide, +2.0 V, 0.1 nA)

which one can image an area of the surface while touching down another probe. In practice, with etched tungsten tips, it is not possible to image the surface any closer than ∼50 nm from the touch-down point of another tip. To work around this problem, we developed techniques to deposit or grow elongated metal contacts on Si surfaces. One technique we have used is the growth of self-formed TiSi islands on Si(100) and Si(111) surfaces [8, 9]. The results in this chapter, however, used metal patterns deposited by electron-beam lithography, which we describe next.

2.2.1 Titanium Contacts on Si(111)-7 × 7

Electron-beam lithography (EBL) was used to define a set of Titanium contacts on a surface of Si(111). A positive photoresist (PMMA 950 A2) was spin-coated to a thickness of ∼90 nm on a cleaned Si(111) wafer. A Raith 150 EBL instrument was used to write the pattern, using a beam current of ∼0.08 nA and a line writing speed of ∼1.8 mm/sec. After development in MIBK:IPA, the metal was deposited using a sputter deposition system with a deposition rate of 0.5 Å/s. We deposited from 30 to 40 nm of Ti. The resist and remaining metal was then lifted-off using a 60°C acetone bath. The SEM image in Fig. 1 shows part of the pattern deposited.

After EBL and metal deposition, the samples were brought into the STM instrument. Annealing is required in order to clean and degas the crystal; to obtain the Si(111)-7 × 7 surface reconstruction, a temperature of at least 850°C is typically required [10, 11]; flashing to higher temperatures helps to remove impurities. However, we found that excessive heating (e.g. 1200°C) caused the Ti contacts to break up and form smaller $TiSi_2$ islands that were not electrically continuous. The annealing procedure that we found to give good results consisted of flashing the crystal to 900°C, then 950°C and finally 1000°C for 5 s with 60 s of pause between flashes. A final anneal was then produced by lowering the temperature from 950 to 500°C in approx. 2 min. This technique produced high-quality Si(111)-7 × 7 surfaces (see Fig. 2) without adversely affecting the metal contact pads.

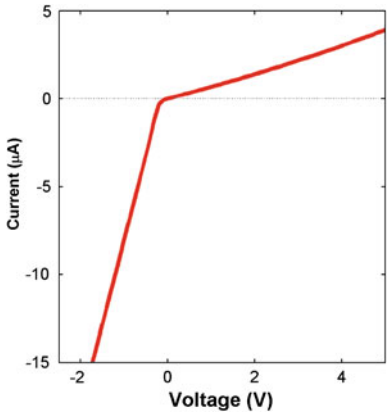

Fig. 3 Typical IV curve showing leaky Schottky-like diode behavior, measured on a single metal contact on low-doped *n*-type Si(111)-7 × 7. The voltage was applied on macroscopic clips far from the contact, which was grounded

2.2.2 Chromium Contacts on H–Si(111)-1 × 1

Using the same EBL procedure described above, we deposited 20 nm of Cr metal on a Si(111) wafer. The surface was then hydrogen-terminated using a standard wet chemical etching technique, as described in [12, 13]. SEM images of the resulting pattern showed good adhesion of the Cr to the surface after etching. Previous tests using Ti metal showed that the hydrogen-termination process etched the metal away; other tests using Pt showed poor adhesion of the metal film. STM imaging of the resulting H–Si(111)-1 × 1 surface showed that it was of very good quality, with large flat areas between the metal contacts that could be suitable experimental sites.

2.3 Finding and Touching Contacts with STM Tips

The STM tips used in this experiment were chemically etched W wires, cleaned in UHV by resistive heating to a dull red glow for a few seconds. Additional cleaning and quality checks were performed using an in situ field-ion microscope (FIM) to image the atoms at the tip.

The EBL pattern used defines large (1 × 2 μm) contact pads that narrow to two sharp points (<100 nm in radius) spaced from 20 to 1000 nm apart. The surface of interest is the area between the contacts; therefore the first step of our three-probe experiments was to use the SEM and STM together in an iterative fashion to place the main STM tip in the surface between the two contacts. STM scans of the main probe revealed the edges of the contacts, confirming the position. Once the main tip position was known, it was retracted by ∼1 μm and the left and right probes performed large scans so as to find the contact pads. Once a probe was centered over a metal pad, the feedback loop was turned off and the tip was pushed into the contact by a fixed distance (typically 10 nm). This established a metal-to-metal

contact between the tip and the metal pad. A current–voltage (IV) curve was measured by applying a varying voltage to the sample while measuring the current flowing to the grounded tip. Figure 3 shows a typical IV curve obtained; the curve reveals the expected Schottky diode-like behavior of a small metal contact on a low-doped semiconductor substrate [14]. The probe was pushed in further, in steps of a few nm, repeating IV curves each time until no change was seen between curves. At that point we considered that the contact resistance between the metal tip and metal contact was insignificant and that the IV curve measured was inherent to the character of the metal–semiconductor contact.

3 Scanning Tunneling Fractional Current Imaging

3.1 Description

In this section, we describe a STM imaging technique that is related to the technique of *scanning tunneling potentiometry* (STP) developed by Muralt and Pohl in 1985 [15]. In STP, a potential gradient is applied across two electrodes deposited on a sample. Using a combination of AC and DC tunneling bias, the technique effectively measures the potential at the surface immediately under the STM tip. One can then process the data to form an image of the potential at the surface with nanometer resolution.

The scanning tunneling fractional current imaging (STFCI) method is a variant on STP. In a normal STM experiment using our setup, the sample is biased to a given voltage and the tip is connected to a preamplifier that measures current while acting as a virtual ground. In STFCI, the STM tip is biased, and both contacts are connected to preamplifiers that act as virtual grounds (see Fig. 4a). Two tunneling currents are measured, I_A and I_B, from both contacts. During a STFCI experiments, the feedback loop is set to maintain a constant *total* tunneling current $I = I_A + I_B$. During the scan, both I_A and I_B currents, as well as the topography are recorded. We then process the images to calculate an image of *fractional current* F_A, where $F_A = I_A/(I_A + I_B)$ is the fraction of current flowing to contact A, and ranges between 0 and 1.

3.1.1 Equivalency to Scanning Tunneling Potentiometry

In this section, we show that, under some assumptions, the fractional current F_A measured by STFCI can be scaled to be equivalent to the measured surface voltage in a STP experiment. The schematic in Fig. 4c shows the electrical connections made to a sample in a traditional STP experiment, with the assumption that the sample is a simple continuous Ohmic resistor split in two parts, R_A and R_B, at the position of the STM tip. We begin by noting that the resistance of the tunneling gap, R_{gap}, will normally be in the range of 1 GΩ or higher (1 nA at 1 V bias). For our experiments, this means *that* $R_{\text{gap}} \gg R_A$ or R_B. Therefore, the tunneling current I_{tunnel} is negligible. The tip measures the voltage at the surface, labeled V_m

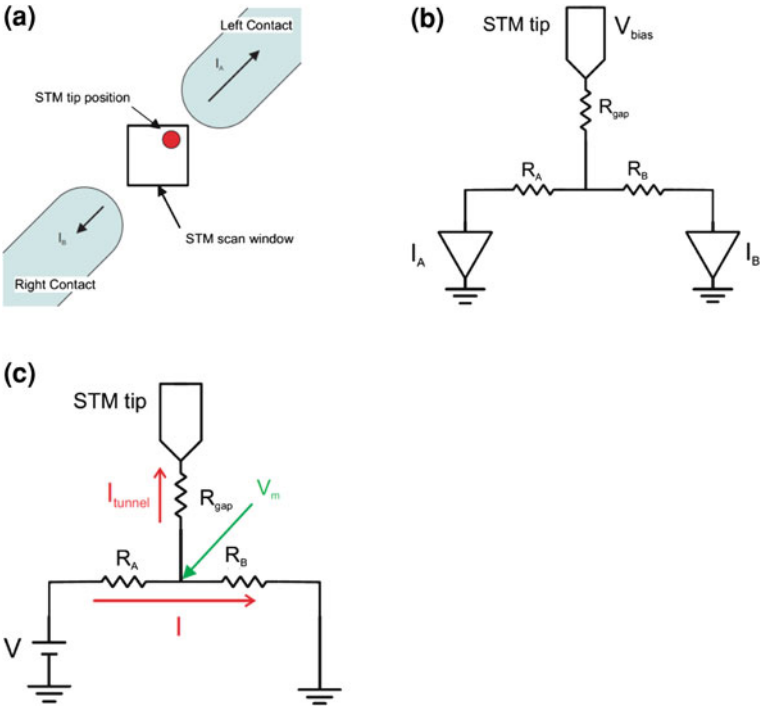

Fig. 4 **a** Schematic of the positions of the contacts and tip during a STFCI experiment. The orientation of the *left/right* contacts corresponds to what is seen in a STM scan. **b** Schematic of the equivalent electrical connections in STFCI. **c** Schematic of a STP experiment

on the schematic. We can easily calculate that the fraction of measured voltage versus applied voltage is given by:

$$\frac{V_m}{V} = \frac{R_B}{R_A + R_B}$$

Let us now evaluate the currents in a STFCI experiment. Most of the bias voltage drop V_b is through the tunneling gap. There is a small voltage remaining at the surface under the tip: V_t. The currents to probes A and B are $I_A = V_t/R_A$, $I_B = V_t/R_B$. The total tunneling current is $I_{\text{tot}} = V_t/R_{\text{tot}}$, with the total resistance given by two parallel resistors $R_{\text{tot}} = \left(R_A^{-1} + R_B^{-1}\right)^{-1}$. With this, we can calculate the fractional current:

$$F_A = \frac{I_A}{I_{\text{tot}}} = \frac{V_t/R_A}{V_t\left(R_A^{-1} + R_B^{-1}\right)} = \frac{R_B}{R_A + R_B}$$

which is the same value as the ration of V_m to V measured in a STP experiment. Therefore, the fractional current F_A found in a STFCI experiment can be directly

scaled to the voltage that would be measured in a STP experiment. This conclusion does not depend on the magnitudes of R_A or R_B so long as they are negligible compared to the tunneling gap. This equivalence also assumes that the material's conductivity is Ohmic.

3.2 Results

The Si(111)-7 × 7 surface is a complex surface reconstruction containing 19 dangling bonds per unit cell [16], giving rise to multiple levels inside the band gap of Si and creating a quasi-metallic 2D conductor [17]. The overall surface conductivity of this surface has been studied in many ways, from 4-point-probe measurements [18–20] to STM experiments [21, 22]. By contrast, the hydrogen-terminated H–Si(111)-1 × 1 surface has no dangling bonds and we do not expect it to contribute to conductivity. We describe below the results of STFCI-mode experiments we performed on H–Si(111)-1 × 1 and Si(111)-7 × 7 surfaces.

3.2.1 STFCI on H–Si(111)-1 × 1

Using the procedure described above, a hydrogen-terminated Si(111)-1 × 1 surface with Cr contacts was prepared on a low-doped, *p*-type Si wafer. We performed STFCI in the region between two contacts spaced 400 nm apart. Figure 5a shows the fractional current image between the contacts. As the cross-section in Fig. 5b shows, the fraction of current flowing to contact A increases smoothly as the STM tip moves closer to the given contact. Away from either contact, the expected linear Ohmic behavior is observed, whereas curvature in the F_A curve is seen close to the contacts where geometric effects become significant. A finite element model simulation of this situation, performed using COMSOL Multiphysics software, predicted very similar behavior (not pictured).

3.2.2 Forming Si(111)-7 × 7 on a H–Si(111)-1 × 1 Surface

If a H–Si(111)-1 × 1 surface is heated sufficiently, it desorbs its surface hydrogen and will reconstruct into Si(111)-7 × 7. We performed local H desorption by flowing a current through the Cr contacts (1 mA for 60 s). Figure 6 shows the result of this localized heating. As one would expect given the geometry of the contacts, the highest current density and therefore the highest temperatures were achieved nearest the contacts. Figure 6a shows a STM image (performed in STFCI mode) near one of the contacts. A "bright" patch, approximately 60 nm wide, is seen near the contact. The close-up view in Fig. 6d shows that the surface appears brighter because it has lost its hydrogen and has partially reconstructed in a 7 × 7 pattern; other images taken away from this bright region showed the unmodified H–Si(111)-1 × 1 surface.

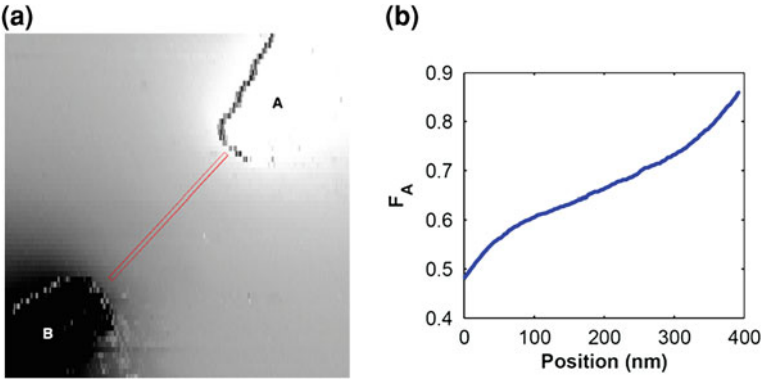

Fig. 5 **a** F_A, fraction of current going to contact A (*upper right*). Color scale: 0.2–0.9. **b** Cross-section of F_A along the *red bar* in (**a**), from *lower left* to *upper right*

The results from fractional current imaging for this composite surface are very interesting. Fig. 6b and c show that F_A barely changes in the desorbed region—changing by <0.01 over 60 nm. By contrast, over the hydrogen-terminated surface, F_A changes by 0.13 over the same distance. This indicates that the resistivity of the surface of the desorbed region is significantly lower than that of the hydrogen-terminated region. The approximately linear change in F_A in the H-terminated region indicates that the surface contributes little or nothing to conduction, which is there dominated by bulk conductance. By contrast, in the desorbed region, the conductance at the tip is dominated by that of the surface.

3.2.3 STFCI across Steps on the Si(111)-7 × 7 Surface

If the Si(111)-7 × 7 surface is a significant conductor, then it follows that the steps on its surface would be measurable breaks in conduction. Such an effect has previously been observed on single atomic steps of the much more conductive Si(111)-($\sqrt{3} \times \sqrt{3}$)-Ag surface [23, 24]. To the best of our knowledge, the resistance of a step on the Si(111)-7 × 7 surface has not been observed previously.

Our initial attempts used EBL-defined contacts that were annealed at a high temperature. Unfortunately, we observed that large "bunches" of several steps separated the contacts after annealing. The majority of the change F_A would occur at these step bunches, making the effect of a single step difficult to observe. Therefore, we instead used a low-doped *n*-type Si(111)-7 × 7 surface prepared without any metal contacts. The two probes (contacts A and B) were touched down directly onto the Si(111) surface, spaced approximately 100 μm apart. The main STM tip was placed very close to contact A. Figure 7 shows the result of a scan taken in STFCI mode; contact B is located near the bottom left corner of the image. Figure 7a shows the topography scan, with several terraces separated by single steps. The corresponding F_A image in Fig. 7b shows that these terraces have distinct values of F_A; the largest change in F_A occurs at step edges, which must be

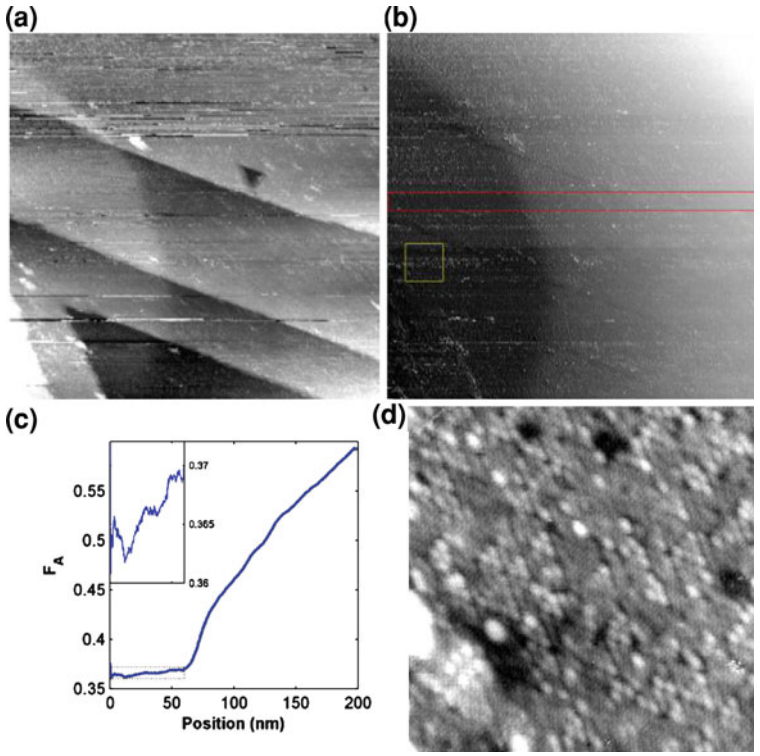

Fig. 6 STFCI image showing the higher conductivity of a patch of Si(111)-7 × 7 desorbed on low-doped, *p*-type Si(111)-1 × 1. 300 nA, +2.0 V tip bias. **a** Topography view, 200 nm wide. **b** F_A image, color scale: 0.3–0.7. **c** Cross-section of F_A taken along the *red box* in (**b**). *Inset* F_A in the 7 × 7 region. **d** STM image taken in the desorbed region (20 nm wide)

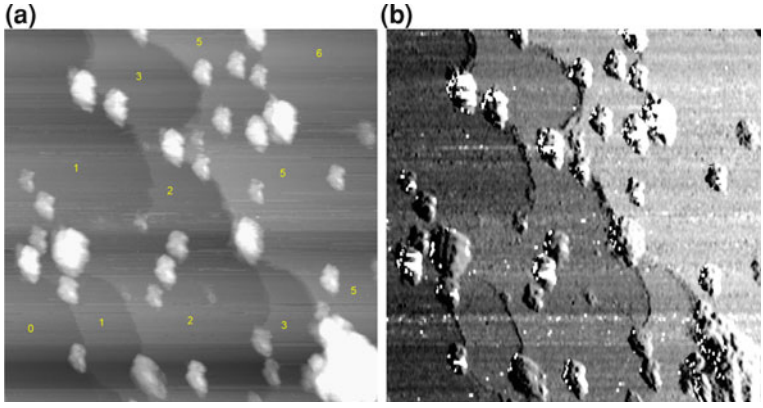

Fig. 7 STFCI experiment showing a few monoatomic steps on Si(111)-7 × 7 (250 nm wide, +2 V, 300 pA). **a** Topography view with numbers indicating the height of each terrace (in monoatomic Si(111) steps). **b** Corresponding F_A image. Color scale: 0.08–0.16

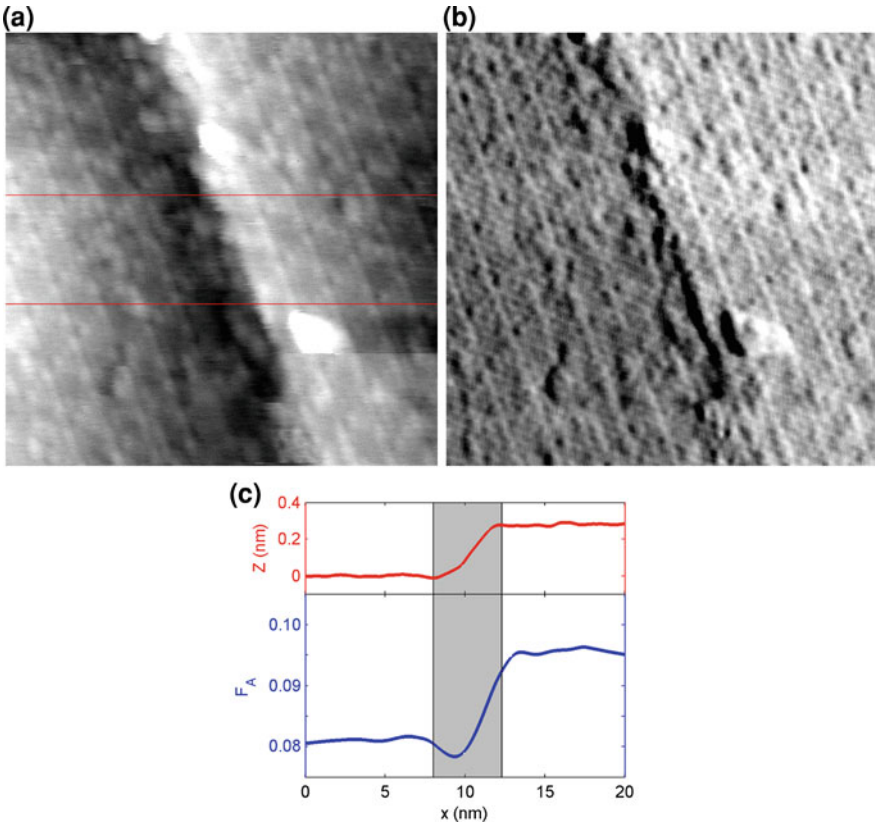

Fig. 8 STFCI measurement of a single monoatomic step on a Si(111)-7 × 7 surface. **a** Topography (20 nm wide, +2 V, 300 pA). **b** F_A, color scale: 0.06–0.11. **c** Cross-section of z and F_A along the *red bar* in (**a**), averaged over 5 nm width with 5 nm smoothing. The *grey bar* indicates the region around the step

significantly more resistive than the terrace. This is highlighted in Fig. 8, a STFCI measurement of a single monoatomic step on Si(111)-7 × 7. The cross-section of Z and F_A in Fig. 8c shows a clear step in F_A corresponding with the monoatomic step.

4 Conclusions

We have demonstrated the use of a custom-built, 3-probe UHV STM in studying the conductivity of Si surfaces. EBL-defined metal contacts were deposited on Si surfaces so as to allow biasing surfaces at distances of only a few nanometers from an STM tip position. The use of the scanning tunneling fractional current imaging technique allowed direct visualization of the conductivity of a sample

with nanometer spatial resolution. On a terminated H–Si(111)-1 × 1 surface, an expected Ohmic pattern of conduction was seen. When a patch of hydrogen was desorbed via resistive heating, the fractional current image showed that the desorbed region (consisting of partially reconstructed Si(111)-7 × 7) was far more conductive than the surrounding H-terminated region. On a Si(111)-7 × 7 viewed in STFCI mode, we observed that the largest change in F_A occurs at the step edges; using this method we were able to observe the resistivity of a single monoatomic step on Si(111)-7 × 7 for the first time.

References

1. Wolkow, R.A.: Controlled molecular adsorption on silicon: Laying a foundation for molecular devices. Annu. Rev. Phys. Chem. **50**, 413–441 (1999)
2. Pitters, J.L., Dogel, I.A., et al.: Charge control of surface dangling bonds using nanoscale schottky contacts. ACS Nano **5**(3), 1984–1989 (2011)
3. Piva, P.G., DiLabio, G.A., et al.: Field regulation of single-molecule conductivity by a charged surface atom. Nature **435**(7042), 658–661 (2005)
4. Wolkow, R.A.: Electrostatically Regulated Atomic Scale Electroconductivity Device (Patent filed 09/10/2007) (2007)
5. Kirczenow, G., Piva, P. G., et al.: Modulation of electrical conduction through individual molecules on silicon by the electrostatic fields of nearby polar molecules: theory and experiment. Phys. Rev. B. **80**(3), (2009)
6. Haider, M.B., Pitters, J.L., et al.: Controlled coupling and occupation of silicon atomic quantum dots at room temperature. Phys. Rev. Lett. **102**(4), 4 (2009)
7. Livadaru, L., Xue, P., et al.: Dangling-bond charge qubit on a silicon surface. New J. Phys. **12**, 15 (2011)
8. Medeiros-Ribeiro, G., Ohlberg, D.A.A., et al.: Titanium disilicide nanostructures: two phases and their surfaces. Surf. Sci. **431**(1–3), 116–127 (1999)
9. Goldfarb, I., Grossman, S., et al.: Evolution of epitaxial titanium silicide nanocrystals as a function of growth method and annealing treatments. Appl. Surf. Sci. **252**(15), 5355–5360 (2006)
10. Binnig, G., Rohrer, H., et al.: 7X7 Reconstruction on Si(111) resolved in real space. Phys. Rev. Lett. **50**(2), 120–123 (1983)
11. Vinh, L.T., Eddrief, M., et al.: Low-temperature formation of Si(111)7 × 7 surfaces from chemically prepared H/Si(111)-(1 × −1) surfaces. Appl. Phys. Lett. **64**(24), 3308–3310 (1994)
12. Higashi, G.S., Chabal, Y.J., et al.: Ideal hydrogen termination of the Si-(111) surface. Appl. Phys. Lett. **56**(7), 656–658 (1990)
13. Angermann, H., Kliefoth, K., et al.: Preparation of H-terminated Si surfaces and their characterisation by measuring the surface state density. Appl. Surf. Sci. **104**, 107–112 (1996)
14. Rhoderick, E.H., Williams, R.H.: Metal-Semiconductor Contacts. Oxford University Press, Oxford (1988)
15. Muralt, P., Pohl, D.W.: Scanning tunneling potentiometry. Appl. Phys. Lett. **48**(8), 514–516 (1986)
16. Losio, R., Altmann, K.N., et al.: Fermi surface of Si(111)7 × 7. Phys. Rev. B **61**(16), 10845–10853 (2000)
17. Northrup, J.E.: Origin of surface-states on Si(111)(7 × 7). Phys. Rev. Lett. **57**(1), 154–157 (1986)
18. Shiraki, I., Tanabe, F., et al.: Independently driven four-tip probes for conductivity measurements in ultrahigh vacuum. Surf. Sci. **493**(1–3), 633–643 (2001)
19. Hasegawa, S., Shiraki, I., et al.: Electrical conduction through surface superstructures measured by microscopic four-point probes. Surf. Rev. Lett. **10**(6), 963–980 (2003)
20. Wells, J.W., Kallehauge, J.F., et al.: Disentangling surface, bulk, and space-charge-layer conductivity in Si(111)-(7 × 7). Phys. Rev. Lett. **97**(20), 206803 (2006)

21. Hasegawa, Y., Lyo, I.W., et al.: Measurement of surface state conductance using STM point contacts. Surf. Sci. **358**(1–3), 32–37 (1996)
22. Heike, S., Watanabe, S., et al.: Electron conduction through surface states of the Si(111)-(7 × 7) surface. Phys. Rev. Lett. **81**(4), 890–893 (1998)
23. Matsuda, I., Ueno, M., et al.: Electrical resistance of a monatomic step on a crystal surface. Phys. Rev. Lett. **93**(23), 236801 (2004)
24. Bannani, A., Bobisch, C.A., et al.: Local potentiometry using a multiprobe scanning tunneling microscope. Rev. Sci. Instrum. **79**(8), 083704 (2008)

Atomic-Scale Devices in Silicon by Scanning Tunneling Microscopy

J. A. Miwa and M. Y. Simmons

Abstract The ability to control matter at the atomic scale and build devices with atomic precision is one of the core challenges of nanotechnology. In this chapter, we outline a complete fabrication strategy for building atomic-scale devices in silicon with atomic precision in all three-dimensions. Using scanning tunneling microscopy (STM)-based lithography we have imaged and placed phosphorus dopant atoms in precise locations on a silicon surface before encapsulating them with silicon using low temperature molecular beam epitaxy to activate the dopants. Etched registration markers allow us to locate and align external electrical contacts to the buried STM-patterned dopant atoms so that we can perform electron transport measurements outside the microscope at cryogenic temperatures. Using this unique strategy we discuss the realization of conducting nanoscale wires, tunnel junctions and all epitaxial single electron transistors. Finally we provide an outlook to achieving truly single atom device architectures toward our ultimate goal of realizing a silicon-based quantum computer.

1 Introduction: Single Atom Device Architectures

Dopants play a critical role in information technology as charge providers that modify the electronic properties of semiconductor materials. As societal demands drive the miniaturization of semiconductor devices toward the atomic scale, transistor characteristics are no longer determined by a distribution of dopants, but by single dopants within the device [1–3]. The exact location and number of

J. A. Miwa · M. Y. Simmons (✉)
Australian Research Council Centre of Excellence for Quantum Computation and Communication Technology, University of New South Wales, Sydney NSW 2052, Australia
e-mail: michelle.simmons@unsw.edu.au

C. Joachim (ed.), *Atomic Scale Interconnection Machines*, Advances in Atom and Single Molecule Machines, DOI: 10.1007/978-3-642-28172-3_14,

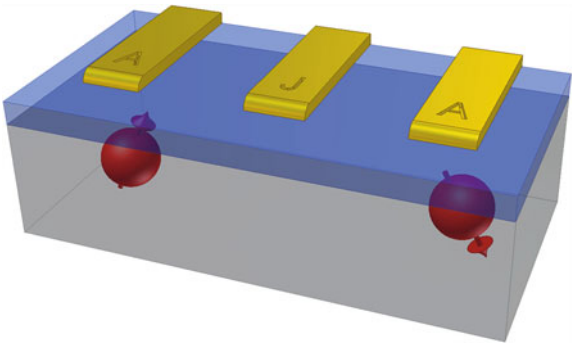

Fig. 1 A schematic of the Kane nuclear spin quantum computer: the *red-colored* ^{31}P atoms are strategically placed $\sim$20 nm apart within a single-crystal silicon host (*gray*). A- and J-type surface gates (*gold*) are deposited on an oxide barrier (*blue*) directly above/between the individual P donors, respectively

dopants within a transistor are known to severely affect device behavior [4]. As a consequence, there is a growing demand to achieve atomically precise placement of individual dopants within a device.

Concurrently there have been proposals to use single dopants as fundamental units for quantum information processing. One immensely attractive proposal is the solid-state implementation of a scalable silicon quantum computer [5]. In a quantum computer, the classical bits are replaced by a robust two-level quantum system, known as a quantum bit or qubit. The field of quantum computation has exploded, since its inception circa 1982 [6], with the development of dedicated quantum algorithms, including the prime factorization of large numbers [7, 8] and exhaustive search [9] algorithms. These are not just mathematical curiosities; in future, quantum computing promises to impact key technologies, including database searching, information processing, storage, cryptography, communication, simulation and metrology.

Interestingly, the quantum mechanics governing quantum computation are universal and therefore independent of the physical implementation of the quantum computer. As a consequence, a vast number of qubit architectures have been proposed in a diverse range of material systems [10]. In 1998, Bruce Kane outlined a scalable quantum computer architecture that exploits the nuclear spin of phosphorus (P) donors in silicon (Si) [5]. Here, information is encoded on the nuclear spin states of ^{31}P donor atoms encased in an isotopically enriched ^{28}Si host matrix. Since then, related donor architectures have been proposed that employ either the donor electron spin [11, 12] or charge [13] as the qubit. In general, donor-based silicon qubits are promising because of their long electron and nuclear spin coherence times [14, 15], i.e. the amount of time that the encoded information persists before the qubit superposition state interacts destructively with its environment. Recent studies have demonstrated electron and nuclear coherence times in the range of 3–10 s [15, 16]. Their resilience is a result of a low natural abundance of ^{28}Si nuclear spins and weak spin–orbit coupling [5].

Originally Kane envisioned a silicon-based architecture in which an array of P donors were buried in a Si host matrix with surface A- and J- control gates, deposited on an oxide barrier directly over the donor array (Fig. 1). Here, a quantum calculation is achieved by suitably biasing these surface gates, with the application of a global oscillating magnetic field. The A-gates serve to controllably

modulate the strength of the hyperfine interactions, i.e. the extent of the electron wavefunction at the nucleus, thereby altering the resonance frequency of its nucleus [17]. Due to the close proximity of the donors ($\sim$20 nm), two nuclear spins can interact with the same electron and it is the J-gates that turn off and on this electron-mediated nuclear spin coupling [18]. Logical operations are performed using the electric fields provided by these surface gates while the external oscillating magnetic field flips the nuclear spins at resonance, and essentially dictates the speed of the logic operation. This silicon-based quantum computer concept is elegant, but requires the notoriously difficult task of patterning individual dopants with atomic accuracy within a silicon host matrix, registered to surface control gates. A critical question is how to control matter at the atomic scale to achieve this device architecture.

The early 1980s welcomed the invention of the scanning tunneling microscope, enabling individual atoms on a surface to be resolved [19, 20]. This instrument garnered creators, Gerd Binning and Heinrich Rohrer, the Nobel Prize and ushered in a new era of surface science. In 1990, Eigler and Schweizer demonstrated the atomically precise manipulation of single xenon atoms on a nickel (110) surface by spelling out their company logo, IBM, using a STM tip [21]. This feat has since paved the way forward for numerous achievements over the past three decades in STM tip engineering of atomic-scale structures on metallic surfaces [22–25]. However it is not easy to transfer this capability to the technologically relevant surface of silicon, where relatively stronger molecule-surface interactions prevail and severely hamper atomic manipulation.

One successfully adopted approach to manipulate atoms in silicon is STM-based lithography, developed in the 1990s by Lyo and Avouris [26] and Lyding and Tucker [27]. Analogous to conventional optical lithography, this method involves the use of a monolayer of hydrogen 'resist' in which individual hydrogen atoms can be selectively removed by a STM tip. Here atomic-scale templates of highly reactive dangling bonds sites on the silicon surface can be created and subsequently functionalized with various atomic and molecular adducts [27–31]. Following this, several groups proposed the possibility of using this technique toward the realization of atomically ordered structures for potential device applications [28–33]. Our group has since gone on to combine STM-lithography with low temperature molecular beam epitaxy [34, 35] to realize a complete fabrication scheme for atomic-scale devices in silicon. We have employed an etched-based registration marker scheme in silicon [36, 37] to electrically contact atomic-scale devices once they are removed from the ultra-high vacuum (UHV) environment of the microscope. Encapsulating the dopants in epitaxial silicon ensures the donors reside in a single-crystal silicon environment thereby preventing the interaction of the patterned dopants with surface states. The clean and durable registration marker scheme, designed to seamlessly integrate with the STM-based lithographic process, is used to contact the atomic-scale device so that it may process electronic inputs from the macroscopic world. This chapter provides an in-depth description of this unique atomic-scale device fabrication scheme, showcases exemplary dopant-based devices, and demonstrates the necessary steps to reach the single donor limit.

2 A Complete Atomic-Scale Device Fabrication Strategy

Over the last 10 years, our group has successfully developed and refined a complete atomic-scale device fabrication scheme in silicon [36–41]. Notably, the work includes the following achievements in device fabrication:

- The development of UHV-compatible registration marker scheme for aligning *ex-situ* surface electrodes to the atomic-scale device buried in a single-crystal silicon host [36, 37]
- A detailed atomistic understanding of the doping process, i.e. the surface chemistry of PH_3 on Si(001) and how to controllably incorporate single dopants in silicon with atomic precision [38, 42, 43]
- Hundred percent electrical activation with minimal diffusion and segregation of the dopants by optimizing the low temperature MBE silicon overgrowth [34, 44–46]

Our fabrication process flow is depicted in Fig. 2 and STM images of the UHV steps are shown in Fig. 3.

2.1 Registration Markers Used to Locate Devices

Registration markers, patterned by either optical or electron beam lithography, are first etched directly into the surface of a nominally flat Si(001) substrate (Fig. 2a). These markers serve ultimately as in situ guides during STM-lithography and as alignment makers for ex situ deposition of surface electrodes [36, 37]. Under UHV conditions, the registration maker sample surface is atomically reconstructed by heating to 1100°C for 10 s (Fig. 2b). These registration markers are remarkably robust and are able to survive these high temperature treatments. Moreover, the registration marker fabrication process does not contaminate the surface so that we can routinely achieve low defect density Si(001)-2 × 1 surfaces, as shown in Fig. 3a. The highly reactive Si(001) surface is then capped with atomic hydrogen, from a thermal cracking source, to produce a uniform monohydride phase that acts as resist for subsequent STM-lithography (Fig. 2c).

2.2 Atomically Precise Lithography

Following hydrogen termination of the Si(001) surface, the STM tip is used to selectively desorb hydrogen atoms by applying appropriate tunneling parameters (i.e. sample bias and feedback current) [27]. Field emitted electrons can stimulate desorption of molecular hydrogen by either an increase in electron kinetic energy or electron current; the prevailing mechanism depends on the tunneling

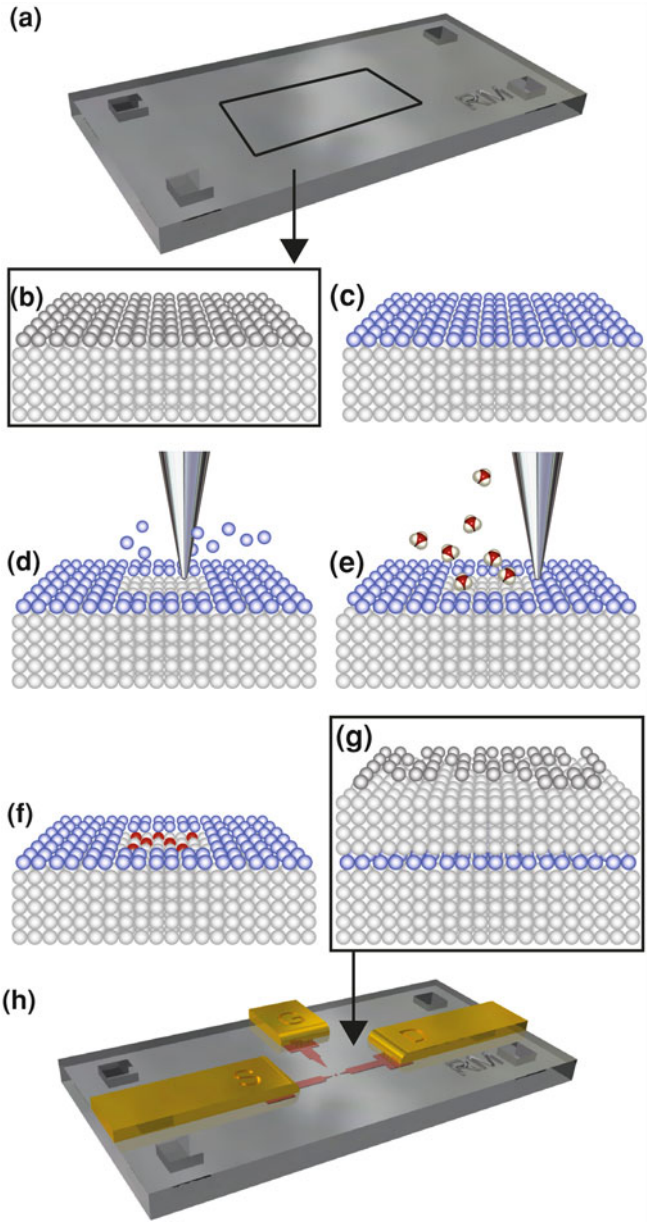

Fig. 2 Schematic of our unique, atomic-scale device fabrication strategy. **a** We begin with a clean registration marker sample. **b** The surface is flashed to high temperatures to promote a 2 × 1 surface reconstruction. **c** The surface is then passivated with atomic hydrogen (*blue*). **d** The STM tip is used to locally desorb regions of the hydrogen resist. **e** The surface is then dosed with phosphine gas which only adsorbs to the exposed and highly reactive Si surface. **f** The sample is then gently heated to ∼350°C to promote incorporation of P dopants (*red*) into the surface. **g** The dopants are then encapsulated with epitaxial Si grown by low temperature silicon molecular beam epitaxy. **h** Surface metal electrodes (*gold*) are aligned to the buried STM-patterned dopants (*red*) after removing the sample from UHV

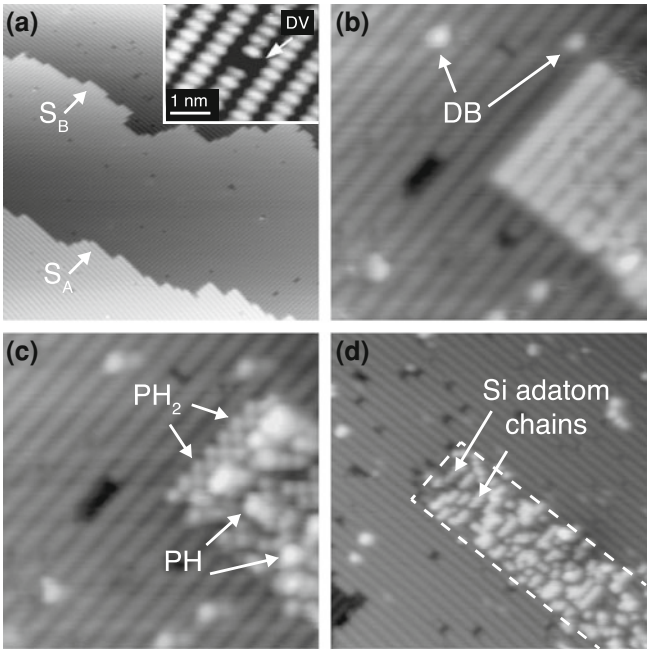

Fig. 3 STM images acquired during device fabrication. **a** The clean starting Si(001)-2 × 1 surface clearly showing S_A and S_B type terraces. A high resolution image of the reconstructed surface is shown in the inset. A typical dimer vacancy (DV) defect is highlighted at the center of this image. **b** The lithographically patterned region of the surface (*lower right* of the image) showing that the desorbed region appears bright in comparison to the surrounding hydrogen terminated surface. Some dangling bonds (DB) are visible. **c** The same area after dosing with phosphine gas. Both PH_2 and PH fragments are visible within the desorbed area. **d** The presence of Si adatom chains indicates successful P incorporation

parameters used [27]. Upon hydrogen removal, an atomically flat Si(001)-2 × 1 surface is exposed (Fig. 2d). Relatively low biases (∼2–4 V) and high tunneling currents (∼10–15 nA) generally produce exceptionally fine lithography with minimal spurious hydrogen desorption due to stray electrons from the STM tip. This is demonstrated in the STM images of Fig. 3b where a distinct boundary and low density of dangling bonds outside of the pattern are observed. Here, the desorbed areas appear brighter than the surrounding hydrogen termination due to additional contributions to the tunneling current from Si surface states [47]. Employing high biases (∼5–7 V) and low currents (∼3–5 nA) reduces the achievable resolution at the pattern edges but increases the overall desorption efficiency (i.e. dose). These tunneling parameters are thus better suited for desorbing micron-size regions where atomically sharp pattern edges are not requisite. The flexibility and potential for unprecedented lithographic resolution (e.g. 3.8 Å on Si(001)) afforded by the hydrogen lithography technique are ideally suited for its use in the fabrication of atomic-scale devices.

2.3 Controlled Incorporation of Phosphorus Dopants in Silicon

After the desired structure is patterned by STM-lithography, the highly reactive silicon surface is exposed to saturation dosing of the gaseous dopant precursor molecule, PH_3 (Fig. 2e). The surface chemistry of PH_3 on the clean Si(001) surface is well-documented [42, 43, 48, 49] and proceeds as follows:

$$PH_{3(\mathbf{ads})} \rightarrow PH_2 + H \rightarrow PH + 2H \rightarrow P + 3H \rightarrow P_{(\mathbf{incorp})}$$

Upon adsorption at room temperature, PH_3 undergoes a series of successive dissociations until it loses all of its three hydrogen atoms. During the initial dosing step, PH_3 datively bonds to the surface and immediately dissociates to $PH_2 + H$. The PH_2 fragments further dissociate to $PH + 2H$ on the order of minutes [42]. PH then undergoes a final dissociation step to $P + 3H$. The STM image shown in (Fig. 3c) was acquired only minutes after dosing and thus both PH_2 and PH fragments can be discerned. Thermal activation is required to promote the incorporation of the P atom into the top layer of the Si surface, ejecting a Si atom in the process (Fig. 2f). These ejected Si atoms then form 1D chains that assemble perpendicular to the underlying dimer rows [46], as shown in the STM image of (Fig. 3d). These chains are useful indicators of successful donor incorporation [38, 46].

PH_3 molecules adsorb only to the exposed silicon surface and not to the hydrogen resist layer. Across the edges of the STM-pattern, the doping concentration thus decreases precipitously by six orders of magnitude from 10^{21} to 10^{15} cm^{-3}, leading to atomically sharp confinement of the dopants [50]. Importantly the hydrogen resist remains intact during the incorporation anneal and the integrity of nano-patterned dopants is maintained.

2.4 Silicon Encapsulation and Dopant Activation

Once the donors have been incorporated, the patterned region is subsequently overgrown with $\sim$25 nm of epitaxial silicon which serves to (i) fully activate the donors, and (ii) eliminate the influence of surface defects (Fig. 2g and h). While P dopants are known to segregate upwards during Si encapsulation, the low thermal budget ($\sim$250°C) keeps vertical dopant segregation to a minimum. We have carried out detailed studies of the overgrowth to maximize the doping sheet density to 2×10^{14} cm^{-2} [45, 46] and minimize dopant segregation to an upper limit of 6 Å [44, 45].

3 Atomically Fine Wires

Having developed a complete device fabrication strategy, initial studies focused on the characterization of a series of quantum wires with widths ranging from 90 nm down to 7 nm [39, 40, 51]. Nanowires are an elemental building block of atomic-scale devices as they serve as both electrical leads and interconnects,

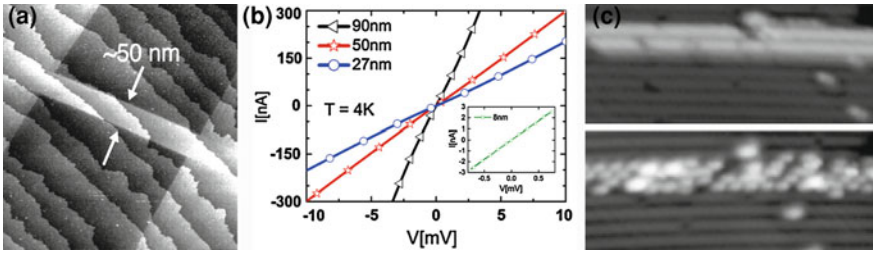

Fig. 4 Atomic-scale wires realized by STM-lithography **a** An STM image of a 50 nm wide and 310 nm long wire patterned by STM-lithography. **b** Current–voltage characteristics for 90, 50 and 27 nm wide wires. Notably, they all exhibit Ohmic behavior even at these nanometer length scales. **c** Using the STM we are able to realize wires that are two dimer rows wide (*top*). After PH_3 dosing (*bottom*) we observe both PH_2 and PH fragments within the template. Figure adapted from [54]

as well as providing an interesting system in themselves to study. A STM image of an exemplary $\sim$50 nm wide nanowire is depicted in Fig. 4a.

By performing constant current imaging tunneling spectroscopy (CITS) on the buried nanowires we were able to confirm their structural quality, in particular, their uniformity and the minimal extent of lateral dopant diffusion from the atomically precise regions defined by STM-lithography [41, 51]. *Ex-situ* electrical measurements at 4 K demonstrated that individually contacted nanowires exhibit Ohmic behavior [51]. From the IV characteristics shown in (Fig. 4b), four-terminal resistances from tens to hundreds of kΩ were determined depending on the wire width. We note that these nanowires are highly planar with conduction spanning less than a few atomic planes allowing us to achieve low 2D resistivities on the order of 10^{-8} Ω cm. For device applications, a low resistivity is desirable to avoid resistive heating during low temperature measurements and to allow for fast operation of the devices. Using STM-lithography we are able to define nanowires that are only two dimers ($\sim$1.5 nm) wide (Fig. 4c). More recent results have shown that we can maintain low resistivities all the way to this length scale [52]. This demonstrates the suitability of these nanowires as electrical leads and interconnects in atomic-scale devices. We have also adapted this technology to produce highly doped nanowires in Ge [53].

4 An All Epitaxial Silicon Quantum Dot

The STM-based approach to fabricating atomic-scale devices has led to the successful realization of individual device components, such as tunnel gaps [55] and nanowires [39, 41, 51]. However, a major roadblock toward the pursuit of broader applications of this technology is the ability to electrically gate and control resistances within devices. In this section, we present the first controllably gated dopant-based quantum dot device engineered using this unique fabrication strategy.

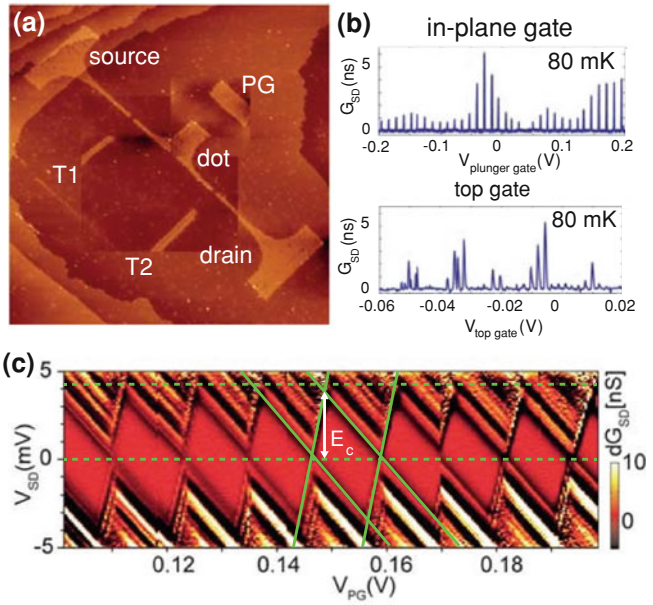

Fig. 5 **a** A composite STM image of the 5 terminal all epitaxial quantum *dot*. The three in-plane gates (PG, T1 and T2) are used to tune the electron number on the top *hat-shaped dot* located at the center of the image. **b** Clear Coulomb oscillations are observed as the PG is swept over a range of accessible voltages (*top*). Similar current versus gate voltage measurements were made using a top-gate (*bottom*). In the latter case, the signal is noisy due to interface-related defects. **c** Colormap showing the differential conductance as a function of V_{SD} and V_{PG}. Figure adapted [57]

Quantum dots are typically small regions confined in three-dimensions within a semiconductor material. They have been a topic of much interest over the past two decades because they manifest a wide range of quantum phenomenon due to their small size. In particular they have a quantized energy spectrum, not unlike real atoms, and are thus referred to as 'artificial atoms' [56]. But more intriguingly, quantum dots cannot only be studied by their interaction with light, in the same manner as real atoms, but by their ability to carry an electronic current. Consequently, an interesting challenge is to connect current and voltage leads to measure their atomic states.

By further restricting our planar 1D P doped nanowires to 0D, we can fabricate 'planar islands' of P donors, and study their quantum properties. A composite image of an STM-engineered multi-terminal quantum dot device is shown in Fig. 5a, with integrated donor-based in-plane leads and gates [57]. A large top hat-shaped dot is situated between exceptionally fine ($\sim$4 nm wide) source and drain leads. The leads are separated from the dot by $\sim$8 nm wide tunnel gaps. The plunger gate (TG) along with two additional gates (T1 and T2) serve to tune the electrochemical potential of the dot and modulate the tunnel barriers, respectively, thereby controlling the transport of quantized amounts of charge on and off the dot.

The transport properties of this device were measured at mK temperatures. At these low temperatures, the silicon substrate becomes insulating due to carrier freeze-out, and thus acts as both a tunnel barrier between the dot and the leads and as a gate dielectric. Tunneling of a single charge on or off the dot will change the electrostatic energy (i.e. charging energy, E_c) of the dot by a discrete value. The plunger gate, however, modulates the electrostatic energy of the dot in a continuous manner such that the electrochemical potential of the dot is tuned into resonance with either the source or the drain, resulting in charge tunneling on or off the dot. These charge fluctuations, referred to as Coulomb oscillations, can be measured as we plunge the voltage on the gate [56]. From the plot shown in Fig. 5b (top), we can see peaks in the conductance when the dot and lead energies are aligned at the same energy allowing electrons to hop on and off the central dot. We also fabricated a surface top-gate aligned above the buried quantum dot on the same device and used this to measure the Coulomb oscillations as seen in Fig. 5b (lower). Due to the stronger capacitive coupling we are able to tune the number of electrons on the dot by a factor of ~ 10 larger than with the in-plane gate. However, there was also a reduced signal-to-noise ratio and the gate was observed to be more hysteretic than the in-plane gate. This highlights the overall stability of our in-plane gating scheme, where the gates are themselves made of epitaxial silicon with no interfaces present. In the long term we envision combining both in-plane and surface-gated [58] device architectures for maximum device tunability.

By repeating the in-plane gate sweeps for different source-drain biases we can build up a 2D color map known as a stability diagram for this quantum dot device, see Fig. 5c. The dark Coulomb diamonds are regions were the current is blockaded since the electrochemical potentials of the dot and leads are misaligned. The charging energy of the dot can be determined from the height of the Coulomb diamonds; for this device it is ~ 3.3 meV [57]. Notably, the height of the diamonds remains constant over the entire accessible gating range (-300 to 250 mV). This indicates that the dot behaves classically, where the change in the number of electrons on the dot does not change its physical size and thus quantum corrections to the charging energy are negligible. This is not surprising because the number of electrons on the dot is ~ 4000 based on the electron density of a Si:P delta layer [45, 46] and the dot area. Importantly, this device has opened the door to controlled scaling of silicon devices toward the single donor limit.

5 Downscaling Devices: A Few Electron Silicon Quantum Dot

In order to create a smaller dot that operates in the quantum regime, the dot architecture was optimized so that despite smaller gate areas we could maintain capacitive coupling to the dot while increasing the gating range, i.e. controllability, of the device [50]. An STM overview of a few donor device is presented in Fig. 6a. Similar to the previous device structure, the dot is coupled to coplanar

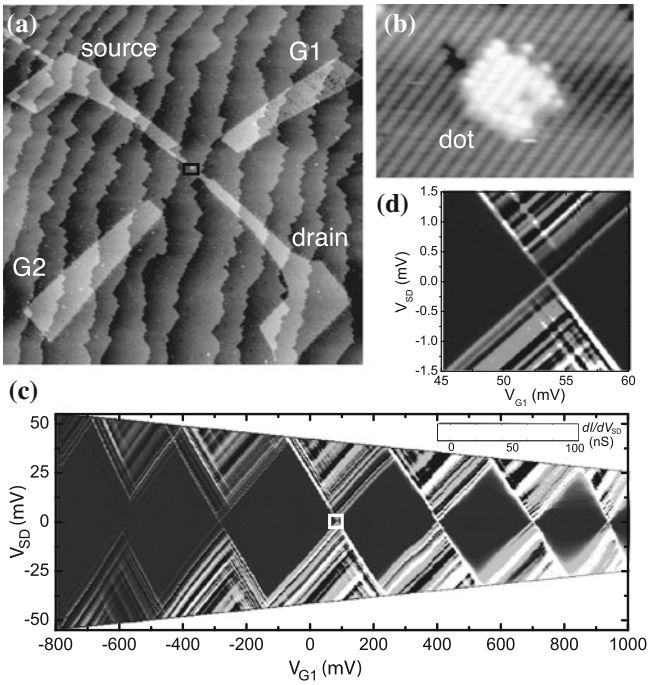

Fig. 6 **a** STM image of a 7 donor dot after STM-lithography. **b** A close-up image of the patterned *dot region* which contains 46 contiguous dimers. This area is estimated to contain 6 ± 3 P dopants. **c** The height of the Coulomb *diamonds* decreases dramatically in the conductance versus gate voltage plot. **d** Close-up of one of the charge transitions which reveals a surprisingly dense set of resonances spaced ~ 100 μeV apart. Figure adapted [50]

source and drain leads (~ 5.5 nm wide) via tunnel gaps of ~ 10 nm. In contrast, only two in-plane gates (G1 and G2) were patterned and deliberately misaligned with respect to the dot. Gate G1 was patterned closer to the drain than the source, enabling the ratio of the tunnel rates between the dot and each of the leads to be controlled by the voltages VG1 and VG2 [50]. In this latest design we were able to extend the gating range to ~ 2 V.

From the stability diagram shown in Fig. 6c, the height of the diamond changes dramatically over the entire gating range, as we deplete electrons from the dot. This quantum behavior is only possible when the dot is in the few electron limit where changing the number of electrons on the smaller dot has a big impact on its overall physical size. This observation is not surprising since, as seen from Fig. 6b, we have significantly reduced the size of the dot. The lithographic dot region contains 46 contiguous dimers and thus holds an estimated 6 ± 3 phosphorus dopants.

On closer inspection of the stability diagram, the data reveals a rich set of conductance resonances that manifests as bright lines of increased conductance running parallel to the diamond edges. Despite fabricating a smaller dot, where one might expect the spacing between the quantum confined energy levels to

increase, we observe that these excited state resonances are surprisingly close together, being $\sim$100 μeV apart. We can estimate the energy level spacing, ΔE expected for this dot from the lateral quantum confinement, $\Delta E = \pi\hbar^2/m^*A$, where A is the dot area for a dot diameter $d = \sim$4.6 nm, $m^* = 0.28m_e$ is the effective mass of silicon and where the dot has a degeneracy, the product of the spin and valley degeneracies $g = 12$. We find ΔE to be $\sim$10 s of meV [50, 56] in sharp contrast to the experimentally measured energy level spacing. Another possible source of these closely spaced resonances could be due to the strong lateral confinement of the lead states giving rise to density of states (DOS) fluctuations in the leads [59]. However, again we find a mean energy spacing of $\sim$10 s of meV. Both these values are much larger than the 100 μeV observed in the experimental stability diagram, and therefore cannot be the source of these excited state resonances.

The band structure of our highly doped atomically thin layers of phosphorus in silicon is another source of these excited state resonances. The conduction band of silicon is six-fold degenerate, i.e. 2 gamma (Γ)-bands and 4 delta (Δ)-bands [60]. The degeneracy of the Γ-bands is lifted by the strong vertical confinement of the dopants to a single atomic plane. The energy splitting of the Δ-bands is essentially determined by the *sharpness* of the lateral confinement of the nano-scale size of the dot [61]. Thus, it is likely that the observed excited states arise from the many possible filling combinations of the valence electrons in the Δ-bands. Using a multi-electron, multi-valley effective mass approximation, energy levels for all different combinations of donor and electron numbers on the dot, consistent with the 6 ± 3 dopant number predicted by STM, were computed [50, 62]. The best match to the experimental data with the 100 μeV energy level spacing (Fig. 6d) corresponded to a 7 donor dot at the seventh to eighth electron transition. This result confirms that valley splitting in silicon can be significant if we engineer devices with atomically abrupt dopant profiles.

6 Outlook: Toward the Silicon Donor Limit

In this chapter, we have demonstrated the successful implementation of this unique approach for fabricating devices that operate in both the classical and quantum regimes. More recently, we have pushed this to the single donor limit. To reach this goal, we have combined our STM-lithography capabilities with a detailed knowledge of the surface chemistry of phosphine on silicon and extensive device modeling. As previously outlined, phosphine requires a minimum number of dimer sites for the complete dissociation and incorporation of a single P atom into the Si(001) surface [38]. It is a very simple but elegant reaction that fulfills our requirement to deterministically place an individual P dopant with an astonishing accuracy of ±1 atomic lattice spacing. As shown in the first panel of Fig. 7, we can use STM-lithography to open up a small desorbed region that is $\sim$1 nm in length. This patch is able to accommodate the entire reaction pathway, as illustrated in the center panels. The same area is then imaged after our dosing and

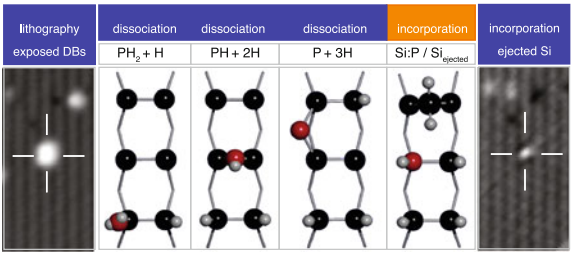

Fig. 7 Controllable incorporation of a single P atom in silicon with an accuracy of ±1 atomic lattice spacing. The first panel shows an image of ~1 nm long patch defined by STM-lithography. The dissociation and incorporation pathway of a single PH_3 molecule within the patch is illustrated. The final panel shows the same area after dosing and incorporation. A Si adatom is visible at the location of the patch indicating successful incorporation of a solitary P dopant

annealing steps, and is shown in the final panel. The small bright feature centered at patch location is an ejected Si adatom, the tell-tale sign of an incorporated P atom. Notably, dangling bond sites do not react with PH_3 molecules impinging on the surface; leaving the area surrounding the desorbed region bereft of stray phosphorus dopants [43].

7 Summary

To date we have developed a complete and unique strategy for fabricating atomic-scale devices in silicon. We have fabricated elemental device components and shown how they can be electronically controlled using novel, all epitaxial in-plane gates. Furthermore, we have demonstrated all the necessary steps for the realization of a fully functional, deterministically placed single atom transistor in a single-crystal silicon environment. These results open the door to the exciting possibility of creating atomic-scale device architectures in silicon and their scaling up for broader applications in quantum information processing.

Acknowledgments This work was supported by the Australian Research Council Centre of Excellence for Quantum Computation and Communication Technology (Project No. CE110001027) and the Army Research Office under contract number W911NF-08-1-0527. M. Y. S acknowledges a Federation Fellowship. J. A. M. thanks S. Mahapatra, G. Scappucci and M. Fuechsle for many useful discussions.

References

1. Koenraad, P.M., Flatte, M.E.: Single dopants in semiconductors. Nat. Mater. **10**(2), 91–100 (2011)
2. Shinada, T., Okamoto, S., Kobayashi, T., Ohdomari, I.: Enhancing semiconductor device performance using ordered dopant arrays. Nature **437**(7062), 1128–1131 (2005)

3. Lansbergen, G.P., Rahman, R., Wellard, C.J., Woo, I., Caro, J., Collaert, N., Biesemans, S., Klimeck, G., Hollenberg, L.C.L., Rogge, S.: Gate-induced quantum-confinement transition of a single dopant atom in a silicon FinFET. Nat. Phys. **4**(8), 656–661 (2008)
4. Roy, S., Asenov, A.: Where do the dopants go? Science **309**(5733), 388–390 (2005)
5. Kane, B.E.: A silicon-based nuclear spin quantum computer. Nature **393**(6681), 133–137 (1998)
6. Feynman, R.P.: Feynman Lectures on Computation. Addison-Wesley, Reading (1996)
7. Shor, P.W.: Algorithms for quantum computation: discrete logarithms and factoring. In: Goldwasser, S. (ed.) 35th Annual Symposium on Foundations of Computer Science, Proceedings IEEE Computer Society Press, Los Alamitos (1994)
8. Ekert, A., Jozsa, R.: Quantum computation and Shor's factoring algorithm. Rev. Mod. Phys. **68**(3), 733–753 (1996)
9. Grover, L.K.: Quantum mechanics helps in searching for a needle in a haystack. Phys. Rev. Lett. **79**(2), 325–328 (1997)
10. Nielsen, M.A., Chuang, I.L.: Quantum Computation and Quantum Information. Cambridge University Press, Cambridge (2000)
11. Vrijen, R., Yablonovitch, E., Wang, K., Jiang, H.W., Balandin, A., Roychowdhury, V., Mor, T., DiVincenzo, D.: Electron-spin-resonance transistors for quantum computing in silicon-germanium heterostructures. Phys. Rev. A **62**, 012306 (2000)
12. de Sousa, R., Delgado, J.D., Das Sarma, S.: Silicon quantum computation based on magnetic dipolar coupling. Phys. Rev. A **70**(5), 052304 (2004)
13. Hollenberg, L.C.L., Dzurak, A.S., Wellard, C., Hamilton, A.R., Reilly, D.J., Milburn, G.J., Clark, R.G.: Charge-based quantum computing using single donors in semiconductors. Phys. Rev. B **69**(11), 4 (2004)
14. Tyryshkin, A.M., Lyon, S.A., Astashkin, A.V., Raitsimring, A.M.: Electron spin relaxation times of phosphorus donors in silicon. Phys. Rev. B **68**(19), 193207 (2003)
15. Morton, J.J.L., Tyryshkin, A.M., Brown, R.M., Shankar, S., Lovett, B.W., Ardavan, A., Schenkel, T., Haller, E.E., Ager, J.W., Lyon, S.A.: Solid-state quantum memory using the ^{31}P nuclear spin. Nature **455**(7216), 1085–1088 (2008)
16. Morton, J.J.L., Lovett, B.W.: Hybrid solid-state qubits: the powerful role of electron spins. In: Langer, J.S. (ed.) Annual Review of Condensed Matter Physics, vol. 2, pp. 189–212. Annual Reviews, Palo Alto (2011)
17. Kohn, W.: Shallow impurity states in silicon and germanium. Solid State Phys. Adv. Res. Appl. **5**, 257–320 (1957)
18. Loss, D., DiVincenzo, D.P.: Quantum computation with quantum dots. Phys. Rev. A **57**(1), 120–126 (1998)
19. Binnig, G., Rohrer, H.: Scanning tunneling microscopy. Helv. Phys. Acta **55**(6), 726–735 (1982)
20. Binnig, G., Rohrer, H., Gerber, C., Weibel, E.: Surface studies by scanning tunneling microscopy. Phys. Rev. Lett. **49**(1), 57–61 (1982)
21. Eigler, D.M., Schweizer, E.K.: Positioning single atoms with a scanning tunnelling microscope. Nature **344**(6266), 524–526 (1990)
22. Crommie, M.F., Lutz, C.P., Eigler, D.M.: Confinement of electrons to quantum corrals on a metal surface. Science **262**(5131), 218–220 (1993)
23. Hla, S.W.: Scanning tunneling microscopy single atom/molecule manipulation and its application to nanoscience and technology. J. Vac. Sci. Technol. B **23**(4), 1351–1360 (2005)
24. Moresco, F.: Manipulation of large molecules by low-temperature STM: model systems for molecular electronics. Phys. Rep. **399**(4), 175–225 (2004)
25. Otero, R., Rosei, F., Besenbacher, F.: Scanning tunneling microscopy manipulation of complex organic molecules on solid surfaces. In: Annual Review of Physical Chemistry, vol. 57. pp. 497–525. Annual Reviews, Palo Alto (2006)
26. Lyo, I.W., Avouris, P.: Atomic scale desorption processes induced by the scanning tunneling microscope. J. Chem. Phys. **93**(6), 4479–4480 (1990)

27. Lyding, J.W., Shen, T.C., Hubacek, J.S., Tucker, J.R., Abeln, G.C.: Nanoscale patterning and oxidation of H-passivated Si(100)-2 × 1 surfaces with an ultrahigh-vacuum scanning tunneling microscope. Appl. Phys. Lett. **64**(15), 2010–2012 (1994)
28. Hersam, M.C., Guisinger, N.P., Lyding, J.W.: Silicon-based molecular nanotechnology. Nanotechnology **11**(2), 70–76 (2000)
29. Lopinski, G.P., Wayner, D.D.M., Wolkow, R.A.: Self-directed growth of molecular nanostructures on silicon. Nature **406**(6791), 48–51 (2000)
30. Pitters, J.L., Piva, P.G., Tong, X., Wolkow, R.A.: Reversible passivation of silicon dangling bonds with the stable radical TEMPO. Nano Lett. **3**(10), 1431–1435 (2003)
31. Miwa, J.A., Eves, B.J., Rosei, F., Lopinski, G.P.: Selective adsorption of pyridine at isolated reactive sites on Si(100). J. Phys. Chem. B **109**(43), 20055–20059 (2005)
32. Tucker, J.R., Shen, T.C.: Prospects for atomically ordered device structures based on STM lithography. Solid-State Electron. **42**(7–8), 1061–1067 (1998)
33. Wada, Y.: Atom electronics: a proposal of atom/molecule switching devices. Surf. Sci. **386**, 13 (1997)
34. Goh, K.E.J., Oberbeck, L., Simmons, M.Y., Hamilton, A.R., Clark, R.G.: Effect of encapsulation temperature on Si:P delta-doped layers. Appl. Phys. Lett. **85**(21), 4953–4955 (2004)
35. Oberbeck, L., Hallam, T., Curson, N.J., Simmons, M.Y., Clark, R.G.: STM investigation of epitaxial Si growth for the fabrication of a Si-based quantum computer. Appl. Surf. Sci. **212**, 319–324 (2003)
36. Fuechsle, M., Ruess, F.J., Reusch, T.C.G., Mitic, M., Simmons, M.Y.: Surface gate and contact alignment for buried, atomically precise scanning tunneling microscopy-patterned devices. J. Vac. Sci. Technol. B **25**, 2562 (2007)
37. Ruess, F.J., Oberbeck, L., Goh, K.E.J., Butcher, M.J., Gauja, E., Hamilton, A.R., Simmons, M.Y.: The use of etched registration markers to make four-terminal electrical contacts to STM-patterned nanostructures. Nanotechnology **16**(10), 2446–2449 (2005)
38. Schofield, S.R., Curson, N.J., Simmons, M.Y., Ruess, F.J., Hallam, T., Oberbeck, L., Clark, R.G.: Atomically precise placement of single dopants in Si. Phys. Rev. Lett. **91**(13) (2003)
39. Ruess, F.J., Oberbeck, L., Simmons, M.Y., Goh, K.E.J., Hamilton, A.R., Hallam, T., Schofield, S.R., Curson, N.J., Clark, R.G.: Toward atomic-scale device fabrication in silicon using scanning probe microscopy. Nano Lett. **4**(10), 1969–1973 (2004)
40. O'Brien, J.L., Schofield, S.R., Simmons, M.Y., Clark, R.G., Dzurak, A.S., Curson, N.J., Kane, B.E., McAlpine, N.S., Hawley, M.E., Brown, G.W.: Towards the fabrication of phosphorus qubits for a silicon quantum computer. Phys. Rev. B **64**(16), 161401(R) (2001)
41. Ruess, F.J., Pok, W., Reusch, T.C.G., Butcher, M.J., Goh, K.E.J., Oberbeck, L., Scappucci, G., Hamilton, A.R., Simmons, M.Y.: Realization of atomically controlled dopant devices in silicon. Small **3**(4), 563–567 (2007)
42. Wilson, H.F., Warschkow, O., Marks, N.A., Schofield, S.R., Curson, N.J., Smith, P.V., Radny, M.W., McKenzie, D.R., Simmons, M.Y.: Phosphine dissociation on the Si(001) surface. Phys. Rev. Lett. **93**(22), 4 (2004)
43. Wilson, H.F., Warschkow, O., Marks, N.A., Curson, N.J., Schofield, S.R., Reusch, T.C.G., Radny, M.W., Smith, P.V., McKenzie, D.R., Simmons, M.Y.: Thermal dissociation and desorption of PH_3 on Si(001): a reinterpretation of spectroscopic data. Phys. Rev. B **74**(19), 195310 (2006)
44. Oberbeck, L., Curson, N.J., Hallam, T., Simmons, M.Y., Bilger, G., Clark, R.G.: Measurement of phosphorus segregation in silicon at the atomic scale using scanning tunneling microscopy. Appl. Phys. Lett. **85**(8), 1359–1361 (2004)
45. Oberbeck, L., Curson, N.J., Simmons, M.Y., Brenner, R., Hamilton, A.R., Schofield, S.R., Clark, R.G.: Encapsulation of phosphorus dopants in silicon for the fabrication of a quantum computer. Appl. Phys. Lett. **81**(17), 3197–3199 (2002)
46. McKibbin, S.R., Clarke, W.R., Fuhrer, A., Reusch, T.C.G., Simmons, M.Y.: Investigating the regrowth surface of Si:P delta-layers toward vertically stacked three dimensional devices. Appl. Phys. Lett. **95**(23), 233111 (2009)

47. Boland, J.J.: Evidence of pairing and its role in the recombinative desorption of hydrogen from the Si(100)-2x1 surface. Phys. Rev. Lett. **67**(12), 1539–1542 (1991)
48. Warschkow, O., Wilson, H.F., Marks, N.A., Schofield, S.R., Curson, N.J., Smith, P.V., Radny, M.W., McKenzie, D.R., Simmons, M.Y.: Phosphine adsorption and dissociation on the Si(001) surface: an ab initio survey of structures. Phys. Rev. B **72**(12), 125328 (2005)
49. Schofield, S.R., Curson, N.J., Warschkow, O., Marks, N.A., Wilson, H.F., Simmons, M.Y., Smith, P.V., Radny, M.W., McKenzie, D.R., Clark, R.G.: Phosphine dissociation and diffusion on Si(001) observed at the atomic scale. J. Phys. Chem. B **110**(7), 3173–3179 (2006)
50. Fuechsle, M., Mahapatra, S., Zwanenburg, F.A., Friesen, M., Eriksson, M.A., Simmons, M.Y.: Spectroscopy of few-electron single-crystal silicon quantum dots. Nat. Nanotechnol. **5**(7), 502–505 (2010)
51. Ruess, F.J., Goh, K.E.J., Butcher, M.J., Reusch, T.C.G., Oberbeck, L., Weber, B., Hamilton, A.R., Simmons, M.Y.: Narrow, highly P-doped, planar wires in silicon created by scanning probe microscopy. Nanotechnology **18**(4) (2007)
52. Weber, B., Mahapatra, S. Ryu, H. Lee, S. Fuhrer, A., Reusch, T.C.G., Thompson, D. L., Lee, W.C.T., Klimeck, G., Hollenberg, L. C. L., Simmons, M.Y. : Ohm's law survives to the atomic-scale. Science **335** (6064), 64–67 (2012)
53. Scappucci, G., Capellini, G., Johnston, B., Klesse, W.M., Miwa, J.A., Simmons, M.Y.: A complete fabrication route for atomic-scale, donor-based devices in single-crystal germanium. Nano Lett. **11**(6), 2272–2279 (2011)
54. Simmons, M.Y., Ruess, F.J., Goh, K.E.J., Pok, W., Hallam, T., Butcher, M.J., Reusch, T.C.G., Scappucci, G.: Atomic-scale silicon device fabrication. Int. J. Nanotechnol. **5**(2–3), 352–369 (2008)
55. Ruess, F.J., Pok, W., Goh, K.E.J., Hamilton, A.R., Simmons, M.Y.: Electronic properties of atomically abrupt tunnel junctions in silicon. Phys. Rev. B **75**(12) (2007)
56. Kouwenhoven, L.P., Marcus, C.M., McEuen, P.L., Tarucha, S., Westervelt, R.M., Wingreen, N.S.: Electron transport in quantum dots. In: Sohn, L.L., Kouwenhoven, L.P., Schon, G. (eds.) NATO Advanced Study Institute on Mesoscopic Electron Transport, Curacao, Neth Antilles, p. 105–214. Springer (1997)
57. Fuhrer, A., Fuechsle, M., Reusch, T.C.G., Weber, B., Simmons, M.Y.: Atomic-scale, all epitaxial in-plane gated donor quantum dot in silicon. Nano Lett. **9**(2), 707–710 (2009)
58. Lee, W.C.T., Scappucci, G., Thompson, D.L., Simmons, M.Y.: Development of a tunable donor quantum dot in silicon. Appl. Phys. Lett. **96**(4) (2010).
59. Pierre, M., Wacquez, R., Jehl, X., Sanquer, M., Vinet, M., Cueto, O.: Single-donor ionization energies in a nanoscale CMOS channel. Nat. Nanotechnol. **5**(2), 133–137 (2010)
60. Carter, D.J., Warschkow, O., Marks, N.A., McKenzie, D.R.: Electronic structure models of phosphorus delta-doped silicon. Phys. Rev. B **79**(3) (2009)
61. Boykin, T.B., Klimeck, G., Eriksson, M.A., Friesen, M., Coppersmith, S.N., von Allmen, P., Oyafuso, F., Lee, S.: Valley splitting in strained silicon quantum wells. Appl. Phys. Lett. **84**(1), 115–117 (2004)
62. Qian, G.F., Chang, Y.C., Tucker, J.R.: Theoretical study of phosphorous delta-doped silicon for quantum computing. Phys. Rev. B **71**(4), 9 (2005)

Electronic Transport on the Nanoscale

C. A. Bobisch, A. M. Bernhart, M. R. Kaspers, M. C. Cottin, J. Schaffert and R. Möller

Abstract A scanning tunneling microscope with several tips is ideally suited to analyze the electronic transport through objects on the nanoscale. Two different configurations will be discussed. The lateral transport of electrons may be studied by using two tips to drive a current parallel to the surface. A third tip enables to map the corresponding electrochemical potential μ_{ec}. Measurements for a 2D conducting layer will be discussed. To analyze the transport perpendicular to the surface, a thin metallic layer is placed on a semiconducting surface. At the interface a Schottky barrier is formed, which can only be overcome by electrons of sufficient energy. This may be used to split the tunneling current coming from the tip of the microscope, into the ballistic electrons and the electrons which underwent inelastic scattering processes. This technique has been applied to study the ballistic transport of electrons through a thin epitaxial Bi(111) layer as well as through individual molecules.

This chapter is divided into three parts. The first covers the lateral transport of electrons within a surface while the second and the third part focus on the electronic transport perpendicular to the surface.

1 Local Potentiometry at a 2D Electron Gas

Scanning Tunneling Potentiometry (STP) was developed by Muralt and Pohl in 1986 to study the electric transport in a conductor [1]. It allows analyzing the potential distribution at the surface while a lateral current is applied to a

C. A. Bobisch · A. M. Bernhart · M. R. Kaspers · M. C. Cottin · J. Schaffert · R. Möller (✉)
Faculty of Physics, Center for Nanointegration Duisburg-Essen, University of Duisburg-Essen, Duisburg, Germany
e-mail: Rolf.moeller@uni-due.de

C. Joachim (ed.), *Atomic Scale Interconnection Machines*, Advances in Atom and Single Molecule Machines, DOI: 10.1007/978-3-642-28172-3_15,

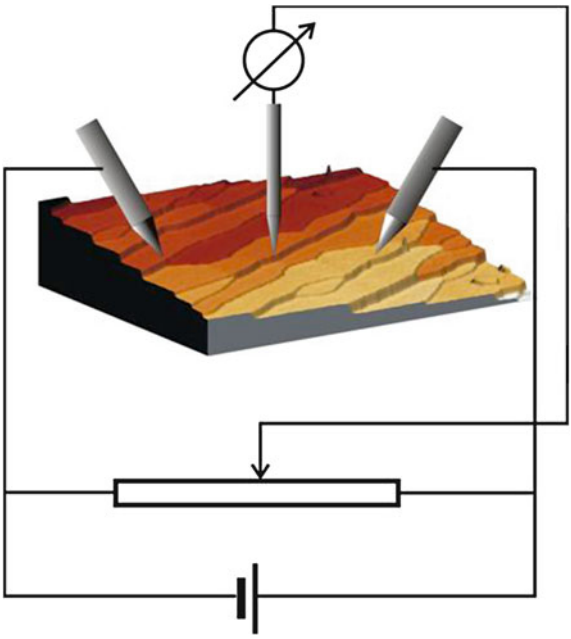

Fig. 1 Scheme of the experiment: a thin conducting layer, e.g., bismuth is prepared on a Si-substrate. The *left* and the *right* tip are in contact to the layer applying a current through the metal layer. The resulting potential distribution $U(x, y)$ is measured by the STM tip in the *middle* by adjusting the potential applied to the tip such that the average tunneling current vanishes

conducting sample. The method is based on scanning tunneling microscopy (STM) [2, 3] providing simultaneously real space images of the potential distribution and the surface topography. A review on STP by Baddorf [4] summarizes the work done in this field. For high resolution studies an almost perfect surface is required for an unambiguous interpretation of the potentiometry data. This points to the necessity to prepare and to analyze the samples as well as the tips in ultra-high vacuum (UHV), imposing significant challenges to the experimental setup. So far only a few UHV experiments with sufficient good film quality are reported [5].

The scheme of the STP experiment is displayed in Fig. 1. Contacts to the metal film are provided by the left and the right tip, which are gently pushed into the surface and a voltage U_{bat} is applied leading to a lateral current in the surface. To evaluate the distribution of the electrochemical potential, which is associated to the current flow along the surface of the conducting film, an STM tip (middle) is brought into tunneling regime to the surface. It scans across the sample surface and simultaneously maps the topography and the local potential distribution $\mu_{\mathrm{ec}}(x, y)$.

The electric circuitry of our STP is very similar to the configuration which was proposed originally by Muralt and Pohl. The tunneling current is measured with a current-to-voltage converter (IVC) with a conversion factor of 10^9 V/A. Its output is connected to two feedback loops. Since an additional small ac-voltage is applied to the tip, the distance between tip and sample surface can be adjusted by the ac-component of the tunneling current as in normal STM operation.

To evaluate the local potential of the sample at the position of the tip, the scheme of a Wheatstone bridge is applied. If the potential at the tip matches the

one at the potentiometer, the dc average of the tunneling current vanishes. The adjustment of the bridge, can be performed electronically by integrating the (dc-component of the) tunneling current. Details of the methods are described in Ref. [6].

Our study is performed on the silver induced $\sqrt{3} \times \sqrt{3}$ superstructure on the Si(111) surface. It is formed by covering the surface of a (111) oriented silicon single crystal with a monolayer of silver. As shown by photoelectron spectroscopy and scanning tunneling spectroscopy (STS) the reconstruction yields a partially occupied electronic surface state providing a sufficient conductivity directly accessible at the surface. Electrons in this state behave as a two-dimensional free electron gas (2DEG). Especially on *n*-type silicon charge transport through the 2DEG is electrically isolated from the bulk states of the silicon by a space charge layer. The experiments were performed in situ in UHV.

The samples were prepared from *n*-type (phosphorus) Si(111) wafers with a specific resistivity of 130 Ω cm. Wafers with a miscut of 0.5° were chosen, leading to rather parallel steps with a density of about 30 steps/μm. As can be seen by the insets in Fig. 2b and e the lateral current was applied by two gold tips of a three probe scanning tunneling microscope, which were brought into contact with metallic silver islands in close vicinity (50–300 μm). The handling was controlled by means of a scanning electron microscope (SEM) with a resolution better than 100 nm. Prior to the presented experiments the macroscopic resistance was evaluated as function of the contact probe spacing confirming transport within a two-dimensional system. Figure 2a displays the geometric structure of an area of $1.2 \times 1.2\ \mu m^2$. Most of the steps visible correspond to monoatomic steps. About one-third of them correspond to double steps and a few to threefold steps. The terraces in between the steps are atomically flat.

Figure 2b and c shows that the local electrochemical potential $\mu_{ec,\ STP}$ measured simultaneously to the data of Fig. 2a exhibits only a minor monotonous gradient constant on the terraces and varies abruptly at the step edges.

Figure 2d shows cross sections of the topography and $\mu_{ec,\ STP}$-data at a particular step. The variation of $\mu_{ec,\ STP}$ is monotonous and occurs within 6 Å (20–80%). The transition is displaced relative to the step by about 12 Å.

The observation of constant values of $\mu_{ec,\ STP}$ on the terraces and abrupt variation at the steps proves that the current transport is restricted to a 2D-layer at the surface and is not much bypassed via the silicon substrate. Probing $\mu_{ec,\ STP}$ at the same step for different current densities as well as for the opposite direction of the current reveals a linear response.

To analyze the relation between the electrochemical potential and the current density at any position of the surface, an iterative numerical procedure was applied to the data, using the equations $\mathrm{div}\,\vec{j} = 0$ and Ohm's law $\vec{j} = \sigma\, \nabla \mu_{ec,STP}(x, y)$. The first guarantees the continuity of the current and the latter yields the local relation between the current density $\vec{j}(x, y)$, the conductivity $\sigma(x, y)$ and the electrochemical potential $\mu_{ec,\ STP}(x, y)$. Based on the topography, any point is attributed to either the plane surface or a monoatomic step, each having a constant

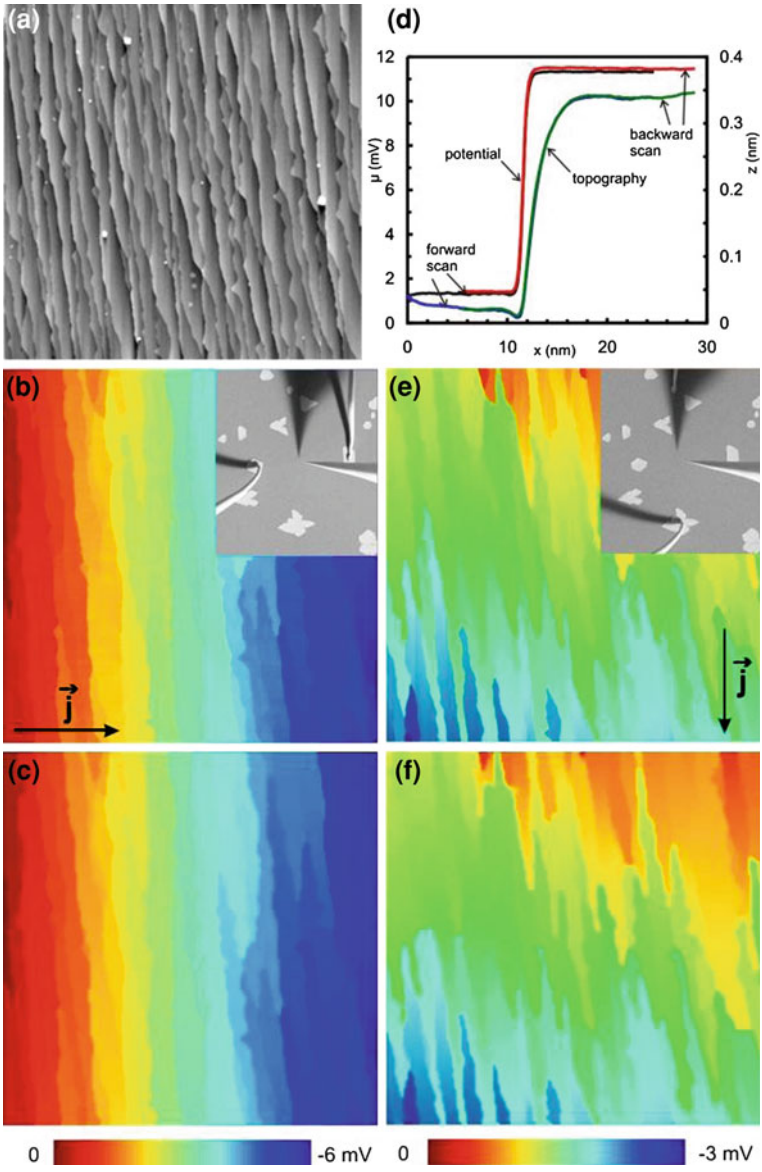

specific conductivity within the frame. Using the boundary condition given by $\mu_{ec,\ STP}(x, y)$ at the four sides of the frame and the average external current density, the problem can be solved analytically yielding $\mu_{ec,\ STP}(x, y)$ at any point inside. Iteratively, the conductivities are varied until the best-fit between calculated and measured $\mu_{ec,\ STP}(x, y)$ data is achieved.

Figure 2c and f illustrates the calculated potential distributions for the data of Fig. 2b and e based on the specific conductivities for the step edge and the

◀ **Fig. 2** Scanning tunneling microscopy and potentiometry of the Si(111)-($\sqrt{3} \times \sqrt{3}$)-Ag surface. The area is 1.2 × 1.2 μm^2. The *insets* in **b** and **e** show scanning electron microscope images for an area of 250 × 290 μm^2. Two gold tips, to the *left* (*top*) and to the *right* (*bottom*), are in contact to silver islands. The tip for the tunneling experiments can be seen in the *middle*. **a** The topographic image, the *gray* scale covers about 1 nm. **b** The electrochemical potential simultaneously measured at an average current density of $j_{\text{extern},\perp} = 0.4$ A/m perpendicular to the steps. The result of the corresponding simulation based on a network of "Ohmic" resistors is displayed in (**c**). **d** *Line* scans across the edge of a monatomic step displaying the tip height in constant conductivity mode (*blue* and *green*) and the effective electrochemical potential (*red* and *black*). To improve the signal-to-noise ratio, a step edge with rather large signal was chosen, the lateral current was increased ($j = 2$ A/m) and the signal was averaged over several *lines*. **e** The electrochemical potential simultaneously measured at an average current density of $j_{\text{extern},\parallel} = 0.26$ A/m parallel to the steps. The result of the corresponding simulation is displayed in (**f**). Extracted from [7]

two-dimensional electron gas (2DEG). The excellent agreement between the calculation and the measured $\mu_{\text{ec, STP}}(x, y)$ data is evident. A more detailed discussion is given in Ref. [2].

Our experiment gives access to the spatial variations of the electrochemical potential within an electric conductor with nanometer resolution. At a step edge the local electrochemical potential exhibits a rather localized monotonous transition. Our measurements cover the transition from the microscopic transport processes, i.e. quantum mechanical tunneling at step edges and diffusive scattering in the two-dimensional electron gas, to the macroscopic resistance. This finally bridges the gap between the elementary processes and the electric resistance observed in macroscopic experiments. Although the transport is ballistic on the nanometer scale a correct numerical description of the electrochemical potential is obtained using the model of diffusive transport. This gives the unique opportunity to evaluate the specific conductivities of the defect free surface and across monatomic steps.

2 Inelastic Mean Free Path of Hot Electrons by Ballistic Electron Emission Microscopy

In the scheme for ballistic electron emission microscopy (BEEM) and spectroscopy (BEES) introduced by Bell and Kaiser [8, 9], a thin metallic layer on top of a semiconductor is studied. If a thin metallic layer is brought into contact with a semiconductor, a Schottky barrier is formed at the interface [10, 11]. The barrier height varies from 0.4 to 1 eV depending on the combination of the metal and the semiconductor [12]. The BEEM arrangement allows the evaluation of how the tunneling current is split into a ballistic contribution that reaches the underlying semiconductor and a current of scattered electrons that remains in the metal film. BEEM experiments have primarily focused on the studies of the buried interface between the metal and the semiconductor. Overview articles on BEEM were given, for example, by Bell and Kaiser [8, 9], Narayanamurti et al. [13], Prietsch [14], or by Wei et al. [15].

In this work we report on BEES studies on ultra-thin Bismuth films. Using a shadow mask two different film thicknesses were prepared in situ on the same silicon (100) *n*-type substrate. Ballistic electron emission spectroscopy was performed under UHV conditions on 11.2 and 22.4 nm thick Bismuth films. This allows gaining insight into the inelastic mean free path (MFP) of electrons in Bi(111) at low energies close to the Fermi level.

The BEEM and BEES are three terminal extensions to STM [2]. By evaluating the onset of the ballistic current, BEES offers the possibility to determine the Schottky barrier height on a local scale with the same lateral resolution as the STM. The energy resolution has an accuracy of about 10 meV. For metallic films the transmission of ballistic charge carriers, i.e. electrons, can be determined in the low-energy regime. If this transmission is analyzed with respect to the traveling distance of the electrons through the film, i.e. the film thickness, the attenuation length for ballistic transport yielding the inelastic MFP can be measured.

Metallic layers on semiconducting substrates like gold, silver or bismuth films on silicon surfaces exhibit a rectifying behavior and are often used as energy filters or e.g. as detectors for hot charge carriers [16, 17]. Therefore their properties concerning the height of the Schottky barrier or the inelastic MFP within the metal layer need to be known.

We conducted BEES studies on the system bismuth on Si(100). The experiments were carried out under UHV conditions (5×10^{-10} mbar) in a commercial multiprobe STM setup (Omicron Nanoprobe). As a substrate *n*-type silicon in (100) orientation with resistivities between 1 and 30 Ωcm was used. Prior to transfer into UHV the Si(100) surface was treated by etching in hydrofluoric acid. In UHV the Si(100) was further cleaned by repeated cycles of flash annealing at 1500 K. At a temperature of 150 K an equivalent of about 11.2 nm of bismuth was deposited onto the surface followed by a slow annealing to 350 K. As reported elsewhere this procedure results into very homogeneously bismuth surfaces with low surface roughness [18, 19]. Using a shadow mask rectangular Bi areas on the Si(100) surface with a size of about 0.4×1 mm^2 were created. Onto this sample an additional amount of 11.2 nm of bismuth was deposited using the same preparation conditions, but with the mask rotated by 90°. This leads to a cross-like structure of the two consecutively deposited bismuth films, exhibiting two different film thicknesses (compare Figs. 3 and 4). The thickness in the middle of the cross-like structure is about (22.4 ± 0.4) nm while at the ends of the structure the film thickness can be evaluated to (11.2 ± 0.4) nm. This was also verified by ex situ Tolansky microscopy [20].

The scheme of the experimental BEES setup is shown in Fig. 3. To conduct BEES one Au tip (2) was gently pressed against an area of the bismuth surface setting the film to ground potential, i.e. the same potential as the Si substrate (tip 2 in Fig. 3). The choice of Au as tip material avoids piercing the Bi film. An Ohmic back contact of the silicon substrate to the sample plate is established by a high dopant layer at the backside of the Si(100) substrate. An STM tip (1), in this case tungsten, is brought into tunneling contact in order to inject hot electrons into the metal film. Both tips are electrochemically etched and cleaned in UHV prior to the experiment.

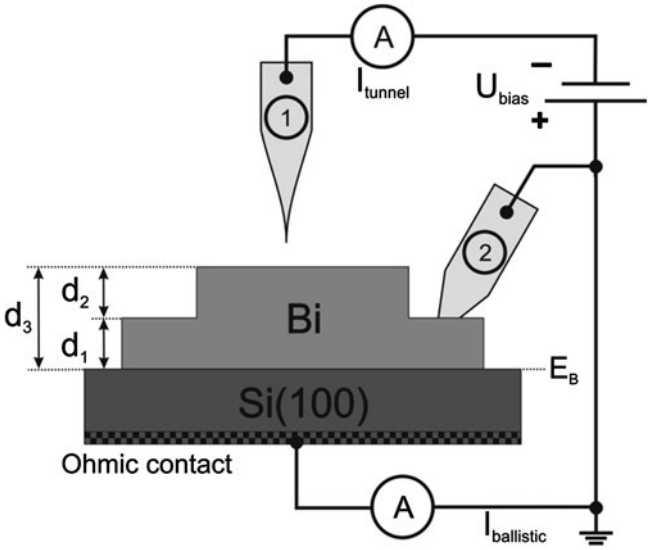

Fig. 3 Scheme of the BEEM and BEES setup for a sample with two different thicknesses d_1 and $d_3 = d_1 + d_2$. A Au tip (*2*) sets the Bi(111) film to the same potential as the Si substrate. The STM tip (*1*) injects hot electrons into the Bi(111) film. The ballistic fraction of the total tunneling current is measured at the semiconductor as the BEEM current $I_{\text{ballistic}}$

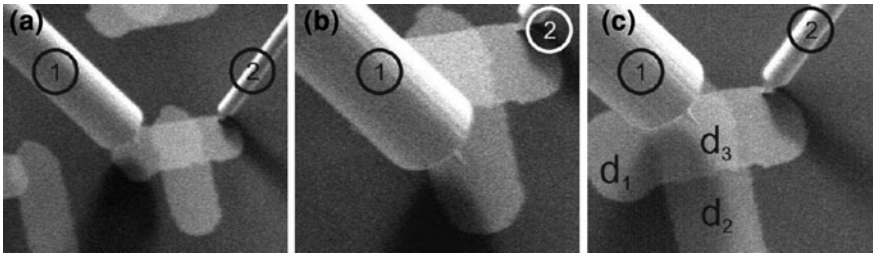

Fig. 4 Measurement sequence of the prepared cross like Bi structure taken by an SEM. Two different film thicknesses $d_1 = d_2$ and d_3 are present on the sample. The STM tip (*1*) is placed at the different measurement positions for the spectra. Tip (*2*) connects the Bi(111) film to the same potential as the Si substrate

Electrons undergoing an energy loss within the metal film or without sufficient energy to overcome the Schottky barrier thermalize within the metal film and are collected by the contacting Au tip (2). However, ballistic electrons, which can enter the semiconductor due to sufficient high energy, are collected and measured as the so-called BEEM-current $I_{\text{ballistic}}$ at the back contact of the Si substrate. At constant tunneling current and for a given lateral position above the bismuth surface the BEEM-current was collected versus the injection energy which can be varied by tip bias voltage (BEES).

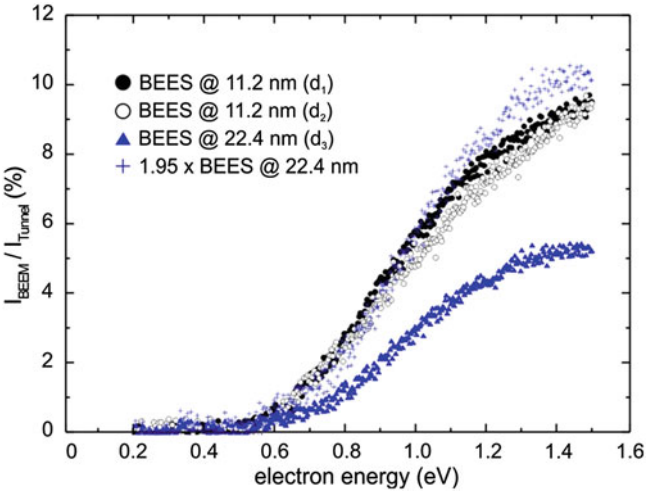

Fig. 5 BEES data for both film thicknesses, 11.2 nm at position (d_1) (*filled black circles*), and at position (d_2) (*open black circles*) and 22.4 nm at position (d_3) (*filled blue triangles*). The BEES spectrum of (d_3) multiplied by a factor of 1.95 (*blue cross*) overlaps quite well with the data for 11.2 nm thickness

Two different thicknesses of the Bi surface $d_1 = d_2 = 11.2$ nm and $d_3 = d_1 + d_2 = 22.4$ nm were analyzed by BEES. The selection of measurement points on the bismuth structure and the tip positioning were monitored using a scanning electron microscope (SEM) (Staib Instruments) prior to each BEES spectrum.

Figure 4 shows the SEM images of the sequence of three different injecting tip-positions [(a), (b) and (c)]. On each position, BEES spectra were acquired.

During data acquisition the sample was cooled down to 130 K. Figure 5 shows a summary of the BEES data collected on the three different positions. For each thickness BEES spectra were taken at randomly distributed positions across the sample. The filled blue triangles represent data taken on the 22.4 nm thick area while the open and filled black circles represent data taken on 11.2 nm thick Bi areas. The difference in film thickness is clearly visible in the SEM images. For all spectra the total injecting tunneling current was kept constant at 180 pA. The spectra were normalized with respect to this total injecting current in order to yield the ratio of ballistically transmitted electrons.

In Fig. 5 representative spectra (an average of 10 for each) are shown. It is obvious that the transmission through the metal film depends on the film thickness. While the film thickness increases, the transmission of the "ballistic" electrons decreases. Furthermore beyond an injection energy of 1.2 eV a decrease of the slope due to diffusive scattering is visible. At tip-positions (d_1) and (d_2) (Fig. 3) the film thickness as well as the transmission is almost equal. At tip-position (d_3) the transmission is attenuated by a factor of 1.95.

The fit function for the spectra is given by the well known Bell and Kaiser model [10, 11]:

$$I_{\text{ballistic}} = R\frac{(E - E_B)^2}{E}$$

where R is a measure of attenuation due to scattering, $E = eU$ the injection energy as provided by the tunneling voltage U, E_B the Schottky barrier. In this theory R is assumed as an energy independent constant and can be described using an exponential function $R = R_0 e^{-\frac{d}{\lambda}}$. λ denotes the inelastic MFP and d the film thickness. Multiplying the BEES data of the 22.4 nm thick film (c) by 1.95 gives a good agreement with the spectra at 11.2 nm thickness (a, b). This suggests that the transmission rate R is almost constant in the energy range of 0.6–1.2 eV which justifies the Bell and Kaiser approximation. Girardin et al. [21] also found a constant transmission rate R in thin gold films on a Si(111) n-type substrate by using a similar method.

Assuming that the transmission through the Schottky barrier and the injection of the electrons into the metal film does not depend on the thickness of the metal film, the ratio of the ballistic currents through both films can be written as:

$$\frac{I_{\text{ballistic}_1}}{I_{\text{ballistic}_2}} = \frac{R_1}{R_2} = \frac{R_0 e^{-\frac{d_1}{\lambda}}}{R_0 e^{-\frac{d_2}{\lambda}}} = e^{\frac{d_2 - d_1}{\lambda}}$$

where d_1 and d_2 denotes the different film thickness, and λ the inelastic MFP.

This allows to calculate a minimum value for the MFP λ. Since the thickness is a crucial factor within this formula the exact value for the metal film thickness is necessary. The thickness of the metal films was determined by two independent studies. During the deposition of Bi the rate was controlled in situ by a quartz microbalance. In addition a Tolansky measurement was taken ex situ after collecting the BEES data. Both agree well to a thickness of 11.2 nm for each simple Bi film and 22.4 nm for the double film. With this result the MFP is determined to 16.8 ± 0.7 nm. This agrees well with the estimated inelastic MFP of electrons in metals if the universal curve denoted by Seah and Dench [22] is further extrapolated to lower energies. Due to the high crystallinity of the Bi film [23], only a relatively low rate of defect scattering sites within the film is assumed. In addition the low density of charge carriers in thin Bi films [24] favors a low rate of electron–electron scattering. Both result in a relatively large inelastic MFP of several nm. In reality the inelastic MFP of the electrons could be even larger, if one considers elastic reflections at the Schottky interface and the surface layer. These electrons would conserve their energy and travel multiple distances through the metal film until they finally overcome the Schottky barrier. As denoted in a prior publication the onset of the ballistic current E_B can be evaluated to 0.58 eV [25].

Summarizing, the lower limit of the inelastic MFP of electrons at 130 K in highly crystalline ultrathin bismuth films of 16.8 nm was assigned using BEES. This provides information on the inelastic MFP of electrons in metal films in the low energy range between the vacuum energy and the Fermi energy. Therefore the universal curve can be expanded to low energies [22, 26, 27].

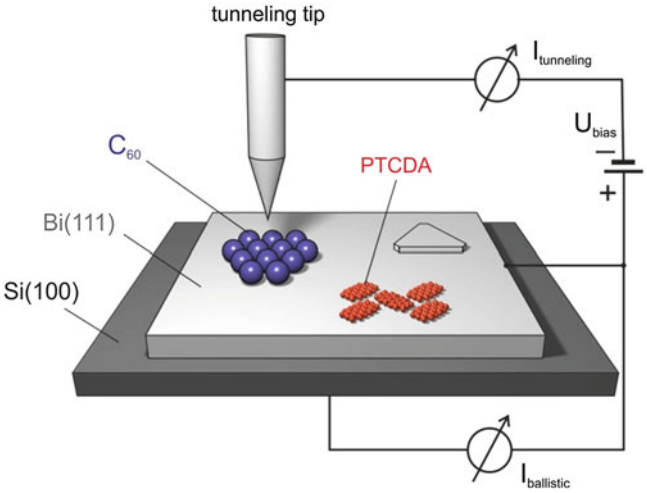

Fig. 6 Sketch of the experimental setup to conduct BEEM on organic adsorbates. Extracted from [25]

3 Ballistic Electron Microscopy of Individual Molecules

In contrast to the BEEM experiments presented before, adsorbates such as organic molecules can be used to partially cover the top metallic layer of the Schottky diode. This has a major influence to the injection process of tunneling electrons from the STM tip.

The present experiment analyzes the transmission of electrons through an organic molecule on top of the metallic layer. Complementary to STS, by which the specific excitation of electronic states [28, 29] or even of a molecular vibration [30] may be analyzed, our experiment provides information on the electrons traversing the molecules without encountering significant scattering processes.

The setup of the experiment is sketched in Fig. 6. The adsorbate to be studied was deposited onto the metal layer. Using the tip of a STM at a negative bias voltage relative to the sample, electrons were injected into the sample surface either directly into the metallic layer or via the adsorbates. In the case of ballistic transport, the electrons reached the interface and overcame the barrier if their energy was sufficient and the momentum parallel to the interface was conserved. These conditions yielded a current, $I_{\text{ballistic}}$, that could be measured at a back contact of the semiconductor. We will refer to this as the "BEEM-current". The majority of the electrons remains in the metallic layer; the BEEM-current only represents a very small percentage of the total current of tunneling electrons. Because the feedback of the STM adjusts the distance between tip and sample in such a way that the total tunneling current remains constant, the BEEM-current directly yields the relative contribution of the ballistic electrons.

The injection and transmission of electrons was studied for two prototype molecules, C_{60} and perylene-tetracarboxylic dianhydride (PTCDA), adsorbed on an atomically flat bismuth film at 130 K. The experiments including the sample preparation were performed under UHV conditions at $p < 3 \times 10^{-10}$ mbar. To prepare the sample, the Si(100) substrate was flashed to 1500 K to produce a clean (2×1) reconstructed surface. Approximately 3 nm of Bi was evaporated on the sample at a low temperature (130 K). The sample is brought to room temperature, and the Bi forms an epitaxial layer that is flat on an atomic scale [18]. The quality of the surface of both the Si and the Bi surfaces was verified by low-energy electron diffraction (LEED). Finally, about half of a monolayer of C_{60} or PTCDA was deposited by thermal evaporation onto the Bi surface at room temperature.

The interface between the Si and the Bi prepared by the procedure described above was found to be very homogeneous, leading to an almost constant signal of BEEM electrons on the clean metallic surface[1]. The transmission of ballistic electrons is very high compared to other systems [31] such as gold on silicon. Considering that the injection of tunneling electrons occurs preferentially with a small component of the k-vector parallel to the surface, the high transmission may be explained by the good overlap between an electronic state of the Bi which is very close to the $\bar{\Gamma}$-point of the surface Brillouin zone [32] and the truncated bulk states of the Si(100) surface.

The topography observed by the STM as well as the simultaneously measured BEEM signal for the C_{60} molecules are shown in Fig. 7a and b. On the flat Bi surface, which appears dark in the topography, triangular islands of Bi formed by one additional double layer of Bi and hexagonally ordered islands of C_{60} can be recognized. The molecules are arranged in a superstructure aligned to the underlying Bi structure and similar to a structure found on Au(111) [33]. The BEEM-current is strongly reduced by a factor of about 8 for the C_{60} layer and shows a faint contrast on the Bi surface that reflects the hexagonal arrangement of the Bi atoms in the (111) surface, which is not visible in the topographic image.

We studied the BEEM-current as a function of the electron energy, which is given by $E = -eU_{\text{bias}}$, where e is the elementary charge and U_{bias} is the applied bias. The spectra for the clean surface (upper curve) and the covered surface (lower curve) are shown in Fig. 8. The onset of the BEEM-current above the threshold can be described by a function as a power of $E - E_{\text{B}}$, where E_{B} is the height of the Schottky barrier [14]. The dashed curve shows a fit with $I_{\text{Ballistic}} \propto \frac{(E-E_B)^2}{E}$ yielding a value of 0.58 eV for E_{B}. For further details on the used fit function see [25]. Above 1.1 eV, saturation effects not included in the formula given above lead to deviations from the experimental curve.

[1] To conduct "BEEM", tunneling currents between 10 and 50 pA were chosen as a compromise between the threshold for damaging the molecular layer and a reasonable signal to noise ratio for the current of ballistic electrons. At a tunneling current of 50 pA the BEEM current typically amounts to 4 pA on the clean bismuth surface and to 0.5 pA for most of the C_{60} molecules or to 3 pA for the PTCDA molecules.

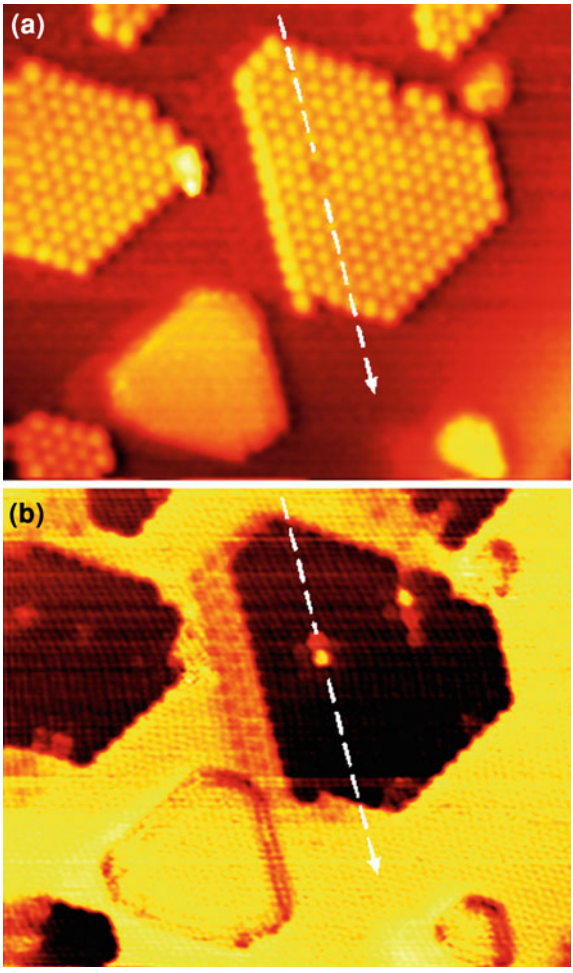

Fig. 7 **a** Topography and **b** BEEM-current for C_{60} on Bi(111). The area is 30 nm by 25 nm, and a bias of −1.3 V has been applied to the tip leading to a total tunneling current of 40 pA; the images show truncated triangular islands of C_{60} and bismuth (*bright*). Topography varying by 0.6 nm from low (*dark*) to high (*bright*). To the *left* of the central island of C_{60} a "ghost-image" caused by a double tip can be seen. However, this double tip does not influence the imaging of the island. Extracted from [25]

The BEEM-current through the C_{60} molecules exhibits a more complex dependence on the electron energy. At about 1.5 eV, the signal strongly increases indicating the opening of an additional channel for the ballistic electrons. A numerical fit to the data displayed in Fig. 8 taking into account a second threshold provides an energy of 1.48 eV for the latter. For the range up to 1.8 eV, an almost perfect fit to the data was obtained; again, saturation was found for higher energies. These results correspond well to the data reported by Yamachika et al. [34], who analyzed C_{60}, on Ag(001) by STS as a function of doping by potassium atoms. For the undoped C_{60}, they found two empty electronic states: the lowest unoccupied molecular orbital (LUMO) at about 0.5 eV and the LUMO+1, the next higher orbital, at 1.6 eV shifting toward a lower energy with increasing doping. Because the first orbital is below the threshold given by the Schottky barrier, only the second orbital will efficiently contribute to ballistic transport.

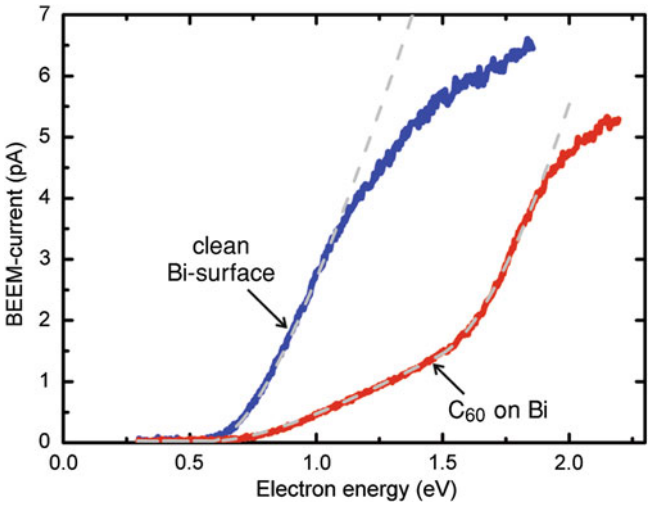

Fig. 8 BEEM spectra for the clean Bi surface and the C_{60} on bismuth. Extracted from [25]

The data obtained for a small area near the center of Fig. 7a and b, are shown in Fig. 9 for *E* values 1.3 and 2.1 eV. One molecule appeared somewhat lower in the topography and yielded a rather strong BEEM-current. Typically, the effect was not completely localized at one molecule; the neighboring molecules were also slightly affected, as expressed by the "halo" in Fig. 9d. Data recorded at various electron energies revealed that the signal was as strong as for the clean Bi surface over the whole range of energy.

In view of the results discussed for the PTCDA molecule (see below), this observation can be explained by an increased coupling of the electronic states of the particular C_{60} to those of the underlying Bi. This effect is not caused by different adsorption geometries, because the bright appearance of the C_{60} hops back and forth only between the same two molecules in a series of measurements, implying that the effect is pinned by a localized defect or adsorbate. Hence, we suggest that an impurity, e.g. an alkaline atom, localized on the surface dopes either the one or the other C_{60} nearby, which shifts the energy of the electronic states of the C_{60} [34] and leads to enhanced coupling. The scattering of the electrons injected by the tunneling tip is thereby reduced and the contribution of ballistic electrons increases.

The images in Fig. 9c and d display the BEEM-current at an electron energy of 2.1 eV; to improve the visibility of the low signal, Fig. 9d shows the same data as Fig. 9c with an enhanced brightness. Each C_{60} molecule exhibits a ring with a slight hexagonal deformation separated by lower transmission regions. Hence, an increase of BEEM-current occurs at the sides of each C_{60} molecule, and not between the molecules as can be clearly seen in Fig. 9d. According to the spectroscopic data discussed above, it can be concluded that this observation is related to the first excited unoccupied electronic state of the C_{60} (LUMO+1).

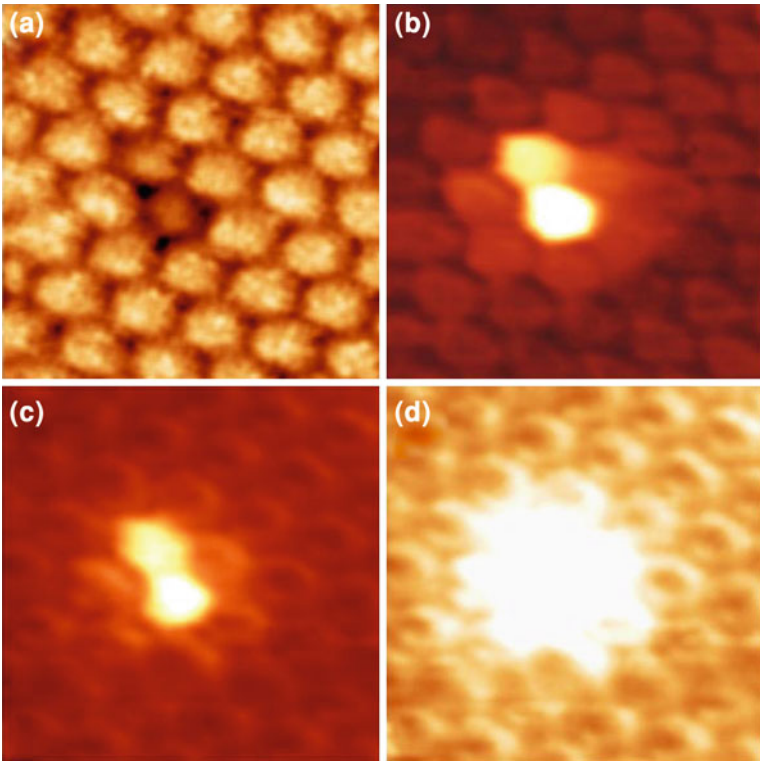

Fig. 9 Topography and BEEM-current for a small area of a C_{60} island. The displayed area is about 5 nm by 5 nm, and the total tunneling current is 40 pA; **a** topography varying by 0.2 nm from low (*dark*) to high (*bright*) measured at a bias of −1.3 V applied to the tip. **b** BEEM-current ranging from 0.2 to 4 pA at a bias of −1.3 V. **c** BEEM-current ranging from 0.2 to 4 pA at a bias of −2.1 V. **d** BEEM-current ranging from 0.2 to 1 pA at a bias of −2.1 V. The contrast has been strongly raised to enhance the features at low current. Extracted from [25]

Although rigorous theoretical consideration requires one to treat the transition from an electron through the tunneling gap, the molecules, the metal layer and the Schottky barrier as a whole, it is useful to consider the ballistic transport stepwise to understand the observations.

The first step is the tunneling process from the metallic tip through the vacuum barrier into the molecule. Neglecting thermal broadening of the Fermi distribution of the electrons only electrons of the tip with energies ranging from E_F of the sample to eU_{bias} above E_F, contribute to the tunneling current. The molecule does not provide a continuous density of electronic states but provides discrete levels which are broadened by the interaction with the substrate. Tunneling is enabled for those electrons with an energy matching one of these molecular states, e.g. the LUMO, LUMO+1, etc.

The second step is given by the intramolecular transport. If inelastic scattering occurs, the energy of the electrons is reduced and the electrons are no longer "ballistic".

The third step is the transition from the molecule to the metal layer.

The fourth step is the transport within the metal layer.

The fifth and last step is the transition across the Schottky barrier between the metal and the semiconductor. It requires that the energy associated with the motion of the electron perpendicular to the interface exceeds the Schottky barrier. Furthermore, the component of the wave vector parallel to the surface must match to an empty state of the semiconductor.

In contrast to STS, in which only the first step is considered, BEEM takes into account each of these additional steps.

The recent calculation [35] for the electron conduction through individual C_{60}-molecules bridging two metallic electrodes shows, that the current runs along the C–C bonds and that from the unoccupied molecular orbitals with different symmetries only specific ones provide the major contribution to the electron transport. They predict the highest density at the sides and the lowest density at the center of the molecule. Both are in good agreement with our observation, e.g. in Fig. 9.

To learn more about the transmission of ballistic electrons through molecules a rather different organic molecule was studied. PTCDA is a planar, almost rectangular molecule. It has significant partial charges due to the strong electronegative anhydride groups at both of the short sides. The topography and the BEEM-current for a small area around a Bi island which is not covered by PTCDA is shown in Fig. 10.

The molecules are arranged in a so-called "herringbone structure" observed for PTCDA on many other metallic substrates [36, 37]. The insets of Fig. 10a and b, at the lower right corners, sketch the rectangular unit cell containing two molecules which are rotated by about 90° relative to each other. The displayed data corresponds to an electron energy of 1.7 eV. As for C_{60}, a reduction of the BEEM-current is observed ranging from 2 (dark areas) to 35% (bright areas) relative to the uncovered surface. In contrast to the findings for C_{60}, the results do not change significantly as a function of energy in the range between 0.6 and 2.0 eV.

As can be seen in detail in Fig. 10d and e, the appearance of the PTCDA molecule completely differs for the observed topography and the map of the measured BEEM-current. The topographic image is dominated by two maxima located on both sides parallel to the long axis of the molecule. As discussed in [38] the maxima can be attributed to the LUMO. Probably because of the semimetallic character of the Bi film, the LUMO remains above E_F, in contrast to a silver substrate, and it is imaged at a negative tip bias. However, the major contribution to the BEEM-current occurred in one longish area centered on top of the long axis. As pointed out in [38] this feature corresponds to the LUMO+1 state, which has a significant coupling to the bulk states of the substrates. A close inspection of the BEEM signal reveals an important difference to the STS images of the LUMO+1. The maximum of the BEEM signal is not at the center of the perylene core but at

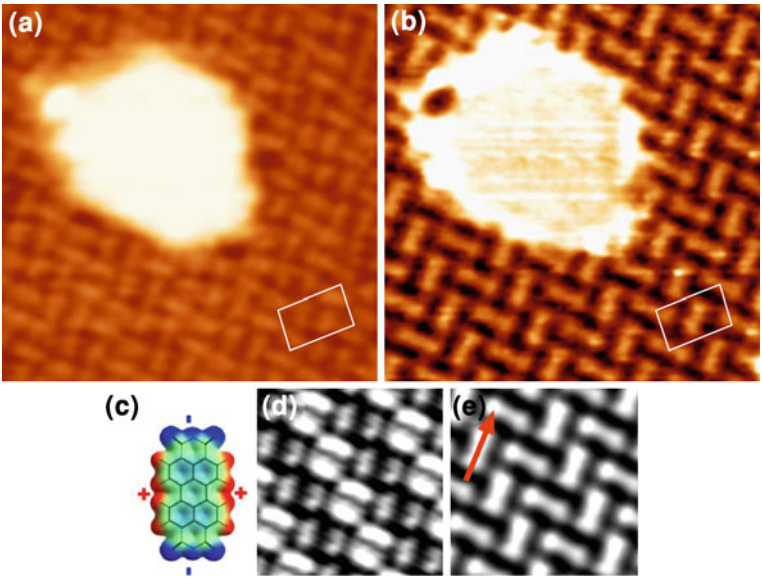

Fig. 10 Topography and BEEM-current for a small area covered by PTCDA molecules. The displayed area is about 9.3 nm by 9.3 nm, and the total tunneling current is 40 pA with a bias of −1.7 V applied to the tip; **a** topography of a bismuth island surrounded by a PTCDA domain arranged in a herringbone structure. **b** BEEM-current ranging from 0.2 to 5.4 pA. **c** Partial charge distribution of the PTCDA molecule and structure model. **d** Detailed view of the PTCDA topography averaged over the unit cell. **e** Averaged BEEM-current of the PTCDA structure in **b**

the anhydride groups. Hence it can be concluded that the electron transport through the molecule or the transition to the Bi substrate works best at these positions.

The presented variation of STM/BEEM allows the analysis of the electronic transport through a thin layer of adsorbates in great detail. If the Schottky contact supporting this layer is prepared homogeneously, it provides a detector for ballistic electrons with an almost constant efficiency as a function of the lateral position. The setup represents a "scanning near field transmission electron microscope" operating at electron energies ranging from 0.5 to 3 eV and capable of submolecular resolution for a monolayer of adsorbates. Specific paths for the ballistic transport of electrons through the molecules could be identified for C_{60} and PTCDA. They result from tunneling into the LUMO+1 electronic state followed by intramolecular transport and coupling to the bulk states of the underlying metal.

4 Conclusion

By extending the experimental techniques scanning tunneling microscopy can be used to study the electronic transport on the nanoscale. Using additional contacts the scattering of conduction electrons, e.g. at step edges, grain boundaries,

etc. can be studied. For the silver induced reconstruction of the Si(111) surface the specific resistivity of the defect free surface, step edges and other defects can be evaluated. The electronic transport normal to the surface may be studied by ballistic electron microscopy and spectroscopy. While the MFP for ballistic electrons is rather long for a metal film, e.g. bismuth, the scattering by organic molecules is significant. Moreover it reveals details of the transport through the molecule [25]

Acknowledgments The work has been supported by the Deutsche Forschungsgemeinschaft (DFG) through the Sonderforschungsbereich 616 "Energy Dissipation at Surfaces". Additional support to M.C.C. is granted by the Studienstiftung des deutschen Volkes. D. Utzat is gratefully acknowledged for designing and constructing the STM electronics. We gratefully acknowledge M. Wenderoth for stimulating discussions and providing the simulations for the Ohmic network.

References

1. Muralt, P., Pohl, D.W.: Scanning tunneling potentiometry. Appl. Phys. Lett. **48**(8), 514 (1986)
2. Binnig, G., Rohrer, H., Gerber, Ch., Weibel, E.: 7 × 7 reconstruction on Si(111) resolved in real space. Phys. Rev. Lett. **50**, 120 (1983)
3. Binnig, G., Rohrer, H., Gerber, Ch., Weibel, E.: Tunneling through a controllable vacuum gap. Appl. Phys. Lett. **40**, 178 (1982)
4. Baddorf, A.P.: Scanning tunneling potentiometry: the power of STM applied to electrical transport. In: Kalinin, S.V., Gruverman, A. (eds.) Scanning Probe Microscopy, pp. 11–30. Springer, New York (2007)
5. Briner, B.G., Feenstra, R.M., Chin, T.P., Woodall, J.M.: Local transport properties of thin bismuth films studied by scanning tunneling potentiometry. Phys. Rev. B **54**(8), R5283 (1996)
6. Bannani, A., Bobisch, C.A., Möller, R.: Local potentiometry using a multiprobe scanning tunneling microscope. Rev. Sci. Instrum. **79**, 083704 (2008)
7. Homoth, J., Wenderoth, M., Druga, T., Winking, L., Ulbrich, R.G., Bobisch, C.A., Weyers, B., Bannani, A., Zubkov, E., Bernhart, A.M., Kaspers, M.R., Möller, R.: Electronic transport on the nanoscale: ballistic transmission and Ohm's law. Nano Lett. **9**, 1588 (2009)
8. Kaiser, W.J., Bell, L.D.: Direct investigation of subsurface interface electronic structure by ballistic-electron-emission microscopy. Phys. Rev. Lett. **60**, 1406 (1988)
9. Bell, L.D., Kaiser, W.J.: Observation of interface band structure by ballistic-electron-emission microscopy. Phys. Rev. Lett. **61**, 2368 (1988)
10. Schottky, W.: Experimental measurement of the total-energy distribution of field-emitted electrons. Zeits. f. Physik **113**, 367 (1939)
11. Braun, F.: Über die Stromleitung durch Schwefelmetalle. Pogg. Ann. **153**, 556 (1874)
12. Mönch, W.: Electronic Properties of Semiconductor Interfaces, 43rd edn. Springer, Berlin (2004)
13. Narayanamurti, V., Kozhevnikov, M.: BEEM imaging and spectroscopy of buried structures in semiconductors. Phys. Rep. **349**, 447 (2001)
14. Prietsch, M.: Ballistic electron emission microscopy (BEEM): studies of metal/semiconductor interfaces with nanometer resolution. Phys. Rep. **253**, 163 (1995)
15. Yi, W., Narayanamurti, V., Ku, K.-C., Zhu, M., Samarth, N.: Magnetoresistance in an asymmetric $Ga_{1-x}Mn_xAs$ resonant tunnelling diode. Phys. Rev. B **80**, 201307(R) (2009)
16. Nienhaus, H., Weyers, S.J., Gergen, B., McFarland, E.W.: Thin Au/Ge Schottky diodes for detection of chemical reaction induced electron excitation. Sens. Actuators B Chem. **87**, 421 (2002)
17. Krix, D., Nünthel, R., Nienhaus, H.: Generation of hot charge carriers by adsorption of hydrogen and deuterium atoms on a silver surface. Phys. Rev. B **75**, 073410 (2007)

18. Bobisch, C., Bannani, A., Matena, M., Möller, R.: Ultrathin Bi-films on Si(100). Nanotechnology **18**, 055606 (2007)
19. Jnawali, G., Hattab, H., Krenzer, B., Horn-von Högen, M.: Lattice accommodation of epitaxial Bi(111) films on Si(001) studied with SPA-LEED and AFM. Phys. Rev. B **74**, 195340 (2006)
20. Tolansky, S., Emara, S.H.: Precision multiple-beam interference fringes with high lateral microscopic resolution. J. Opt. Soc. Am. **45**, 792 (1955)
21. Girardin, C., Coratger, R., Pechou, R., Ajustron, F., Beauvillain, J.: Study of the electron mean free path by ballistic electron emission microscopy. J. Phys. III France **6**, 661 (1996)
22. Seah, M.P., Dench, W.A.: Quantitative electron spectroscopy of surfaces: a standard data base for electron inelastic mean free paths in solids. Surf. Interface Anal. **1**, 2 (1979)
23. Hattab, H., Zubkov, E., Bernhart, A., Jnawali, G., Bobisch, C., Krenzer, B., Acet, M., Möller, R., Horn-von Hoegen, M.: Epitaxial Bi(111) films on Si(001): strain state, surface morphology, and defect structure. Thin Solid Films **516**, 8227 (2008)
24. Smith, G.E., Baraff, G.A., Rowell, J.M.: Effective *g* factor of electrons and holes in bismuth. Phys. Rev. **135**, A1118 (1964)
25. Bannani, A., Bobisch, C., Möller, R.: Ballistic electron microscopy of individual molecules. Science **315**, 1824 (2007)
26. Palm, H., Arbes, M., Schulz, M.: Nanometer-microscopy of the electron transmission through an ultrathin (3–22 nm) Au film and of the Au-Si Schottky barrier height. Appl. Phys. A **56**, 1 (1993)
27. Niedermann, P., Quattropani, L., Solt, K., Maggio-Aprile, I., Fischer, O.: Hot-carrier scattering in a metal: a ballistic-electron-emission microscopy investigation on PtSi. Phys. Rev. B **48**, 8833 (1993)
28. Feenstra, R.M., Stroscio, J.A., Tersoff, J., Fein, A.P.: Local state density and long-range screening of adsorbed oxygen atoms on the GaAs(110) surface. Phys. Rev. Lett. **58**, 1668 (1987)
29. Hamers, R.J., Tromp, R.M., Demuth, J.E.: Surface electronic structure of Si(111)-(7x7) resolved in real space. Phys. Rev. Lett. **56**, 18 (1986)
30. Stipe, B.C., Rezaei, M.A., Ho, W.: Single-molecule vibrational spectroscopy and microscopy. Science **280**, 1732 (1998)
31. Sirringhaus, H., Lee, E.Y., von Känel, H.: Hot carrier scattering at interfacial dislocations observed by ballistic-electron-emission microscopy. Phys. Rev. Lett. **73**, 577 (1994)
32. Ast, C.R., Höchst, H.: Electronic structure of a bismuth bilayer. Phys. Rev. B **67**, 113102 (2003)
33. Altmann, E.I., Colton, R.J.: Determination of the orientation of C_{60} adsorbed on Au(111) and Ag(111). Phys. Rev. B **48**, 18244 (1993)
34. Yamachika, R., Grobis, M., Wachowiak, A., Crommie, M.F.: Controlled atomic doping of a single C60 molecule. Science **304**, 281 (2004)
35. Ono, T., Hirose, K.: First-principles study of electron-conduction properties of C_{60} bridges. Phys. Rev. Lett. **98**, 026804 (2007)
36. Chizhov, I., Kahn, A., Scoles, G.: The influence of steps on the orientation of copper phthalocyanine monolayers on Au(111). J. Cryst. Growth **208**, 449 (2000)
37. Umbach, E., Sokolowski, M., Fink, R.: Substrate interaction, long-range order, and epitaxy of large organic adsorbates. Appl. Phys. A **63**, 565 (1996)
38. Temirov, R., Soubatch, S., Luican, A., Tautz, F.S.: Free-electron-like dispersion in an organic monolayer film on a metal substrate. Nature **444**, 350 (2006)

Solid State Nano Gears Manipulations

Cedric Troadec, Jie Deng, Francisco Ample, Ramesh Thamankar and Christian Joachim

Abstract The detailed fabrication and manipulations of solid state nano gears up to 350 nm in diameter is reported. Atomic force microscopy (AFM) and ultra high vacuum (UHV) scanning tunneling microscopy (STM) are used to maneuver the gears. The aim is to bridge the gap between the current solid state gears and the now available nanoscale gears. As in many technology integrations, miniaturization is a way to boost efficiency and an opening to new applications.

1 Introduction

Gears in many different designs and materials have been in use for thousands of years [1]. One of the earliest mentions of gear usage was in the South Pointing Chariot originating from China, around 2600 BC, whereas the Antikythera mechanism, from around 85 BC, is the oldest know complex mechanical calculator that used gears. The development of gears over the years has come from different drives like speed reduction, power transmission, torque multiplication and also accurate measurement. With the demand in efficient and ever more complex and integrated systems, there has been a drive to miniaturize gears. Trains of gears down to the hundreds of micrometers, with reduction ratio of 3000000:1 have been successfully demonstrated [2]. Even smaller gears, about 500 nm in diameter, have been fabricated from single gold crystals using focused ion beam [3], but no controlled rotation was shown. The smallest gear to date (Guinness World Records

C. Troadec (✉) · J. Deng · F. Ample · R. Thamankar · C. Joachim
Institute of Materials Research and Engineering, A*STAR (Agency for Science, Technology and Research), 3 Research Link, Singapore 117602, Singapore
e-mail: cedric-t@imre.a-star.edu.sg

C. Joachim
Nanoscience Group and MANA Satellite, CEMES/CNRS, 29 Rue Marvig, BP 94347, 31055 Toulouse Cedex, France

C. Joachim (ed.), *Atomic Scale Interconnection Machines*, Advances in Atom and Single Molecule Machines, DOI: 10.1007/978-3-642-28172-3_16,

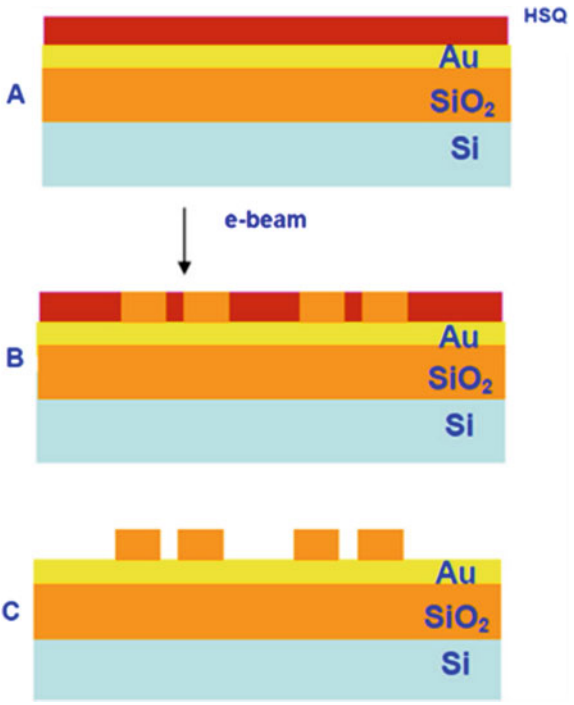

Fig. 1 Fabrication process for the gears, using HSQ as resist on a Silicon substrate covered with an adhesion layer of chromium (5 nm) and a sacrificial layer of gold (30 nm)

2012) is a molecule called hexa-t-butyl-pyrimidopentaphenylbenzene, which mimics a 6 teeth gear of 1.2 nm in diameter [4]. The gap between these two types of gears spans over two orders of magnitude.

In this chapter, we report on the fabrication of mesoscopic sizes solid state gears, which will be manipulated by an AFM tip in air, then by multiple STM tips, when loaded in a UHV multiprobe system in order to design a train of gears. The manipulations, results and challenges will be discussed.

2 Experiment and Results

2.1 Fabrication

The fabrication of the solid state gears has been reported previously [5] and the same process has been used here. The gears are fabricated out of a negative tone e-beam resist, hydrogen silsesquioxane (HSQ). This resist has demonstrated very good resolution below 10 nm [6] and can be baked post development to form a material with properties and composition close to silicon dioxide. The substrate is a piece of silicon wafer with native oxide, covered with an adhesion layer of chromium (5 nm) and a sacrificial 30 nm thick gold layer (see Fig. 1). The gold layer is important to release the gears as without it the components do not show any sign of movements on

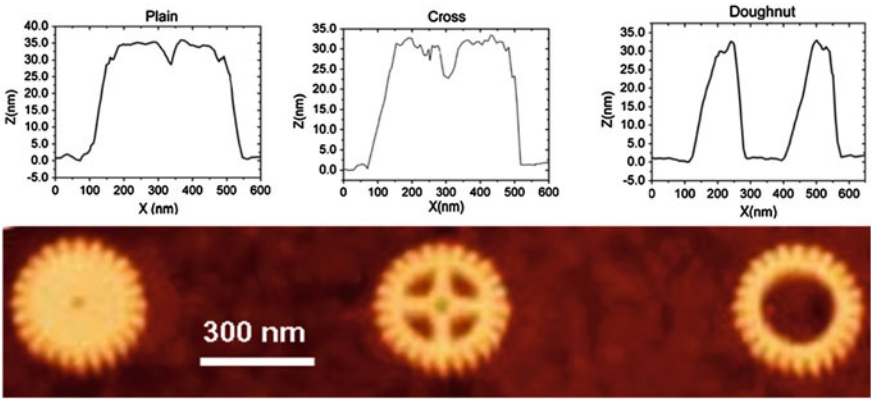

Fig. 2 AFM images of the different designs for the 350 nm HSQ gears, along with their lien profile taken horizontally at the center line

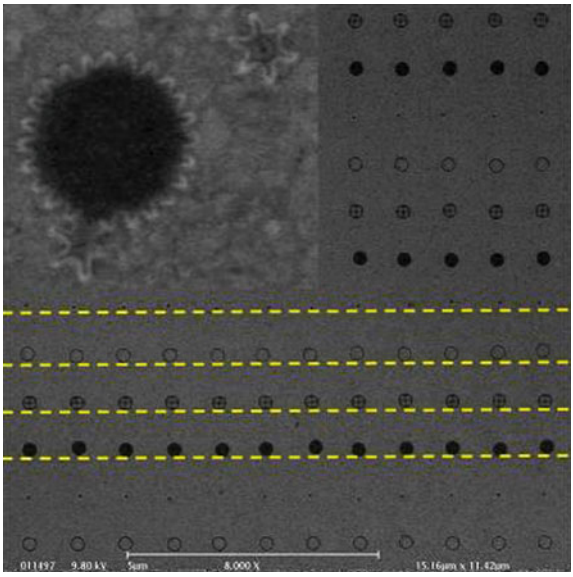

Fig. 3 SEM images of the gears after gold etching. Notice that all the gears show a misalignment from a perfect line, as they had been patterned to follow. This is a positive observation and a necessary one to have a successful AFM manipulation. Inset: small gears have moved toward a 350 nm gear, starting to self-assemble

the surface, even after baking. AFM manipulation was not successful in that situation. The gold etching is done in a solution of potassium iodide and iodine. The etching time can be as long as 150 s, interceded by bursts of ultrasonic agitation for about 10 s.

Gears of 350, 100 and 60 nm in diameter have been fabricated and imaged using AFM (Fig. 2) and SEM. The teeth of the gears, less than 20 nm in length and about 15 nm in pitch, are the same on all the different designs and sizes so that any can be used to construct a train of gears.

After the gold etching, the usual observation is a shift in the position of the gears, with regards to their original line pattern and 1 μm spacing. This displacement can be seen in Fig. 3 in the SEM images, with dashed horizontal lines

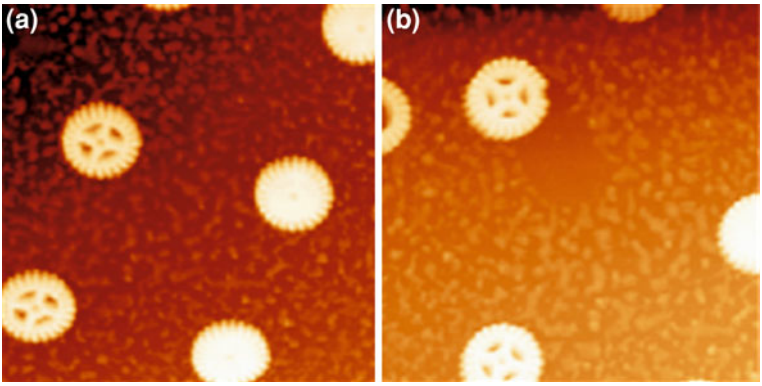

Fig. 4 AFM manipulation of a cross gear before (**a**) and after (**b**). The contact point of the tip can be determined by the slight damage to the teeth as seen in (**b**). Note also that the path of the gear leaves a clear trail on the substrate, indicating a close contact to the substrate

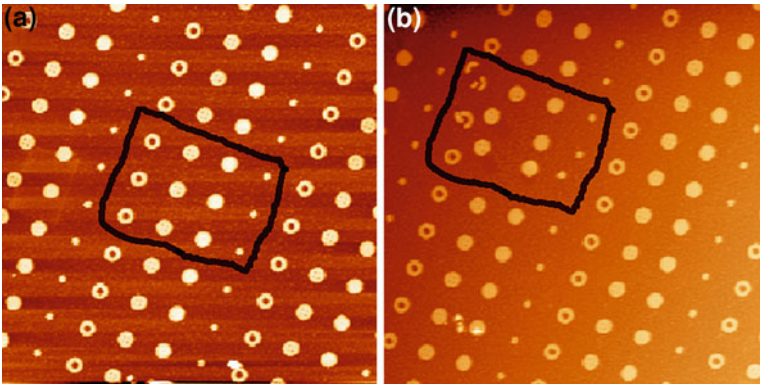

Fig. 5 AFM images taken before (**a**) and after (**b**) manipulation of all types of gears. The area of interest is delimited in each image. Note that the doughnut types of gears are broken after the manipulation. It is the only type that could not be moved

as guide to the eyes. This observation is important if one wants to carry on manipulating these gears. Unless a shift in the position of, at least, the small gears is observed, the chances of the gears being stuck to the surface of the substrate are very high. We have never been able to move a gear in air with an AFM tip unless we had a positive observation after the etching. In some cases, the small gears are so mobile that they can start to assemble with other gears to form trains of gears (see inset of Fig. 3).

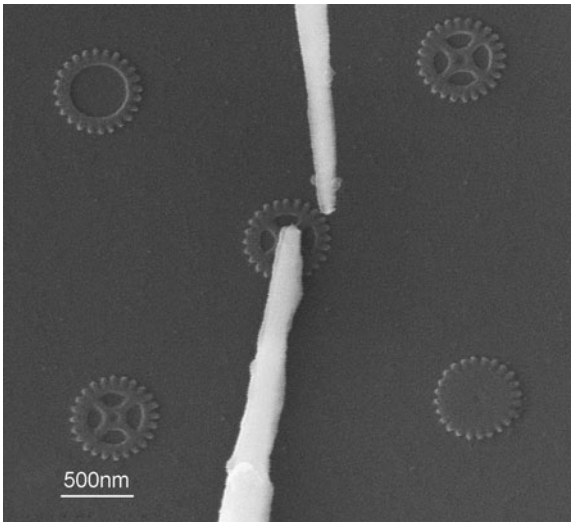

Fig. 6 Two etched tungsten tips on a 350 nm gear. The tip apex is less than 50 nm

2.2 Manipulation

The sample is then placed in a Digital Instrument Nanoscope IV AFM in tapping mode. The cantilevers used are 50 N/m stiff with a resonant frequency of about 250 kHz. The manipulation is done by switching to a "scratch" mode where the direction and the length of the tip movement can be controlled, as well as the height at which the tip will be positioned before the scratch. In all manipulations, the tip was set to move vertically upward.

Figure 4 gives an example of a gear manipulation in which an AFM image is taken before (Fig. 4a) and after manipulation (Fig. 4b). Comparing the two images gives a lot of information about the manipulation process. After the manipulation, a slight damage to the teeth on the right side of the gear can be observed. It most probably comes from the interaction with the AFM tip, which suggests also that the gear was not only translated, but rotated as well. The path of the gear is clearly marked by the clean trail, as seen on Fig. 4b. The origin of the particulates on the substrate here is not known, probably some remnants from the development or gold etching as such contamination is not always observed. The fact is that it is not present below the gear and it is also easily moved by the gear.

The same manipulation procedure is then used on the other type of gears, to ensure that all can be moved in a reproducible manner. Figure 5 shows two AFM images taken before and after manipulations of the gears. The 100 nm gear could be moved as well as the plain and cross 350 nm gears. The doughnut rings could not be moved, and were broken into pieces during the manipulations. The strength of the arch of the gear was no match to the force applied on it by the AFM tip.

The next step is to load the sample in a UHV multiprobe system, which offers four individually actuated sharp tungsten tips under the eye of an SEM. The system and its possible applications are described in detail in other

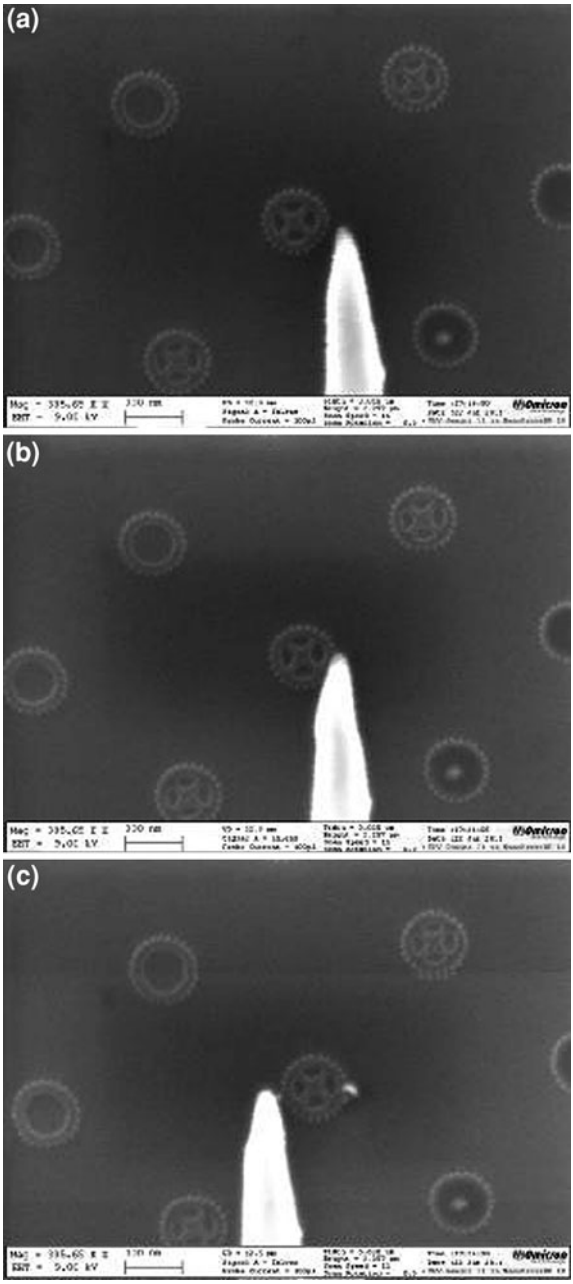

Fig. 7 Sequence of manipulation using a sharp tungsten tip on a cross type gear. **a** The tip is positioned next to the gear, just above the surface. **b** The tip is moved from right to left and a small bending of the tip is occurring as it interacts with the gear. **c** The gear has not moved and the site of interaction between the tip and the gear has some bright residue, either from the tip or the gear

publications [7–9]. The base pressure of the system is in the mid 10^{-10} mBar, and the sample was not heated prior to inserting or inside the load-loack. In Fig. 6 is shown two of the etched tungsten tips in proximity to a cross gear.

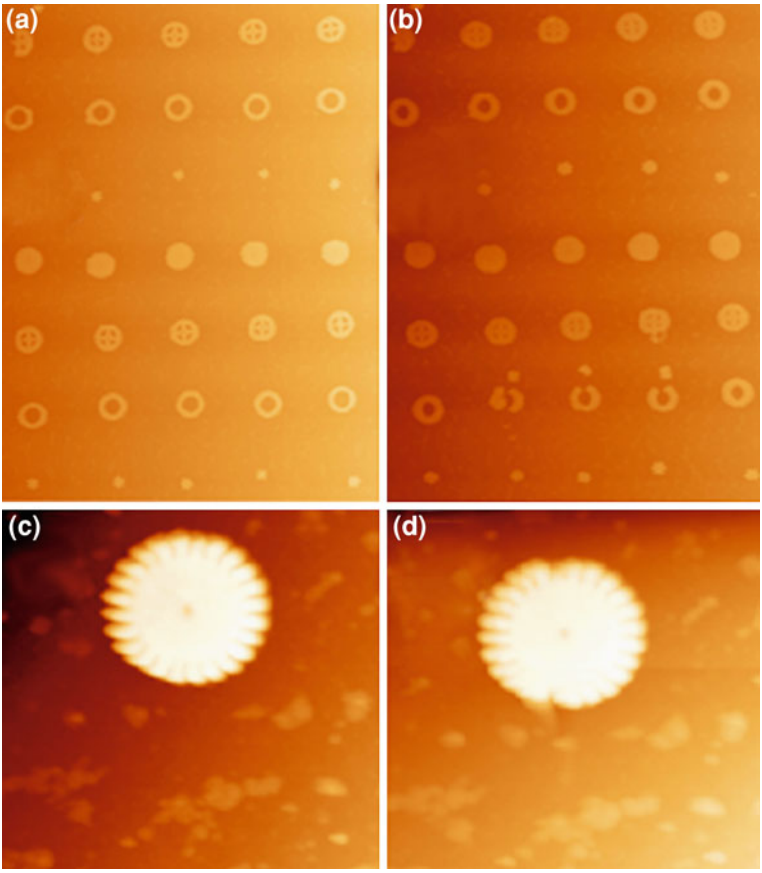

Fig. 8 AFM image before (**a**) and after (**b**) manipulation in air by AFM. None of the gear moved, and the doughnut gears could still be broken. The tip left marks on all the gears with, for example, the plain gear (**c**) after manipulation (**d**). Two indents opposite to each other were made by the AFM tip

First, we tried to manipulate with only one tip. A tungsten tip is brought within tunneling range to the surface (moderate voltage and low current), which is possible in our case as the substrate is silicon with a native oxide (see Fig. 7a). The feedback loop is then switched off and the tip is moved across the gear location. The tip interaction with the gear is well established as we see the tip bending (Fig. 7b). At a certain push threshold, the tip would just jump out of its position and leave a small mark on the gear where the contact was made. The gear could not be moved, and repeated efforts in all possible directions, and every gear design did not yield any result.

As the gear might have been stuck to the substrate due to some reaction with the HSQ or the contaminants, an elevated temperature might help the gear to be moved from its original position. For this, the temperature was raised in 10°C steps

up, to 80°C and the tip was brushed across the gear. The results were also negative for the whole temperature range.

Following this UHV experiment, the sample was taken out of the chamber and put back in the ambient AFM. The same type of manipulations was performed as previously and the results are shown in Fig. 8. None of the gears moved, although some dents in the gears were observed. The doughnut gears were broken in a similar way as in Fig. 5.

3 Discussion and Future work

The detailed process presented here is complementary to the experiment reported earlier [4]. The availability of many probes should allow the fabrication of train of gears, but as demonstrated, the process is not yet successful especially in vacuum. This environment is needed as imaging at the nanoscale level is best achieved by SEM. The fact that the manipulation can occur in air, but not after the sample was subjected to vacuum, points to some drastic changes at the gear/substrate interface. The presence of a water film on the sample in ambient atmosphere could act as a lubricant or passivation layer. In UHV, this water film would have completely evaporated which could lead to a lack of movement. An additional layer below the gold could help reduce the friction in vacuum, but further experiments are required to determine the nature of the material that would satisfy the requirements involved.

Once this problem is solved, the first step will be the demonstration that a tip can be used as a temporary shaft and that the gear can be rotated by another tip. If successful, a train of gear will be the next achievement.

Acknowledgments This work was supported by the Agency for Science, Technology and Research (A*STAR) funding under project no. 1021100972.

References

1. Darle, W.D.: The evolution of the gear art. American Gear Manufacturers Association, Washington (1969)
2. Rogers, M.S., Sniegowski, S.S., Miller, S., LaVigne, G.F.: Designing and operating electrostatically driven microengines. In: Proceedings of the 44th International Instrumentation Symposium, Reno, NV, May 3–7, pp. 56–65 (1998)
3. Yun, Y.J., Ah, C.S., Kim, S., Yun, W.S., Park, B.C., Ha, D.H.: Manipulation of freestanding Au nanogears using an atomic force microscope. Nanotechnology **18**, 505304 (2007). doi:10.1088/0957-4484/18/50/505304
4. Manzano, C., Soe, W.-H., Wong, H.S., Ample, F., Gourdon, A., Chandrasekhar, N., Joachim, C.: Step-by-step rotation of a molecule-gear mounted on an atomic-scale axis. Nat. Mater. **8**, 576 (2009). doi:10.1038/nmat2467
5. Deng, J., Troadec, C., Ample, F., Joachim, C.: Fabrication and manipulation of solid-state SiO2 nano-gears on a gold surface. Nanotechnology **22**, 275307 (2011). doi:10.1088/0957-4484/22/27/275307

6. Häffner, M., Haug, A., Heeren, A., Fleischer, M., Peisert, H., Chassé, T., Kern, D.P.: Influence of temperature on HSQ electron-beam lithography. J. Vac. Sci. Technol. B **25**, 2045 (2007). doi:10.1116/1.2794324
7. Neucheva, O.A., Thamankar, R., Yap, T.L., Troadec, C., Deng, J., Joachim, C.: Atomic scale interconnection machine. In: Joachim, C. (ed.) Advances in Atom and Single Molecule Machines, Springer, Berlin (2012)
8. Thamankar, R., Neucheva O.A., Yap, T.L., Joachim, C.: Surface conductivity measurements on MoS_2 using UHV-NANOPROBE. In: Joachim, C. (ed.) Advances in Atom and Single Molecule Machines, Springer, Berlin (2012)
9. Joachim, C., Martrou, D., Rezeq, M., Troadec, C., Deng, J., Chandrasekhar, N., Gauthier, S.: Multiple atomic scale solid surface interconnects for atom circuits and molecule logic gates. J. Phys. Condens. Matter **22**, 084025 (2010) doi:10.1088/0953-8984/22/8/084025

Probing Single Molecular Motors on Solid Surface

Haiming Guo, Yeliang Wang, Min Feng, Li Gao and Hongjun Gao

Abstract Understanding structures and mechanisms of single molecular motors on solid surfaces is of critical importance for nanoscale engineering and bottom-up construction of complex devices at single molecular scale. In this chapter, two different kinds of single molecular motors at surfaces are studied with scanning tunneling microscopy (STM) technique. We discuss the structural and conductance transitions of one H2 rotaxane molecule at the sub-rotaxane scale, and then present a molecular rotor with a fixed off-center axis formed by chemical bonding on Au(111) substrate. These results represent important advances in single molecular-based machines and devices.

1 Introduction

Single molecules with intriguing physical properties are important building blocks for fabricating functional nanodevices [1–3]. Integrating device functions into single molecules is a crucial issue in molecule-based nanoengineering and is being considered as an ideal solution for the device miniaturization pushed by the Moore's Law. Molecular machines, or molecular actuators, are kinds of typical nanodevices, usually capable of converting external chemical, electrical, or optical energy into mechanical motion. They, in fact, exist widely in nature and play an important role in many biological processes [4, 5]. For instance, kinesin protein

H. Guo · Y. Wang · M. Feng · L. Gao · H. Gao (✉)
Nanoscale Physics and Devices Laboratory, Institute of Physics,
Chinese Academy of Sciences, P. O. Box 603
100190 Beijing, China
e-mail: hjgao@iphy.ac.cn

C. Joachim (ed.), *Atomic Scale Interconnection Machines*, Advances in Atom and Single Molecule Machines, DOI: 10.1007/978-3-642-28172-3_17,

can burn adenosine triphosphate (ATP) and generate linear motion along cytoskeleton [6]. Other proteins, driven by proton gradients across membranes, mechanically rotate flagella to propel bacteria [7]. Mimicking biological design is believed as one of main routes to synthesize artificial molecular machines and put them to work [8, 9]. So far, attempts on design, synthesis, and controllable operation of molecular machines have yielded analogs of rotors [10–12], gears [13], switches [14], shuttles [15, 16], turnstiles [17], ratchets [18], wheels [19], even complex wheelbarrows [20, 21], nanocars [22], elevators [23], and refrigerators [24].

Generally the movements of molecular actuators can be simply classified into two groups according to their motion styles, i.e. linear motion and rotational motion. ATP-driven Kinesin protein [6] and rotation of flagella [7] are the examples of these two groups, respectively, in biological systems. The motions of a single molecule can be used as a matter of course to introduce new design perception or control approaches of molecular movements. Rotaxanes and molecular rotors, which produce linear motions and rotational motions, respectively, are among the most studied artificial molecular actuators.

Rotaxane is a well-known class of linear molecular motors with bistable properties. Its structure is composed of a dumbbell-shaped chain and an encircling macrocycle. The chain incorporates two recognition sites whose energy state is stable when the macrocycle is positioned on them. The macrocycle can move between two recognition sites upon external stimuli (electrochemical [25, 26], light [27–29], or pH [30, 31]), resulting in switching of the electronic configuration. If such reciprocating of the ring component can be controlled, rotaxanes would be interesting candidates for single molecular switches or recording units in the future. So far, exploring the mechanism of conductance switching in rotaxane-based solid-state devices is still a task of great necessities and challenges [32–35].

Molecular rotors can rotate with respect to their surrounding environments or involve one part that rotates relative to another part [36, 37]. It has been proved, able to be powered by many ways such as thermal [38, 39], optical [40–42], electrical [43, 44], chemical means [45], and even by more complicated ratchet-like principles [46–48]. Compared with motors in solid bulks and solutions, molecular rotors at solid surfaces have advantages of being easily accessible by external fields [49, 50] and addressable by surface analysis methods [51, 52], as well as being easily organized due to the reduced dimensions. Surface-mounted rotors could be either controlled by molecule–substrate interactions or confined in a supramolecular assembly by intermolecular interaction [53–57]. Thus mastering the properties of molecular rotors bound on surface is a logical step toward their practical utilization.

The development of STM techniques [58, 59] has allowed the study of individual molecules with atomic scale precision and high energy resolution at surfaces. Moreover, STM can offer scientists the opportunity to manipulate atomic and molecular events that operate not only on ensemble-averaged populations of species but also on single functional group of the chemical entities [60–63]. It was previously demonstrated that electron tunneling can induce periodic vibrational [4] and translational motions in molecules [64–66]. STM has been further developed

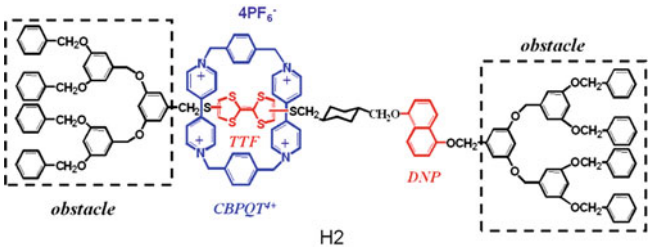

Fig. 1 Structure of the H2 rotaxane molecule

to investigate the dynamic behavior in real time and motion mechanism of molecular motors/machines at single molecule level. The single molecular motors probed on the surface with STM become of particular interest and benefit greatly for such advance.

In this chapter, we will report two different kinds of single molecular motors at surfaces probed with the technique of STM. First, structural and conductance transitions of one H2 rotaxane molecule at the sub-rotaxane scale were studied. It provides the evidence to date that the conductance transition originating from single molecules arises from motion of the encircling ring component along the molecular backbone and correlates with changes in molecular conformation. In the second part, STM was used to investigate single (t-Bu)$_4$-ZnPc molecular rotors on Au(111) substrate. The rotor possesses a well-defined and off-centered rotation axis, and further, these single molecule rotors can self-assemble to form large scale ordered arrays based on the reconstruction of the gold surface.

2 Structural and Conductance Transitions of Single Rotaxane Molecules

2.1 Overview

Rotaxanes, as one kind of inter-locked supermolecules, have been widely investigated in past years because of their good performance in both molecular electronic devices and nanoscale data-storage media [25–31, 67–70]. The key structure of these molecules contains a π-electron-deficient macrocycle that is locked around a π-electron-rich component along the molecular "thread," which is terminated with two bulky "stoppers". Here we are interested in a single H2 rotaxane molecule, whose chemical structure is shown in Fig. 1. The macrocycle is cyclobis(paraquat-p-phenylene)(CBPQT4+), and two recognition sites are TTF and DNP groups. Recent theoretical calculations [34, 35, 71] predicted that the conductance transition originates from the movement of the CBPQT4+ ring along the molecular backbone, but as of yet there has been no experimental verification.

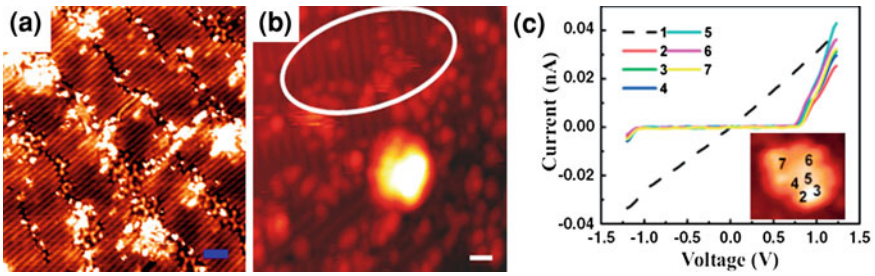

Fig. 2 STM images of **a** CH_2Cl_2 self-assembled monolayer and **b** a H2 rotaxane molecule on it. Scanning conditions are $V_b = -1.3$ V, $I_t = 0.08$ nA. The scale bar is 2.5 nm in **a** and 1.0 nm in (**b**). **c** I–V curves at different points of single rotaxane molecule are roughly the same. Curve 1 is measured on the substrate. Numbers on the inset image indicate the corresponding measuring positions on a molecule. All the STM images and I–V curves are recorded at 78 K. Reprinted with permission from Ref. [72]

In this section, we use low-temperature scanning tunneling microscopy to investigate the structure and conductance of a single H2 rotaxane molecule on a buffer-layered Au(111) substrate at 78 K. It is demonstrated that the conductance switching in rotaxane-based, solid-state devices is an inherent property of the rotaxane molecules. These results provide evidence that the conductance switching might arise from the movement of the cyclobis(paraquat-p-phenylene) ring along the rod section of the dumbbell-shaped backbone of the rotaxane molecule. It provides direct evidence that the conductance transition originates from single molecules and correlates with changes in molecular conformation. We also achieved the reversible writing and erasing of information dots on solid-state H2 rotaxane films at room temperature. Ab initio and molecular mechanics (MM) calculations are employed to explain the transition mechanism.

2.2 Sample Preparation and STM Observations

A sample of a single H2 rotaxane molecule for STM study was prepared on a buffer-layered Au(111) surface. Metal surfaces typically have strong interaction with organic molecules. Such an interaction may hybridize the metal wavefunctions with molecular orbitals and let the molecule lose its intrinsic properties. In our experiments, a self-assembled monolayer (SAM) of CH_2Cl_2 solvent molecules was used as an insulating layer. Such a layer is formed by dropping a CH_2Cl_2 solvent containing H2 molecules on a freshly-prepared Au(111) substrate with the protection of pure N_2 gas. Thereafter, the sample was transferred into an ultrahigh vacuum (UHV) chamber and annealed at 330 K.

Subsequent UHV-STM observations showed high-quality SAM had been achieved, as shown in Fig. 2a. H2 molecules are adsorbed on the SAM film rather than directly on the Au(111) substrate. Fig. 2b shows one H2 molecule in a

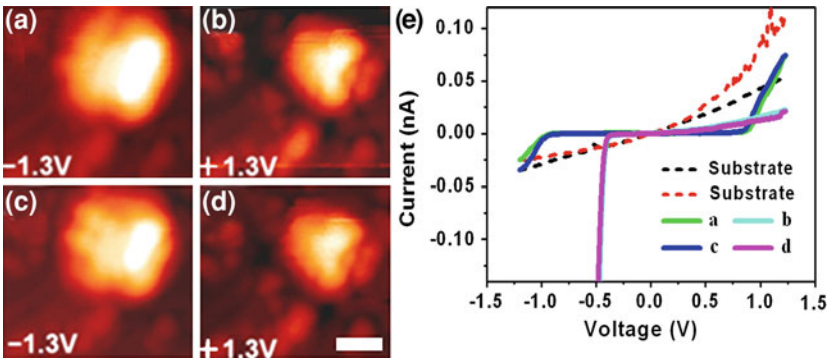

Fig. 3 Reversible conductance transitions induced sequentially in an individual H2 molecule by the STM field. **a–d** STM images show different but consistent forms on sequentially reversing the bias polarity from −1.3 to 1.3 V. The scale bar is 1 nm. **e** I–V characteristics show the molecule is in an insulating state under negative bias and a high-conductance state under positive bias. Reprinted with permission from Ref. [72]

scanning area on a monolayer of ordered solvent molecules. Auger electron spectroscopy reveals that the monolayer contains Cl and C elements, which is consistent with a monolayer of CH_2Cl_2 on the Au(111) substrate [72].

Scanning tunneling spectroscopy (I–V curves) measurements have been conducted on the adsorbed rotaxane molecules. As STM is capable of high-spatial-resolution measurements, we collected I–V data at several different points on a single rotaxane molecule, see Fig. 2c. The obtained I–V curves are almost the same across the molecule, which indicates that the electron tunneling is occurring via the whole molecule. The result agrees with a recent theoretical calculation [34, 35, 71], which pointed out that the tunneling will occur through the whole molecule if these groups are crowded together as in our case.

2.3 Conductance Switching of Single H2 Rotaxane Molecules

The calculations [34, 35, 71] also predicted the existence of two stable molecular configurations with different electronic structures, due to movement of CBPQT4+ between the TTF and DNP groups acting as a switch. We therefore attempted to induce a structure/conductance transition in a single H2 molecule on the surface, and it was realized by varying the polarity of the voltage bias applied between the tip and the sample in the STM experiments. Figure 3 shows STM images acquired sequentially, changing the scanning bias between each image, together with corresponding measured I–V curves. The obtained STM image and its conductance of the H2 molecule change repeatedly with reversing the polarity from −1.3 to 1.3 V. These observations show that conductance switching can be directly observed in a

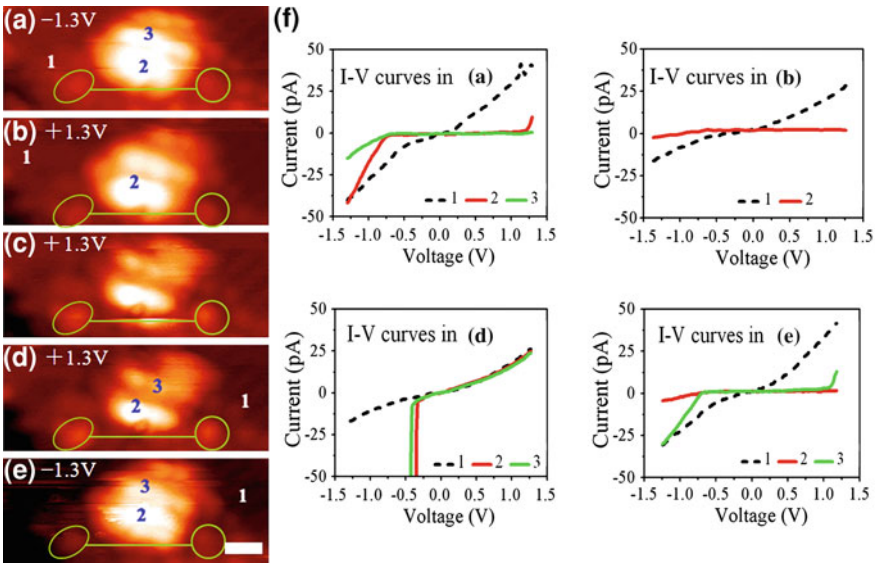

Fig. 4 A sequence of STM images of a single H2 molecule showing a reversible conductance transition correlated with a change in molecular configuration. **a**–**b** STM images obtained with changes of bias polarity from −1.3 to 1.3 V. They show similar configuration, indicating similar HOMO and LUMO distribution. **c** A sudden structure transition happens as the tip approaches the molecule during the next scanning (+1.3 V). **d** The molecule maintains its new conformation at the following scan, but **e** recovers its original configuration when the voltage bias is set back to −1.3 V. The green lines mark features on the substrate for reference; scale bar size is 1 nm. **f** I–V characteristics showing that the conformation change is associated with a transition to a high-conductance state. Numbers on the images represent positions of the I–V measurements. Reprinted with permission from Ref. [72]

single molecule, and the conductance state can be controlled easily and reversibly by changing the voltage polarity.

We next present evidence that the conductance transition is induced by the intramolecular structural transition but not by the difference between the spatial distributions of the lowest unoccupied molecular orbital (LUMO) and highest occupied molecular orbital (HOMO). Figures 4a and b show an example when the voltage bias changes from −1.3 to +1.3 V, but the molecular image and the I–V curve are not immediately changed. I–V curves from the numbered points show that molecule is in its low-conductance state. For the next scanning, however, the STM image captures the instant of change for the molecular conformation (Fig. 4c). The new image is maintained during the subsequent scan (Fig. 4d) and I–V curves show the molecule is now in its high conductivity state. Analysis of the process concludes that the change of the molecular STM image is induced by the structural change instead of the difference between LUMO and HOMO imaging. Finally, we change the bias voltage back to the initial negative polarity and the STM image reappears precisely in its initial state (Fig. 4e), with I–V curves

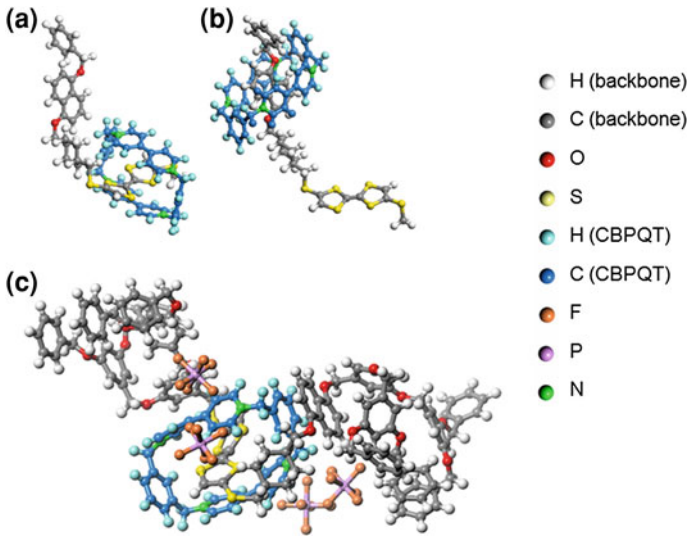

Fig. 5 Fully optimized configuration of a simplified model of the H2 molecule with the CBPQT ring positioned over the TTF group **a** and the DNP group **b**. **c** Molecular mechanics calculation of the entire molecule. All calculations confirm a curved morphology for the molecule

corresponding to the low conductivity state once again. The molecular conformational changes the correlate perfectly and repeatedly with the conductance changes and are fully reversible. This suggests that we are seeing the effects of the intra-molecular structural transition proposed theoretically, specifically the reversible movement of the CBPQT4+ ring, which acts as a switch and induces the conductance transition. Note that, however, not all deposited molecules observed could be switched, implying that, for application in devices, it might be necessary to induce a preferred molecular orientation.

2.4 Understanding the Geometry of Molecules by DFT and MM Calculations

Meanwhile, density functional theory quantum chemistry calculations and molecular mechanics calculations were also performed to understand transitions at an atomistic level. To identify the molecular conformation of a free rotaxane molecule, we carried out fully optimized density functional theory (DFT) calculations and classical force-field calculations. Owing to numerical limitations and the size of the molecule, we initially built two simplified models by removing the two large obstacle groups (as shown in Fig. 1) and the four PF_6^- ligands from the H2 molecule (see Fig. 5a and b). Structure optimization was performed using the Gaussian03 program package at the DFT-B3LYP(3-21G) level31 for these two

models [73]. Whether the CBPQT4+ macrocycle is at TTF or DNP site, the simplified backbone is not linear but curved. In addition, structure optimization for the entire H2 molecule was carried out using molecular mechanics with an MM+ force field [74]. The result shows a curved backbone also (see Fig. 5c). These curved structures indicate that the backbone cannot form a close-packed structure of linear molecules due to steric hindrance. Moverover, the two big obstacles and four ligands strengthen this effect. The curved structure provides more space for CBPQT4+ to move between TTF and DNP. Besides this, the calculation results explain the ellipsoidal appearance of the rotaxane molecules on CH_2Cl_2/Au(111), Rotaxane is a large, flexible molecule that can adopt many possible molecular conformation, some of which facilitate the movement of the CBPQT4+ in the case of individual rotaxane molecules on a solid surface.

2.5 Rotaxane Thin Films for Nanorecording

Beyond the single molecular level, we have also investigated the possibility of inducing conductance transitions in rotaxane Langmuir–Blodgett (LB) thin films [75]. Using the STM tip, we achieved writable, erasable, and rewritable recording by applying different polarity voltage pulses. Throughout this entire process the recording dots remained at about 3 nm in size and were stable in air for more than four weeks. The conductive contact AFM imaging shows that the marks are indeed induced by conductance transitions. Micro-Raman spectra of the rotaxane films before and after the transition from the low-conductance state to the high-conductance state also found that the conductance transition is caused by the intramolecular motion of the CBPQT4+, just as in the case of single rotaxane molecules [76].

3 A Single Molecular Rotor Anchored on Au(111) Solid Surfaces

3.1 Overview

In 1998, Prof. C. Joachim and his cooperators reported for the first time a STM observation on a real single molecular (HB-TC) rotor at solid surface [48]. In the sequel they demonstrated to realize controlling decently a single molecule (HB–NPB, $C_{64}N_2H_{76}$) rotation by a STM tip manipulation with atomic scale precision [77]. The controllability of molecular motion is critical for molecular rotors, which may convert external energy into orchestrated motion at the molecular level [78, 79]. So far most of the molecular rotors reported at surfaces are mobile translationally with either one or two degrees of freedom. For molecular rotors a

high level of control over the rotation axis and, equivalently, self-assembly on a very large scale, are the key ingredients for their integration into complex molecular machines [80]. In addition, the studies mainly focused on single molecules, while it is desirable, for eventual applications, that individual molecular rotors self-assemble into large scale ordered arrays while keeping their original functions.

Our recent STM studies [38] show that single tetra-tert-butyl zinc phthalocyanine [(t-Bu)$_4$ZnPc] molecules on the reconstructed Au(111) surface possess a well-defined rotation axis fixed (i.e. the single molecular rotor is "anchored") on the surface, and also, that these single molecule rotors form large scale ordered arrays due to the reconstruction of the gold surface. Gold adatoms at the surface function as the stable contact of the molecule to the surface. An off-center rotation axis is formed, by a chemical bonding between a nitrogen atom of the molecule and a gold adatom on the surface, which gives them a well-defined contact while the molecules can have rotation-favorable configurations.

3.2 Array of (t-Bu)$_4$-ZnPc Molecular Rotors at Au(111) Surface

The clean Au(111) surface has a well-known $22 \times \sqrt{3}$ herringbone structure [81, 82]. Figure 6a shows typical STM topographic images of this reconstruction structure. The top layer consists of atoms in alternating face-centered cubic (FCC) and hexagonal close-packed (HCP) domains. The width of the FCC region is approximately 50% larger than that of the HCP region. Atoms within the transition region between the FCC and HCP domains appear as bright discommensuration lines (the "ridge" structure) in the STM image. The elbow site is the connection position of ridges.

(t-Bu)$_4$ZnPc is one kind of molecules looking like a windmill with four protruding vanes surrounding an axis (Fig. 6b). Figure 6c shows a STM image of a large scale array of (t-Bu)$_4$ZnPc molecules on Au(111) reconstructed surface. The molecules adsorb predominantly at the elbow positions of the $22 \times \sqrt{3}$ structure, which in this case acts as an atomically precise template for the selective adsorption. Figure 6d shows the detailed configuration of the molecules. Each molecule shows a "folding-fan" structure, which is different from the molecular configuration shown in Fig. 6b. The folding-fan structures at two different elbow sites show different features due to the modulation by corrugation ridges. Further investigation revealed that each folding-fan structure corresponds to one molecule which was rotating at the elbow site. Gold adatoms [83, 84], serving as the stable contact of the molecules to the surface, provide a stationary rotating axis for the molecular rotor. This axis is formed by a chemical bond between a nitrogen atom of the molecule and a gold adatom on the surface, which gives them a well-defined contact while the molecules can have rotation-favorable configurations.

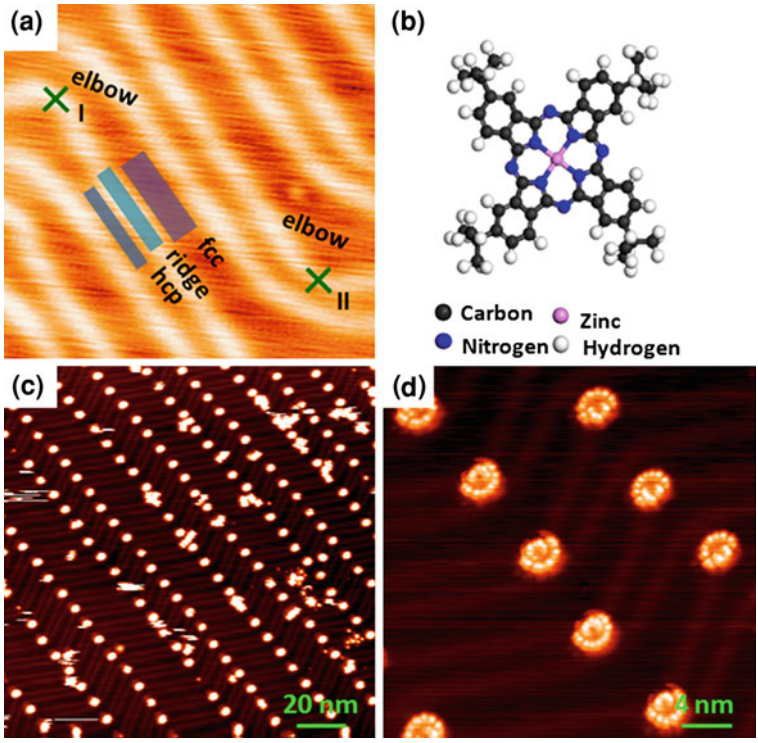

Fig. 6 **a** STM image of a reconstructed clean Au(111) surface, in which four special regions are marked; **b** Structure of a $(t\text{-Bu})_4$ZnPc molecule; **c** STM image of a large scale ordered array of single $(t\text{-Bu})_4$ZnPc molecular rotors on a reconstructed Au(111) surface. **d** High-resolution STM image of single molecular rotors showing a "folding-fan" structure at elbow sites. ($I = 0.07$ nA, $V = -1.3$ V at 78 K)

These single molecular rotors form large scale ordered arrays due to the regular reconstruction of the Au(111) surface. Both the stationary axis and the self-assembly ability of the molecular rotors provide potential application possibility for the development of molecular nanodevices.

3.3 (t-Bu)$_4$-ZnPc Single Molecular Rotors Studied with STM

At very low coverage, $(t\text{-Bu})_4$ZnPc molecules were found adsorbing on different regions of the reconstructed Au(111) surface, elbow, ridge, FCC, and HCP. Appearances of the adsorbates depends to a large extent on the adsorbed surface sites with different atomic arrangements, as shown in Fig. 7. The molecules located at the elbow sites show a folding-fan feature, while the STM images of the molecule located in the FCC, HCP region and on the corrugation ridges, show

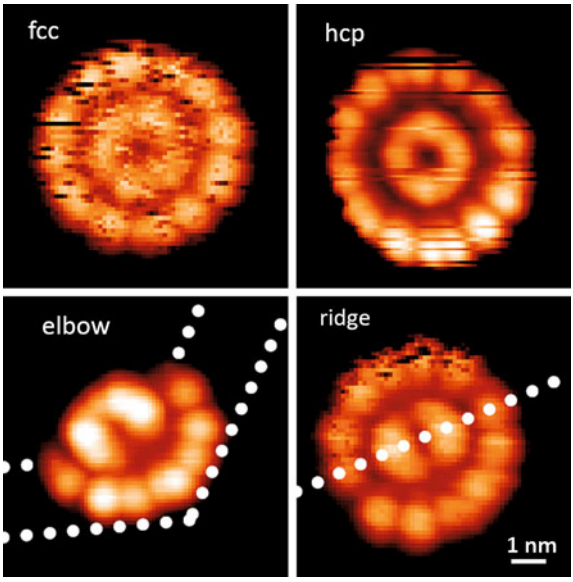

Fig. 7 High-resolution STM images of single molecular rotors, formed by (*t*-Bu)$_4$ZnPc molecules at different substrate regions, show different features due to the modulation by corrugation ridges (0.07 nA, −1.3 V). Images were taken at 78 K

"flower" features. More specifically, STM images of molecules in the FCC and HCP regions are composed of two concentric cirques: twelve bright lobes form the outer torus, just like twelve "petals", while the inner torus has no obvious divisions. Similarly but not completely the same, the STM image of the molecular rotors at the corrugation ridges is composed of an outer torus by twelve bright lobes, but with two inner elliptic protrusions. We need to note that both the folding-fan and flower features can only be seen at temperature of 78 K, while a (*t*-Bu)$_4$ZnPc molecule shows a four-lobe structure in the STM image at 5 K.

The tunneling current versus time (*I*-*t*) spectroscopy was measured by locating the STM tip at a fixed point on the "folding-fan" structure (Fig. 8a). We applied a constant bias voltage of −1.8 V to the sample, and recorded the tunneling current as a function of time. Figure 8b shows the tunneling current curves within a time interval of 80 ms. The amplitude of the current oscillates frequently between 0 and 5 nA. The oscillation provides a direct evidence for that the "folding-fan" feature is really due to rapid molecular motion.

However, an important question remains that how many molecules there are in one "folding-fan" structure. It can be proved that this feature is involved only by one (*t*-Bu)$_4$ZnPc molecule. At 78 K different aggregates of stationary molecular dimers, trimers, tetramers, or larger clusters can be found, however, a stationary single (*t*-Bu)$_4$ZnPc molecule embodying four lobes does not appear in STM images. This indicates that single molecules are not stationary but instable on the surface at this temperature. Besides that, Fig. 9a shows one molecule (marked by white arrow) adsorbed at the elbow position and attached by two large adjacent molecular clusters. By shifting its neighboring molecules in one cluster with a STM tip, the four-lobe structure is changed to a "folding-fan" structure, as shown

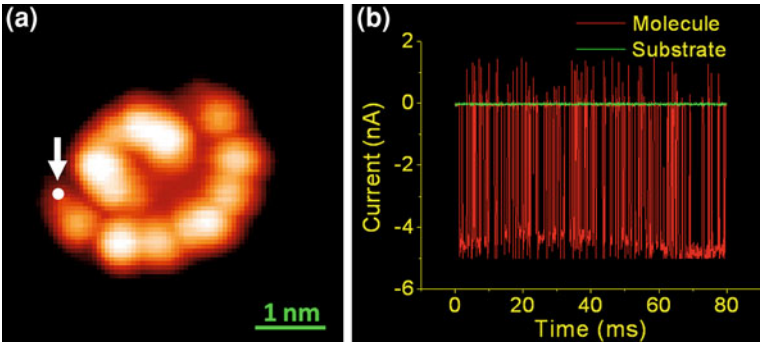

Fig. 8 **a** A high-resolution STM image of single (t-Bu)$_4$ZnPc molecular rotor showing a "folding-fan" feature (0.05 nA, −2 V). **b** Curves of tunneling current versus time (I-t), measured on the molecular rotor (*red curve*) and the substrate (*green curve*). The I-t spectroscopy of the molecule was measured at the position indicated by the arrow in **a**. Reprinted with permission from Ref [38]

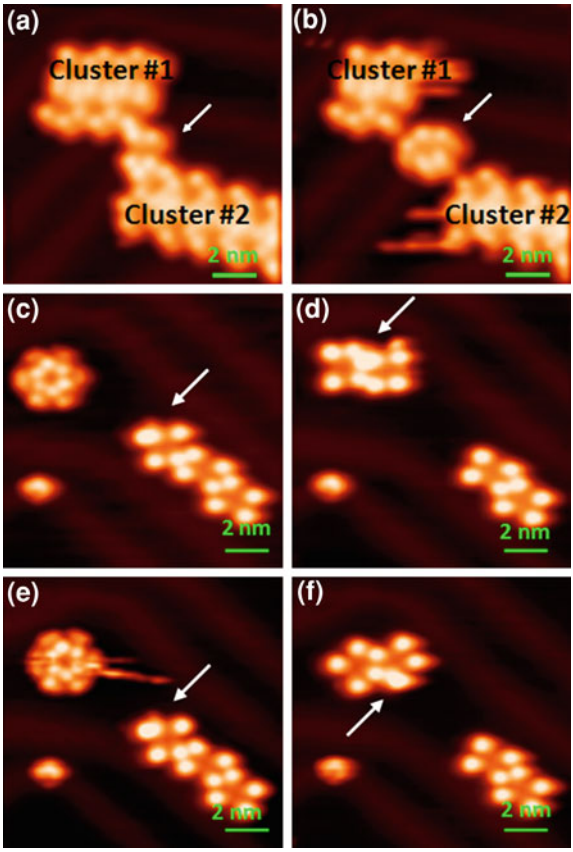

Fig. 9 Sequences of STM images show the manipulation of (t-Bu)$_4$ZnPc molecular rotors on Au(111) surface with a STM tip. The arrowed molecule in **a** remains stationary, due to attaching by two adjacent molecular clusters formed by same molecules. It keeps rotary status while it is released when the blocking molecules were scanned off in **b**. **c**–**f** Show a repeatable process in which the arrowed molecule bounced between a rotating molecule (*up-left*) and a dimer (*bottom-right*), switching the rotor (*up-left*) between rotation and standstill

in Fig. 9b. It is clear that the molecule remains stationary when it is attached by the clusters, but it starts rotation showing the folding-fan feature as soon as it was released from the adjacent clusters.

Another sequence of images shows that such kind of start-stop process is reversible. One molecule (marked with white arrow in Fig. 9c-f) is bounced between the molecular dimer at bottom-right and an individual molecule at up-left. The arrowed molecule can block the rotating molecule (up-left) by forming a new molecular dimer (Fig. 9d), and then this new dimer was dismantled if detaching the arrowed molecule by the STM tip, the original rotary molecule was released and restarted to rotate (Fig. 9e). Reversibly, it remained stationary if it was attached again by the arrowed molecules (Fig. 9f). These manipulations also demonstrate clearly that the folding-fan and flower features are due to the rotation of a single molecule.

The existence of a rotation center is the prerequisite for rotation, otherwise a lateral diffusion of (t-Bu)$_4$ZnPc molecules along the surface would be hard to block at elevated temperatures. The rotation center cannot be at the position of the tert-butyl groups which appear as bright protrusions in STM measurements. Based on the further STM observations combined with the first-principle calculations, we revealed that the rotation center is a trapped gold adatom at the surface. By manipulation with a STM tip, one molecule of the "folding-fan" rotor, located at the elbow position of the Au(111) substrate (Fig. 10a), was removed. A small bright spot at the center position of the molecular rotor was observed, as shown in Fig. 10b. This bright spot, observed after the removal of a single molecule, is proposed as a gold adatom. Metal adatoms are normally considered as evaporates from kinks and steps onto the terraces of the homogeneous metal surfaces [85, 86]. Adatoms are hard to observe alone by STM due to their very high mobility on the metal surface, but they can be trapped by some molecules, like the gold adatoms are captured by the deposited thiol-group-terminated molecule on Au(111) surface [83]. Gold adatoms on the reconstructed gold surface are stable and prefer to adsorb at the elbow sites at 78 K [83], and capable of enhancing the interaction between the adsorbed molecule and the surface, forming a potential energy well that prevents lateral diffusion of the molecule along the surface.

Figure 10c–d shows the top and side view of the optimized configuration for a single (t-Bu)$_4$ZnPc molecule adsorbed on a gold adatom on Au(111) surface. The first-principle calculations show that the distance between the zinc atom and its nearest neighboring gold atom is 4.60 Å, the distance between the bottom nitrogen (colored in yellow) and the gold atom is 2.25 Å; the adsorption energy of this configuration in this case is 804 meV. In contrast, in the case of lack of Au adatom, the calculation results [38] for a single (t-Bu)$_4$ZnPc molecule adsorbed directly on Au(111) show that the distance between the zinc atom and its nearest-neighbor gold atom is 4.35 Å, the distance between the bottom nitrogen atom and its nearest neighboring gold atom 4.40 Å; the adsorption energy of this configuration is 219 meV. Obviously, the gold adatom significantly enhances the molecular bonding, which is most likely due to the surface dipole originating from smeared out electron charge at the position of the adatom [84]. Thus the strong

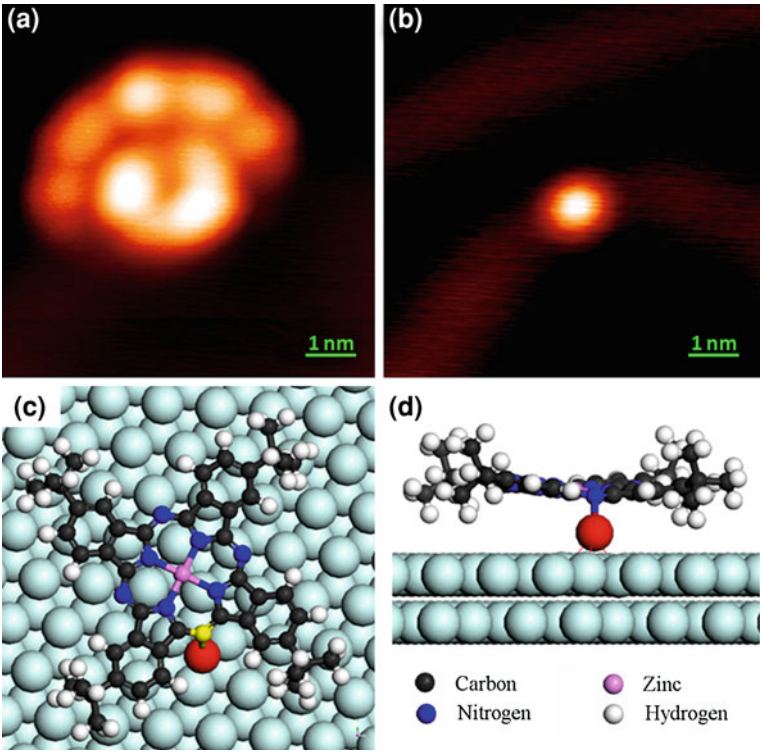

Fig. 10 **a** STM image of a $(t\text{-Bu})_4$ZnPc molecular rotor located at the elbow position of the substrate. **b** STM image after STM manipulation, bright spot indicates a gold adatom after removing the attached molecule. **c-d** Top view and side view of the optimized configuration of a $(t\text{-Bu})_4$ZnPc molecule adsorbed on an Au(111) surface via a gold adatom (colored by *red*), respectively. The adatom acts as an off-center rotation axis for molecular rotation. Reprinted with permission from Ref. [38]

chemical bond between N and Au adatom prevents lateral molecular diffusion along the surface, and in particular offers a fixed off-center axis for the rotation of single $(t\text{-Bu})_4$ZnPc molecules. The experimentally measured distance between the rotor center and the bright lobes on the outer torus is $1.3 \sim 1.4$ nm, in reasonable agreement with the distance between the nitrogen atom and the tert-butyl groups (1.10 ± 0.05 nm), considering that the rotation center is the gold adatom which is not exactly under the nitrogen atom.

For a single $(t\text{-Bu})_4$ZnPc molecular rotor on a flat Au(111) surface, the calculations find that there are twelve stable adsorption configurations, which are 30° apart from each other and can be interpreted as intermediate states. The differences in adsorption energies between these stable configurations are only 10s of meV. The molecule switches between them with high frequency under thermal excitation. Since four tert-butyl groups are imaged as the bright lobes in STM measurements (see Fig. 11a), the proposed STM image for 360° rotation is in good

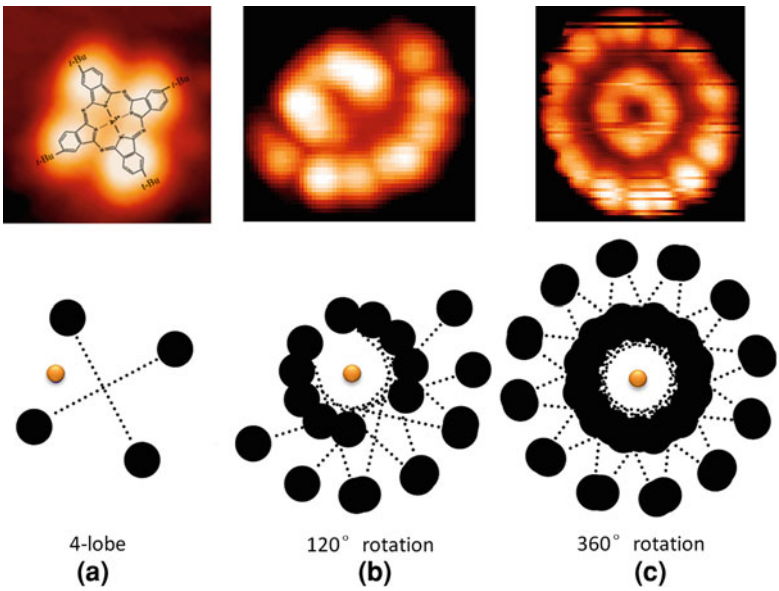

Fig. 11 STM images and schematic drawing of a single (t-Bu)$_4$ZnPc molecule on an Au(111) surface. **a** Stationary molecule looks like four-lobe flower, the image is taken at the sample temperature of 5 K. **b** and **c** rotors with rotation angles of 120 and 360° with the appearance of folding-fan, and flower, respectively. These two images are obtained at 78 K. The black solid circles depict the bright lobes for stationary single molecules, and the yellow circle represents the rotation center (Au adatom)

agreement with the "flower" features observed in the experiments (Fig. 11c). The rotation of single (t-Bu)$_4$ZnPc molecule at the elbow sites can also be interpreted based on the model. The corrugation of the ridges forms barriers for the molecular rotation at the elbow sites. Thus the rotation is limited within an angle of 120°, leading to the "folding-fan" feature, which is in great agreement with the experimental STM image (Fig. 11b). There are two types of elbow sites arranging alternately along the corrugation ridges. The molecular rotation is limited in the FCC region at one type of elbow site, but in the HCP region at the other type of elbow site [see Fig. 6d].

3.4 STM Current Manipulation of a Single Rotor

STM tunneling currents can also affect the rotation of molecular rotors. Figure 12 shows the current dependence of the (t-Bu)$_4$ZnPc molecular rotors. When increasing the tunneling current from a small current of 0.1 nA (Fig. 12a) to a larger one of 0.2 nA (Fig. 12b), the molecule rotates more actively so that the degree of circular arc of the rotation pattern becomes larger, which became more

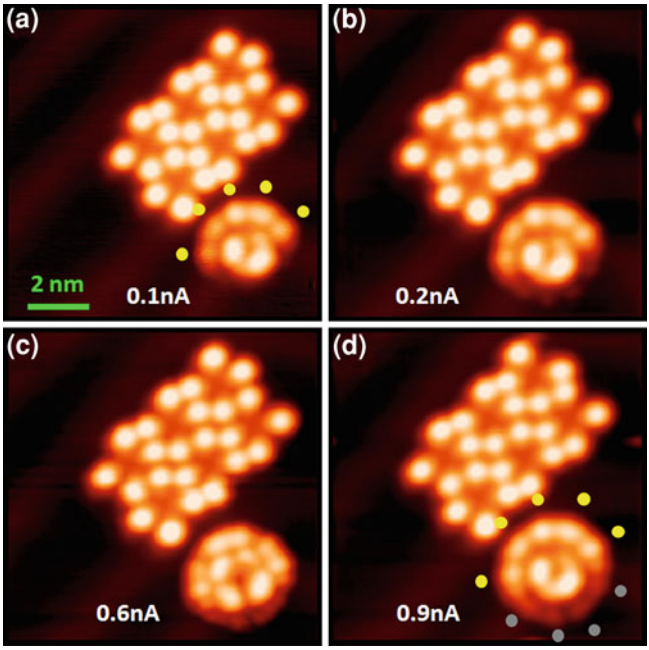

Fig. 12 Sequences of STM images show tunneling current effect on the $(t\text{-Bu})_4$ZnPc molecular rotor when the sample bias kept at −1.3 V. Tunneling current for each image are **a** 0.1 nA, **b** 0.2 nA, **c** 0.6 nA, **d** 0.9 nA, respectively. The molecular rotor can sweep faster and more degree ranges as the tunneling current increases

obvious when the current kept for a period of time (Fig. 12c). When the current is increased to 0.9 nA, a full circle of rotation pattern can be clearly observed (Fig. 12d). This gradual increase in the degree of the circular arc means that the molecular rotation movement becomes more active and can gradually override the barrier formed by the Au(111) reconstruction and covers the whole circle eventually. The above result shows a gradual activation process while increasing the current. Since the molecular rotation can be driven by thermal energy, the STM current provides another way of drives for the molecular rotors.

4 Conclusion

In summary, our investigations at a single H2 rotaxane molecule scale give a better understanding of its structural and conductance transition. The ellipsoidal appearance of the rotaxane molecules was obtained on a buffer layer via self-assembly on Au(111) substrate. The conductance transition of single rotaxane molecule is attributed to the movement of the macrocycle between TTF and DNP groups based on such structure together with ab initio and MM calculations.

The application of rotaxane-based LB thin films in nanorecording is also demonstrated. In order to realize the control of molecular rotors at solid surfaces, a fixed rotation axis is of essential necessity. In the second part, it is inspiring that some functionality has been observed for single molecular rotors. Our data demonstrate single molecular rotation with an off-center rotation axis fixed to surfaces, and self-assembly of molecular rotors into large scale arrays. This is realized by designing the chemical bond between an atom of the molecule and an adatom on the surface. The gold adatom, which provides the fixed rotation axis, can also be used as an atomically well-defined electrode. These results represent a potential step forward in the large scale construction of molecular motors arrays and even the integration of molecular machines.

Acknowledgements We are grateful for S. X. Du, D. X. Shi, Q. Liu, H. G. Zhang,X. Lin, Z. H. Cheng, Z. T. Deng, N. Jiang, W. Ji, J. T. Sun, Y. Y. Zhang for invaluable assistance in experiments and theoretical simulations. This research is supported by Chinese Academy of Sciences, the Natural Science Foundation of China (NSFC) and the Chinese National "863" and "973" projects.

References

1. Eigler, D.M., Lutz, C.P., Rudge, W.E.: An atomic switch realized with the scanning tunnelling microscope. Nature **352**, 600 (1991)
2. Barth, J.V., Costantini, G., Kern, K.: Engineering atomic and molecular nanostructures on surfaces. Nature **437**, 671 (2005)
3. Gao, H.J., Gao, L.: Scanning tunneling microscopy of functional nanostructures on solid surfaces: Manipulation, self-assembly, and applications. Prog. Surf. Sci. **85**, 28 (2010)
4. Svoboda, K., Schmidt, C.F., Schnapp, B.J., Block, S.M.: Direct observation of kinesin stepping by optical trapping interferometry. Nature **365**, 721 (1993)
5. Schliwa, M., Woehlke, G.: Molecular motors. Nature **422**, 759 (2003)
6. Schnitzer, M.J., Block, S.M.: Kinesin hydrolyses one ATP per 8-nm step. Nature **388**, 386 (1997)
7. Atsumi, T., Mccarter, L., Imae, T.: Polar and lateral flagellar motors of marine Vibrio are driven by different ion-motive forces. Nature **355**, 182 (1992)
8. Park, H., Park, J., Lim, A.K.L., Anderson, E.H., Alivisatos, A.P., McEuen, P.L.: Nanomechanical oscillations in a single-C60 transistor. Nature. **407**, 57 (2000)
9. Joachim, C., Gimzewski, J.K., Aviram, A.: Electronics using hybrid-molecular and monomolecular devices. Nature **408**, 541 (2000)
10. Stipe, B.C., Rezaei, M.A., Ho, W.: Inducing and viewing the rotational motion of a single molecule. Science **279**, 1907 (1998)
11. Zheng, X.L., Mulcahy, M.E., Horinek, D., Galeotti, F., Magnera, T.F., Michl, J.: Dipolar and nonpolar altitudinal molecular rotors mounted on an Au(111) surface. J. Am. Chem. Soc. **126**, 4540 (2004)
12. Schliwa, M.: Molecular Motors. Wiley-VCH, Weinheim, Germany (2003)
13. Clayden, J., Pink, J.H.: Concerted rotation in a tertiary aromatic amide: Towards a simple molecular gear. Chem. Int. Ed. **37**, 1937 (1998)
14. Huck, N.P.M., Jager, W.F., de Lange, B., Feringa, B.L.: Dynamic control and amplification of molecular chirality by circular polarized light. Science **273**, 1686 (1996)

15. Bissell, R.A., C′ordova, E., Kaifer, A.E., Stoddart, J.F.: A chemically and electrochemically switchable molecular shuttle. Nature **369**, 133 (1994)
16. Ashton, P.R., Ballardini, R., Balzani, V., Baxter, I., Credi, A., Fyfe, M.C.T., Gandolfi, M.T., Lpez, M.G., Daz, M.V.M., Piersanti, A., Spencer, N., Stoddart, J.F., Venturi, M., White, A.J.P., Williams, D.J.: Acid−Base controllable molecular shuttles. J. Am. Chem. Soc. **120**, 11932 (1998)
17. Bedard, T.C., Moore, J.S.: Design and synthesis of molecular turnstiles. J. Am. Chem. Soc. **117**, 10662 (1995)
18. Kelly, T.R., Tellitu, I., Sestelo, J.P.: In search of molecular ratchets. Angew. Chem. Int. Ed. Engl. **36**, 1866 (1997)
19. Grill, L., Rieder, K.H., Moresco, F., Rapenne, G., Stojkovic, S., Bouju, X., Joachim, C.: Rolling a single molecular wheel at the atomic scale. Nat. Nanotechnol. **2**, 95 (2007)
20. Joachim, C., Tang, H., Moresco, F., Rapenne, G., Meyer, G.: The design of a nanoscale molecular barrow. Nanotechnology **13**, 330 (2002)
21. Jimenez, B.G., Rapenne, G.: Technomimetic molecules: synthesis of a molecular wheel-barrow. Tetrahedron Lett. **44**, 6261 (2003)
22. Shirai, Y., Osgood, A.J., Zhao, Y., Kelly, K.F., Tour, J.M.: Directional control in thermally driven single-molecule nanocars. Nano Lett. **5**, 2330 (2005)
23. Badjic, J.D., Balzani, V., Credi, A., Silvi, S., Stoddart, J.F.: A molecular elevator. Science **303**, 1845 (2004)
24. Van Den Broeck, C., Kawai, R.: Brownian refrigerator. Phys. Rev. Lett. **96**, 210601 (2006)
25. Juluri, B.K., Kumar, A.S., Liu, Y., Ye, T., Yang, Y.-W., Flood, A.H., Fang, L., Stoddart, J.F., Weiss, P.S., Huang, T.J.: A mechanical actuator driven electrochemically by artificial molecular muscles. ACS Nano **3**, 291–300 (2009)
26. Ye, T., Kumar, A.S., Saha, S., Takami, T., Huang, T.J., Stoddart, J.F., Weiss, P.S.: Changing stations in single bistable rotaxane molecules under electrochemical control. ACS Nano **4**, 3697–3701 (2010)
27. Brouwer, A.M., Frochot, C., Gatti, F.G., Leigh, D.A., Mottier, L.C., Paolucci, F., Roffia, S., Wurpel, G.W.H.: Photoinduction of fast, reversible translational motion in ahydrogen-bonded molecular shuttle. Science **291**, 2124 (2001)
28. Serreli, V., Lee, C.-F., Kay, E.R., Leigh, D.A.: A molecular information ratchet. Nature **445**, 523 (2007)
29. Berna, J., Leigh, D.A., Lubomska, M., Mendoza, S.M., Perez, E.M., Rudolf, P., Teobaldi, G., Zerbetto, F.: Macroscopic transport by synthetic molecular machines. Nat. Mater **4**, 704 (2005)
30. Anelli, P.L., Spencer, N., Stoddart, J.F.: A molecular shuttle. J. Am. Chem. Soc. **113**, 5131 (1991)
31. Nguyen, T.D., Leung, K.C.F., Liong, M., Pentecost, C.D., Stoddart, J.F., Zink, J.I.: Construction of a pH-driven supramolecular nanovalve. Org. Lett. **8**, 3363 (2006)
32. Collier, C.P., Mattersteig, G., Wong, E.W., Luo, Y., Beverly, K., Sampaio, J., Raymo, F.M., Stoddart, J.F., Heath, J.R.: A [2]Catenane-based solid state electronically reconfigurable switch. Science **289**, 1172–1175 (2000)
33. Collier, C.P., Jeppesen, J.O., Luo, Y., Perkins, J., Wong, E.W., Heath, J.R., Stoddart, J.F.: Molecular-based electronically switchable tunnel junction devices. J. Am. Chem. Soc. **123**, 12632 (2001)
34. Jang, Y.H., Hwang, S., Kim, Y.H., Jang, S.S., Goddart, W.A.: Density functional theory studies of the Rotaxane component of the Stoddart−Heath molecular switch. J. Am. Chem. Soc. **126**, 12636 (2004)
35. Deng, W.Q., Muller, R.P., Goddard, W.A., III.: Mechanism of the Stoddart−Heath bistable Rotaxane molecular switch. J. Am. Chem. Soc. **126**, 13562 (2004)
36. Rapenne, G.: Synthesis of technomimetic molecules: Towards rotation control in single-molecular machines and motors. Org. Biomol. Chem. **3**, 1165–1169 (2005)
37. Vacek, J., Michl, J.: Artificial surface-mounted molecular rotors: Molecular dynamics simulations. Adv. Funct. Mater. **17**, 730 (2007)

38. Gao, L., Liu, Q., Zhang, Y.Y., Jiang, N., Zhang, H.G., Cheng, Z.H., Qiu, W.F., Du, S.X., Liu, Y.Q., Hofer, W.A., Gao, H.J.: Constructing an array of anchored single-molecule rotors on gold surfaces. Phy. Rev. Lett. **101**, 197209 (2008)
39. Zhong, D., Blomker, T., Wedeking, K., Chi, L., Erker, G., Fuchs, H.: Surface-mounted molecular rotors with variable functional groups and rotation radii. Nano Lett. **9**, 4387 (2009)
40. Vacek, J., Michl, J.: Molecular dynamics of a grid-mounted molecular dipolar rotor in a rotating electric field. Proc. Natl. Acad. Sci. USA **98**, 5481 (2001)
41. Tan, S., Lopez, H.A., Cai, C.W., Zhang, Y.: Optical trapping of single-walled carbon nanotubes. Nano Lett. **4**, 1415 (2004)
42. Berna, J., Leigh, D.A., Lubomska, M., Mendoza, S.M., Perez, E.M., Rudolf, P., Teobaldi, G., Zerbetto, F.: Macroscopic transport by synthetic molecular machines. Nat. Mater **4**, 704 (2005)
43. Petr, K., Tamar, S.: Current-induced rotation of helical molecular wires. J. Chem. Phys. **123**, 184702 (2005)
44. Green, J.E., Wook Choi, J., Boukai, A., Heath, J.R.A., et al.: 160-kilobit molecular electronic memory patterned at 1011 bits per square centimeter. Nature **445**, 414 (2007)
45. Kelly, T.R., De Silva, H., Silva, R.A.: Unidirectional rotary motion in a molecular system. Nature **401**, 150 (1999)
46. Astumian, R.D.: Thermodynamics and kinetics of a brownian motor. Science **276**, 917 (1997)
47. Davis A.P.: Molecular machines: Knowledge is power! Nat. Nanotechnol. **2**, 135 (2007)
48. Gimzewski, J.K., Joachim, C., Schlittler, R.R., Langlais, V., Tang, H., Johannsen, I.: Rotation of a single molecule within a supramolecular bearing. Science **281**, 531 (1998)
49. Bellisario, D.O., Baber, A.E., Tierney, H.L., Sykes, E.C.H.: Engineering dislocation networks for the directed assembly of two-dimensional rotor arrays. J. Phys. Chem. C **113**, 5895 (2009)
50. Van Delden, R.A., ter Wiel, M.K.J., Pollard, M.M., Vicario, J., Koumura, N., Feringa, B.L.: Unidirectional molecular motor on a gold surface. Nature **437**, 1337 (2005)
51. Henningsen, N., Franke, K.J., Torrente, I.F., Sehulze, G., Priewisch, B., Ruck-Braun, K., Dokic, J., Klamroth, T., Saalfrank, P., Pascual, J.I.: Inducing the rotation of a single phenyl ring with tunneling electrons. J. Phys. Chem. C **111**, 14843 (2007)
52. Merz, L., Guentherodt, H.J., Scherer, L.J., Constable, E.C., Housecroft, C.E., Neuburger, M., Hermann, B.A.: Octyl-Decorated Frechet-Type dendrons: A general motif for visualisation of static and dynamic behaviour using STM? Chem. Eur. J. **11**, 2307–2318 (2005)
53. Pollard, M.M., Lubomska, M., Rudolf, P., Feringa, B.L.: Controlled rotary motion in a monolayer of molecular motors. Angew. Chem. Int. Ed. **46**, 1278 (2007)
54. Katsonis, N., Lubomska, M., Pollard, M.M., Feringa, B.L., Rudolf, P.: Synthetic light-activated molecular switches and motors on surfaces. Prog. Surf. Sci. **82**, 407 (2007)
55. Alvey, M.D., Yates, J.T., Uram, K.J.: Electron-stimulated-desorption ion angular distributions of negative ions. J. Chem. Phys. **87**, 7221 (1987)
56. Wintjes, N., Bonifazi, D., Cheng, F.Y., Kiebele, A., Stohr, M., Jung, T., Spillmann, H., Die-derich, F.A.: Supramolecular multiposition rotary device. Angew. Chem. Int. Ed. **46**, 4089 (2007)
57. Baber, A.E., Tierney, H.L., Sykes, E.C.H.: Quantitative single-molecule study of thioether molecular rotors. ACS Nano **2**, 2385 (2008)
58. Binnig, G., Rohrer, H.: Scanning tunneling microscopy. Helv. Phys. Acta. **55**, 726 (1982)
59. Binnig, G., Rohrer, H.: Scanning tunneling microscopy—from birth to adolescence. Rev. Mod. Phys. **59**, 615 (1987)
60. Gimzewski, J.K., Joachim, C.: Nanoscale science of single molecules using local probes. Science **283**, 1683 (1999)
61. Stroscio, J.A., Eigler, D.M.: Atomic and molecular manipulation with the scanning tunneling microscope. Science **254**, 1319 (1991)
62. Avouris, P.: Manipulation of matter at the atomic and molecular-levels. Acc. Chem. Res. **28**, 95 (1995)
63. Rosei, F., Schunack, M., Naitoh, Y., Jiang, P., Gourdon, A., Laegsgaard, E., Stensgaard, I., Joachim, C., Besenbacher, F.: Properties of large organic molecules at surfaces. Prog. Surf. Sci. **71**, 95 (2003)

64. Mikkelsen, K.V., Ratner, M.A.: Synthesis and properties of viologen functionalized poly(3-alkylthienylenes). Chem. Rev. **87**, 113 (1987)
65. Kral, P.: Nonequilibrium linked cluster expansion for steady-state quantum transport. Phys. Rev. B **56**, 7293 (1997)
66. Kaun, C.C., Seideman, T.: Current-driven oscillations and time-dependent transport in nanojunctions. Phys. Rev. Lett. **94**, 226801 (2005)
67. Mendes, P.M., Flood, A.H., Stoddart, J.F.: Nanoelectronic devices from self-organized molecular switches. Appl. Phys. A **80**, 1197 (2005)
68. Jang, S.S., Jang, Y.H., Heath, J.R., et al.: Structures and properties of self-assembled monolayers of bistable Rotaxanes on Au (111) surfaces from molecular dynamics simulations validated with experiment. J. Am. Chem. Soc. **127**, 1563 (2005)
69. Flood, A.H., Peters, A.J., Vignon, S.A., Steuerman, D.W., Tseng, H.R., Kang, S., Heath, J.R., Stoddart, J.F.: The role of physical environment on molecular electromechanical switching. Chem. Eur. J. **10**, 6558 (2004)
70. Cavallini, M., Biscarini, F., León, S., Zerbetto, F., Bottari, G., Leigh, D.A.: Information storage using supramolecular surface patterns. Science **299**, 531 (2003)
71. Kim, Y.H., Jang, S.S., Jang, Y.H., Goddard, W.A., III.: First-principles study of the switching mechanism of [2]Catenane molecular electronic devices. Phys. Rev. Lett. **94**, 156801 (2005)
72. Feng, M., Gao, L., Du, S.X., Deng, Z.T., Cheng, Z.H., Ji, W., Zhang, D.Q., Guo, X.F., Lin, X., Chi, L.F., Zhu, D.B., Fuchs, H., Gao, H.J.: Observation of structural and conductance transition of Rotaxane molecules at a submolecular scale. Adv. Funct. Mater **17**, 770 (2007)
73. Frisch, M.J., Trucks, G.W., Pople, J.A. et al.: Gaussian 03, revision C.02. Gaussian Inc., Wallingford, CT (2004)
74. Allinger, N.L.: Conformational analysis. 130. MM2. A hydrocarbon force field utilizing V1 and V2 torsional terms. J. Am. Chem. Soc. **99**, 8127 (1977)
75. Feng, M., Guo, X.F., Lin, X., He, X.B., Ji, W., Du, S.X., Zhang, D.Q., Zhu, D.B., Gao, H.J.: Reproducible nanorecording on rotaxane thin films. J. Am. Chem. Soc. **127**, 15338 (2005)
76. Feng, M., Gao, L., Deng, Z.T., Ji, W., Du, S.X., Guo, X.F., Zhang, D.Q., Zhu, D.B., Gao, H.J.: Reversible, erasable, and rewritable nanorecording on an H2 Rotaxane thin film. J. Am. Chem. Soc. **129**, 2204 (2007)
77. Chiaravalloti, F., Gross, L., Rieder, K.H., Stojkovic, S.M., Gourdon, A., Joachim, C., Moresco, F.: A rack-and-pinion device at the molecular scale. Nat. Mater **6**, 30 (2007)
78. Browne W.R., Feringa B.L: Making molecular machines work. Nat. Nanotechnol. **1**, 25 (2006)
79. Kay, E.R., Leigh, D.A., Zerbetto, F.: Synthetic molecular motors and mechanical machines. Angew. Chem. Int. Ed. **46**, 72–191 (2007)
80. Kottas, G.S., Clarke, L.I., Horinek, D., Michl, J.: Artificial molecular rotors. Chem. Rev. **105**, 1281–1376 (2005)
81. Woell, C., Chiang, S., Wilson, R.J., Lippel, P.H.: Determination of atom positions at stacking-fault dislocations on Au(111) by scanning tunneling microscopy. Phys. Rev. B **39**, 7988 (1989)
82. Barth, J.V., Brune, H., Ertl, G., Behm, R.J.: STM observations on the reconstructed Au(111) surface—atomic-structure, long-range superstructure, rotational domains, and surface-defects. Phys. Rev. B **42**, 9307 (1990)
83. Maksymovych, P., Sorescu, D.C., Yates, J.T., Jr.: Gold-adatom-mediated bonding in self-assembled short-chain alkanethiolate species on the Au(111) surface. Phys. Rev. Lett. **97**, 146103 (2006)
84. Peter, M., Dan, C.S., John Yates, T., Jr.: Phys. Rev. Lett. **97**, 146103 (2006)
85. Limot, L., Kröger, J., Berndt, R., Garcia-Lekue, A., Hofer, W.A.: Atom transfer and single-adatom contacts. Phys. Rev. Lett. **94**, 126102 (2005)
86. Perry, C.C., Haq, S., Frederick, B.G., Richardson, N.V.: Face specificity and the role of metal adatoms in molecular reorientation at surfaces. Surf. Sci. **409**, 512 (1998)
87. Röder, H., Hahn, E., Brune, H., Bucher, J.P., Kern, K.: Building one-dimensional and two-dimensional nanostructures by diffusion-controlled aggregation at surfaces. Nature **366**, 141 (1993)